In-situ observations of compressible turbulence in planetary magnetosheaths and solar wind

Lina Hadid

To cite this version:

Lina Hadid. In-situ observations of compressible turbulence in planetary magnetosheaths and solar wind. Astrophysics [astro-ph]. Université Paris Saclay (COmUE), 2016. English. NNT : 2016SACLS255 . tel-01425307

HAL Id: tel-01425307
https://theses.hal.science/tel-01425307v1

Submitted on 3 Jan 2017

NNT: 2016SACLS255

Université Paris-Saclay
École Doctorale d'Astronomie et d'Astrophisique
d'Île-de-France (ED127)

THÈSE DE DOCTORAT

Spécialté: Physique des Plasmas

Soutenue par

Lina Hadid

Observations in-situ de la turbulence compressible dans les magnétogaines planétaires et le vent solaire

---

Directeurs: **Fouad Sahraoui** et **Patrick Canu**

Préparée au

Laboratoratoire de Physique des Plasmas (LPP), École Polytechnique

soutenue le 20 Septembre, 2016

Jury:

Président :	M. Frédéric Moisy	-	Professeur (Université Paris-Sud - FAST)
Reviewers :	M. Thierry Passot	-	Directeur de recherche (Observatoire de Nice)
	M. William Matthaeus	-	Professeur (University of Delaware)
Advisor :	M. Fouad Sahraoui	-	Directeur de recherche (Ecole Polytechnique - LPP)
Examinators :	Mme Karine Issautier	-	Directeur de recherche (Observatoire de Meudon - LESIA)
	M. Vincent Genot	-	Astronome (Université Paul Sabatier - IRAP)
Invited :	M. Patrick Canu	-	Directeur de recherche (Ecole Polytechnique - LPP)
	M. Eric Buchlin	-	Chargé de recherche (Université Paris-Sud - IAS)

University of Paris-Saclay

Doctoral school of Astronomy & Astrophysics of Paris Area

PHD THESIS

Specialty: **Plasma Physics**

Defended by

Lina Hadid

In-situ observations of compressible turbulence in planetary magnetosheaths and the solar wind

---

Advisors: **Fouad Sahraoui** & **Patrick Canu**

Prepared at the

Laboratory of Plasma Physics (LPP), Ecole Polytechnique

defended on the 20th of September, 2016

Jury:

President :	M. Frédéric Moisy	-	Professeur (Université Paris-Sud - FAST)
Reviewers :	M. Thierry Passot	-	Directeur de recherche (Observatoire de Nice)
	M. William Matthaeus	-	Professeur (University of Delaware)
Advisor :	M. Fouad Sahraoui	-	Directeur de recherche (Ecole Polytechnique - LPP)
Examinators :	Mme Karine Issautier	-	Directeur de recherche (Observatoire de Meudon - LESIA)
	M. Vincent Genot	-	Astronome (Université Paul Sabatier - IRAP)
Invited :	M. Patrick Canu	-	Directeur de recherche (Ecole Polytechnique - LPP)
	M. Eric Buchlin	-	Chargé de recherche (Université Paris-Sud - IAS)

We shall not cease from exploration
and the end of all our exploring
will be to arrive where we started
and know the place for the first time.
T. S. Eliot's Little Gidding.

To my Zafer Hadid.

Abstract

Among the different astrophysical plasmas, the solar wind and the planetary magnetosheaths represent the best laboratories for studying the properties of fully developed plasma turbulence. Because of the relatively weak density fluctuations ($\sim 10\%$) in the solar wind, the low frequency fluctuations are usually described using the incompressible MHD theory. Nevertheless, the effect of the compressibility (in particular in the fast wind) has been a subject of active research within the space physics community over the last three decades.

My thesis is essentially dedicated to the study of compressible turbulence in different plasma environments, the planetary magnetosheaths (of Saturn and Earth) and the fast and slow solar wind. This was done using in-situ spacecraft data from the Cassini, Cluster and THEMIS/ARTEMIS satellites.

I first investigated the properties of MHD and kinetic scale turbulence in the magnetosheath of Saturn using Cassini data at the MHD scales and compared them to known features of the solar wind turbulence. This work was completed with a more detailed analysis performed in the magnetosheath of Earth using the Cluster data. Then, by applying the recently derived exact law of compressible isothermal MHD turbulence to the in-situ observations from THEMIS and CLUSTER spacecrafts, a detailed study regarding the effect of the compressibility on the energy cascade (dissipation) rate in the fast and the slow wind is presented. Several new empirical laws are obtained, which include the power-law scaling of the energy cascade rate as function of the turbulent Mach number. Eventually, an application of this exact model to a more compressible medium, the magnetosheath of Earth, using the Cluster data provides the first estimation of the energy dissipation rate in the magnetosheath, which is found to be up to two orders of magnitude higher than that observed in the solar wind.

Keywords: Turbulence, compressible turbulence, astrophysical plasmas, solar wind, planetary magnetosheaths, Earth, Saturn, in-situ observations

Résumé

Parmi les différents plasmas spatiaux, le vent solaire et les magnétogaines planétaires représentent les meilleurs laboratoires pour l'étude des propriétés de la turbulence. Les fluctuations de densité dans le vent solaire étant faibles, à basses fréquences ces dernières sont généralement décrites par la théorie de la MHD incompressible. Malgré son incompressibilité, l'effet de la compressibilité dans le vent solaire a fait l'objet de nombreux travaux depuis des décennies, à la fois théoriques, numériques et observationnels.

Le but de ma thèse est d'étudier le rôle de la compressibilité dans les magnétogaines planétaires (de la Terre et de Saturne) en comparaison avec un milieu beaucoup plus étudié et moins compressible (quasi incompressible), le vent solaire. Ce travail a été realisé en utilisant des données in-situ de trois sondes spatiales, Cassini, Cluster et THEMIS B/ARTEMIS P1.

La première partie de mon travail a été consacrée à l'étude des propriétés de la turbulence dans la magnétogaine de Saturne aux échelles MHD et sub-ionique, en comparaison avec celle de la Terre en utilisant les données Cassini et Cluster respectivement. Ensuite j'ai appliqué la loi exacte de la turbulence isotherme et compressible dans le vent rapide et lent en utilisant les données THEMIS B/ARTEMIS P1, afin d'étudier l'effet et le rôle de la compressibilité sur le taux de transfert de l'énergie dans la zone inertielle. Enfin, une première application de ce modèle dans la magnétogaine de la Terre est présentée en utilisant les données Cluster.

Mots clés: Turbulence, turbulence compressible, plasmas astrophysiques, vent solaire, magnétogaines planétaires, Terre, Saturne, analyse de données

Acknowledgments

My experience at the Laboratory of Plasma Physics (LPP) has been nothing short of amazing. This thesis represents not only my work at the keyboard, it is a milestone in 3 years of work within the space plasma group. My research has been also the result of many experiences I have encountered in the lab and on the campus from dozens of remarkable individuals who I also wish to acknowledge.

At first, I could not have finished my work without the help and patience of my dear supervisor Dr. Fouad Sahraoui who gave me the opportunity to work with him even before my PhD, since my master internship and has been supportive since then. Fouad, I would like to express my sincere gratitude, for your confidence, patience and encouragements. Your scientific insights, advices, and remarks have always guided me to progress in my work, not to forget the scientific arabic that you taught me!

I would like to thank as well to Dr. Patrick Canu for his fruitful comments on the use of the Cassini data and on this manuscript. Prof. Sebastien Galtier and Dr. Supratik Banerjee with whom I got to work in the last part of my thesis and I had the chance to "see" the turbulence problem from a theoretician point of view, a different angle than a data analysist. Dr. Shiyong Huang for the fruitful collaboration on analyzing the Cluster data. Dr. Ronan Modolo who enlighted me regarding the pointing problem of the CAPS on Cassini and gave me his code to recompute the ion velocity in the field-of-view of the intsrument. I have to mention and thank as well Dr. Thierry Passot for the interesting discussions we had, Dr. Vincent Génot and Dr. Adam Masters for providing me the Cassini data events that I used during my work, and for their valuable scientific advices.

I must recognize that this work would have not been possible without the support of the the doctoral school of Astronomy and Astrophysics (ED127), and the University of Paris-Sud.

I would like to thank as well all the members of the jury for their participation and for evaluating this work, in particular the referees for their interest in carefully reading and commenting my manuscript.

Dozens of people have helped and taught me immensely at LPP: Gerard Belmont with whom I had the opportunity to learn how to use WHAMP, who shared not only his wide knowledge in plasma phyics, but also in music and theater. Rodrigue, who was ready to answer my frequent questions at any time. Dr. Olivier Le Contel with whom I worked on the calibration of the Search-Coils, he shared his expertise and took his time explaining me all the technical and instrumental issues regarding the calibration procedure. Dr. Alessandro Retino, for his contributions and motivations. Nahuel Andres for helping with latex. Dr. Dominique Fontaine, the Co-Investigator of PEACE on Cluster, who explained to me some calibration issues regarding the instrument. Colette Jan, Marylin Bazin, Cherifa Ighoud, for their priceless administrative and personal support. Nicolas Marsac, Stephane Ravenel, Philippe Auvrey, for their technical support.

A special thanks to Dr. Khurom Kiyani, with whom I had the chance to share my office and profit from his deep knowledge and special lessons about data analysis, plasma turbulence but also life. To Patrick Robert, who has been a main source of invaluable motivation and support since I started working at LPP. Alexis Jeandet who introduced me to Python and shared his unique and massive knowledge in programming, I thank him as well for his great and inspiring suggestions and comments.

Part of the data analysis was done with the AMDA science analysis system provided by the Centre de Données de la Physique des Plasmas (CDPP) supported by the CNRS and the CNES. So I thank them for this practical platform, that helped me choosing and ploting the data.

A warm thanks also for my friends and colleagues in the lab: Sergey Stepanyan, Sergey Sherbanev, Alexandros Chasapis, Claudia Rossi, Sumire Kobayashi, Malik Mansour, Ralph Katra, Alexis Jeandet, Pierre Morel, Pascaline Grondin, Katy Ghantous, Christelle Barakat, and the great evennings we spent "Chez Richard". I would also like to humbly thank the various undergraduate students of the physics dept who, through the course of tutoring them, helped me learn some of the physics I should have learnt when I was an undergraduate.

Not to forget of course Eva, Anais and Iyad, with whom I shared the flat for almost three years, during all my PhD period. I thank you "froomies" for the many amazing memories I have now with you and for all the great and priceless times we lived and spent together!!! My close lebanese friends, Iman, Hiba, Julie, Violette, Angy, Nidale, I thank you so much for your daily encouragements, and for making me feel home especially with the great food you prepared!

I would like also to thank my running team (Michael Molle, Catherine Sarazin, Vanessa Moreau), who motivated me to keep on running and exercising, in order to de-stress during the toughest period of writing my thesis.

Last but not least!! A big thanks to my family (Elham, Iraj, Lama & Jawad) and especially my parents Mrs Nabila Faraj and Mr. Zafer Hadid, for all their countless and unique contributions, encouragements and sacrifices since my childhood. Mum and dad, I dedicate this work to you.

Abbreviations

ACE Advanced Composition Explorer

AIC Alfvén Ion Cyclotron

AMDA Automated Multi Dataset Analysis

AMPTE Active Magnetospheric Particle Tracer Explorers

ARTEMIS Acceleration Reconnection Turbulence and Electrodynamics of the Moon's Interaction with the Sun

ASI Agenzia Spaziale Italiana

AU Astronomical Unit

BG13 Banerjee & Galtier 2013

C09 Carbone et al. 2009

CAPS Cassini Plasma Spectrometer

CETP Centre d'Etude des Environnements Terrestre et Planétaires

CIR Corotating Interaction Region

CIS Cluster Ion Spectrometer

CNES Centre National d'Etudes Spatiales

CNRS Centre National de la Recherche Scientifique

CODIF Composition Distribution Function

CSA Cluster Science Archive

ED Ecole Doctorale

EFI Electric Field Instrument

EFW Electric Field and Waves

ELS Electron Spectrometer

EM Engineering Model

EMIC Electromagnetic Ion Cyclotron

ESA European Space Agency

ESAs Electrostatic analyser

FAST Fluides Automatique et Systèmes Thermiques

FFT Fast Fourrier Transform

FGM Fluxgate Magnetometer

FM Flight Model

GMC Giant Molecular Clouds

GPS Global Positioning System

GSE Geocentric Solar Ecliptic

GSM Geocentric Solar Magnetospheric

HBR High Bit Rate

HIA Hot Ion Analyser

IAS Institut d'Astrophysique Spatiale

IBS Ion Beam Spectrometer

IDL Interactive Data Language

IDPU Instrument Data Processing Unit

IK Iroshnikov-Kraichnan

IMS Ion Mass Spectrometer

IRAP Institut de Recherche en Astrophysique et Planétologie

IRF Institutet for RymdFysik

IRM Ion Release Module

ISM Interstellar Medium

JPL Jet Propulsion Laboratory

KAW Kinetic Alfvén Waves

KRTP Kronocentric Coordinate system

KSM Kronocentric Solar Magnetospheric

LATMOS Laboratoire Atmosphères Milieux Observations Spatiales

LESIA Laboratoire d'Etudes Spatiales et d'Instrumentation en Astrophyisque

LFR Low Frequency Receiver

LPP Laboratoire de Physique des Plasma

MAG Magnetometer

MFA Mean Field Aligned

MFR Medium Frequency Receiver

MHD Magnetohydrodynamics

MMS Magnetospheric Multiscale

MS Magnetosheath

MSSL Mullard Space Science Laboratory

NASA National Aeronautics and Space Administration

NBR Normal Bit Rate

NEMI Noise Equivalent Magnetic Induction

NI Nearly Incompressible

PDF Probability Density Function

PDS Planetary Data Science

PEACE Plasma Electron and Current Experiment

PIC Particle In Cell

PP98 Politano and Pouquet 1998

PSD Power Spectral density

RPWS Radio and Plasma Waves Science

SA Spectrum Analyser

SCM Search-Coils Magnetometer

SNG Single

SST Solid State Telescope

STAFF Spatio-Temporal Analysis of Field Fluctuations

SW Solar Wind

THEMIS Time History of Events and Macroscale Interactions during Substorms

ToF Time of Flight

UCL University College London

ULF Ultra Low Frequency

VAP Van Allen Probes

VDF Velocity Distribution Function

WFR Waveform Receiver

WHAMP Waves in Homogeneous Anisotropic Magnetized Plasma

WHISPER Waves of HIgh frequency Sounder for Probing the Electron density by Relaxation

Contents

List of Figures

List of Tables

Part I

Turbulence in space and astrophysical plasmas.

Chapter 1

Introduction

Contents

1.1 Turbulence overview

Turbulence is ubiquitous in the universe; it is almost the rule in flowing fluids. In everyday life, the turbulent motion covers a wide range of time and scales: it is observed in any disturbed **hydrodynamical fluid** (tap water, smoke rising from a cigarette or a fire, large-scale structure of the atmospheric circulation, etc...), **in plasma laboratories** (Laser- matter interactions, nuclear fusion reactors) and in **astrophysical plasmas** (e.g, the solar wind streaming outward from our Sun, magnetospheric plasmas and the interstellar medium). Other than the usual hydrodynamical fluids and space plasmas, turbulence is also believed to occur in other fields like **quantum mechanics** [Proment *et al.*, 2009], **non-linear optics and dynamics** [Garnier *et al.*, 2012; Parker *et al.*, 2015] and in **vibrational mechanics** [Barba & Velasco Fuentes, 2008]. From the quantum scales up to the macroscopical ones, turbulence is characterized by the formation/presence of randomly moving eddies (Figure 1.1).

It is often claimed that there is no good definition of turbulence [Tsinober, 2001], and most of the time we are inclined to forego a formal definition in favor of intuitive characterizations. In a general way, one can associate turbulence to a "disorder", "disturbance", "complexity", "chaos", "unpredictability", or "non-linearity" in space and time. Turbulence is actually the process by which a fluid attempts to self-organize its energy. Hence an important advantage of turbulent flows is their ability to mix the transported quantities (via convection) much more rapidly than if only molecular diffusion were involved. Certainly this latter property is crucial for people interested in turbulence because of its practical applications. Engineers for instance are mainly concerned with the knowledge of the turbulent heat diffusion coefficients. Turbulence is also essential for the weather and climate forcasting, especially that with climate change, it is a key for understanding the heat exchange between the ocean and the atmosphere. Perhaps even market fluctuations [Mandelbrot, 1999] may benefit from a better understanding of the problem of turbulence. Yet, despite its importance, turbulence largely remains an "unsolved" problem in the sense that a clear physical understanding of the observed phenomena does not exist. Indeed we still do not understand in complete detail how or why turbulence occurs, nor can we predict turbulent behavior with any degree of reliability, even in very simple flow situations. And worse, we even disagree about what we think we know about it.

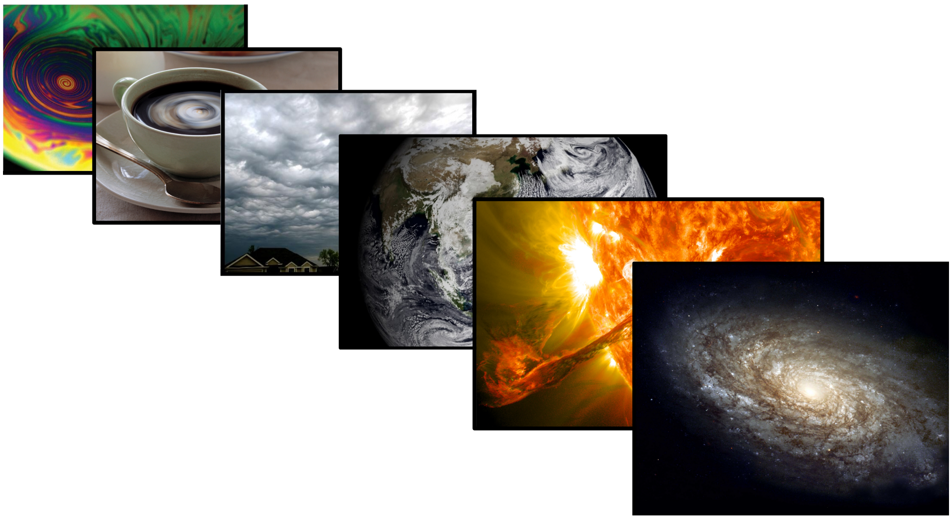

Figure 1.1: From left to right: turbulent motions in thin film of soapy water, in coffee, in clouds, in the atmosphere, in the Sun and in the galaxy.

From the theoretical point of view, turbulence was described by three different and overlapping "Movements" termed as: *statistical*, *structural* and *deterministic* [Chapman & Tobak, 1985]. The statistical approach was motivated by the view that turbulence must surely be random and unpredictable, and so encouraged focusing the observations on the means and higher order statistics. The structural movement was basically dominated by observations, mainly those of coherent structures and vortices or eddies which are, as we have seen in the introduction, the building blocks in the turbulent analysis. Finally, the deterministic era pioneered by the work of Poincaré [1899], essentially began with the work of Lorenz [1963]. Lorenz discovered via numerial computation the presence of "strange attractors" which became later a model for turbulence (Figure 1.2). He understood that even though the non-linear dynamical systems are deterministic, it is still not possible to predict exactly the state of the flow on a giving instant due to the high sensitivity to initial conditions. Despite the long and fundamental debate regarding the deterministic or stochastic nature of turbulence, we note that for describing the physics of turbulence, these three movements are complementary to each other. Turbulence is indeed characterized by large numbers of degrees of freedom which is seen for example when numerous spatial scales are excited non-linearly. However, from the statistical point of view, it is possible to predict the turbulent behavior, the reason for which it is important to study turbulence with statistical tools, as we will see in Chapter 2.

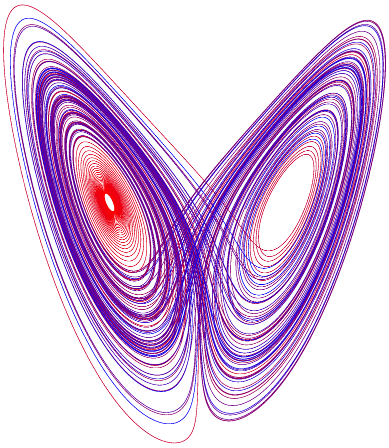

Figure 1.2: A solution in the Lorenz attractor.

1.2 Physical context: the solar wind and planetary magnetospheres

Among the different astrophysical plasmas, the solar wind and the planetary magnetospheres represent the best laboratories for studying the properties of a fully developed plasma turbulence. The reason for this being the availability of high quality in-situ data (fields and particles) from different space missions, in particular those orbiting in near-Earth space such as Cluster, THEMIS, Wind and more recently MMS [Burch *et al.*, 2016]. Obviously, distant astrophysical plasmas are not accessible to those direct measurements, but these latter are also hardly available in laboratory plasmas, such as in tokamaks because direct measurements are generally perturbed by the instruments, their size being of the order of the physical scales involved. In space plasmas, the size of the spacecraft ($\sim 1-4$ m diameter) is much smaller than the Debye length (~ 100 m) which implies that measurements can be done without being affected by the spacecraft itself. Moreover, some of the space missions are multispacecraft (four satellites in the case of Cluster and MMS, and five in the case of THEMIS), which allows us to make simultaneous measurements in different locations of space and, therefore, to disentangle spatial from temporal variations of the fields and plasma fluctuations. The multispacecraft configuration allows us as well to explore the 3D spatial structures of complex phenomena such as turbulence and magnetic reconnection [Sahraoui *et al.*, 2006; Matthaeus *et al.*, 2005; Retinò *et al.*, 2007] and to compute spatial gradients of quantities such as the magnetic field **B** and plasma flow velocity **V**, yielding key quantities like the electric current **J** and the vorticity ω. Last but not least, the near-Earth space and the planetary magnetospheres cover a wide range of values of the plasma parameters (e.g., the plasma $\beta = V_{thi}/V_A$, the Alfvén Mach number $M_A = V_{flow}/V_A$ and turbulent Mach number $\mathcal{M}_s = \sqrt{\delta v^2/Cs^2}$, where $V_{thi} = \sqrt{2KT_i/m_i}$ is ion the termal speed, $V_A = B_0/\sqrt{\mu_0 n_0 m_i}$ represents the Alfvén speed, V_{flow}, the flow velocity, δv, the velocity fluctuations, Cs the ion sound speed. K, T_i, m_i, B_0, μ_0, n_0 are respectively, the Boltzmann constant, the ion temperature, the ion mass, the background magnetic field, the vacuum permeability, and the plasma density), which allow us to extrapolate the results obtained in these regions to other astrophysical plasmas that have (or thought to have) similar values (See table 1.1).

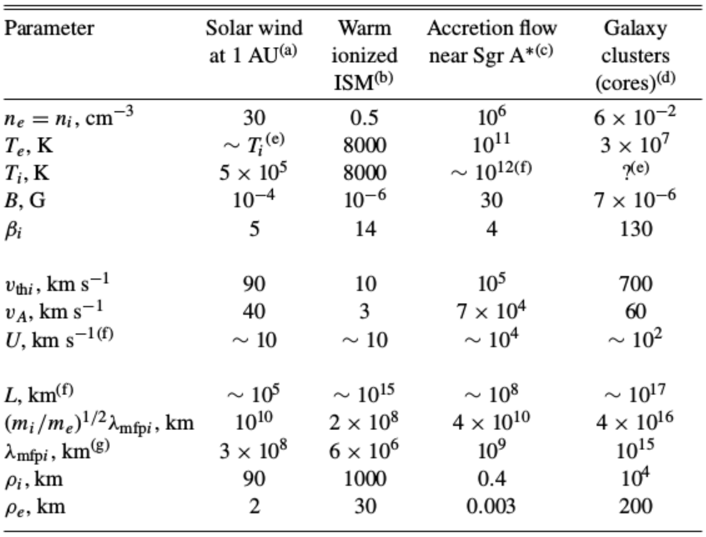

Parameter	Solar wind at 1 AU$^{(a)}$	Warm ionized ISM$^{(b)}$	Accretion flow near Sgr A*$^{(c)}$	Galaxy clusters (cores)$^{(d)}$
$n_e = n_i$, cm^{-3}	30	0.5	10^6	6×10^{-2}
T_e, K	$\sim T_i^{(e)}$	8000	10^{11}	3×10^7
T_i, K	5×10^5	8000	$\sim 10^{12(f)}$	$?^{(e)}$
B, G	10^{-4}	10^{-6}	30	7×10^{-6}
β_i	5	14	4	130
v_{thi}, km s^{-1}	90	10	10^5	700
v_A, km s^{-1}	40	3	7×10^4	60
U, km s$^{-1(f)}$	~ 10	~ 10	$\sim 10^4$	$\sim 10^2$
L, km$^{(f)}$	$\sim 10^5$	$\sim 10^{15}$	$\sim 10^8$	$\sim 10^{17}$
$(m_i/m_e)^{1/2}\lambda_{mfpi}$, km	10^{10}	2×10^8	4×10^{10}	4×10^{16}
λ_{mfpi}, km$^{(g)}$	3×10^8	6×10^6	10^9	10^{15}
ρ_i, km	90	1000	0.4	10^4
ρ_e, km	2	30	0.003	200

Table 1.1: Typical parameters for astrophysical plasmas. Adapted from [Schekochihin *et al.*, 2009].

1.2.1 The solar wind

The solar wind is a stream of ionized particles that comprises ionized hydrogen (96%), a small proportion (4%) of ionized helium and a small fraction of heavy ions like Fe, Si and O [Bame *et al.*, 1968, 1975]. It is continuously blowing out from the solar corona into the interplanetary space to terminate somewhere in the interstellar space around 120 AU (Astronomical Unit $\sim 150 \times 10^6$ km). It originates from the solar atmospheric plasma which is untrapped by the stretched out magnetic field lines, the so-called coronal holes. The magnetic field configuration prevent the solar wind to be radially symmetric even far away from the complex coronal loops. As a result, it is generally classified into two categories: The fast solar wind with an average velocity between 500 km/s and 800 km/s and the slow solar wind between

300 km/s and 400 km/s at 1 AU. The origin of those two types of winds is still debated, however, the fast wind apparently emanates from the magnetically open coronal holes which are representative of the inactive Sun at the polar region [Hassler *et al.*, 1999]. The slow wind on the contrary is generally ejected from lower solar latitudes, the equatorial zone of the Sun [McComas *et al.*, 2000].

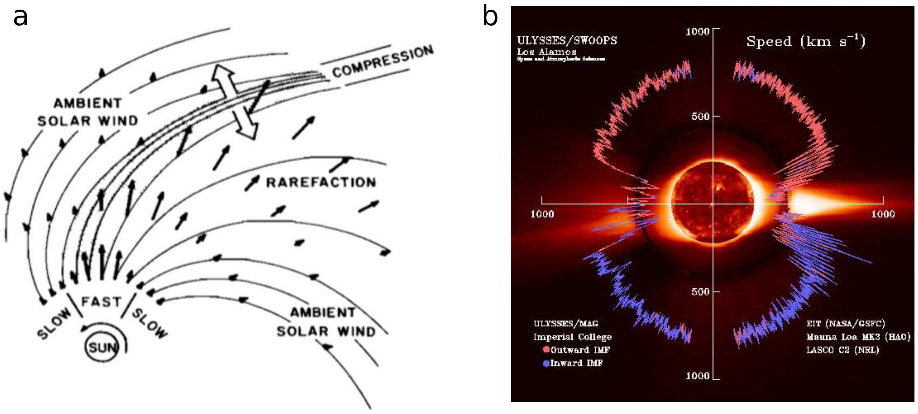

Figure 1.3: (a) Fast and slow solar wind resulting in compression zone because of the solar rotation (adapted from Pizzo [1978]), (b) The different solar wind speed and the magnetic field polarity observations from the Ulysses spacecraft (adapted from McComas *et al.* [1998]).

The acceleration process of the fast wind is still not fully understood and cannot be fully explained by Parker's theory. In fact, the latter predicts a velolcity of 500 km/s for a coronal temperature of around 10^6 K, but in reality the speed of the fast wind is around 700 km/s for a lower temperature at the coronal holes ($\sim 10^5$ K). It has been suggested that some acceleration processes related to the dissipation of high frequency Alfvén waves could explain the higher wind speed [Tu & Marsch, 1997]. The origin of the slow wind is also unclear. One can see in Figure 1.3 (b) that the slow wind emanates from the equatorial belt which is magnetically complex.
The fast and the slow winds have generally different plasma and thermodynamic properties:

1. The density in the slow wind is higher than that in the fast wind, and so its mass flow (ρv) gets even higher than the fast one.

2. The fast wind is relatively stationnary and displays slower changes with time, while the slow one is highly variable.

3. Because of the solar rotation, the fast wind catches up the slow wind forming a compression region characterized by high density and magnetic field regions with spirals in the solar equatorial plane that corotate with the Sun, hence the name Corotating Interaction Regions (CIRs) (Figure 1.3 (a)). At large

heliocentric distances the pressure waves bounding a CIR commonly steepen into a shock front [Gosling & Pizzo, 1999].

4. Interestingly, data from Helios showed that the proton temperature parallel to the magnetic field in the slow wind drops more rapidly with the radial distance than in the fast flow [Marsch *et al.*, 1982] (Figure1.4 (a)).

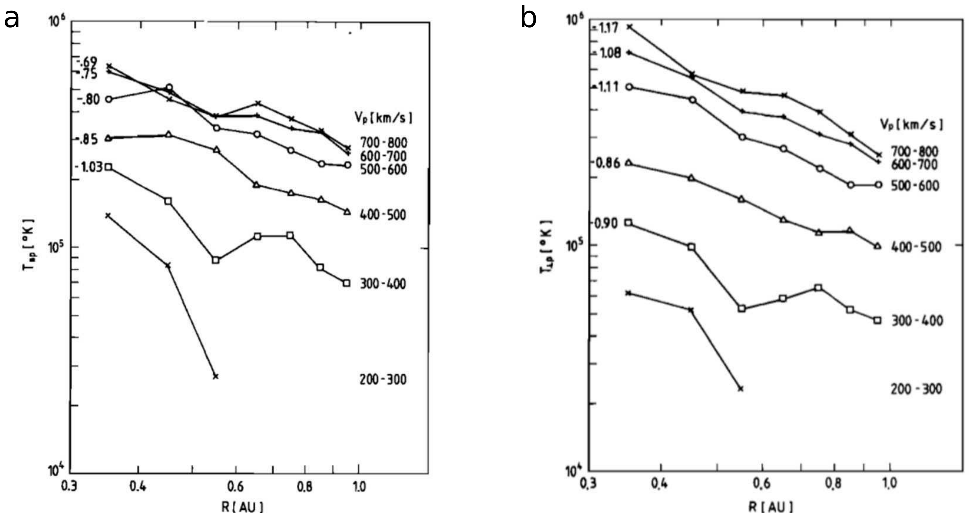

Figure 1.4: Dependence of the proton (a) parallel and (b) perpendicular temperatures on the radial distance from the sun. Adapted from Marsch *et al.* [1982].

The perpendicular temperature exhibits a steeper radial decline than the parallel one with no differences regarding the solar wind speed. In any case, a weaker than adiabatic cooling was observed which suggests that local heating processes or heat conduction are occuring (Figure 1.4 (b)). This has been shown as well by Gazis & Lazarus [1982]; Richardson *et al.* [1995] using Voyager 2 data. Looking for a possible mechanism for the local heating of the solar wind has been one of the major motivation in studying plasma turbulence in it. Indeed, a major characteristic of the solar wind is being a collisionless (or weakly collisional) plasma. This makes the use of classical viscous terms in the turbulence equations (as usually done in fluid turbulence) irrelevant. Therefore, it is turbulence that is expected to play a leading role, through the small scales it creates in the plasma, in the processes of dissipation at kinetic scales (e.g., [Schekochihin *et al.*, 2009]). This is supported both by clear signatures of turbulence, in particular, power-law spectra of the magnetic flucutations that have been reported since the late sixties [Coleman Jr., 1968]. However, the processes by which turbulence dissipates energy into particle heating (or acceleration) remain hotly debated nowadays. The debate is indeed very polarized between those who think that wave-particle interactions (e.g., Landau-damping, cyclotron resonance) play a significant role in the processes of dissipation in collisionless plasmas (e.g.,Leamon *et al.* [1998]; Passot & Henri [2007];

Howes *et al.* [2008*a*]; Schekochihin *et al.* [2009]; Sahraoui *et al.* [2009, 2010]; Gary *et al.* [2012]) and those who do not call into play those processes and rather argue in favor of localized dissipation. This latter can occur via magnetic reconnection within the current sheets that form naturally in turbulent plasmas (Matthaeus & Goldstein [1986]; Matthaeus *et al.* [2005]; Osman *et al.* [2011*a*]; Karimabadi *et al.* [2014]). Note however that this view is called into question by other authors who argue that wave-particles interactions can still play a role within the reconnection regions (Loureiro *et al.* [2013]; Howes [2015]). These questions will not be further developed in this thesis.

1.2.2 Planetary magnetospheres

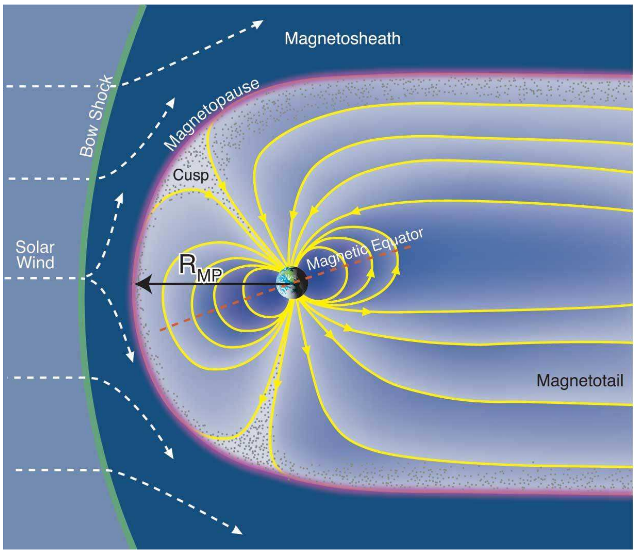

Figure 1.5: Schematic of the terrestrial magnetosphere showing the distended field lines of both day and night side magnetospheres. R_{MP} denotes the distance to sub-solar magnetopause. © Fran Bagenal & Steve Bartlett.

The highly turbulent solar wind while travelling in the heliosphere encounters the planets with their magnetic fields, which it compresses and shapes into planetary magnetospheres. The term magnetosphere was first coined by Gold [1959] as the name for *"the region above the ionosphere in which the magnetic field of [Earth] has a dominant control over the motions of gas and fast charged particles"*. It quickly took a broader connotation, as being the region of space around a central object held by its own gravity in which the objects' magnetic field has a dominant influence on the dynamics of the local medium. Qualitatively, one can define a planetary magnetosphere as the volume of space from which the solar wind is excluded by the planet's magnetic field. However, this definition is far from being precise. Firstly, because most of the time the solar wind is never totally excluded from the region

around the planet and, secondly, even if the central object is umagnetized or weakly magnetized its interaction with the magnetic field of the environment, say the solar wind, may create a magnetospheric-like system (like the planets Venus, Mars or Saturn's moon Titan, and Jupiter's moon Io, or even the interaction of a comet with the solar wind). On a much larger scale the entire heliosphere can be described as a magnetospheric-like system produced by the interaction of the sun (the central object) and the interstellar medium (the external medium). A basic configuration of a planetary magnetosphere is presented in Figure 1.5.
The ionized solar wind, is diverted around the magnetosphere. It actually hits the strongly magnetized planets magnetosphere and since it is super-Alfvénic and super sonic a *bow-shock* is formed (analogous to the sonic boom in supersonic aerodynamic flow past an obstacle). As a consequence, behind the bow shock, the shocked solar wind is slowed down, compressed and heated. The bounding surface of the magnetosphere is called the *magnetospause*. The magnetopause is defined as the discontinuity of the magnetic field, the region where the direction of the magnetic field changes: inside the magnetopause the controlling magnetic field is that of the planet, while outside it is the solar wind magnetic field. The region between the bow-shock and the magnetopause is called the *magnetosheath*, a term first introduced by Dessler & Fejer [1963]. Whatever are the details of the interaction between the solar wind and the magnetospheres, in nearly all cases, the interaction region has a magnetotail that can extend for long distance (several $R_p \equiv$ planet radius) in the night side of the magnetosphere.

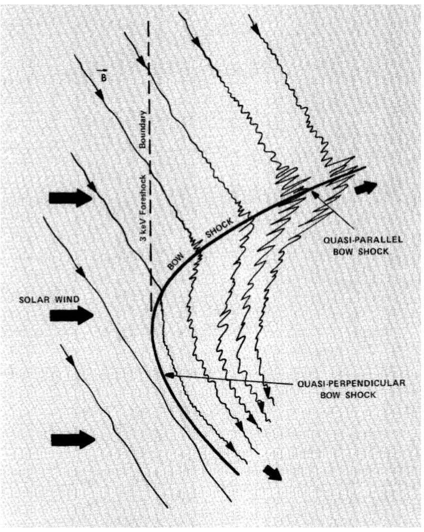

Figure 1.6: Schematic representation of a quasi-parallel and a quasi-perpendicular bow-shock.

The curved nature of the bow shock means that at a given position and time one can distinguish between two different types of geometries determined by the angle between the normal to the shock and the interplanetary magnetic fields $\Theta_{\mathbf{Bn}}$ (see Figure 1.6). In a quasi-perpendicular shock, ($\Theta_{\mathbf{Bn}} \sim 90°$), usually referred as "quiet magnetosheath" the transition in the plasma properties upstream and downstream the shock is abrupt. Whereas in a quasi parallel shock ($\Theta_{\mathbf{Bn}} \sim 0°$ or $180°$), which is referred to as "disturbed magnetosheath" the transition is "fuzzier" (or broader) and characterized by large-amplitude magnetic field, velocity and density fluctuations. Noting that these boundaries are dynamically unstable (due essentially to the change in the dynamical pressure of the solar wind) and were shown to control some properties of the turbulence within the magnetosheath [Sahraoui *et al.*, 2006; Yordanova *et al.*, 2008]. They are also the cause that generates various wave phenomena, instabilities and large scale inhomogeneities (e.g., Kelvin-Helmotz instability [Hasegawa *et al.*, 2004]).
One of the reasons that makes the magnetosheath important in magnetospheric physics is that it is the interface of the solar wind-magnetosphere interaction, affecting the physical processes occurring within the magnetopause. It is in fact the magnetosheath magnetic field and plasma that interact with the magnetopause and, consequently with the magnetosphere. Therefore, studying the properties of turbulence in the magnetosheath should help to better understand the dynamical coupling between the solar wind and the magnetosphere by improving the current reconnection models at the magnetopause (e.g.,Belmont & Rezeau [2001]). Indeed, most of those models consider a large scale "laminar" current sheet in which magnetic reconnection proceeds to allow the solar wind particules to penetrate into the magnetosphere [Lundin *et al.*, 2003]. A more realistic model would be to consider the effects of turbulence in the upstream (magnetosheath) region whose properties remain to be determined. In addition to the relevant role of the magnetosheath turbulence to the problems of particles transfer through the magnetopause, its compressible nature (as we will see in the course of this thesis) makes it also relevant for a better understanding of other highly compressible astrophysical media that spacecraft cannot reach such as the interstellar medium or the supernova remnants [Vázquez-Semadeni *et al.*, 1996]. Furthermore, the fact that the magnetosheath is a bounded region, on one side by the bow shock and on the other side by the magnetopause, makes it useful to study the effect of large scales boundaries on the nature of the turbulence properties as we will see in Chapter 4.

1.3 Motivations and outline.

The main goal of my thesis is to study the properties of the compressible fluctuations in different plasma environments, the planetary magnetosheaths (particularly of Saturn and Earth) in order to compare them with the most studied and known one, the solar wind. This is essentially an observational work that uses in-situ spacecraft data (fields and particles) from three missions, Cassini (magnetosheath of Saturn), Cluster (magnetosheath of Earth) and THEMIS B/ARTEMIS P1 (in the solar wind at 1 AU). The comparative studies conducted during this thesis on the properties of turbulence in those different plasma environments could help developing (when possible) a unified description of the turbulence physics and phenomenology that is applicable to a variety of different systems.

The first motivation of this work was to explore the turbulence properties in the magnetosheath of Saturn from the MHD scales down to the electron ones using the set of plasma and wave instruments available for the first time in the Saturn's environment. The waves instruments (gathered within the consortium of RPWS that will be described in Section 4.1.2) include in particular the tri-axial Search-Coil magnetometer (built by LPP), which measures the high frequency magnetic field fluctuations. Prior to the arrival of Cassini-Huygens mission to Saturn in 2004, there were no dedicated mission to orbit continuously around this planet. Indeed, Saturn's magnetoshpere was visited only 3 times by spacecraft which were only rapid flybys: Pioneer 11 in 1979, Voyager 1 in 1980 and Voyager 2 in 1981. The properties of turbulence around Saturn remained therefore almost entirely unexplored.
The interest in exploring the plasma turbulence near Saturn lies in its plasma conditions: it has more tenuous density and magnetic field, yielding a higher plasma β, Alfvén and turbulent Mach numbers that are not available for near-Earth space (see Table 1.2). The Mach numbers could indeed reach very high values (up to ~ 100) comparable to the ones expected in highly compressible astrophysical media such as supernova remnants or accretion disks [Masters *et al.*, 2013]. Making comparative studies between Earth and Saturn should allow us to study turbulence in wide range of plasmas conditions, which could serve as a proxy for studies of astrophysical turbulence that spacecraft cannot reach.

Distance (A.U.)	0.5 (Mercury)		1 (Earth)		10 (Saturn)	
	SW	**MS**	**SW**	**MS**	**SW**	**MS**
n (cm^{-3})	6	50	4	12	0.005	0.5
B_0 (nT)	6	70	5	20	0.5	2
T_i (eV)	18	600	50	250	5	300
ρ_i (km)	17	50	200	95	700	1800
β_i	1	4	3	6	0.05	13
M_A	4	1	6	2	15	7
$\mathcal{M}_s$	–	–	0.05	0.2	–	–

Table 1.2: Typical (approximated) plasma parameters at different radial distances in the solar wind and in different planetary magnetosheaths (the density (n), background magnetic field (B_0), ion Larmor radius ($\rho_i = V_{th_i}/2\pi f_{ci}$ where $f_{ci} = qB_0/2\pi m_i$ is the ion gyro-frequency), the ion plasma (β_i), the Alfvénic Mach number ($M_A = V_{flow}/V_A$) and the turbulent Mach numbers ($\mathcal{M}_s = \sqrt{\delta v^2/Cs^2}$)).

As we will see in the course of this thesis, the importance of compressible fluctuations in the planetary magnetosheaths in comparison with the solar wind raises questions about the applicability of the theoretical models based on incompressible MHD turbulence, which have been used to investigate large scale solar wind to planetary magnetosheaths turbulence and so underlies the need to develop more realistic models to explore those complex media. While a realistic model of turbulence that would include kinetic effects or plasma instabilities (both observed in the magnetosheath, see e.g., Sahraoui *et al.* [2006]) remains out of reach, the new exact law for compressible isothermal MHD turbulence derived by Banerjee & Galtier [2013] provides the most general theoretical framework available to analyze the effect of compressibility in turbulent plasmas. I first used the model in a weakly compressible medium, namely the (fast and slow) solar wind, which has been extensively studied in the past three decades using the incompressible MHD model of Politano & Pouquet [1998], before applying it to a more compressible (and more complex) medium that is the magnetosheath of Earth.

Throughout my thesis, using in-situ spacecraft data from the Cassini, Cluster and THEMIS B/ARTEMIS P1 satellites, I tried to answer the following questions ordered in three separate categories:

- What are the scaling laws of the magnetosheath turbulence at MHD and kinetic scales ? Are they "universal" or do they depend on the local (or distant) plasma conditions ?
- What is the nature of the plasma fluctuations (Alfvénic ? magnetosonic ?) that carry the energy cascade from the MHD to the sub-ion scales in the magnetosheath ? How do they compare with the solar wind observations ?
- What is the role of the compressible fluctuations in the solar wind and the magnetosheath ? How do they affect the cascade (dissipation) rate ? Do they influence the spatial anisotropy of the turbulence ? How do they depend on the turbulent Mach number ? Is the Iroshnikov-Kraichnan phenomenology applicable in compressible MHD turbulence or a new phenomenology is needed to characterize the energy cascade ?

I tried to write my thesis from a pedagogical point of view so to make it accessible and useful to advanced researchers who want to know some specific details regarding these three points, but also for students and new researchers in the field.

My thesis is organized into two main parts. The first one is focused on the main properties of turbulence in space and astrophysical plasma. It consists of 3 chapters, including this introduction. Chapter 2 gives an overview regarding the main theoretical concepts of incompressible hydrodynamical turbulence (basic definitions, spectral properties, phenomenologies and exact laws) and for incompressible and compressible MHD turbulence. Moreover a summary of the main statistical tools that I used in my work and are used for turbulence studies in general, is presented.

Chapter 3 gives a brief overview of the main observational, theoretical and numerical works of turbulence done in the solar wind and the magnetosheaths of Earth and Saturn (scaling laws, wave modes identification, mono/multifractlity, and compressibility).

Part II focuses on my research work on compressible turbulence in the planetary magnetosheaths and the solar wind. It divides into three chapters as well: Chapter 4 is dedicated to the investigation of the magnetosheath of Saturn using Cassini data, and so the properties of turbulence are studied with a comparison to the mostly known ones in the solar wind. Those results are accompanied with a more detailed analysis performed in the magnetosheath of Earth using Cluster data. Data selection and caveats are addressed as well with a brief overview regarding the different plasma and the waves instruments I used from Cassini spacecraft. Chapter 5, using the exact compressible model of isothermal MHD turbulence, I present the effect and the role of the compressibility in the fast and the slow wind separately using the THEMIS B/ARTEMIS P1 spacecraft data. Eventually, in Chapter 6, I show the first application of this model to a more compressible medium, the magnetosheath of Earth, using Cluster data, with a preliminary study regarding the scaling properties of turbulence.

In Chapter 7, I give a brief summary of the main results and discuss some open and new questions raised by my thesis work. I end up with my perspectives by proposing some other possible observational and numerical works.

CHAPTER 2

Theoretical Background

Contents

The goal of this second chapter is to present briefly the theoretical background on which my research work is based. I show how the theoretical works first done in incompressible hydrodynamics (hereafter HD) and MHD were refined taking into account compressibility.
The chapter consists of three main sections. Section 1 is focused on the fundamental concepts of hydrodynamical turbulence, "the less complicated" theory in turbulence we know. Section 2, points out the main statistical tools for studying turbulence. Section 3, deals with the three exact laws and the corresponding phenomenologies (when present) derived for incompressible HD [Kolmogorov, 1941], MHD [Politano & Pouquet, 1998], and compressible MHD [Banerjee & Galtier, 2013].

2.1 Fully developed turbulence

The beginning of the scientific studies of turbulence is marked with Osborne Reynolds observations of transition from a laminar to a turbulent flow in water pipe [Reynolds, 1883]. His observations led to the identification of a single dimensionless parameter, called the Reynolds number, and denoted:

$$R_e = \frac{UL}{\nu} \tag{2.1}$$

Where U and L are respectively a "*typical*" (average) velocity and scale of the flow, and ν is the kinematic viscosity of the flow.

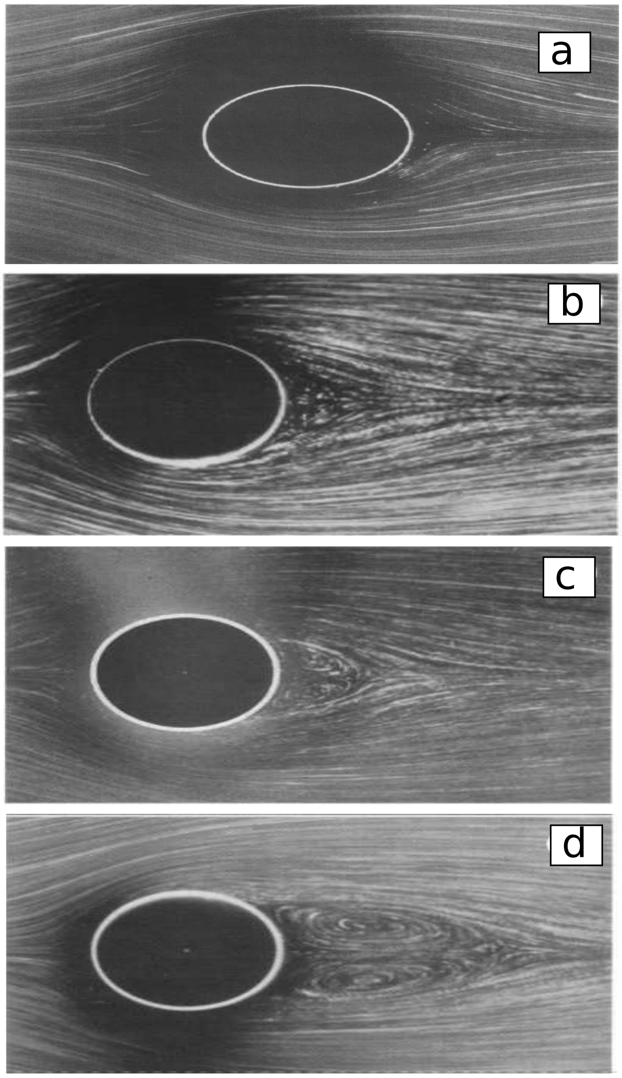

Figure 2.1: Transition from a (a) laminar to a (d) turbulent regime as function of the Reynolds number R_e for a flow passing a cylindrical obstacle. a) $R_e = 1.54$, b) $R_e = 9.6$, c) $R_e = 13.1$, d) $R_e = 26$. Adapted from Frisch [1995].

On Figure 2.1 we see how the flow passes from laminar to a fully developed state when the Reynolds number R_e increases to $\gg 1$. We recall that R_e expresses the relative importance of inertial and viscous forces. A heuristic argument emerges by comparing the inertial and the dissipation terms of the Navier-Stokes equations (2.2) for incompressible fluids ($\rho = constant$):

$$\begin{gathered}\nabla \cdot \mathbf{u} = 0 \\ \frac{\partial \mathbf{u}}{\partial t} + (\mathbf{u} \cdot \nabla)\,\mathbf{u} = -\nabla P + \nu \nabla^2 (\mathbf{u}) + F\end{gathered} \tag{2.2}$$

where $(\mathbf{u}.\nabla)\,\mathbf{u}$ represents the nonlinear (in velocity) term, $\nu\nabla^2(\mathbf{u})$ corresponds to the viscous term, ∇P denotes the pressure gradient and F represents the external force injecting the energy. The nonlinear and the viscous terms have dimensions respectively $\frac{[U^2]}{[L]}$ and $\nu\frac{[U]}{[L^2]}$. The nonlinear term clearly dominates over the viscous term when

$$R_e = \frac{[L][U]}{\nu} \gg 1 \tag{2.3}$$

In the Kolmogorov phenomenology, the previous argument defines the inertial range characterizing the turbulent cascade: it is characterized by the range of scales where dissipation is negligible in comparison with the nonlinear effect and also much smaller than energy containing scales. The energy is therefore transfered through scales with a cascade rate that is constant in the inertial range. This cascade rate equals the rate at which energy is injected at the largest scale into the system and the rate at which it is dissipated at the very small scales. The estimation of this cascade rate for compressible turbulence in the solar wind and the magnetosheath is part of my thesis work.

2.2 Structure functions and intermittency

A self-consistent statistical tool to characterize a random turbulent process is the probability density function (PDF) $\mathcal{P}(v)$ of a continuous random variable like the velocity v of a fluid element, which is defined as $\mathcal{P}(v)dt = P(t < v < t + dt)$.
For a given turbulent process, the velocity fluctuations at different spatial scales ℓ can be approximated by the increments, defined as:

$$\delta v_\ell(t) = v_\ell(x+\ell) - v_\ell(x) \tag{2.4}$$

As a consequence, the relative likelihood of the turbulent process at different scales ℓ can be investigated by estimating the probability density $\mathcal{P}(\delta v_\ell)$. We will see in Chapter 4 how the behaviour and the shape of the PDFs play an essential role in characterizing the multifractal character of the turbulence.

Multifractality is a phenomenon in which a system cannot be reproduced by a magnification of some part of it: zooming in and zooming out in the system reveals the irregular variation of the dynamics even if it is apparently periodic and chaotic. In other words, multifractality characterizes large sharp fluctuations in the turbulent fields. In order to describe statistically those bursty events, higher order moments of $\mathcal{P}(\delta v_\ell)$ are needed.
The n-th moment of a probability distribution function is obtained by integrating the appropriate power of a random variable over all possible values. If the variable represents the increments at the different scales ℓ defined in Equation (2.4), the statistical moments of the different orders are called the structure functions:

$$S_n(\ell) =< (\delta v_\ell(x))^n >= \int_{-\infty}^{+\infty} \mathcal{P}(\delta v_\ell(x))(\delta v_\ell(x))^n dx \tag{2.5}$$

The different moments give information about the shape of the probability density function, and *vice versa*. One can easily see that the *zero*-th order moment of the structure function is the total probability (i.e. one), the *1st* order is the mean, for stationary process one can easily verify that the 2^{nd} order structure function is related to the autocorrelation function defined in Equation (2.6).

$$R(\ell) = \langle u\,(x) u\,(x+\ell) \rangle \tag{2.6}$$

However, the structure functions are proved to be more constructive than the correlation functions in turbulence theory. One should note two main interests regarding the study of the structure functions. By varying the scale ℓ and keeping n constant we determine particular features of turbulence at different scales. Whereas varying n for a particular scale ℓ is suitable to study intermittency. Another interest of the structure functions arises from their scaling properties which is found to obey a scaling law within the inertial range [Kolmogorov, 1991] :

$$S_n(\ell) = a_n \ell^{\xi_n} \tag{2.7}$$

where a_n is a proportionality constant. For statistically monofractal processes, the scaling exponents ξ_n are a linear function of the order n; deviations from this linear behaviour corresponds to multifractality. The third order moment of the structure function ($n = 3$) defines one of the most famous laws of a fully developed turbulence, the Kolmogorov law (discussed in Section 2.3.1), which implies the linear relation $\xi_n = n/3$.

It is also useful to define the normalized versions of the 3^{rd} and the 4^{th} order moments, the *skewness* and *kurtosis* respectively because of their essential role in characterizing the shape of the PDFs. The *skewness* is defined as the third order moment divided by the three-halves power of the second order moment; i.e.,

$$S(\ell) = \frac{S_3(\ell)}{(S_2(\ell))^{3/2}} \tag{2.8}$$

A non-zero skewness indicates a skewed or asymmetric PDF, which means that larger excursions in one direction are more probable than in the other direction.

The *kurtosis* K (or the *flatness* $F = K - 3$) is defined as the fourth order moment divided by the square of the second; i.e.,

$$K(\ell) = \frac{S_4(\ell)}{(S_2(\ell))^2} \tag{2.9}$$

The kurtosis can be used to quantify how “tailed” is a PDF. A higher kurtosis indicates that relatively large excursions from the mean are more probable. For a Gaussian PDF, the skewness is zero and the kurtosis is equal to three. Higher-order statistics involving nonlinear combinations of the data are used to capture multifractal events in turbulent flows. The higher is the moment the closest we get to have information on the "rare" or "bursty" events present in the tails of the PDFs (as it is illustrated in Figure 2.2). However, the higher is the moment the harder it is to be estimated accurately in the sense that larger statistical samples are required. A review on a more detailed check on convergence tests could be found in Dudok de Wit [2004].

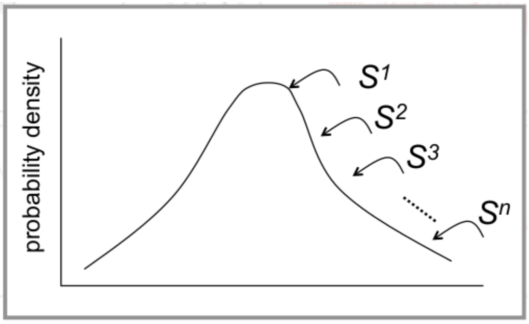

Figure 2.2: A schematic showing the importance of the higher-order statistics. The higher is the moment, the more information it gives regarding the few bursty events in the tails of the PDFs.

We note that in turbulence studies, we use stationary (more precisely weakly stationary) time series, in which the mean and the variance (and possibly higher order moments) do not change significantly when shifted with time. Moreover, it is necessary to use long time intervals with respect to the scales we are interested in order to apply the ergodic theorem which ensures that time averages coincide with ensemble averages.

2.3 Exact laws and phenomenologies

2.3.1 Exact law for incompressible HD turbulence and K41 phenomenology

The first exact law of a fully developed incompressible turbulence was derived by Kolmogorov in 1941 [Kolmogorov, 1941], known as the 4/5 law. Starting from the basic continuity and momentum conservation equations for an incompressible flow (Equation 2.2) one can derive analytically the Kolmogorov law using velocity correlation tensors between two points separated by the distance l.
Considering scales much larger than the dissipative ones l_{dissip} and much smaller than the injection ones l_0, and using the classical *homogeneity, stationarity, isotropy* assumptions of the turbulent fluctuations [Frisch, 1995], we obtain:

$$\boxed{-\frac{4}{5}\varepsilon l =< (\delta v_l)^3 >} \tag{2.10}$$

where δv_l is the velocity increments at the scale l and ε is the energy cascade (or dissipation) rate. As a consequence, we can expect that the properties of the small scales of a well developed turbulence to be independent of the details of the large scales, i.e., as the cascade develops we expect the turbulence to have "forgotten" how it was created. This has implications of which the most important is that for small scales that belong to the inertial range, the turbulence exhibits universal behaviour. The second important implication is that the turbulence is locally isotropic, since any anisotropy would mean that the details of large scales still have an influence (note however that this do not apply to spatial anistropy due to the presence of a magnetic field in plasmas, which persists in the system even at the very small scales).

It is noteworthy that Equation (2.10) shows that the third-order moment of the velocity structure function scales linearly with the corresponding length scale l inside the inertial range. This relation can therefore be used to define the inertial range in the physical space.

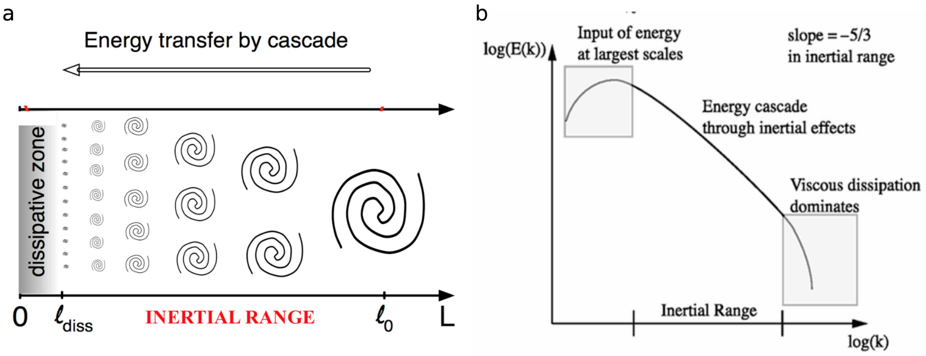

Figure 2.3: Illustration of the Richardson-Kolmogorov cascade, in the real space (a) and Fourier space (b).

This exact law (unsigned third order law) could be rederived using dimensional analysis, a powerful tool in the arsenal of a student of turbulence. This phenomenological approach is based on the turbulent image first suggested by Richardson [1922] who proposed the highly influential cartoon that characterizes the turbulent flows as composed by eddies of different size interacting with each other at the large scales and breaking up into smaller ones, and so on (Figure 2.3-(a)). The energy is transferred and cascaded from the large scales of the motion to smaller scales forming the inertial range until it reaches a sufficiently small length scale such that the viscosity of the fluid can effectively dissipate the kinetic energy (Figure 2.3-(b)).

Let us restrict our analysis to the inertial range and consider eddies of size l. To these eddies we associate a velocity v_l and a characteristic time required for a complete distortion of the eddies τ_{eddie} (known as the eddie turnover time). In these conditions one can define the average transfer rate of the (kinetic) energy from one scale to another as:

$$\varepsilon = \varepsilon_l \equiv \frac{dE_l}{dt} \sim \frac{{v_l}^2}{\tau_{tr}} \sim \frac{{v_l}^2}{\tau_{eddie}} \sim \frac{{v_l}^3}{l} \Rightarrow v_l = \varepsilon \ell^{1/3} \tag{2.11}$$

where τ_{tr} represents the energy transfer time and $\tau_{tr} \sim \tau_{eddie}$. Since in the inertial range, the energy is supposed to be neither injected nor dissipated, the average energy transfer rate ε_l should be equal to the average energy dissipation or injection rate ε. Using the definition of the energy spectral density in homogeneous turbulence, we can obtain the following $K41$ phenomenological relation:

$$E_k \sim {v_l}^2 k^{-1} \sim (\varepsilon k^{-1})^{2/3} k^{-f1} \sim \varepsilon^{2/3} k^{-5/3} \tag{2.12}$$

This approximate relation can be converted into an equation by introducing a dimensionless constant α_k, called Kolmogorov's constant, determined experimentaly to be about ~ 1.4 or ~ 1.6. The equation is written as:

$$\boxed{E_k = \alpha_k \varepsilon^{2/3} k^{-5/3}} \tag{2.13}$$

Recently, the incompressible Kolmogorov's 4/5 exact law has been generalized to compressible fluid turbulence described within the isothermal and the polytropic closure equations [Galtier & Banerjee, 2011; Banerjee & Galtier, 2014].

2.3.2 Exact law for incompressible MHD turbulence and IK phenomenology

Similarly to the incompressible hydrodynamic turbulence, an exact relation for incompressible MHD turbulence was derived in terms of the Elsässer variables [Politano & Pouquet, 1998]. These Elsässer variables, which were first proposed by Elsasser [1950], combine the magnetic and the velocity fields and are particularly relevant to study incompressible MHD turbulence:

$$\mathbf{z}^{\pm} \equiv \mathbf{v} \pm \mathbf{v_A} \tag{2.14}$$

where $\mathbf{v_A} = \mathbf{b}/\sqrt{\mu_0 \rho}$ is the Alfvén speed. Writing the basic MHD equations in terms of the Elsässer fields and assuming full *isotropy*, *homogeneity*, and *incompressibility*, and that the dissipation remains non zero as the Reynolds number goes to infinity, they obtained the exact relations corresponding to longitudinal structure functions:

$$\boxed{-\frac{4}{3}\varepsilon^{\pm}\ell =< (\delta \mathbf{z}^{\pm} \cdot \delta \mathbf{z}^{\pm}) \delta z_{\ell}^{\mp} >} \tag{2.15}$$

where $\varepsilon^{\pm}$ denotes the mean rate of pseudo-energies input flux ($E^{\pm} = \frac{1}{2}\mathbf{z}^{\pm} \cdot \mathbf{z}^{\pm}$). As one can see, Equation (2.15) represents the MHD version of the Kolmogorov's 4/5 law for hydrodynamic turbulence. In the limit of incompressible hydrodynamics ($\mathbf{b} = 0$), $\mathbf{z}^{\pm} = \mathbf{v}$, the MHD relations reduce to the four-fifth law of HD turbulence.

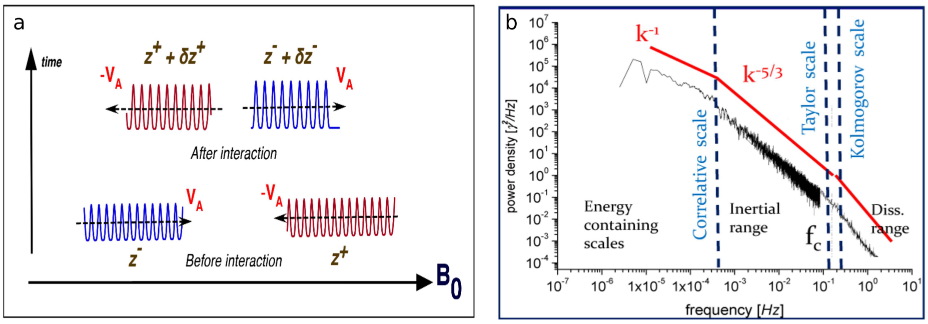

Figure 2.4: (a) Illustration of the Iroshnikov-Kraichnan phenomenology of incompressible MHD turbulence and (b) the corresponding image à la Richardson-Kolmogorov in Fourier space showing a typical interplanetary magnetic field power spectrum at 1 AU. Adapted respectively from [Supratik, 2014] and [Bruno & Carbone, 2005].

In order to have a better understanding of the multi-scale dynamics in a magnetized fluid, Iroshnikov [1964] and Kraichnan [1965] proposed independently a physical image of MHD turbulence known as the "IK phenomenology" based on the nonlinear interactions (collisions) between counter-propagating Alfvén wavepackets. According to this image, the energy is transferred from one length scale to another by the deformation of one Alfvén wavepacket by the other one as it is illustrated in Figure 2.4-(a), by analogy with the K41 phenomenology of hydrodynamic turbulence in which the energy is transferred from one scale to another via "eddies-interactions" (instead of waves).

Unlike the K41 phenomenology, the IK phenomenology involves two characteristic times: The Alfvén time ($\tau_A \sim \ell/v_A$) and the nonlinear time $\tau_{NL} = \ell/z^{\pm}_{\ell}$. τ_A corresponds to the interaction (collision) time between two wavepackets of typical length ℓ, and τ_{NL} measures the time required for a sufficient distortion of z^+ or z^- by another wavepacket of the same size (locality hypothesis). In the IK phenomenology, turbulence is fully developed due to the stochastic collisions between the Alfvén wavepackets at a scale ℓ in the inertial range. The uniform magnetic field is supposed to be much larger than the magnetic field fluctuations, which means that $\tau_{NL} \ll \tau_A$ ($\tau_{NL} \gg \tau_A$ corresponds to the weak turbulence regime, while $\tau_{NL} \sim \tau_A$ corresponds to the *critical balance* regime [Sridhar & Goldreich, 1994; Goldreich & Sridhar, 1995]).

In these conditions, we can define the effective energy transfer time as:

$$\tau_{tr} \sim N\tau_A \sim \frac{\tau_{NL}^2}{\tau_A} \tag{2.16}$$

where $N \sim (\frac{\tau_{NL}}{\tau_A})^2$, is the number of "collisions" needed to have a sufficient deformation of the Alfvén waves amplitude. Assuming as well a weak velocity-magnetic field cross-correlations, one obtains:

$$z_\ell^+ \sim z_\ell^- \sim z_\ell \sim v_\ell \sim B_\ell \tag{2.17}$$

and

$$E^+ \sim E^- \sim v_\ell^2 \tag{2.18}$$

As a consequence, the total energy flux rate ε can be written as:

$$\varepsilon \sim \frac{dE_\ell}{dt} \sim \frac{z_l^2}{\tau_{tr}} \sim \frac{z_\ell^4}{v_A \ell}. \tag{2.19}$$

Passing to the Fourier space and expressing $z_\ell^2 \sim E(k)k$ we get:

$$\boxed{E(k) = C_{IK}(\varepsilon v_A)^{1/2} k^{-3/2}} \tag{2.20}$$

C_{IK} is the generalization of the Kolmogorov constant in hydrodynamics to the incompressible MHD turbulence. However, it is less universal than the latter, since it depends on the degree of correlation between $\mathbf{B}$ and $\mathbf{v}$ (if the correlations are not negligible one can show in a similar, but more complex analysis, a power-law $\sim k^{-2}$ Biskamp [1993]). As a consequence, a universality of the scaling in the inertial range is found as well in incompressible MHD turbulence. What about the compressible MHD turbulence?

2.3.3 Exact law for compressible isothermal MHD turbulence

The first analytical derivation of the exact law for the two-point correlation functions for isothermal compressible MHD turbulence was done by Banerjee & Galtier [2013]. When including compressibility in the MHD equations, the new resulting system possesses two new linear eigenmodes (in addition to the Alfvén mode) known as the fast and slow magnetosonic modes (see Section 4.3.3 where the properties of those modes are used). The model of Banerjee & Galtier [2013] includes therefore the full nonlinear coupling between the three MHD modes, which makes it the most general exact model to date for studying low frequency compressible fluctuations in magnetized space plasmas, with however, the limitation of the isothermal closure equation which is used.

Starting from the basic equations of ideal MHD written in terms of $\mathbf{v}$ and $\mathbf{v_A}$, and following the same formalism as that of the compressible hydrodynamic case [Galtier & Banerjee, 2011] and assuming statistical homogeneity and stationarity and large kinetic and magnetic Reynolds numbers, the authors showed that the magnetic field brings new "source" and "flux" terms into the dynamics, which may act on the inertial range similarly as a source or a sink for the mean energy transfer rate.

The exact relation is too long and "bulky" to be presented here (see Appendix A). However, a simplified view of the relation can be written as:

$$-4\varepsilon_C = \nabla_{\boldsymbol{\ell}} \cdot \mathcal{F}_C - \Phi + \mathcal{S} \tag{2.21}$$

Where ε_C denotes the mean total energy transfer rate (equal to the mean total energy injection and dissipation rate), $\mathcal{F}_C$ corresponds to the flux terms written in terms of the Elsässer variables $\mathbf{z}^{\pm}$:

$$\begin{aligned} \mathcal{F}_C =& < \frac{1}{2}[\delta(\rho\mathbf{z}^{+}) \cdot \delta\mathbf{z}^{+}]\delta\mathbf{z}^{-} + \frac{1}{2}[\delta(\rho\mathbf{z}^{-}) \cdot \delta\mathbf{z}^{-}]\delta\mathbf{z}^{+} > \\ &+ < 2\delta\rho\delta e\delta\mathbf{v} > + < 2\overline{\delta}(e + \frac{v_A^2}{2})\delta(\rho\mathbf{v}) >, \end{aligned} \tag{2.22}$$

and Φ which is not a pure flux term is given by:

$$\Phi =< \frac{1}{\beta'}\nabla' \cdot (\rho\mathbf{v}e') + \frac{1}{\beta}\nabla \cdot (\rho'\mathbf{v}'e) >, \tag{2.23}$$

where by definition $\overline{\delta}\psi \equiv (\psi(\mathbf{x}+\boldsymbol{\ell})+\psi(\mathbf{x}))/2$, $e = C_s^2 \ln(\rho/\rho_0)$ is the internal energy, with C_s the constant isothermal sound speed, the primed and unprimed variables correspond to the variables at points $\mathbf{x}+\boldsymbol{\ell}$ and $\mathbf{x}$ respectively and $\beta = 2C_s^2/v_A^2$ gives the local ratio of thermal to magnetic pressure.
The term $\mathcal{S}$ represents the "source" terms given in Appendix A and so includes the local divergences of the velocity $\mathbf{v}$, and the compressible Alfvén velocity $\mathbf{v_A}$.
When β is quasi-stationary (uniform) in expression (2.23) Φ can be reduced to a flux term written as:

$$\Phi = \frac{1}{\beta}\nabla_{\boldsymbol{\ell}} \cdot < \rho\mathbf{v}e' - \rho'\mathbf{v}'e >= -\frac{2}{\beta}\nabla_{\boldsymbol{\ell}} \cdot < \overline{\delta}e\delta(\rho\mathbf{v}) >, \tag{2.24}$$

This term can now be merged with the flux terms in equation 2.22. This results in modifying the third term of $\mathcal{F}_C$ from $\overline{\delta}(e + v_A^2/2)\delta(\rho\mathbf{v})$ to $\overline{\delta}[(1 + \beta^{-1})e + v_A^2/2]\delta(\rho\mathbf{v})$. As a last step, one can integrate relation (2.22) over a ball of radius ℓ and get the equivalent of the isotropic relation (2.15) for isothermal compressible MHD turbulence, namely:

$$\boxed{-\tfrac{4}{3}\varepsilon_C\ell = \mathcal{F}_{C+\Phi}(\ell) + \mathcal{S}} \tag{2.25}$$

where

$$\mathcal{F}_{C+\Phi}(\ell) = \mathcal{F}_1(\ell) + \mathcal{F}_2(\ell) + \mathcal{F}_3(\ell) \tag{2.26}$$

and

$$\begin{aligned} \mathcal{F}_1(\ell) =& < \frac{1}{2}[\delta(\rho\mathbf{z}^{-}) \cdot \delta\mathbf{z}^{-}]\delta z_\ell^{+} + \frac{1}{2}[\delta(\rho\mathbf{z}^{+}) \cdot \delta\mathbf{z}^{+}]\delta z_\ell^{-} > \\ \mathcal{F}_2(\ell) =& < 2\delta\rho\delta e\delta v_\ell > \\ \mathcal{F}_3(\ell) =& < 2\overline{\delta}[(1 + \frac{1}{\beta})e + \frac{v_A^2}{2}]\delta(\rho v_\ell) > \end{aligned}$$

In the course of my thesis, I used these equations to quantify the role of the compressible fluctuations on the new cascade rate ε_C and evaluated the role of each of these three different flux terms in the fast and the slow wind separately using the THEMIS/ARTEMIS P1 data, and in the Earth's using the Cluster spacecraft data.

Chapter 3

In-situ observations of space plasma turbulence: State-of-the-Art

Contents

Since Mariner 2 in 1962, we saw a flurry of spacecraft missions exploring the near-Sun and Earth environments, which include Voyager 1 & 2, Helios A & B, Wind, ACE, Ulysses, but also near other planetary systems like Galileo (Jupiter), Messenger (Mercury), Voyager 1 & 2, Cassini-Huygens (Saturn), yielding a better understanding of different plasma processes occurring in different regions of the solar system. Advances in technology and instrumentation enabled to novel space missions triggering new observational studies. These improvements include the use of particles and fields detectors, higher time and energy resolution, multipoint measurements, higher rate of data transmission and onboard autonomy. This is particularly true for the recent magnetospheric missions such as Cluster, THEMIS B/ARTEMIS P1 and MMS (launched in 2015). In this chapter, the main observations regarding the properties of plasma turbulence are presented firstly in the most studied space medium, the solar wind, and secondly in a less studied ones, namely the planetary magnetosheaths. This brief review does not cover all the work done about turbulence, but focuses on the aspects related to the questions addressed in this thesis and recalled in Section 1.3.

3.1 Solar wind turbulence.

3.1.1 Nature of the turbulent fluctuations

Clear signatures of turbulence were observed at the MHD scales ($f \ll f_{ci}$ and $L \gg \rho_i$ and d_i, where f_{ci}, ρ_i and d_i are the ion gyro-frequency, the Larmor radius and the inertial length ($d_i = V_A/2\pi f_{ci}$), respectively) in the fast and the slow solar wind with large amplitude oscillations of the magnetic field and the velocity perpendicular to the background magnetic field ($\mathbf{B}_0$) [Belcher & Davis, 1971].

The magnetic and velocity fields fluctuation in the fast wind, are shown to exhibit a strong correlation in the form $\delta v_\perp = \pm \delta B_\perp$ which actually correspond to the incompressible Alfvén waves [Belcher & Davis, 1971; Matthaeus *et al.*, 1983, 1990; Goldstein & Roberts, 1999; Bale *et al.*, 2005; Sahraoui *et al.*, 2009]. The high correlation, which is also referred to as high Alfvénicity, and the positive sense of the correlation for sunward-pointing magnetic field implies that the fluctuations are propagating outward from the Sun. The reason for which the Alfvén waves survive much longer than other waves is probably the fact that the compressive waves (the slow and the fast magnetosonic modes) are heavily damped by dissipation in shocks or by Landau absorption [Barnes, 1966]. The slow wind is of more complex nature with low Alfvénicity and the amplitude of the fluctuations are smaller than in the fast wind [Tu & Marsch, 1995; Bruno & Carbone, 2005]. The density fluctuations appear to be higher, and so the compression effects in the slow wind should be stronger.

To measure the Alfvénicity of the fluctuations, the cross-helicity is generally used and is defined as:

$$H_c = \langle \delta \mathbf{v} \cdot \delta \mathbf{b} \rangle \tag{3.1}$$

$\delta \mathbf{v}$ and $\delta \mathbf{b}$ denote respectively the velocity and the magnetic fields fluctuation vectors. It is useful to define another equivalent quantity, the normalized cross-helicity:

$$\sigma_c = \frac{H_c}{(1/2)\langle \delta \mathbf{v}^2 + \delta \mathbf{b}^2 \rangle} \tag{3.2}$$

As already noticed by Smith *et al.* [1983, 1984], knowing the sign of σ_c it is possible to infer the sense of polarization of the fluctuations. The maximum value, $\sigma_c = +1$ corresponds to pure outward Alfvén waves (anti-parallel to $\mathbf{B}_0$) and $\sigma_c = -1$ to pure inward Alfvén waves (parallel direction to $\mathbf{B}_0$). Many in-situ measurements show that the fast wind is generally characterized by high values of σ_c ($|\sigma_c| > 0.5$). On the other hand, in the slow wind there is no preference for the outward or inward propagating Alfvén waves, they are more mixed [Tu *et al.*, 1990; Goldstein *et al.*, 1995; Bruno & Carbone, 2005]. For both wind speeds, the cross-helicity is shown to decrease with radial distance of the sun [Matthaeus *et al.*, 2004; Breech *et al.*, 2008].

Another feature of the MHD fluctuations is the breaking of the isotropy in the properties of the turbulent fluctuations resulting from the presence of a mean magnetic field, first suggested by Montgomery & Turner [1981]. The first evidence that the presence of the magnetic field affects the properties of turbulence was pointed out in the early 70's by several authors [Belcher & Davis, 1971; Burlaga & Turner, 1976; Bavassano *et al.*, 1982]. They showed that the magnetic and velocity fields fluctuations are larger in the components perpendicular to the mean field than those in the parallel direction ($\delta B_\perp \gg \delta B_{||}$). This is referred to as *variance anisotropy*. Anisotropy in the solar wind is also reflected in the wavenumber space. Crooker *et al.* [1982]; Matthaeus *et al.* [1990] first demonstrated the *wavevector anisotropy* by computing the correlation function of the magnetic field fluctuations in funtion of the angle $\Theta_{\mathbf{VB}}$ between the magnetic field and the velocity vectors. Dasso *et al.* [2005] made similar analysis using multi-spacecraft measurements for the fast and slow streams separately. They showed that wavevectors quasi-parallel to the local magnetic field ("Slab" waves) dominate more in the fast solar wind, while quasi-perpendicular wavevectors ("2D" fluctations) dominate in the slow wind. In the absence of multi-spacecraft measurements, wavenumber can be estimated only along the flow direction using the Taylor frozen-in-flow hypothesis ($\omega_{sc} \sim \mathbf{k}.\mathbf{V} = k_v V$), and so only at a particular angle relative to the background magnetic field (a discussion regarding the validity of the Taylor hypothesis is given in Section 4.4.4). However, using a statistical variation of $\Theta_{\mathbf{VB}}$ one can explore (to some extent) the anisotropy of turbulence [Bieber *et al.*, 1996] (I will return to this point in more details in Chapter 5).

At the sub-ion scales ($f \gg f_{ci}$), the ions decouple from the magnetic field and so the physics at those scales becomes more complex because of the dispersive and (kinetic) dissipative effects that become important. This reason for which the corresponding scales are referred to either the *dispersive range* [Stawicki *et al.*, 2001] or the *dissipation range* [Goldstein *et al.*, 1994; Leamon *et al.*, 1998]. The nature of the plasma fluctuations that carry the turbulence cascade at the sub-ion scales, is still a subject of heated debates. Indeed, below the proton gyro-radius, at least three different modes are present as derived form the Hall-MHD theory: Left-hand polarized Alfvén mode and a right-hand polarized fast magnetosonic mode. A third ion-acoustic (slow) mode exists but is generally thought to be Landau damped (e.g., Howes *et al.* [2008*a*]; Sahraoui *et al.* [2012]). At quasi-perpendicular propagation, the Alfvénic branch evolves into Kinetic Alfvén Waves (KAW), while fast magnetosonic modes may propagate as whistler modes. Note however that this high frequency branch that emerges from the fast mode can be highly damped by kinetic effects in high oblique angles and large β values [Sahraoui *et al.*, 2012; Boldyrev & Perez, 2013].

Whether the fluctuations at the kinetic scales are Alfvénic or whistler-like is still a matter of open debate. Many analyses support a whistler-like cascade based on observations [Goldstein *et al.*, 1994; Leamon *et al.*, 1998; Stawicki *et al.*, 2001] and numerical simulations using electron-MHD and Particle in Cell (PIC) codes [Biskamp *et al.*, 1996; Cho & Lazarian, 2004; Gary *et al.*, 2008; Saito *et al.*, 2008; Gary *et al.*, 2012; Meyrand & Galtier, 2013]. On the other side, other studies showed that it is the Alfvénic turbulence in the inertial range that transfers the energy down to the proton gyro-radius where the fluctuations are subject to the proton Landau damping [Howes *et al.*, 2008*a*; Schekochihin *et al.*, 2009]. The remaining fluctuations at quasi-perpendicular propagation continue the cascade to small scales as KAW [Bale *et al.*, 2005; Sahraoui *et al.*, 2010; Podesta & TenBarge, 2012; Chen *et al.*, 2013], which are eventually highly Landau damped at the electron scales [Sahraoui *et al.*, 2009]. The same KAW scenario has been essentially supported by gyrokinetic theory and simulations [Howes *et al.*, 2008*b*; Schekochihin *et al.*, 2009; Howes *et al.*, 2012]. More recently Cerri *et al.* [2016] showed using a hybrid Vlasov-Maxwell code that for low plasma β, turbulence is dominated by whistler like fluctuations, while for high β regimes, it is mostly driven by Alfvénic fluctuations, noting that the difference is only due to their relative importance since the two modes are present in the two regimes. However, other than 2D or 3D PIC simulations, using different setups, Camporeale & Burgess [2011] showed the presence of other type of fluctuations at sub-ion scales while other questioned the relevance of any wave-like signature at those scales by showing the presence of different coherent structures (e.g., current sheets and vortices) in which dissipation occurs via magnetic reconnection instead of the resonant wave-particle interactions discussed above [Karimabadi *et al.*, 2014]. This scenario is also supported by spacecraft observations [Osman *et al.*, 2011*a*].

3.1.2 Spectral properties

The spectral properties of the solar wind turbulence were extensively studied at different radial distances from the Sun using different spacecraft data. A notable property of turbulence in the solar wind is manifested by the presence of different power-law ranges separated by spectral breaks that reflect the different charateristic scales of the plasma (a notable difference with neutral fluid turbulence). Figure 3.1 shows a typical PSD computed in the ecliptic solar wind by combining ACE and Cluster data respectively at the MHD scales $\left(f < 10^{-1}\,\mathrm{Hz}\right)$ and the kinetic ones $(f > 1\,\mathrm{Hz})$ [Kiyani *et al.*, 2015]. This spectrum is characterized by at least three different power-law ranges. First, the *energy containing scales* that scales as $\sim f^{-1}$, its origin is still a matter of debate. There are some indications that it may have an origin from the emergence, cancellation, and sinking of the magnetic field at the photosphere: spectra built from magnetogram data at low-intermediate latitudes show a f^{-1} slope at low wavenumbers [Matthaeus *et al.*, 2007]. It has been also observed to originate from an inverse cascade in homogeneous incompressible MHD simulations [Dmitruk *et al.*, 2011]. Other ideas rely on the superposition of uncorrelated magnetic field fluctuations [Matthaeus & Goldstein, 1986] or on the dynamics in the solar corona related to reflection of Alfvén waves and the interactions between them [Velli *et al.*, 1989].

Regarding the slow wind, the PSDs are shown to be characterized by only the Kolmogorov scaling law $\sim k^{-5/3}$ [Bruno *et al.*, 2009]. The fluctuations in the slow wind are indeed known to be "highly evolved" or "dynamically old" [Grappin *et al.*, 1990, 1991]. The absence of the f^{-1} was attributed to low Alfvénicity of the fluctuations in the slow wind [Bruno & Carbone, 2005]. Indeed, Roberts [2010] showed that highly Alfvénic slow-speed wind do present a region of a shallower slope below the inertial range. The origin of the "energy containing scales" for the fast and the slow wind are still not well understood and remains a subject of active research work.

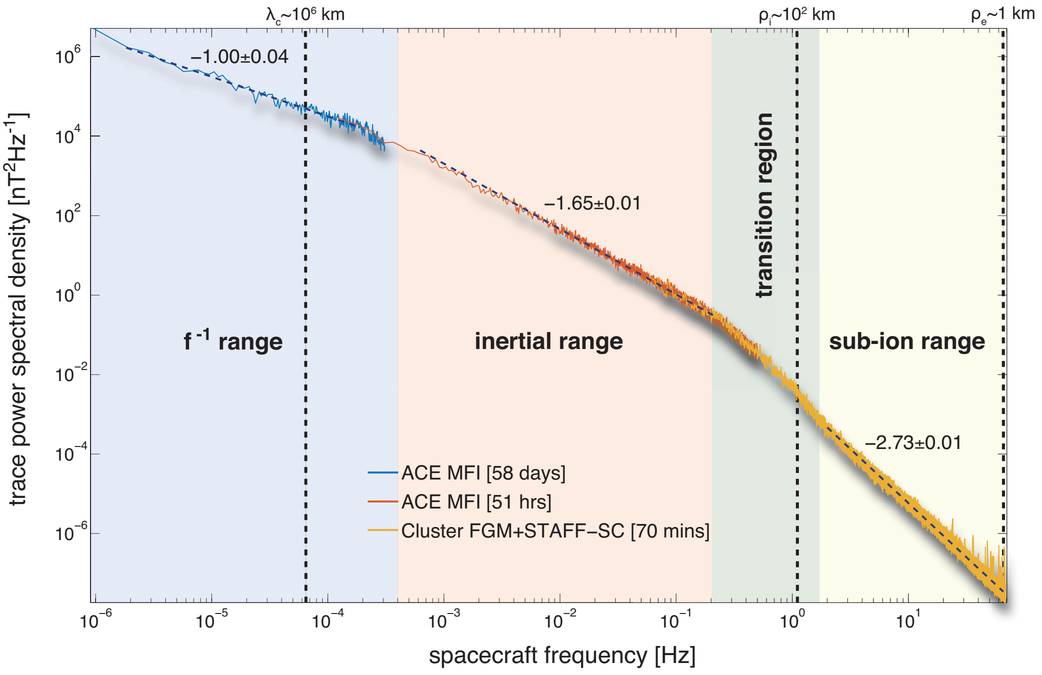

Figure 3.1: Typical power spectral density of the magnetic field fluctuations in the ecliptic solar wind at 1 AU, combining ACE and Cluster data. The vertical dashed lines indicate the correlation length (λ_c), the ion gyro-radius (ρ_i) and the electron gyro-radius ρ_e. Adapted from Kiyani *et al.* [2015].

Once these fluctuations reach the correlation length (λ_c), they start to interact nonlinearly forming the *inertial range* that has a power-law close to the one predicted by Kolmogorov in incompressible hydrodynamics $\sim k^{-5/3}$. It is thought to originate from the nonlinear interactions of counter-propagating incompressible Alfvén wavepackets transferring the energy down to shorter wavelength [Iroshnikov, 1964; Kraichnan, 1965]. The inertial range terminates with a breakpoint occurring near ρ_i or d_i [1] which is generally followed by a steeper power-law $\sim f^{\alpha}$ at the sub-ion scales with a broader range of slopes $\alpha \in\sim [-2.3, -4.5]$ forming the *dissipation scales* [Goldstein *et al.*, 1994; Leamon *et al.*, 1998; Smith *et al.*, 2006; Hamilton *et al.*,

---

[1] The exact scale of the transition between MHD and the kinetic scales is still unclear and whether it is ρ_i or d_i is still debated [Markovskii *et al.*, 2008; Wicks *et al.*, 2010; Bourouaine *et al.*, 2012; Chen *et al.*, 2014].

2008; Sahraoui *et al.*, 2010; Bruno *et al.*, 2014]. Note that this steepest power-law spectra observed sometimes in this range (but not clearly visible on Figure 3.1) were referred to as the *transition range*, in the sense that turbulence passes from MHD to kinetic scales [Sahraoui *et al.*, 2010]. At higher frequencies $\sim [3, 30]$ Hz, Figure 3.1 shows that a power-law appears with a slope $\sim f^{-2.7}$ charaterizing a new cascade of energy down to electron scales, first reported in Sahraoui *et al.* [2009] and later confirmed by Alexandrova *et al.* [2009]; Kiyani *et al.* [2009*b*]. Statistical studies showed that the spectral slopes vary within the range $\sim [-2.3, -3.1]$ with a peak near -2.8 [Alexandrova *et al.*, 2012; Sahraoui *et al.*, 2013]. Near the electron kinetic scales (not visible in Figure 3.1), the spectra were shown to steepen again and this has been interpreted as due to dissipation of the remaining magnetic energy into electron heating via Landau damping of high oblique KAW turbulence [Sahraoui *et al.*, 2009]. Due to instrumental limitations, the actual scaling at sub-electron scales and the fate of the energy cascade remain open questions [Alexandrova *et al.*, 2012; Sahraoui *et al.*, 2013].

Different possible mechanisms have been proposed in order to explain the steepening of the spectra in the sub-ion scales. They include dispersive effects as discussed in Section 3.1.1, wave-particle interactions (ion cyclotron or ion Landau damping) [Tu & Marsch, 1995; Goldstein *et al.*, 1994; Leamon *et al.*, 1998; Howes *et al.*, 2008*b*; Sahraoui *et al.*, 2010; Howes *et al.*, 2011], or coherent structures such as Alfvén vortex-like structures [Lion *et al.*, 2016] or current sheets where magnetic reconnection occurs [Matthaeus *et al.*, 1984; Dmitruk *et al.*, 2004; Parashar *et al.*, 2011; Osman *et al.*, 2011*a*]. Other studies showed that the steepest dissipation range seems to be associated to the highest rate of the total energy cascade and the highest power of the magnetic field fluctuations [Smith *et al.*, 2009*a*; Bruno *et al.*, 2014] suggesting the important role of the energy transfer rate in the inertial range and its effect on the dissipation range. Note that a similar correlation has been observed between the power of the turbulent fluctuations and the spectral slopes at sub-electron scales, which however has been interpreted as due to instrumental limitation [Sahraoui *et al.*, 2013]. Those observations desagree with the results from the 3D PIC simulations of whistler turbulence at the electron scales [Gary *et al.*, 2012] who showed that an increasing energy cascade rate leads to shallower spectra in the dissipation range.

3.1.3 Intermittency and higher order statistics

Another property of the turbulent motion in the solar wind is the burstiness of the fluctuations in the inertial range, known as intermittency (Section 2.2) [Hnat *et al.*, 2004; Kiyani *et al.*, 2007] as observed in fluid flows [Frisch, 1995]. The origin of multifractality in the solar wind is still an open question and is usually ascribed to the presence of coherent structures, like current sheets, shocks and vortices, whose typical lifetime exceeds that of incoherent fluctuations in the background [Veltri & Mangeney, 1998; Sorriso-Valvo *et al.*, 1999; Mangeney *et al.*, 2001; Alexandrova *et al.*, 2006]. As discussed in Section 2.2, investigating the multifractality requires using different orders of the structure functions of the turbulent fluctuations. Sorriso-Valvo *et al.* [1999] showed that the PDFs of the velocity and magnetic fields fluctuations for the high and the slow speed streams in the inertial range develop tails as the scales become smaller, confirming thus the multifractal nature of the fields fluctuations in the inertial range. This indicates that the largest events have a probability to happen larger than if they were normally distributed as can be seen in Figure 3.2. The resulting scaling exponents are not a linear function of the different orders p of the structure functions (see Tu & Marsch [1995]; Bruno & Carbone [2005]; Dudok de Wit *et al.* [2013] for a review on this topic).

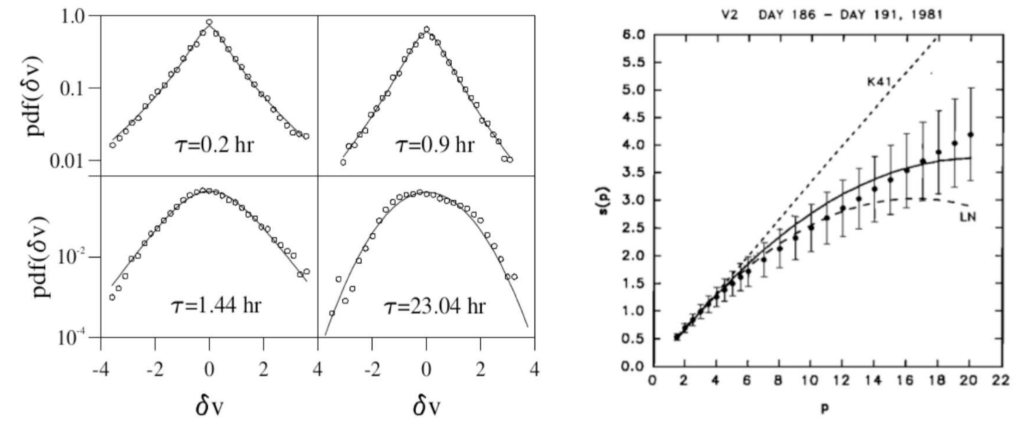

Figure 3.2: Left: Normalized PDF of the velocity field fluctuations at different scales τ using Helios 2 data in the fast solar wind. Solid lines represent the fit made using a log-normal model [Sorriso-Valvo *et al.*, 1999]. Right: The scaling exponent as a function of the different orders p computed in the solar wind at ~ 9 A.U. using Voyager data [Burlaga, 1991].

Similar analysis were done as well at the kinetic scales. Kiyani *et al.* [2009*b*] showed using high-frequency magnetic field measurements from the Cluster spacecraft that in contrast to the inertial range, the dissipation range is mono-fractal, while Alexandrova *et al.* [2008] showed that turbulence remains multifractal in the same dissipation range. No clear physical interpretation has been proposed so far to explain the change from a multifractal to a mono-fractal behaviour in the dissipation range. Wu *et al.* [2013] suggested that even a small amount of incoherent waves in the kinetic range change the character of the intermittency. In fact it is still an open question whether this property is "universal" or not in the solar wind.

3.2 Planetary magnetosheaths turbulence

3.2.1 Nature of the turbulent fluctuations

Since the 80's, observational studies in the Earth magnetosheath have focused on the identification of the nature of the low frequency magnetic fluctuations. This has been done using different spacecraft data such as GEOS, ISEE, AMPTE [Fairfield, 1976; Hubert *et al.*, 1989, 1998; Lacombe *et al.*, 1995]. Several types of waves have been identified in the different regions of the Earth magnetosheath. They can be put into general categories as the following: transverse ($\delta B_\perp >> \delta B_\parallel$) electromagnetic ion cyclotron waves (EMIC), which have phase velocities close to the Alfvén speed and are generated by the cyclotron instability, and the compressional ones ($\delta B_\perp << \delta B_\parallel$), supported by the fast and slow magnetosonic MHD modes or by the kinetic mirror modes generated by the mirror instability [Song *et al.*, 1992; Southwood & Kivelson, 1993*a*; Sahraoui *et al.*, 2004, 2006; Génot *et al.*, 2009].

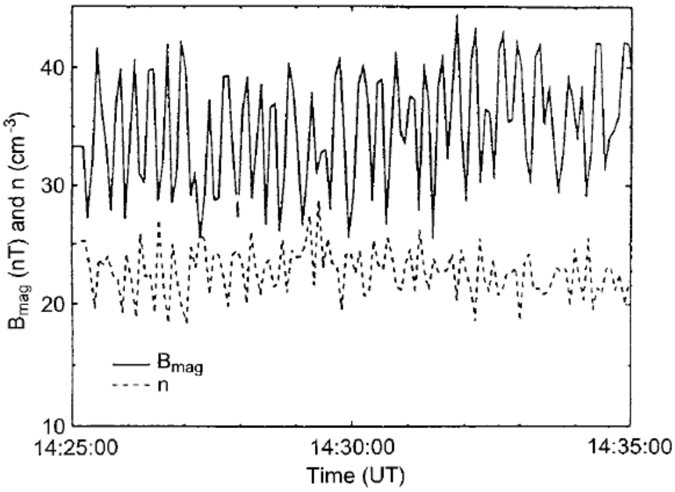

Figure 3.3: Nearly sinusoidal mirror mode evidenced by the strong anti-correlation of the magnetic field (solid) and ion density (dashed) measurements. Adapted from Leckband *et al.* [1995].

.

The nature of the dominant mode/instabilities is mainly controlled by different parameters: The geometry of the shock (whether it is a quasi-perpendicular or quasi-parallel), the β of the plasma, the ion temperature anisotropy $A_i = \frac{T_\perp}{T_\parallel} - 1$ and the frequency range analysed. For instance, behind a quasi-perpendicular shock, low β and large A_i (e.g., $\beta \sim 0.2$ and $A_i \sim 2$) favours EMIC waves [Gary & Winske, 1993; Gary *et al.*, 1993; Anderson *et al.*, 1994] whereas high β and small A_i (e.g., $\beta \sim 2$ and $A_i \sim 0.4$) were found to be favourable to mirror modes ([Southwood & Kivelson, 1993*a*; Song *et al.*, 1994; Lacombe *et al.*, 1995; Kivelson & Southwood, 1996;

Schwartz *et al.*, 1996]). The mirror modes are characterized by a quasi-sinusoidal shape and exhibit dips and peaks due to depressions and enhancements in the amplitude of the magnetic field [Génot *et al.*, 2011]. These structures can act as magnetic bottles, trapping part of the plasma particles [Kivelson & Southwood, 1996]. Note that, most of those studies have been focused on identifying wave-like signatures in spacecraft data to which classical methods of (linear) wave analysis can be applied (e.g., minimum variance analysis, wave polarization). Some exceptions to this are the study of broad band spectra using multi-spacecraft techniques on the Cluster measurements [Sahraoui *et al.*, 2003; Sahraoui *et al.*, 2006; Alexandrova *et al.*, 2004] or the study of the fluctuations anisotropy at the sub-ion scales [Mangeney *et al.*, 2006; Lacombe *et al.*, 2006].

Turbulence in other planetary system, including Saturn's magnetosheath, is even much less studied. Using Voyager 1 and 2 spacecraft data, Cattaneo *et al.* [2000] showed that the magnetic fluctuations strongly depend on the bow shock structure and geometry: downstream of a quasi-parallel shock, they are much more disturbed compared to the quasi-perpendicular shock and transverse waves dominate in the first case, while compressive fluctuations, which were associated to mirror modes, waves prevail in the second case for high plasma β [Tsurutani *et al.*, 1982; Violante *et al.*, 1995; Moreno *et al.*, 1999; Cattaneo *et al.*, 2000].

3.2.2 Spectral properties

From the spectral point of view, few case studies showing a PSD characterized by two different ranges were observed in the magnetosheath of Earth by Czaykowska *et al.* [2001] using AMPTE/IRM spacecraft. At the MHD scales, below f_{ci}, they observed the presence of the f^{-1} scaling, characterized by a mixture of Alfvén and mirror waves, generated by the anisotropic ion distribution function, but did not give any interpretation regarding the formation of this scaling. Above f_{ci}, similarly to the solar wind, the PSDs follow a power-law with a broader range of slopes, $[-2.5, -3]$ [Czaykowska *et al.*, 2001; Huang *et al.*, 2014]. But, contrary to what happens in the solar wind, this spectrum is observed immediately above the range of uncorrelated waves f^{-1}, without forming the inertial range. However, other case studies showed the presence of a power-law close to the Kolmogorov one in the magnetosheath flanks below the ion gyro-frequency (f_{ci}) [Sundkvist *et al.*, 2007; Alexandrova *et al.*, 2008]. Moreover, in some observations, a "spectral knee" was observed behind the quasi-perpendicular bow-shock around f_{ci} which was interpreted as a signature of AIC waves [Czaykowska *et al.*, 2001] or localized structures in the form of Alfvén vortices [Alexandrova *et al.*, 2006; Alexandrova, 2008]. In Saturn's magnetosheath, there were no studies dedicated to the PSDs of the turbulent fluctuations, except the case study analyzed by Alexandrova & Saur [2008]. In fact, they focused on the presence of Alfvén vortices behind a quasi-perpendicular shock, characterized by a steep power-law above the ion scales (~ -3) similarly to their earlier work in the Earth's magnetosheath [Alexandrova *et al.*, 2004].

Other coherent structures have been observed in the Earth's magnetosheath at the ion scales. Retinò *et al.* [2007] reported the first evidence of reconnection and hence to enhanced dissipation in current sheets at the sub-ion scales downstream a quasi-parallel shock. More recently, Chasapis *et al.* [2015] confirmed these results in a larger statistical analysis using the Cluster data. They showed a good correlation between the evidenced ion-scale current sheets and the local heating of the electrons. These results are in agreement with global hybrid and fully kinetic simulations of the magnetosphere which showed that the enhanced turbulence level in quasi-parallel magnetosheath also leads to stronger heating (compared to quasi-perpendiccular ones) Karimabadi *et al.* [2014].

3.2.3 Intermittency and higher order statistics

Similarly to the solar wind, turbulence in the terrestrial magnetosheath is highly intermittent at the MHD scales. Thanks to the advances in technologies, faster computers allowed large hybrid and PIC numerical simulations of turbulence in the magnetosheath.

For instance at the MHD scales, using global hybrid simulations, Karimabadi *et al.* [2014] showed that behind a quasi-parallel shock, where turbulence is more enhanced, the fluctuations are multifractal. Whereas behind a quasi-perpendicular shock turbulence showed almost no signatures of multifractality (see section 4.3.2). Regarding the kinetic scales, similar results were observed as well revealing the multifractal nature of the fluctuations. Dudok de Wit & Krasnosel'Skikh [1996] showed by computing the structure functions of the fluctuating magnetic field upstream and downstream of the bow-shock, that they are comparable to the solar wind turbulence with a departure from gaussianity at small time scales attesting their multifractality. Sundkvist *et al.* [2007] confirmed these results and showed that the highly multifractal nature of the fluctuations behind the bow-shock at the sub-ion scales is due to the presence of some reconnecting current sheets playing an important role in the energy dissipation. Using simultaneous multipoint Cluster measurements behind quasi-parallel shock, Yordanova *et al.* [2008] showed a non-linear dependence in the scaling exponents indicating the multifractal character of the fluctuations at the kinetic scales.

3.3 Example of compressible astrophysical turbulence: interstellar medium

Other than in the solar wind and the planetary magnetosheaths, turbulence has emerged as the leading mechanism for many processes in highly compressible and supersonic astrophysical media where it is thought to play an essential role in star formation, acceleration of cosmic rays and accretion disks. Vázquez-Semadeni *et al.* [1996] showed using numerical simulations that turbulence in the molecular clouds, can lead the formation of the star by preventing the collapse of a self-gravitating cloud. Contrary to the planetary turbulence, astrophysical turbulence cannot be measured in-situ by spacecraft missions. As a consequence, the properties and the fundamental aspects of astrophysical turbulence (e.g scaling, different power laws, etc...) have been mostly investigated via supercomputer numerical simulations. A summary of the numerical modelling studies and technics of the astrophysical turbulence can be found in [Schmidt, 2013]. In this section I briefly summarize few important observational results regarding the characteristics of molecular cloud turbulence in the interstellar medium (ISM).

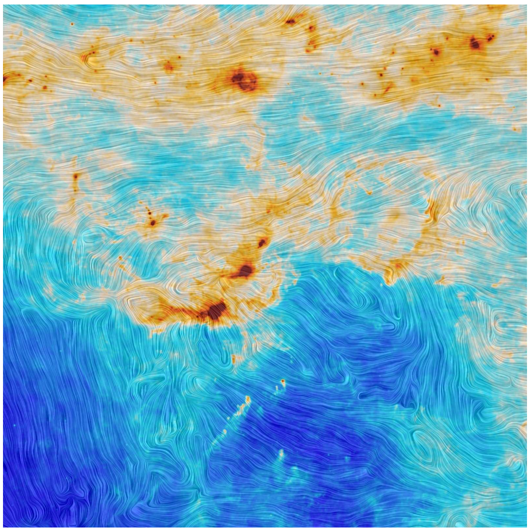

Figure 3.4: "Star formation and magnetic turbulence in the Orion Molecular Cloud". The texture represents the magnetic field's orientation. Blue color correspond to regions with low dust density, while the yellow and red areas reflect denser (and mostly hotter) clouds. © ESA and the Planck Collaboration.

Molecular clouds radiate at infrared and radio wavelengths, providing the information about their temperature, bulk motions and magnetic fields. Most of the molecular gas are organized in Giant Molecular Clouds (GMCs) known as the sites of star formation. They have sizes of around 50 pc (1 parsec $\sim 3.10^{18}$ cm $\sim 2.10^{5}$ AU), masses of $10^4 - 10^5$ $M_{\odot}$, mean density of about 100 cm^{-3}, a relatively low temperature of ~ 10 K and so a very small sound speed ~ 0.2 km/s. As a consequence these flows are supersonic with very high turbulent Mach number ($\gg 10$). The supersonic turbulent character has been observed from the spectral point of view and from the density fluctuations which are supposed to originate from the slow magnetosonic and entropy modes (zero frequency mode in polytropic MHD plasma). Based on the molecular line broadening, Larson [1981] and, later on Falgarone *et al.* [1992], observed that, firstly, the velocity dispersion is comparable to, or greater than, the speed of sound and secondly, that the root mean square (rms) of the velocity fluctuations exhibit a power law dependence on the scale l, where the exponent is close to the Kolmogorov value 1/3. Armstrong *et al.* [1995] studied the spectrum of the interstellar density fluctuations using diffractive processes of radio scintillations measurements in the ISM. Interestingly, they found a Kolmogorov-like $k^{-5/3}$ spectrum extending over wavenumbers from 10^{-17} to 10^{-6} m^{-1}, consistent with the theory of weakly compressible supersonic MHD turbulence proposed by Montgomery *et al.* [1987]. Noting that other numerical simulations for highly compressible, isothermal, supersonic, turbulent flow, indicate a scaling of the velocity power spectrum close to -2, which correspond to the purely shock-dominated turbulence the so called "Burger's turbulence" [Burgers, 1948; Schmidt, 2009; Kritsuk *et al.*, 2007*b*; Federrath *et al.*, 2010]. The physical origin of turbulence in the ISM is not well understood yet. Whether it is driven on large or small scales, is still subject to considerable debate. Numerous observational studies indicate that molecular cloud turbulence is always dominated by the largest-scale modes accessible to the telescope [Ossenkopf & Mac Low, 2002; Brunt *et al.*, 2009]. Some examples of the driving sources for the turbulence on the large scales range from the accretion of gas of extragalactic origin [Klessen & Hennebelle, 2010] or supernova explosions [Mac Low & Klessen, 2004; Dib *et al.*, 2006]. Other sudies showed that it is unlikely that internal sources, like stellar winds could have relevant effects on turbulence at the large scales [Banerjee *et al.*, 2007; Brunt *et al.*, 2009] although some models have investigated their important role as drivers on the small scales [Nakamura & Li, 2007].

Despite the advances in instrumentation and computer modeling, many questions regarding the properties of turbulence in astrophysical processes remain unanswered: What is the shape of the magnetic field spectrum at the large and the small scales ? How is the energy cascaded and dissipated ? How does the turbulent flow enhance (or inhibit) the transport of heat ?

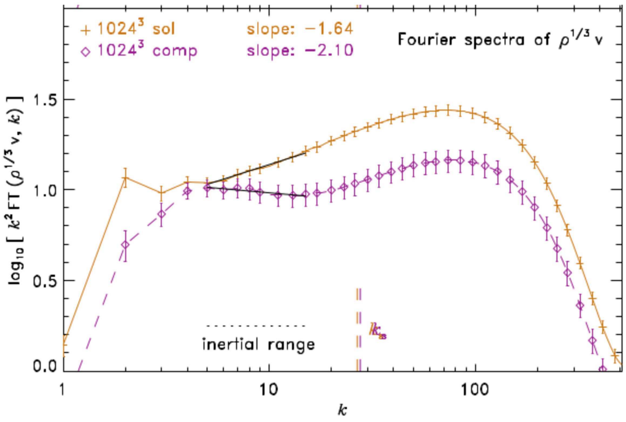

Figure 3.5: Fourier spectra of the density weighted velocity. Adapted from Federrath *et al.* [2010].

Moreover, the properties of the density and the velocity statistics and the spectral scalings seem to be affected by the nature of the forcing in compressible turbulence, whose role is still not very clear. We distinguish between the solenoidal forcing (divergence-free, "vortical") applied in incompressible turbulence vs the compressible one (curl free, "potential"). In a pure solenoidal forcing, the effect of the compressibility decays in time and so is usually not reflected in the stationary regime of the turbulence [Federrath *et al.*, 2010]. However, this is not the case for a pure compressible forcing, being executed by external processes. The effect and the nature of the forcing is of a big interest especially for understanding unclear physical phenomena like the origin of the supersonic interstellar turbulence, the energy injection mechanisms and the processes that lead to the star formation. These aspects are mainly studied in simulations by Federrath *et al.* [2008]; Schmidt *et al.* [2008]; Schmidt [2009].

Performing high-resolution hydrodynamical simulations of driven isothermal compressible turbulence, Federrath *et al.* [2010] observed that the turbulent spectra and the scaling are different whether the forcing is solenoidal or compressible. In the solenoidal case they showed the presence of the approximate Kolmogorov scaling $\sim k^{-1.6}$ for the density weighted velocity. However, under compressible driving no Kolmogorov scaling was observed (Figure 3.5).

Another important difference between the solenoidal and the compressible forcing is related to the statistics of the density fluctuations which play an essential role for the phenomenology of the compressible turbulence, notably in supersonic regimes of astrophysical plasmas. One of the most important properties is the probability density function of the logarithmic mass density fluctuations $s = \ln(\frac{\rho}{\rho_0})$.

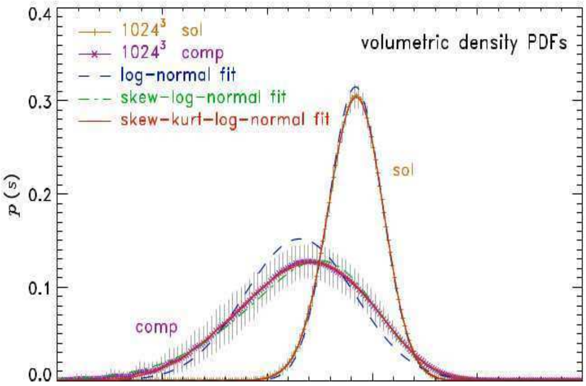

Figure 3.6: Volume-weighted density PDFs $p(s)$ of the logarithmic density s in linear scaling. Adapted from Federrath *et al.* [2010].

The pioneering works done by Padoan *et al.* [1997]; Passot & Vázquez-Semadeni [1998] have shown that the standard deviation of the linear density PDF grows proportional to the rms of the turbulent Mach number M_s. However, Federrath *et al.* [2010] showed that the shape of the PDFs change as well but depending on the nature of the forcing. For purely compressible forcing, the PDF are not log-normal, but develop some tails as one can see in Figure 3.6. The shape of the PDFs could be used as a "tool" for studying the nature of the forcing by computing s using the in-situ density measurements. I recall that these results are based on hydrodynamical simulations and no in-situ studies have been made regarding the compressive and solenoidal forcing in a high turbulent Mach number regime. In fact, I have started to check this for few events in the magnetosheath of Saturn, however because of the low resolution of the ELS density and the constraints regarding the velocity CAPS data (See sections 4.1.2 and 4.4.1), I could not calculate reliable values of the turbulent Mach number and so have a solid interpretation of the results.

3.4 Compressibility in the solar wind

In the previous sections, an overview of the main properties of turbulence was presented in environments with different levels of compressibiliy: the solar wind and the planetary magnetosheaths. Let us now consider the effect of the compressible (density) fluctuations and how they change the macroscopic and spectral behavior of turbulence.
In the solar wind compressible fluctuations are low and the magnetic field and proton number density fluctuations depend on the speed of the wind. On the large scales, compression occurs in the corotating interaction region, but on the smaller scales (but still $\gg \rho_i$ and d_i), the fluctuations are essentially incompressible and differences are found for the high and the low speed solar wind. As a matter of fact, the slow wind is generally more compressive with a fractional density fluctuation of about 30% compared to the fast wind which is about 10% [Bruno & Carbone, 2005]. Moreover, as we have already mentioned in section 3.1.1, the fluctuations in the fast wind are essentially more Alfvénic than the slow one. Different studies have showed that high Alfvénicity is correlated with low compressibility of the density fluctuations [Bruno & Bavassano, 1991, 1993; Klein *et al.*, 1993].
In order to study the nature of those compressible fluctuations, many theoretical and observational works proposed that the solar wind compressive fluctuations could be studied within the "Nearly Incompressible" (NI) model [Montgomery *et al.*, 1987; Matthaeus & Brown, 1988; Zank & Matthaeus, 1990]. In the framework of this model, Montgomery *et al.* [1987] showed that the power density spectrum of the density fluctuations (playing a passive role) and the magnetic field fluctuations follow the same $-5/3$ Kolmogorov law in the inertial range. However, Hnat *et al.* [2005] showed using extended self-similarity that actually the plasma density fluctuations could be "active", implying the importance of the compressiblility in the solar wind.

Another significant observational study regarding the effect of the compressible fluctuations in fast solar wind turbulence was done by Carbone *et al.* [2009]. They proposed an empirical compressible version of the incompressible MHD exact law derived by Politano & Pouquet [1998] (Hereafter, PP98). They actually replaced the incompressible Elsässer variables $\mathbf{z}^{\pm}$ (defined in 2.3.2) by a density weighted compressible Elsässer variables $\mathbf{w}^{\pm} = \rho^{\mathbf{1/3}}\mathbf{z}^{\pm}$. This idea was first proposed by

Kritsuk *et al.* [2007*b*,*a*] who showed using large-scale Euler simulations of supersonic turbulence (rms turbulent Mach number ~ 6) that the mass weighted velocity was the primary variable that governs the energy transfer through the cascade, and moreover, could lead to self-similarity in weakly and highly compressible flows.

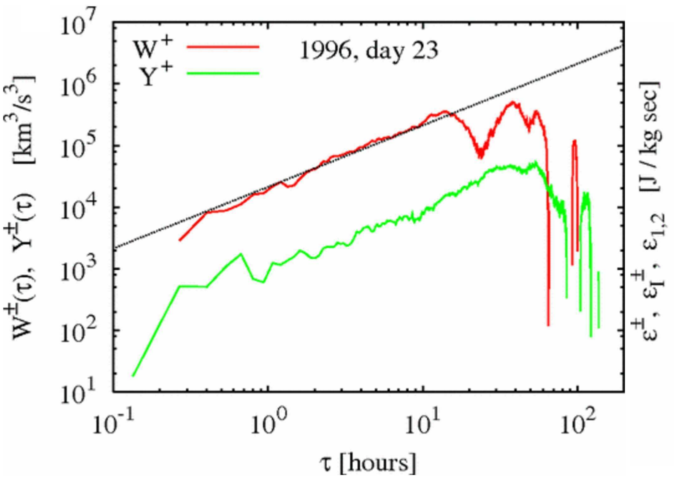

Figure 3.7: Comparison between the mixed third-order compressible pseudo-energy flux $\mathbf{w}^{\pm}$ (red) with the incompressible flux (green) as computed using Ulysses data. Adapted from Carbone *et al.* [2009].

Inspired by this later work, Carbone *et al.* [2009] used Ulysses spacecraft data in the polar solar wind and observed a better scaling with $\mathbf{w}^{\pm}$ as one can see in Figure 3.7. Moreover, their results showed that the compressible energy transfer rate is higher than in the incompressible model (Figure 3.7). They concluded that the compressibility present in the fast solar wind supply the energy dissipation needed to account for the anomalous local heating of the nonadiabatic solar wind.

However, the model is heuristic, in the sense that it was not derived analytically. More recently Banerjee & Galtier [2013], established an exact law for compressible isothermal MHD, which is in some sense the counterpart of PP98 exact relation derived for incompressible MHD turbulence (see section 2.3.3). We will see throughout my thesis, the first applications of this exact isothermal compressible MHD model to the fast and the slow solar wind and to the more compressible planetary magnetosheaths, using a large statistical samples of in-situ data. I will compare in particular the new results to the predictions from PP98 and the Carbone *et al.* [2009] models, and discuss the different reasons of the discrepancy between the heuristic model of Carbone *et al.* [2009] and the exact model of Banerjee & Galtier [2013].

Part II

Research work: spacecraft observations of turbulence in the magnetosheaths and the solar wind

CHAPTER 4

Planetary magnetosheath turbulence.

Contents

This chapter represents the first part of my research work regarding the properties of turbulence in a compressible medium: the planetary magnetosheaths of Saturn and Earth using Cassini and Cluster data respectively. It consists of four sections. In the first two, I will introduce the Cassini-Huygens and Cluster missions, and I will briefly overview the particles and fields instruments that I used for each of the spacecraft during my work. Secondly, I will discuss the different properties of turbulence at MHD and kinetic scales in comparison to the ones observed in a more accessible environment, the magnetosheath of Earth. Eventually, I show and discuss some technical aspects related to Cassini's instruments calibration in which I have worked and point out some caveats that need to be considered while interpreting the results obtained in this part. This work has led to two publications: L. Z. Hadid,

F. Sahraoui, K. H. Kiyani, A. Retino, R. Modolo, P. Canu, A. Masters, and M. K. Dougherty, ApJL 2015 and S. Y. Huang, L. Z. Hadid, F. Sahraoui, 2016 submitted.

4.1 Cassini-Huygens spacecraft mission

4.1.1 Overview and objectives

The Cassini-Huygens spacecraft represents one of the most ambitious efforts in planetary space exploration ever mounted to investigate the Saturnian system. It was developed by the National Aeronautics and Space Administration (NASA), the European Space Agency (ESA), the Italian Space Agency (Agenzia Spaziale Italiana, ASI), and many other European and American academic and industrial contributors. This project is managed by the Jet Propulsion Laboratory (JPL) in the United States, Pasadena, California. The spacecraft was launched in October 1997 and reached Saturn by July 2004 to begin a four-year nominal mission. However, due to its important scientific results, the mission was extended until 2017. The final phase of the mission includes a series of deep dives between the Saturn and its rings. The mission will end on September 15, 2017 when it will fall into Saturn's dense atmosphere.

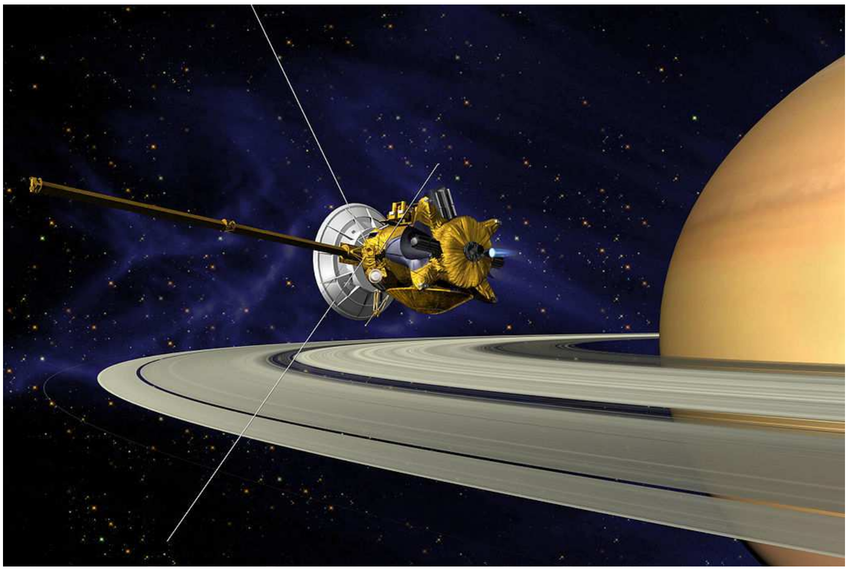

Figure 4.1: Artistic photo of Cassini-Huygens during the Saturn Orbit Insertion (SOI) maneuver. ©NASA/JPL.

The Mission was named in honor of the two seventeenth-century scientists who pioneered the observations of Saturn. The first one is the Italian-French astronomer and astrologer Giovanni Domenico Cassini (1625-1712) who was the first to discover four of Saturn's satellites and the largest gap between its rings (known as the *Cassini*

Divison) and the second one is the Dutch astronomer Christiaan Huygens (1629-1695) who is famous for spotting the presence the planet's largest moon: Titan. The spacecraft combines two main elements: the ESA Huygens probe that was separated from Cassini orbiter to land for the first time on Titan to study its surface and atmosphere; and the ASI/NASA three-axis stabilized Cassini orbiter, which continues to orbit around Saturn sending data back to Earth. The later is equiped with 12 science instruments, the optical and the microwave remote sensing ones (to study Saturn, its atmosphere, its rings and the moons in the electromagnetic spectrum) and the fields and the particles instruments (MAG, RPWS & CAPS respectively), which take in-situ measurements of the environment around the spacecraft. During my research work I used these latter instruments.

Figure 4.2: The Cassini-Huygens spacecraft assembly in Kennedy Space Center's. ©NASA Kennedy Space Center.

It is worth recalling that Saturn's magnetosphere was already visited three times by the spacecraft Pioneer 11 (1979), Voyager 1 (1980) and Voyager 2 (1981); but each one flew very rapidly the planet. Therefore, the prominent goal of Cassini-Huygens mission is to conduct an in-depth exploration of the Saturnian System. Its main objectives are: 1) a close-up study of the Saturn's moons, in particular Enceladus and Titan, which could provide some clues to the chemistry of early Earth (both could enclose liquid water and some organic chemical potential); 2) a deep dives into the giant Saturn environment's, exploring the structure of the planet, and revealing the physics behind the formation of its rings which, in reality, are not ordered and calm as they look (many interacting waves indeed form and dissipate), and 3) a detailed investigation of the magnetized plasma near the planet on which my work is based on. This long-lived mission has afforded to witness never-before-seen events that are enlarging our understanding on how planetary systems form. From the numerous discoveries of Cassini-Huygens spacecraft we can cite: The first landing of the Huygens probe on a moon in the solar system that revealed a soupe of complex hydrocarbons, including benzene, in Titan's atmosphere, concluding Titan to be remarkably like Earth before life evolved. Also, imaging with radar, and with both visible and infrared wavelengths showed that Titan has similarities to Earth with rain, rivers, lakes and seas. The radio and plasma wave instrument showed that the variation in radio waves controlled by the planet's rotation is different in the northern and southern hemispheres. These rotational variations also appear to change with the Saturnian seasons. In fact the length of day at Saturn is still unknown. Moreover, Cassini orbiter discovered as well active and icy plumes on the Saturnian moon Enceladus, and found that the rings around the planet are dynamic, witnessing the possible birth of a new moon. Moreover, the spacecraft imaged for the first time some vertical structures in the rings. Many other discoveries that are intrinsic to Saturn and its atmosphere and to its plasma environment, were made as well.

4.1.2 In-situ fields and particles instruments

Since the Cassini mission is to be the first orbiter of Saturn, this spacecraft provided much better spatial and temporal coverage than those of the 20 years older missions of Voyagers 1 & 2 whose plasma wave subsystem could measure only the electric field components, and Pioneer 11 that did not have a radio and plasma waves instrument. The fields and the particles instruments of Cassini have several new capabilities: improved sensitivity and dynamic range of the Fluxgate Magnetometer (FGM) and the plasma spectrometer (CAPS) and for the first time around Saturn the Search Coils Magnetometer (SCM) measured the three magnetic components of the waves for a broad range of frequencies $[1\,\mathrm{Hz} - 12\,\mathrm{kHz}]$.

The FGM from the Dual-technique magnetometer experiment (MAG), designed at Imperial College (London) [Dougherty *et al.*, 2002], is intended to measure the background magnetic field and its low frequency fluctuations spanning four orders of magnitude from the DC up to 30 Hz. However, it is not sensitive enough to reach the electron scales [f $>$ 30 Hz], the reason for which the SCM are needed in order to cover the higher frequencies (discussed in the next paragraph). The main advantage of using the FGM, is the fact that it could span the MHD scales $\sim [DC - 0.01]$ Hz and the sub-ion ones $\sim [0.05 - 1]$ Hz. In fact since Saturn is much further from the Sun, the magnetic field in the solar wind at $\sim$ 9 AU is lower compared to 1 AU, so all the spatial and temporal scales (Larmor radius (ρ_i), ion gyroperiod ($1/w_{ci}$)) are shifted towards higher values ($\rho_i \sim 1000$ km $\Rightarrow$ Taylor-shifted scale $f_{\rho_i} = \frac{V}{2\pi\rho_i} \sim 0.05$ Hz, where V represents the flow speed in the magnetosheath. A discussion regarding the validity of the Taylor hypothesis is given in Section 4.4.4).

Because the magnetometers are sensitive to the magnetic fields produced by the spacecraft, the FGM of Cassini was installed on an 11 meter non-metallic arm called a "mag boom" to get it as far away from the spacecraft as was possible to reduce interference from the spacecraft. More details about the instrument electronics, modes and controls can be found in Dougherty *et al.* [2002].

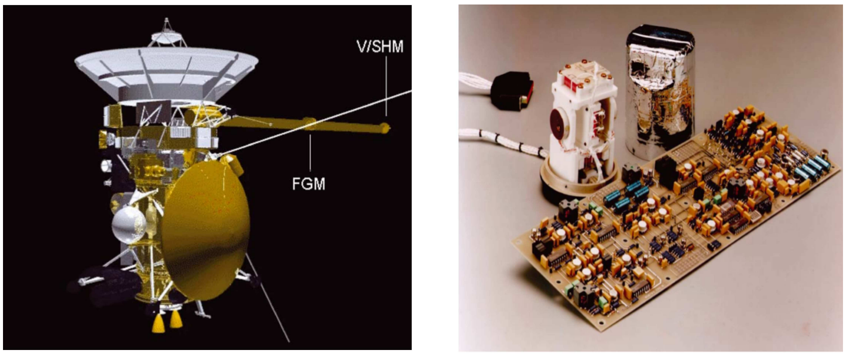

Figure 4.3: Left: The location of the magnetometer hardware on the spacecraft is shown halfway the "mag boom". Right: Electronics photograph of the FGM (with cover off) and electronics board. Adapted from Dougherty *et al.* [2002].

The Radio and Plasma Waves Science (RPWS) experiment [Gurnett *et al.*, 2004] includes the SCM, the electric antennas and the Langmuir probe designed to study mainly radio emissions and plasma waves (Figure 4.4). In my thesis I used the SCM which I will describe now. The SCM, provided by the CETP (now the LPP), is also a tri-axial Search-Coil magnetic antennas allowing the measurements of the three magnetic components of the waves at higher frequency ranges than the FGM, from 1 Hz up to 12 kHz (Figure 4.4).

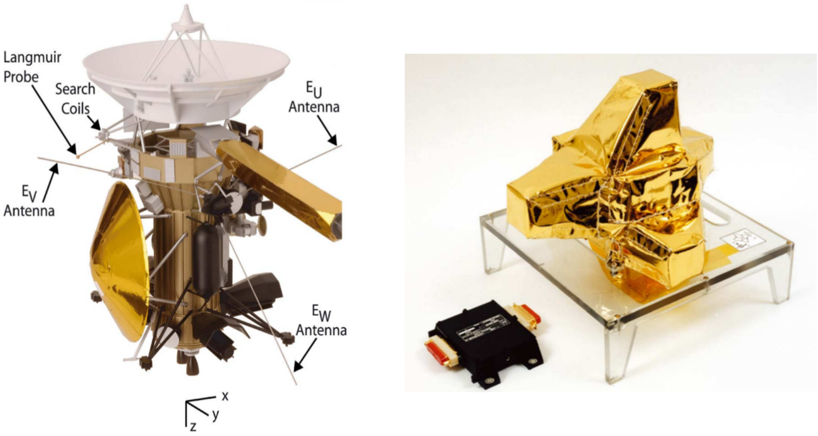

Figure 4.4: Left: The placement of the different RPWS hardware on Cassini Orbiter. Right: The tri-axial magnetic search coils assembly covered by thermal blankets. Adapted from Gurnett *et al.* [2004].

They are connected to at least three receivers, each of them covers a different frequency range. The medium frequency receiver (MFR), which returns only spectral information that covers the frequency range from 24 Hz to 12 kHz. The low frequency receiver (LFR), provides waveforms from 1 Hz to 26 Hz and Fourier transforms them onboard the spacecraft to provide spectral information below 26 Hz. As a consequence it completes the spectral survey when used in conjunction with the MFR receiver. The five channel waveform receiver (WFR) can acquire signals from up to five sensors simultaneously (typically two electric and three magnetic antennas) and is primarly used to capture the waveforms. It consists of two different modes spanning different frequency ranges: [1 Hz − 26 Hz] and [3 kHz − 2.5 kHz]. These waveforms can be analyzed on the ground in either the temporal domain, or in the frequency domain (Fourier transformed) to provide the frequency-time spectrograms. The characteristics of all the receivers are summarized in the block diagram of the RPWS instrument in Figure 4.5.

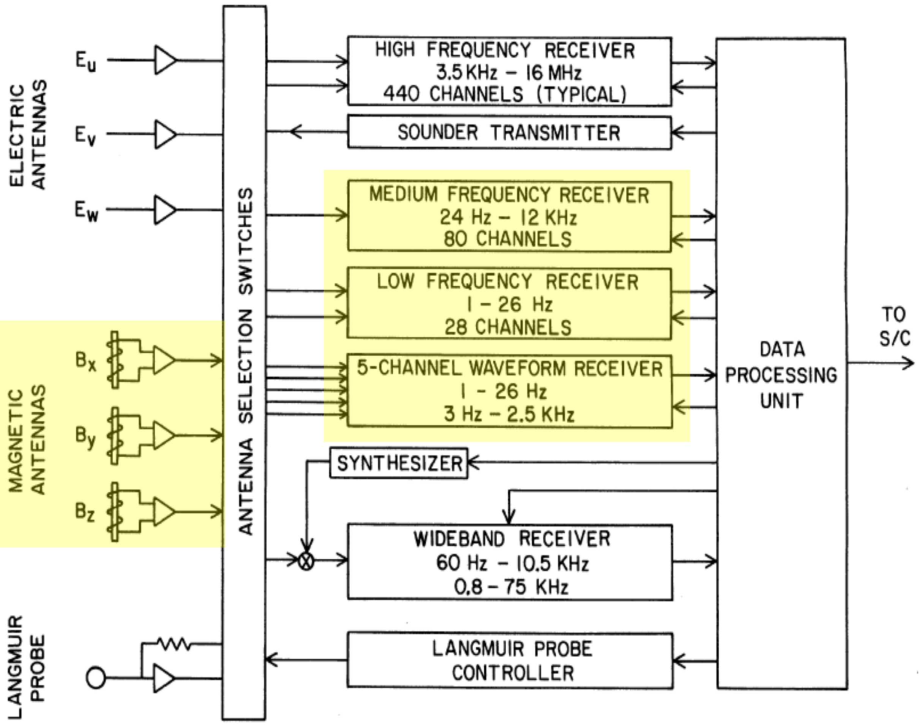

Figure 4.5: The functional block diagram of the RPWS instrument. Adapted from Gurnett *et al.* [2004].

I used the plasma data (density, the flow velocity, temperature) from the ELectron Spectrometer (ELS) instrument of the Cassini Plasma Spectrometer (CAPS) experiment. It consists of two other sensors, the Ion Beam Spectrometer (IBS), and the Ion Mass Spectrometer (IMS) shown in Figure 4.6.

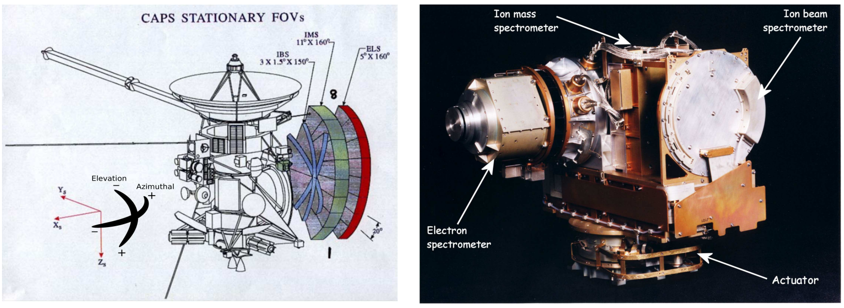

Figure 4.6: Left: Location of the CAPS sensors on Cassini spacecraft. Right: CAPS instrument with its three sensors (ELS, IMS, & IBS) and the actuator motor platform. Adapted from Young *et al.* [2004].

The ELS measures the velocity distribution function (VDF) of the electrons with a time resolution of 32 s. The IBS measures ion VDF and the IMS is designed to measure the composition of hot, diffuse magnetospheric plasmas and low-concentration of the ion species. The IBS and IMS sensors have a resolution of 8 min. Each sensor is composed of 8 wedge-shaped sectors that take single data counts referred to as "SNG" (Figure 4.6). Based on charged particle motion in electrostatic fields, the particle trajectories are dispersed after entering the sensors through each of the SNG, and then measured using electron-multiplier detectors. The ELS and the IBS optics separate electrons and ions respectively by energy/charge (E/Q) ratio and by elevation angle of arrival and the azimuthal angle (obtained by sweeping the sensor fields-of-view using a motor driven actuator). From the knowledge of the detector counting rates as a function of the energy and the two angles, particle velocity distributions can be deduced. The IMS optics also separate ions by E/Q and angle of arrival, but then in addition, disperse them by a time-of-flight (ToF) analyzer for the determination of the ion velocity, and hence the mass-per-charge (m/q) determination. More details regarding the design and the principles of operation of each sensor can be found in Wilson *et al.* [2008]; Young *et al.* [2004].

4.2 Cluster spacecraft mission

4.2.1 Overview and objectives

Cluster is a mission of ESA with NASA participation, which was launched in 2000. Its main objective is to study the magnetic environment in the near-Earth space and its interaction with the solar wind. It consists of four identical probes flying in a tetrahedral formation. Due to the quality of the measurements and its successful scientific outputs, the mission has been extended until December 2016 (and most likely until 2018). Indeed, this mission fulfilled its promise being a revolutionary magnetospheric space mission! The combination of the four spacecraft allowed for the first time the application of multi-spacecraft methods to study complex 3-dimensional processes at the scales of the separation of the spacecraft ($\sim 10^2 - 10^4$ km). More importantly, these methods allow us to differentiate between spatial and temporal variations, to estimate quantities such as the current $\vec{J} = \nabla \times \vec{B}$ (in the low frequency MHD scale approximation) and their small scales structures [Paschmann & Daly, 1998].

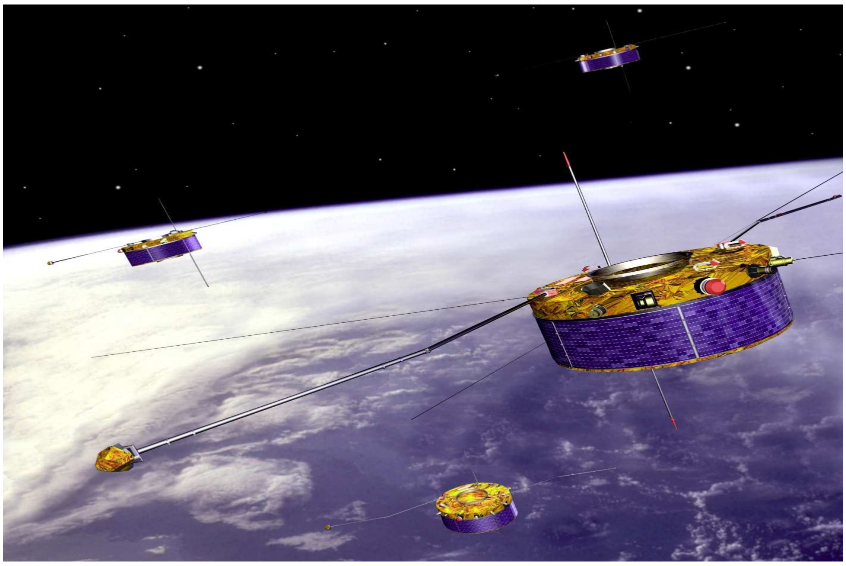

Figure 4.7: Cluster mission with its 4 spacecrafts orbiting around Earth. ©ESA.

4.2.2 In-situ fields and particles instruments

In my thesis work, I used Cluster data from the Cluster Science Archive (CSA) in order to characterize the turbulent properties in the magnetosheath (Chapter 4), but also to study the role of the compressible turbulence in the magnetosheath plasma dynamics at MHD scales, that I will present in chapter 5. For both analyses I used the low frequency magnetic field measurements from the FGM instrument, the high frequency magnetic field fluctuations from the Search-Coils magnetometer (STAFF), the electrons and the ions density, velocity and temperatures from the Plasma Electron and Current Experiment (PEACE) and the Cluster Ion Spectrometer (CIS) respectively, and finally I used the electric field measurements (EFW) to deduce the density of the plasma at higher resolution (0.2 s) than the one measured by the spectrometer (4 s) that I applied in Section 4.3.3. Here is a brief description of each of these instruments that I used for this work:

The Fluxgate Magnetometer (FGM) designed at Imperial College (London), consists of two tri-axial sensors measuring the three components of the magnetic field. One sensor is placed at the end of a 5.2 m boom while the other is placed on the same boom 1.5 m away from the spacecraft body, in order to control the magnetic interference from the spacecraft. The fluxgate sensors are nominally sensitive from the DC up to 10 Hz, although in practice the instrument noise level is such that the sensitivity is degraded above 1 Hz. The highest time resolution of the instrument is $\sim$ 0.01 s known as the burst mode, and the standard mode samples at the 15.5 vectors$/s$ rate. The burst mode mainly targets the high resolution time sampling of discontinuity structures such as the bow shock or the magnetopause. In my work I used both modes for computing the PSDs, depending on the scales I was interested in.

The Spatio-Temporal Analysis of Field Fluctuations (STAFF), designed at LPP (France) [Cornilleau-Wehrlin *et al.*, 2010], is a tri-axial search coils magnetometer allowing the measurements of the three magnetic components of the waves from 0.1 Hz up to 4 kHz. STAFF has the same sensitivity level of Cassini's SCM, however since the former is mounted on 5 m (compared to 1m for Cassini) the magnetic background of the spacecraft is reduced. It consists of 1) a waveform analyser (STAFF-SC) that provides data in two different modes with different frequency ranges, depending on the spacecraft telemetry rate: the Normal Bit Rate (NBR) [0.1-12.5] Hz or the High Bit Rate (HBR) [0.1-225] Hz, and 2) an onboard spectrum Analyser (STAFF-SA) that calculates the spectra for five wave components, the three magnetic components from the STAFF experiment and the two electric components from the Electric Field and Wave (EFW) experiment, from 8 Hz to 4 kHz.

Figure 4.8: Left: FGM instrument ©Imperial College. Right: STAFF covered by the thermal blanket and the preamplifier ©LPP.

Cluster Ion Spectrometer (CIS), designed at IRAP (France), measures the full three-dimensional ion distributions with 4 s time resolution (one spacecraft spin) and with mass-per-charge composition determination from $\sim$ 0 to 40 keV/e. The CIS consists mainly of two different instruments, a Hot Ion Analyser (HIA) and a time-of-flight ion Composition Distribution Function (CODIF) [Reme *et al.*, 1997]. **PEACE** instrument designed at UCL (London), similarly to ESA (THEMIS mission), measures the 3D electron velocity distribution in the energy range 0.7 eV to 32 keV, and makes onboard the calculation of moments (for a restricted energy range) and a spacecraft potential estimate, once every spin [Johnstone *et al.*, 1997]. The CIS package and PEACE instrument are shown in Figure 4.9. The calibration of the density measurements are complex procedures (out of the scope of my thesis), in fact they are cross-calibrated with the WHISPER relaxation sounder that determines the total number density from the propagation characteristics of radio waves (same working principle as the sounder transmitter from the RPWS experiment of Cassini briefly explained in Section 4.4.1).

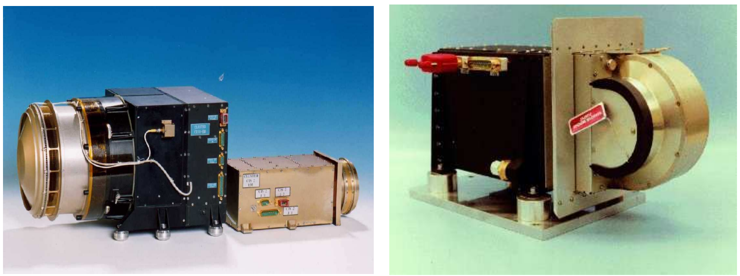

Figure 4.9: Left: The CODIF (on the left) and the HIA (on the right) ion detectors of the CIS experiment ©IRAP. Right: PEACE instrument sensor ©MSSL.

,

The Electric Field and Waves (EFW) instrument, engineered at IRF (Sweden), measures the electric field at 25 or 450 sample per second. Sampling rates up to several 1000 sample per second can be used as well during short time periods (around 12 seconds). EFW consists of two pairs of spherical probes each, with a probe-to-probe separation of 88 m, located at the end of thin wire booms extending outwards from the spacecraft and phased by 90° in that plane [Gustafsson *et al.*, 1997]. The potential difference between two opposed probes yields a measurement of the electric field in the direction along the axis defined by the two probes. The use of the 4 probes allows us to estimate two orthogonal components of the electric field in the plane of the spacecraft spin.

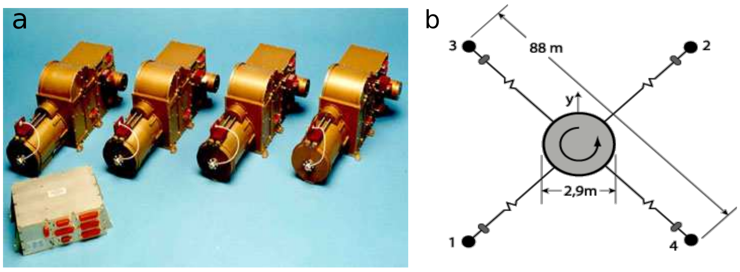

Figure 4.10: a) 4 boxes of boom units and electronic box for EFW experiment. Each boom unit contains spherical probe and 50 m of wire boom. b) EFW probe configuration ©IRF.

In my thesis I used the spacecraft potential data of the EFW instrument to deduce the high resolution (0.2s) density measurements that I needed in order to identify the nature of the wave mode(s) involved in the turbulence cascade at the sub-ion scales (Section 4.3.3).

Estimation of the electron density measurements from EFW. Since the spacecraft and the probes are conductive bodies in a plasma, in sunlight they emit photoelectrons and typically become positively charged. This attracts in turns some of the photoelectrons back to the spacecraft and a return current of electrons from the surrounding plasma, reducing the spacecraft potential relative to the plasma (V_{sc}) until an equilibrium is reached in which the currents to and from the spacecraft are balanced. For higher electron density, n_e, the return current is larger, and so V_{sc} is smaller. Hence, V_{sc} can be used as a proxy for n_e, allowing density fluctuations to be measured at a higher frequency than with particle instruments [Pedersen, 1995]. In fact, only for time scales larger than the time that it takes the spacecraft to charge, V_{sc} can be considered as a good proxy for the density. In the magnetosheath and the solar wind the spacecraft relaxes to the new equilibrium in response to density changes around 6 kHz. Since in my work I study much lower frequencies, then I can infer the high frequency n_e from V_{sc}.

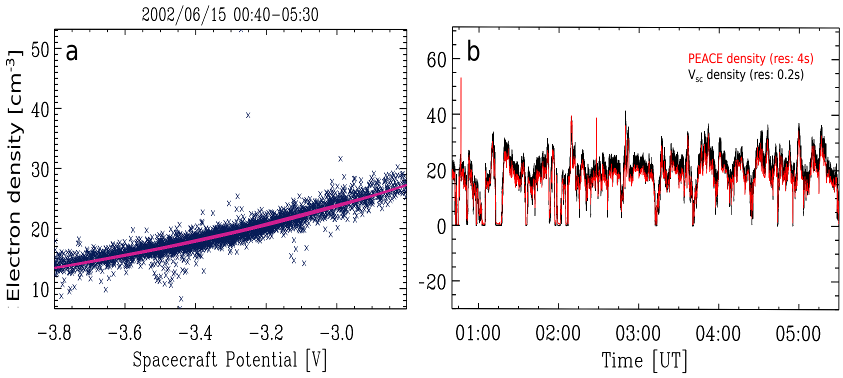

Figure 4.11: a) Density (n_e) as a function of the spacecraft potential (V_{sc}) relative to the solar wind. The best fit exponential calibration curve is shown as a solid purple line. b) Comparison between the high frequency density inferred from the V_{sc} (black) and the lower frequencies measured by PEACE at the spin (4 s) resolution (red).

To convert from V_{sc} to n_e, a calibration curve is obtained by comparing V_{sc} to the density data. An example of this comparison for the time interval 00:40-05:30 on 2002/06/15 is shown in Figure 4.11-a. Since the density is expected to be proportional to the exponential of V_{sc} [Pedersen, 1995; Scudder *et al.*, 2000], a least squares fit (purple line) of the data in Figure 4.11-a to the equation $n_e = C_1 \exp(V_{sc}/C_2)$ was performed, where C_1 and C_2 are the fit parameters. Once these parameters are obtained, one can substitute the high resolution V_{sc} data and deduce the corresponding electron density. Figure 4.11-b shows a comparison between n_e measured directly by PEACE instrument (red) at the spin resolution (4 s) and the density inferred from V_{sc} (black) for a higher time resolution of (0.2 s). As one can see, the high time resolution of the estimated density from V_{sc} corresponds well to the one measured by the particles instrument of lower resolution. Nevertheless one can obviously see some descrepancies between the two data sets, which is normal, since the spacecraft potential is not a density, but rather a density proxy.

4.3 Turbulence properties at MHD and kinetic scales

Using a list of several hours shock crossings of the Kronian magnetosheath by the Cassini spacecraft (list given in Appendix B), I investigated the properties of turbulence at MHD and sub-ion (kinetic) scales. The fields and the particles data were downloaded from different sources, the Automated Multi Dataset Analysis (AMDA), the Planetary Data Science (PDS) and I used IDL programming language for the data analysis. One of the criteria of choosing the time intervals in the magnetosheath is that magnetic fluctuations δB must be much higher than the noise level of FGM. Since we could not obtain the sensitivity floor of the instrument from the FGM team in physical units, I used δB measured in the solar wind near Saturn ($\sim$ 9 AU), which is much lower than in the magnetosheath, as the upper bound of the sensitivity level of the instrument (dotted curve in Figure 4.13). I use the planet centered coordinates systems for the magnetic field data, KRTP in the case of Cassini data, which is a spherical coordinate system with e_r pointing from Saturn to Cassini, $e_\phi = e_s \times e_r$ in the direction of corotation (e_s is aligned with Saturn's spin axis) and $e_\theta = e_\phi \times e_r$ in latitudinal direction forming a right-handed coordinate system.

In this work I tried to answer four main questions regarding turbulence in the magnetosheath at the different scales: What are the scaling laws of turbulence? What is the nature of the plasma fluctuations (e.g., Alfvénic or magnetosonic, or others like rotational discontinuities, structures etc ...) that dominate the energy cascade? How do all these properties compare with known features of turbulence in the solar wind? Do the turbulence properties depend on the local plasma parameters (and the normal angle to the shock $\Theta_{\mathbf{Bn}}$)?

4.3.1 Spectral properties

A typical Kronian magnetosheath crossing for a quasi-perpendicular and quasi-parallel bow-shocks taken respectively on 2005 March 17 at 02:00-08:30 UT and on 2007 February 03 at 00:10-02:00 UT are represented in Figure 4.12. As one can see, for the quasi-perpendicular case, ($\sim$ 08:20 in Figure 4.12-a) the bow shock is characterized by a clear and sharp transition separating two distinct plasma regions: the solar wind on one side and the magnetosheath on the other side. However regarding the quasi-parallel case ($\sim$ 01:10 in Figure 4.12-d), the transition between the upstream and the downstream is broad and complex. The general trend of the magnetic field and the density, measured respectively by the FGM sensor and the CAPS/ELS (Section 4.1.2), to increase going inward across the bow-shock from the solar wind into the magnetosheath can be observed as well for both shocks geometry.

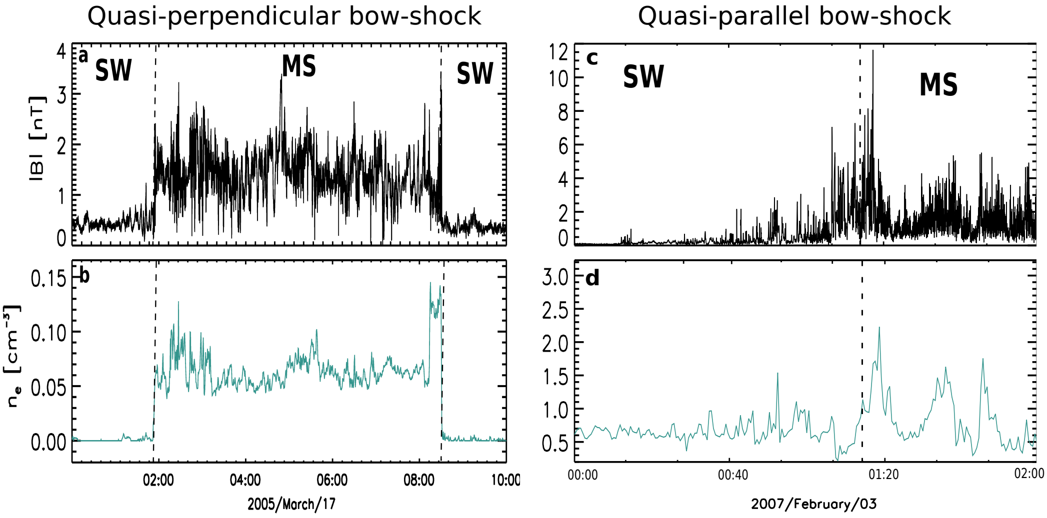

Figure 4.12: (a-c) Magnetic field modulus and (b-d) electron plasma density measured by the Cassini spacecraft in the solar wind (SW) and in the magnetosheath (MS) of Saturn on 2005 March 17 from 00:00 to 10:00 and 2007 February 03 from 00:10 to 02:00 for a quasi-perpendicular and quasi-parallel shocks respectively.

A first step in studying magnetosheath turbulence is to estimate the power spectral density (PSD). An example of the PSD of the magnetic field fluctuations computed in the magnetosheath of Saturn, using a windowed fast Fourier transform (FFT), is presented in Figure 4.13.

The spectrum shows two ranges of scales with distinct power laws: $\sim f^{-1.26}$ at low frequencies ($f < 10^{-2}$) Hz and $\sim f^{-2.54}$ at the higher frequencies. This observation shows a striking result: turbulence transits directly from the *energy-containing scales* down to the ion kinetic scales, without forming the so-called Kolmogorov inertial range with a scaling of 5/3 (The validity of the Taylor-hypothesis is discussed in section 4.4.4). At first sight, the absence of the $-5/3$ law disagree with other observations in the magnetosheath of Earth [Alexandrova *et al.*, 2008; Sundkvist *et al.*, 2007]. It is worth noting that the spectral break is closer to the local ion gyrofrequency and the Taylor shifted (see section 4.4.4) Larmor radius $f_{\rho_i} = V_f/2\pi\rho_i$ than to the Taylor-shifted ion inertial length $f_{di} = V_f/2\pi d_i$ ($V_f \sim 300\,\mathrm{km/s}$ is the average flow speed in the Kronian magnetosheath, $T_i \sim 258\,\mathrm{eV}$, $B_0 \sim 1.4\,\mathrm{nT}$, $n_e \sim 0.06\,cm^{-3}$, and $\beta_i \sim 3.3$). The reason might be that the latter are subject to higher uncertainties due to errors in estimating the plasma parameters using the ion moments from the CAPS-IMS sensor (see Section 4.4.1).

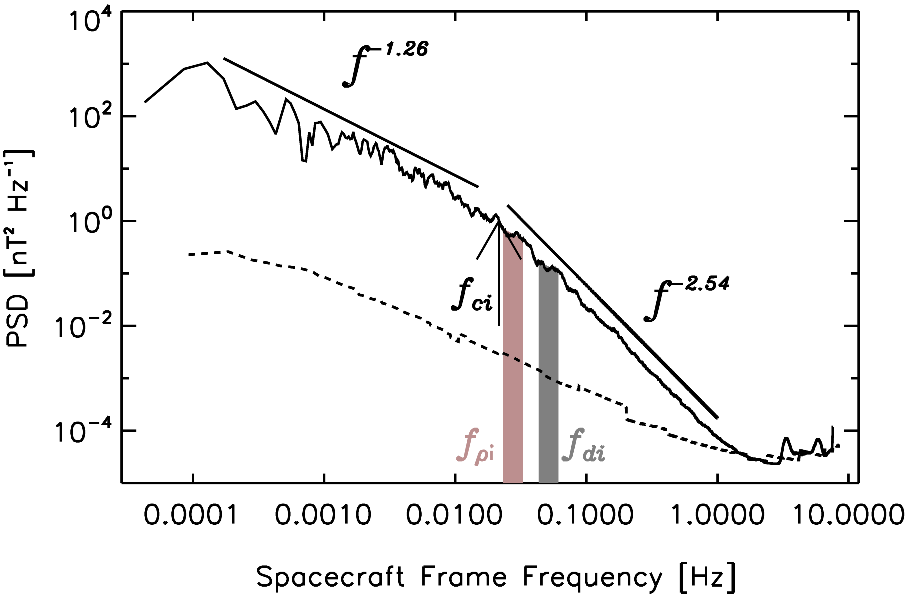

Figure 4.13: Power spectral density of the magnetic field fluctuations (δB) measured between 02:00 and 08:30. The black lines are the power-law fits. The arrow corresponds to the ion gyrofrequency f_{ci}; the gray and the red shaded bands indicate the Taylor-shifted ion inertial length (f_{di}) and Larmor radius (f_{ρ_i}), respectively. The width reflects the uncertainty due to errors in estimating the ion moments (see caveats in Section 4.4.1). Adapted from [Hadid *et al.*, 2015].

In order to investigate the presence of the Kolmogorov $f^{-5/3}$ spectrum and to see if it is related to the structure of the bow-shock or the location within the magnetosheath, I first analyzed a list of 42 shock crossings between 2004 and 2007, for quasi-parallel and quasi-perpendicular shocks separately. For most of the time intervals, the structure of the shock was identified by A. Masters by estimating the angle $\Theta_{\mathbf{Bn}}$ between the interplanetary magnetic field and the normal to the shock using a semi-empirical model of the global shock surface of Went *et al.* [2011]. I recall that $\Theta_{\mathbf{Bn}} > 45°$ indicates a quasi-perpendicular shock, whereas $\Theta_{\mathbf{Bn}} < 45°$ indicates a quasi-parallel one. However, for all the events, because of the model uncertainties (see Section 4.4.3), I visually verified for all the list that the quasi-perpendicular shocks have a sharp gradient in the magnetic field and the plasma measurements, and that the quasi-parallel shocks have large fluctuations.

The results shown in Figure 4.14 indicate that at the MHD scales the bulk of the spectra have slopes near -1 for quasi-perpendicular shocks, whereas behind a quasi-parallel shock shallower slopes ~ -0.5 are observed. For both shocks structures only three events (still more behind a quasi-parallel shock) show a spectral index close to $-5/3$ (black dashed line). The histogram of the slopes at sub-ion scales for a quasi-perpendicular shock peaks around −2.5 and for the quasi-parallel shock ~ -2.6, in general agreement with previous results reported in the solar wind and the terrestrial magnetosheath [Sahraoui *et al.*, 2013; Huang *et al.*, 2014]. A slight indication that steeper spectra are observed behind quasi-parallel shocks can also be seen.

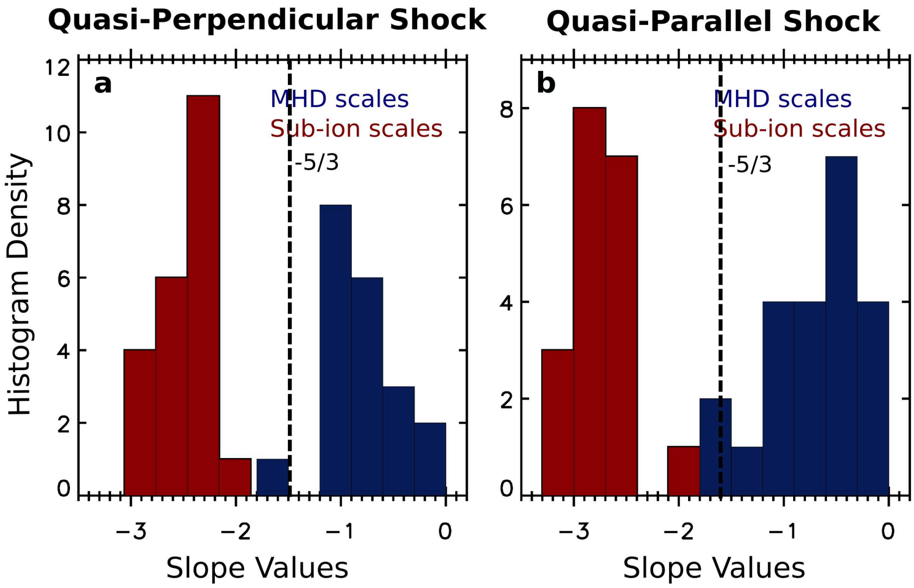

Figure 4.14: Histograms of the spectral slopes at MHD and sub-ion (kinetic) scales downstream of (a) quasi-perpendicular and (b) quasi-parallel shocks of Saturn's magnetosheath using Cassini data. Adapted from [Hadid *et al.*, 2015].

To confirm these results, I performed a much larger statistical study and analyzed the PSDs of δB of around 400 time intervals between 2004 and 2014 of 45 min duration each, in different locations within the Kronian magnetosheath including flanks and subsolar regions. I selected some of these data with respect to the ephemeris of Cassini within the magnetosheath bounded by the bow-shock and magnetopause models of Went *et al.* [2011] and Kanani *et al.* [2010] respectively. The rest of the case studies was provided to me by A. Masters and V. Génot. Nevertheless, I had to go through all the list and check that all the time intervals are relatively stationary and are far away from the bow-shock mainly for the quasi-parallel geometry where the transition between the solar wind and the magnetosheath is not clear. Also, it was necessary to make sure that the start time in the list corresponds to the exact time of when the spacecraft crossed the shock. Moreover, for the different locations within the magnetosheath, I used the KSM (Kronocentric Solar Magnetospheric) coordinate system which is similar to the GSM (Geocentric Solar Magnetospheric) coordinate system used at Earth. Because Saturn's rotation axis and magnetic dipole axis are < 1 degree different, I will not differentiate them when defining this coordinate system. For the Earth, this system would be based on the magnetic dipole axis. Here I will define the system in terms of the rotation axis instead, with the understanding that this is nearly the same as defining it in terms of the dipole axis. X_{KSM} points from Saturn to the Sun, Y_{KSM} is perpendicular to the rotation axis towards dusk and the Z_{KSM} is chosen so that the rotation axis lies in the $X_{KSM} - Z_{KSM}$ plane.

The histograms of the slope values at the MHD and sub-ion scales are presented in Figure 4.15-(a-b), and the corresponding averaged 2D distribution within the magnetosheath are shown in the bottom plots of Figure 4.15-(c-d). One can see that at the MHD scales (Histogram 4.15-a) the spectral indices are disperse and vary between $[-1.7, 0.5]$, only 44 events out of 400 are characterized by a Kolmogorov-like $-5/3$ spectral index (presented by the blue dashed line), whereas the other values are shallower. Looking at the average location of the few Kolmogorov-like cases (dark blue and purple in Figure 4.15-c), some trend appear to be toward the flank regions, whereas the rest of the magnetosheath, and in particular the sub-solar region, is dominated by shallower slope values $\sim -1, -0.5$. A particular presence of positive slopes at the MHD scales can be observed as well. An example of the PSD characterized by a positive or almost flat spectral law below 0.01 Hz is presented in Figure 4.16. The fitting is done locally on the spectrum using a sliding window and the corresponding time-dependent slopes as a function of the frequencies are presented in the second panel. The slopes are fitted by a hyperbolic tangent function curve from which I could verify the average spectral index for the MHD and the sub-ion scales. I think that these spectra with positive slopes could be related to some source near the bow-shock that injects energy at the large scales, but I did not explore further this point. This source might be specific to Saturn as no such positive slopes have been observed in the Earth's magnetosheath as shown below.

Regarding the sub-ion scales, the slope distribution is narrower as shown in histogram 4.15-(b) and are mostly concentrated between $[-2.2, -3]$ confirming the preliminary study shown in histogram 4.14. Moreover, the 2D distribution of these sub-ion slope values (Figure 4.15-d) shows no dependence with respect to the location within the magnetosheath. For the sub-electron scales ($f \gtrsim 30\,\mathrm{Hz}$), the fate of the energy cascade could not be studied yet because of some calibration issues regarding the SCM (see Section 4.4.2 for more details).

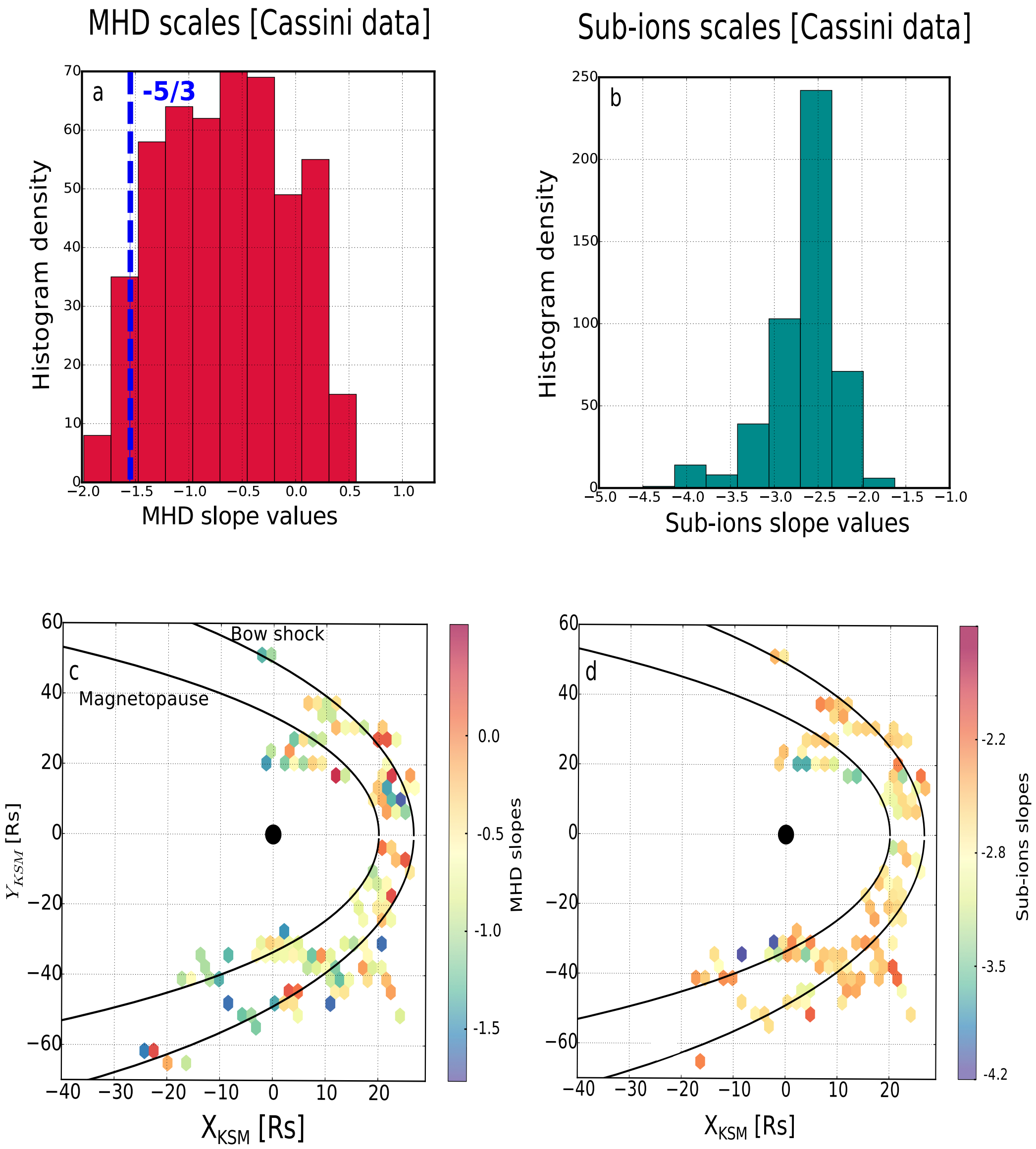

Figure 4.15: Top: Histogram of the spectral slope distribution for the 400 time intervals at the MHD scales (a) and the sub-ion ones (b). Bottom: The corresponding 2D distribution (X_{KSM}, Y_{KSM}) of the spectral slopes at MHD scales (c), and the sub-ion scales (d). The black curves represent the bow-shock and the magnetopause positions computed using the semi-empirical model of Went *et al.* [2011] and the empirical magnetopause model of Kanani *et al.* [2010] respectively.

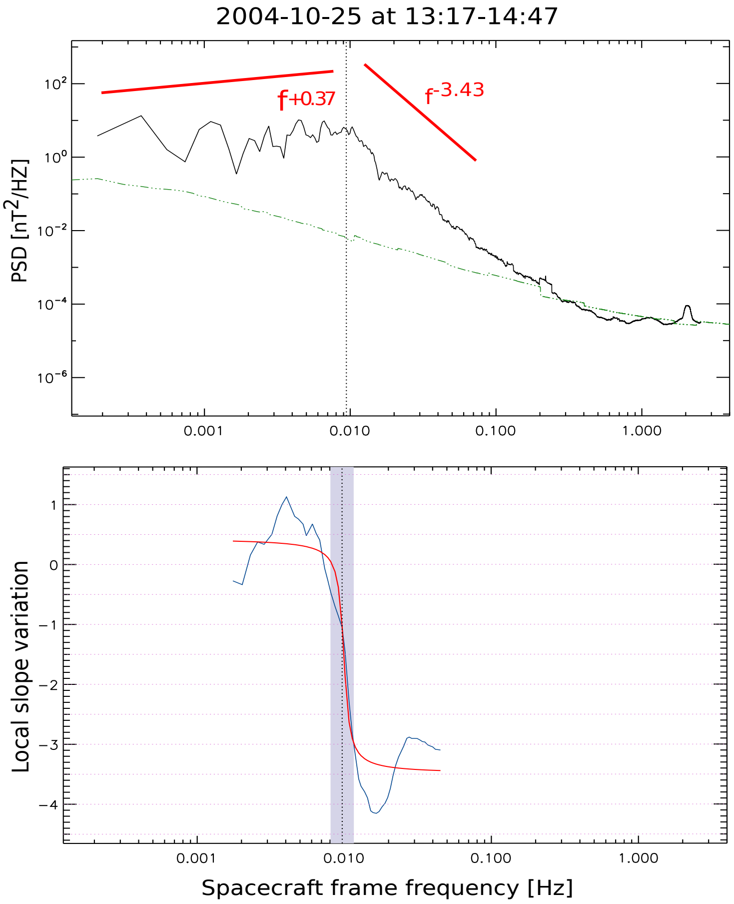

Figure 4.16: Top: Power spectral density of δB showing a positive/flat power law below 0.01 Hz. The red lines are the power-law fits. The green curve corresponds to the estimated noise level of FGM. Bottom: The local slope variation with respect to the frequency. The red curve is a fit using a hyperbolic tangent function and the dashed line correspond to the frequency break at the ion gyro-radius.

Since Cassini spends more time in the night side than the day side of the planet, the statistical study that I performed does not fill uniformly the Kronian magnetosheath (See Figure 4.15). In order to have a better understanding regarding the turbulence properties, for instance the origin of the f^{-1} spectrum and the transition to the Kolmogorov inertial range, We performed, in a collaborative work with Shiyong Huang, a more complete study regarding the existence of the Kolmogorov inertial range in the terrestrial magnetosheath using Cluster 3 data. We used the GSE coordinate system where the X_{GSE} axis coincide with the direction to the Sun, the Z_{GSE} axis is directed to the Ecliptic Pole, and the Y_{GSE} supplements the right-handed coordinate system, toward to the dusk.

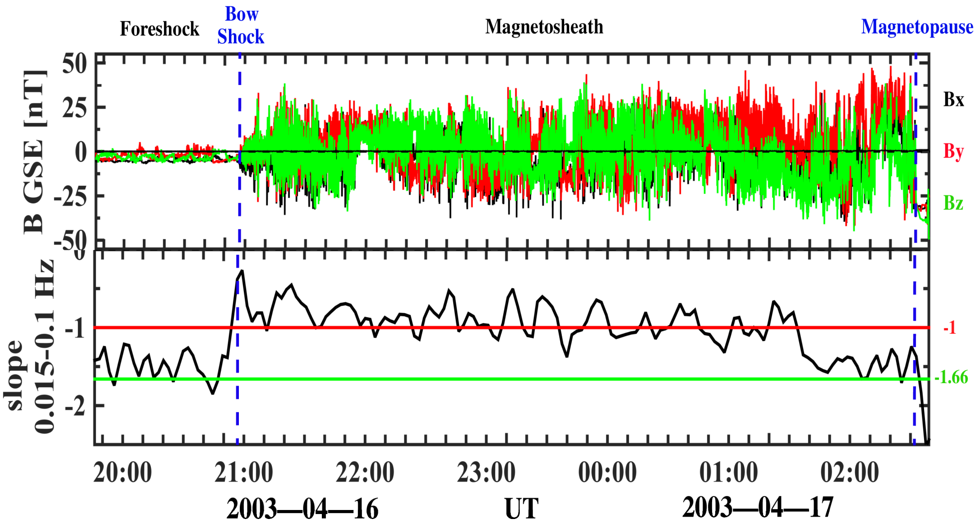

Figure 4.17: First panel: The components of the magnetic field **B** showing a full crossing of the magnetosheath (from 21h00 to 02h00). Second panel: the time-dependent (i.e., local) slope of the power spectrum of **B** between [0.015-0.1 Hz] as function of time indicating variation in the scaling of the turbulence as the spacecraft crosses different regions, from the solar wind/foreshock to the magnetopause.

Figure 4.17 shows a particular case study of a full terrestrial magnetosheath crossing, from the solar wind region (T $<$ 21h on day 2013-04-16) to the magnetopause (T $>$ 02h45 on day 2003-04-17). The local slope PSD of δB shows a clear transition from $\sim -5/3$ to ~ -1 at the shock crossing then stays nearly constant for more than 4h before steepening to $\sim -5/3$ when approaching the magnetopause whose crossing occurs about 01h45. This observation proves that the properties of turbulence as known in the solar wind do not survive after interacting with the bow shock.

To see if this observation is general, we analyzed the PSDs of the magnetic field fluctuations for 1600 events of the Earth bow-shock crossing between 2001-2003 (of $1.5hr$ each). Similar results to the Cassini ones were observed in the terrestrial magnetosheath: In the inertial range (MHD scales), the histogram in Figure 4.18-a shows that the slopes values are mostly near ~ -1 and only 3% of the events showed the Kolmogorov-like spectrum. Contrary to the magnetosheath of Saturn, no positive slopes are observed. From Figure 4.18-c, one can see that the Kolmogorov-like cases mainly appear in the flanks of the magnetosheath or closer to the magnetopause. I point out that the distribution around the magnetopause seems to be asymmetric, with more PSDs with an inertial range in the dusk part of Earth. At the kinetic scales, the spectral indices are mostly between $[-3.1, -2.5]$ with no particular dependence on the location within the magnetosheath.

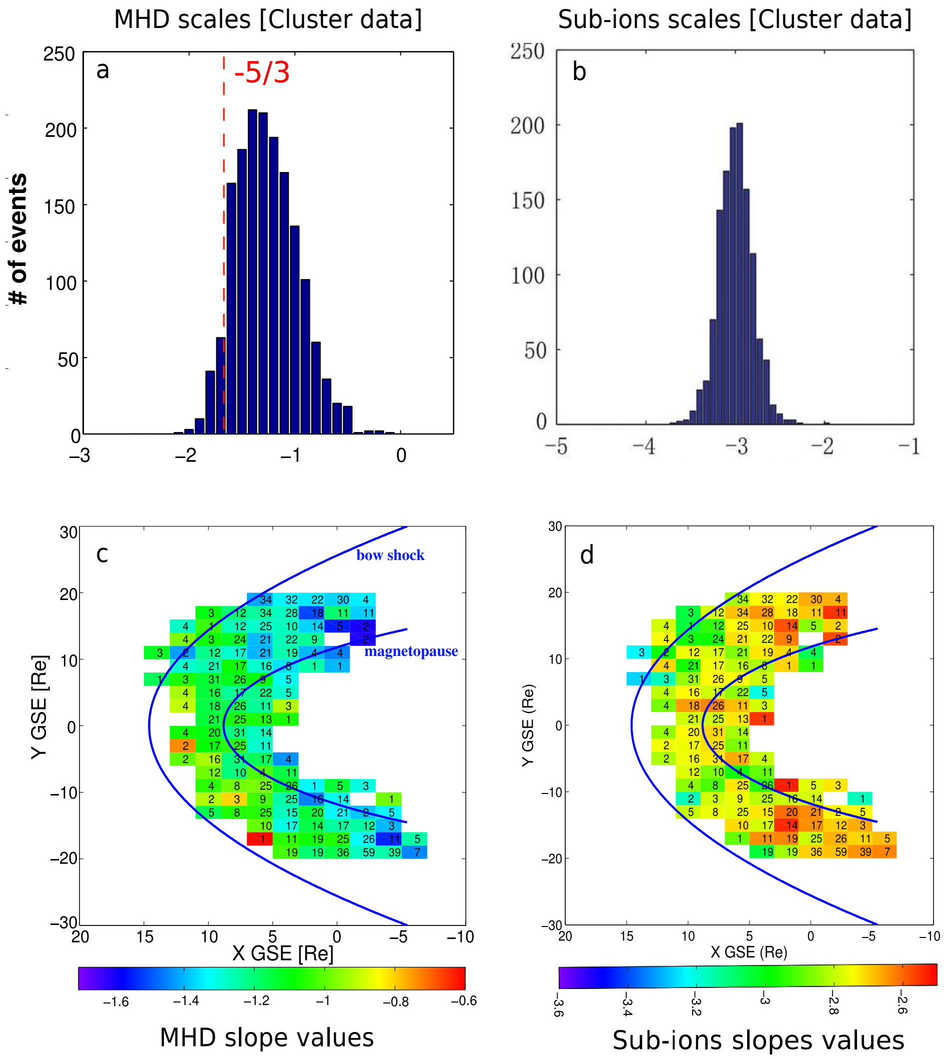

Figure 4.18: Top: Histograms of slope values (a) at MHD scales and (b) the sub-ion ones. Bottom: The corresponding 2D distribution P_α (X_{GSE}, Y_{GSE}) of the spectral slopes (c) at MHD and the (d) the sub-ion scales. The blue curves represent the average magnetopause and bow shock positions computed using the paraboloidal bow-shock model of Filbert & Kellogg [1979] and the magnetopause model of Sibeck *et al.* [1991]. The numbers represent the total number of the case studies.

4.3.2 Multifractality and higher order statistical study

To quantify the nature of the magnetic field fluctuations in the magnetosheath at MHD and sub-ion scales and to investigate the monofractal versus multifractal nature of the observed turbulence, I performed a higher order statistical study in Saturn's magnetosheath. First, I analyzed the PDFs of the magnetic field temporal increments, defined as $\delta B_\tau(t, \tau) = B(t + \tau) - B(t)$ where τ is the time lag. I recall that multifractality is generally characterized by the presence of bursty increments which yield heavy tails in their PDFs at small scales. In general, it is this deviation from Gaussianity that contains the pertinent information about the underlying physics. Figure 4.19 provides three examples of the corresponding PDFs obtained from the list of the analyzed events downstream a quasi-parallel ($\Theta_{\mathbf{Bn}} = 31°$) and quasi-perpendicular shocks ($\Theta_{\mathbf{Bn}} = 86°$ and $\Theta_{\mathbf{Bn}} = 60°$, respectively) for two values of τ, one from the MHD range ($\tau \sim 470$ s) and one from the sub-ion range ($\tau \sim 25$ s). Figures 4.19-(a-b) show that behind the quasi-perpendicular shock, the PDFs are found quasi-Gaussian for both values of τ (i.e., at MHD and kinetic scales) indicating the quasi-randomness of the fluctuations in the energy containing scales and in the sub-ion range. On the contrary, behind the quasi-parallel shock (Figure 4.19-c), the PDFs are non-Gaussian for $\tau \sim 12$ s (red PDF) showing the multifractal nature of turbulence at the kinetic scales as it was observed in the terrestrial magnetosheath [Sundkvist *et al.*, 2007; Yordanova *et al.*, 2008]. In the energy containing scales, which had an f^{-1} spectrum, the PDF is quasi-Gaussian as in the case of quasi-perpendicular shock.

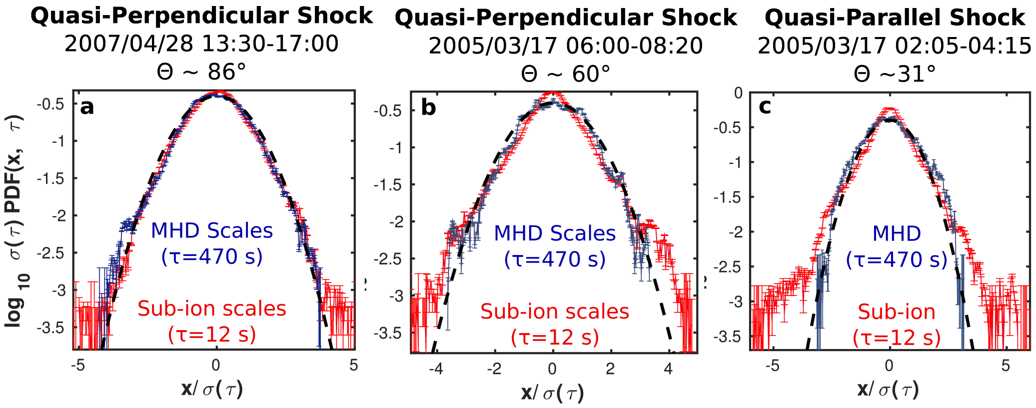

Figure 4.19: PDFs of the magnetic field increments in the energy containing and sub-ion scales (blue and red respectively) downstream of quasi-perpendicular (a-b) and quasi-parallel (c) shocks (with Poisonnian error bars). Normalized histograms with 300 bins each were used to compute the PDFs. The same values of τ were used in both cases, $\tau \sim 12$ s for the kinetic scales and $\tau \sim 470$ s for the MHD scales. All the PDFs have been rescaled to have a unit standard deviation. A Gaussian distribution (black dashed curve) is shown for comparison. Adapted from [Hadid *et al.*, 2015].

These results agree with recent findings using global hybrid simulations [Karimabadi *et al.*, 2014] who demonstrated that behind a quasi-parallel shock, where turbulence is enhanced, the fluctuations were multifractal whereas behind a quasi-perpendicular shock, turbulence showed almost no signatures of multifractality ($K \sim 3$, Figure 4.20).

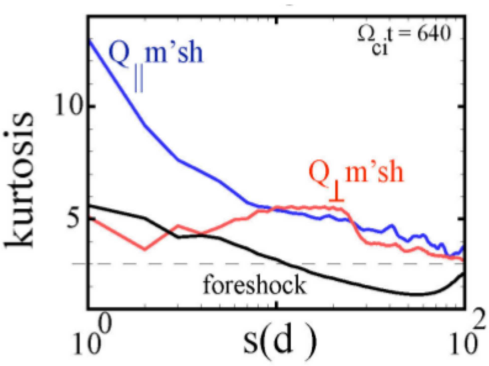

Figure 4.20: Kurtosis (fourth standardized moment) of magnetic field increments as a function of the separation length s. Adapted from [Karimabadi *et al.*, 2014].

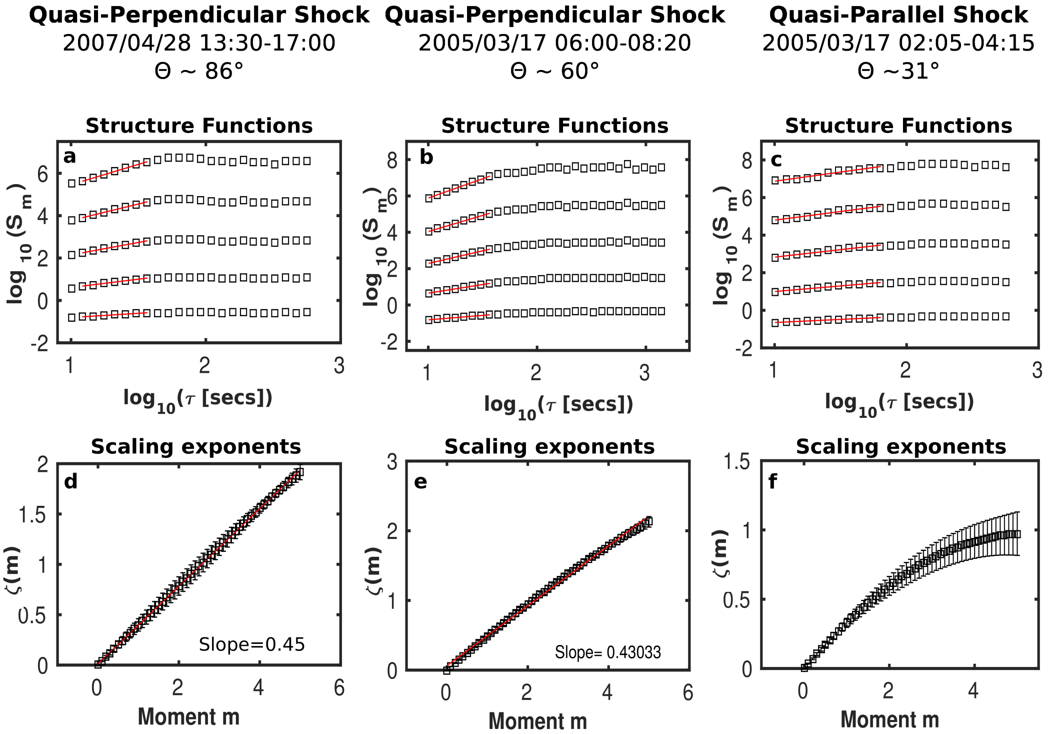

Figure 4.21: Different orders of the structure functions of the magnetic field increments $\delta B_{\tau}(t)$ as function of the time lag τ downstream of quasi-perpendicular (a-b) and quasi-parallel (c) shocks. (d), (e) and (f) represent the corresponding scaling exponent $\zeta(m)$. Adapted from [Hadid *et al.*, 2015].

Moreover, I calculated the higher order statistics given by the structure functions of the magnetic field increments defined in Equation. 2.5. The scaling exponent in Figure 4.21-a shows a clear linear dependence of ζ on the different orders m at the sub-ion scales ($\equiv$ small values of τ) behind a quasi-perpendicular shock supporting thus the monofractal character of the turbulent fluctuations. However, downstream a quasi-parallel shock (Figure 4.21-c), the scaling exponent is a convex function of m, confirming the multifractal nature of turbulence at the kinetic scales. It is noteworthy, that in the solar wind it has been shown that the sub-ion scales were monofractal while the MHD scales were multifractal [Kiyani *et al.*, 2009*a*]. The origin of the multifractal nature of turbulence in the quasi-parallel and the quasi-perpendicular bow shocks are not well understood and require further investigation.

4.3.3 Nature of the turbulent fluctuations: Plasma wave mode identification

For in-situ observations, in the absence of multi-satellite missions, the identification of the waves is based on a set of "transport ratios" that are expressed essentially as a fonction of the magnetic field, the density and the velocity of the plasma [Lacombe & Belmont, 1995]. In my work, I used such parameters to identify the nature of the plasma modes in the planetary magnetosheaths in order to see if it is dominated by the Alfvénic modes (similarly to the solar wind) or compressible magnetosonic ones (slow and fast modes). Among those parameters I used the magnetic compressibility C_B given by the ratio between the PSDs of the parallel global magnetic field component and the magnetic field magnitude (parallel is w.r.t. the background magnetic field B_0) [Gary & Smith, 2009; Salem *et al.*, 2012]:

$$C_B(f) = \frac{|\delta B_{\parallel}(f)|^2}{|\delta B_{\parallel}(f)|^2 + |\delta B_{\perp}(f)|^2} \tag{4.1}$$

Indeed, from the linear theory, the Alfvén and the magnetosonic modes are known to have very different profiles of magnetic compressibility [Sahraoui *et al.*, 2012]. This allows us to verify easily the dominance (or not) of the Alfvénic fluctuations in our data [Podesta & TenBarge, 2012; Kiyani *et al.*, 2013]. Therefore I estimated the magnetic compressibility from the spacecraft data and compared it to the theoretical prediction for the events that showed both f^{-1} spectrum, "f^{-1} events", and the Kolmogorov spectrum, "$f^{-5/3}$ events". To this end I used the linear solutions of the Vlasov-Maxwell set of equations which include in particular, wave-particle interaction that is important for the kinetic damping of the plasma waves or the generation of plasma instabilities. Although the kinetic linearized wave modes are more difficult to calculate [Stix, 1992], widely available tools such as WHAMP [Rönmark, 1982] considerably ease the burden.

4.3.3.1 f^{-1} events: Wave modes at MHD and sub-ion scales

Let us consider first, only the cases that did not show an inertial range at the MHD scales. I computed the theoretical magnetic compressibilities from the Maxwell-Vlasov equations using the WHAMP code for a particular case study in the magnetosheath of Saturn (2005/03/17 02:00-08:30; same as in Figures 4.12-(a) and 4.13), which is actually representative of the other ones. I used the measured plasma parameters (B, n, T_i and T_e) as input parameters into the WHAMP code. For the sake of simplicity, I keep using the terminology of the MHD, slow and fast modes at kinetic scales even if it may be inadequate (because of possible crossings between different dispersion branches). Since the slow mode is heavily damped in kinetic theory at finite β_i [Ito *et al.*, 2004; Howes, 2009], I used the limit $\beta_i = 0$ and $\beta_e = 1$ (therefore, $\beta = \beta_e + \beta_i = 1$) to suppress the ions Landau damping and thus to capture the slow mode solution down to the scale $k\rho_i \geq 1$. In order to compare to spacecraft observations, the knowledge of the three components of the $\mathbf{k}$ vector (or equivalently, the propagation angle $\Theta_{\mathbf{kB}}$ and the modulus k) from the data is required. However, unambiguous determination of those quantities requires having multi-spacecraft data that is not available in planetary magnetospheres other than Earth [Sahraoui *et al.*, 2006]. Therefore, I used the Taylor frozen-in-flow hypothesis, which assumes that the fluctuations have slow phase speeds w.r.t the flow speed, to infer the component of the $\mathbf{k}$ along the flow direction, i.e. $\omega_{sc} \sim \mathbf{k}.\mathbf{V} \sim kv$ (see Section 4.4.4 on the validity of the Taylor hypothesis in the magnetosheath). Under the assumption that turbulence is strongly anisotropic, i.e. $k_\perp >> k_\parallel$, which is supported by previous observations in the magnetosheath of Earth [Sahraoui *et al.*, 2006; Mangeney *et al.*, 2006] and in the solar wind [Sahraoui *et al.*, 2010] (but still unknown in the magnetosheath of Saturn), the estimated wavenumber component along the flow is equivalent to $k_\perp$ for data intervals when $\Theta_{\mathbf{VB}_0} \sim 90°$. In the present data I estimated $\Theta_{\mathbf{VB}_0} \sim 87°$, which I used to compute the theoretical solutions of Figure 4.22 from the Maxwell-Vlasov equations using the WHAMP code, assuming $\Theta_{\mathbf{VB}_0} \sim \Theta_{\mathbf{kB}_0}$. Another consequence of using the Taylor hypothesis when $\Theta_{\mathbf{VB}_0} \sim 90°$ is that the perpendicular component of the fluctuation $\delta B_\perp$ in Eq. 4.2 is reduced to the component perpendicular to both $\mathbf{V}$ (or $\mathbf{k}$, to fulfill $\mathbf{k}.\delta\mathbf{B} = 0$) and to $\mathbf{B}_0$ [Podesta & TenBarge, 2012], namely

$$\delta B_\perp(f) = \delta\mathbf{B}(f).\frac{\mathbf{k}\times\mathbf{B}_0}{|\mathbf{k}\times\mathbf{B}_0|} \sim \delta\mathbf{B}(f).\frac{\mathbf{V}\times\mathbf{B}_0}{|\mathbf{V}\times\mathbf{B}_0|} \tag{4.2}$$

Figure 4.22 shows a comparison between the observed magnetic compressibility compared to theoretical ones calculated using the observed plasma parameters implemented in WHAMP (solid lines). Moreover, since it is much easier to track the different plasma modes at the sub-ion scales using fluid models than using the Maxwell-Vlasov equations, I computed the magnetic compressibilities from the linear solutions of the compressible Hall-MHD [Sahraoui *et al.*, 2003] using Mathematica. First, one can see that the theoretical magnetic compressibilities of the fast and slow modes in the fluid and kinetic models have the same profile being almost constant at the MHD and sub-ion scales. The KAW mode shows an increasing magnetic compressibility as it approaches kinetic scales [Sahraoui *et al.*, 2012]. A similar profile has been reported in solar wind observations [Podesta & TenBarge, 2012; Kiyani *et al.*, 2013]. Second, the measured magnetic compressibility shows a relatively constant and high level ($C_B > 1/3$) at the energy containing scales and in the sub-ion range, which indicates the dominance of the parallel component $\delta B_\parallel$. This clearly rules out the Alfvénic fluctuations as a dominant component of the turbulence at least at MHD scales ($f < 0.05$ Hz).

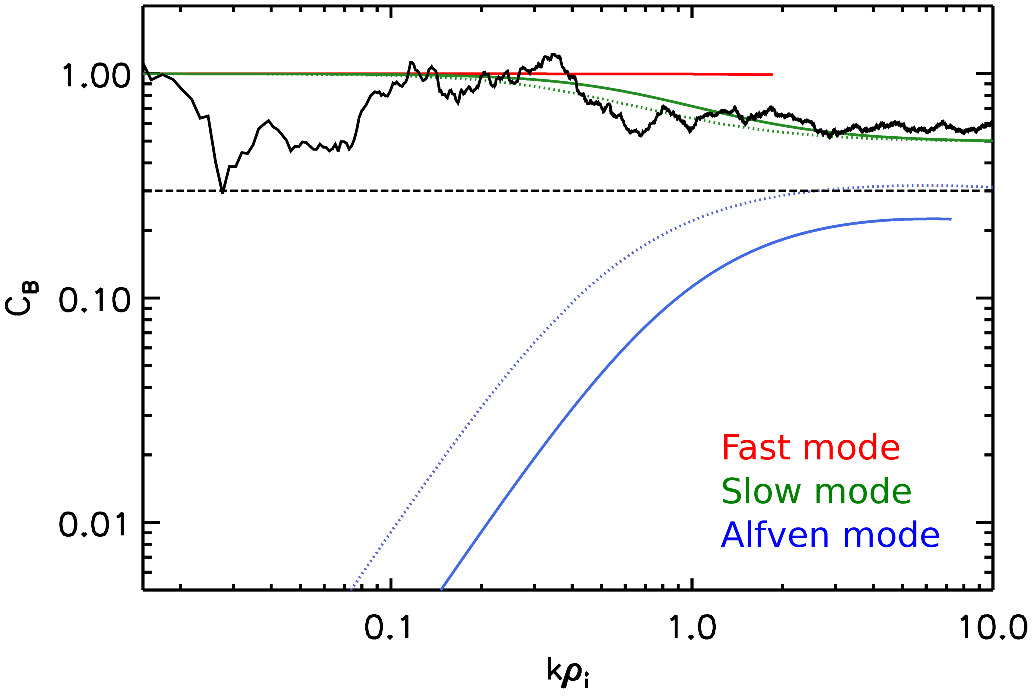

Figure 4.22: Comparison between the theoretical magnetic compressibilities, computed from the linear solutions of the compressible Hall-MHD (color dotted line) and of the Vlasov-Maxwell equations (colored solid line) for $\beta = 1$ and $\Theta_{\mathbf{kB}} = 87°$, with the observed one from the data of Fig. 4.12 (02:00-08:30) (solid black curve). The Taylor hypothesis was used to convert the frequencies in the spacecraft frame into wavenumber. The red, green and blue curves correspond respectively to the theoretical fast, slow and KAW modes. The horizontal dashed black line at $C_B = 1/3$ indicates the power isotropy level. Adapted from [Hadid *et al.*, 2015].

To see how the profile of the magnetic compressibilities changes as a function of β and $\Theta_{\mathbf{kB}}$, I did a parametric study using the compressible Hall-MHD linear solutions. Figure 4.23 verifies that the magnetic compressibilities of the compressible Hall-MHD solutions keep the same profile (but change its magnitude) when varying β in the range $[0.2, 90]$ for a fixed $\Theta_{\mathbf{kB}} = 87°$, and when varying $\Theta_{\mathbf{kB}}$ from quasi-parallel to quasi-perpendicular angles for $\beta = 1$.

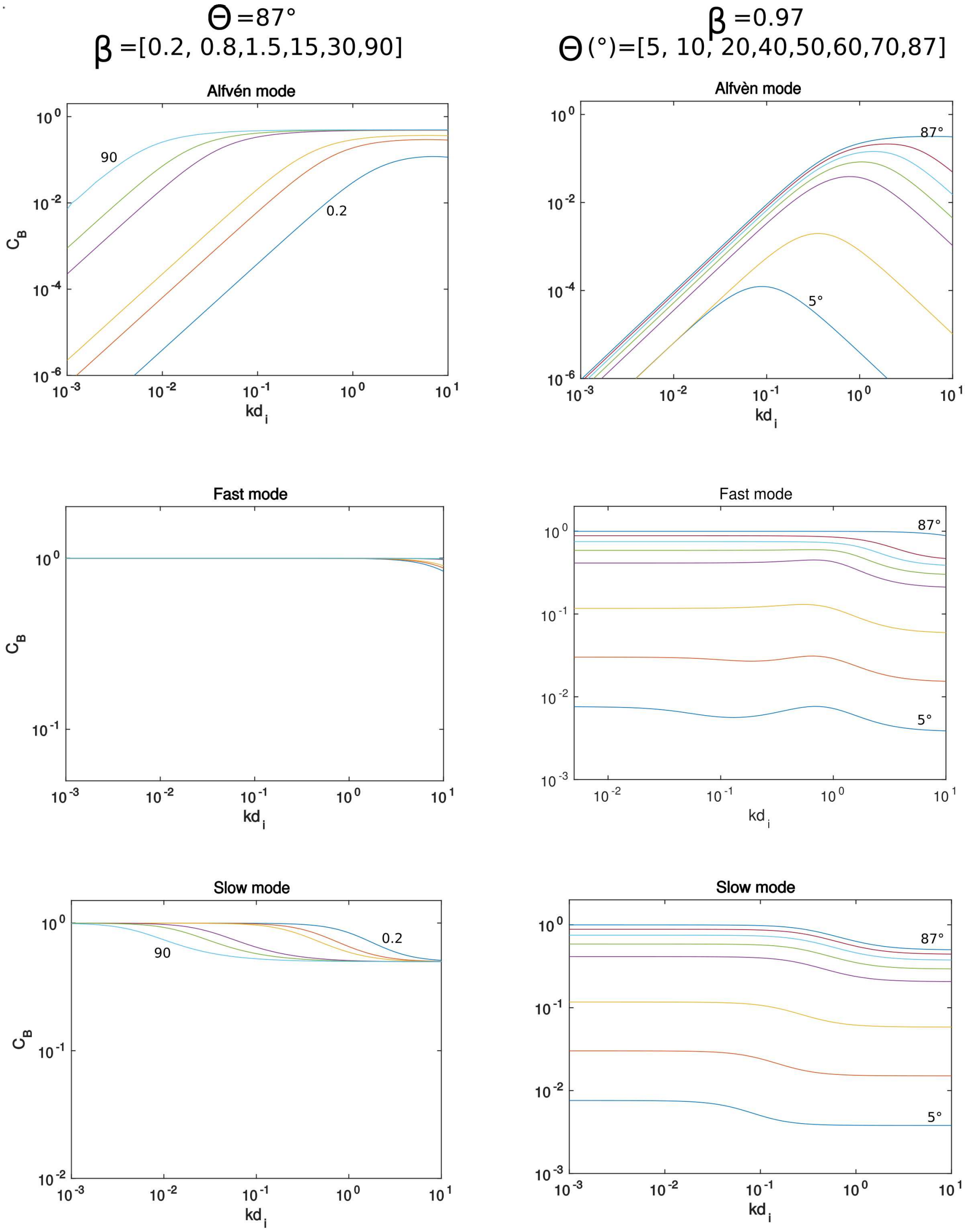

Figure 4.23: The theoretical magnetic compressibilities from the linear solutions of the compressible Hall-MHD, for the Alfvén, fast and the slow modes. The first column represent the solutions by fixing $\Theta_{\mathbf{VB}} = 87°$ and varying β from 0.2 to 90, whereas for the second column, β was fixed to ~ 1 and $\Theta_{\mathbf{VB}}$ varying between a quasi-parallel to a quasi-perpendicular propagation.

However, Figures 4.22 & 4.23 show that the magnetic compressibility cannot be used to reliably distinguish between the fast and slow modes, both having similar values/profiles of C_B. To do so, I used instead the cross-correlation between the magnetic field and the plasma density fluctuations $C(\delta B_{||}, \delta n)$. Indeed, the fast (resp. slow) mode is known to have a correlation (resp. anti-correlation) between its density and parallel magnetic component [Gary & Winske, 1992]. Figure 4.24 shows that locally and on average the electron density and the parallel component of the magnetic fluctuations are anti-correlated, i.e. $C(\delta B_{||}, \delta n_e) < 0$. This clearly rules out the fast mode fluctuation as the dominant component of the turbulence. This analysis establishes that the magnetosonic slow-like mode dominates the turbulent fluctuations analyzed here in agreement with previous results on the Earth's magnetosheath [Kaufmann *et al.*, 1970; Song *et al.*, 1994; Cattaneo *et al.*, 2000], in outer planets [Smith *et al.*, 1983; Violante *et al.*, 1995; Erdos & Balogh, 1996] and in the solar wind [Howes *et al.*, 2012; Klein *et al.*, 2012]. However, one cannot rule out the possible presence of the ion mirror mode as previously reported in the terrestrial magnetosheath [Sahraoui *et al.*, 2006]. The mirror mode, although is of purely kinetic nature [Southwood & Kivelson, 1993*b*], has indeed very similar properties than the slow mode which makes it challenging to distinguish between the two modes in spacecraft data. To check the possibility for the mirror mode to exist in our data requires measuring at least the ion temperature anisotropy, to see if the instability threshold is fullfilled $\beta_i > 1$ and $A_i = \frac{T_\perp}{T_{||}} - 1 > 1$. However, temperature anisotropy measurement from the CAPS instrument is not reliable due to pointing limitations (See section 4.4.1 for more setails).

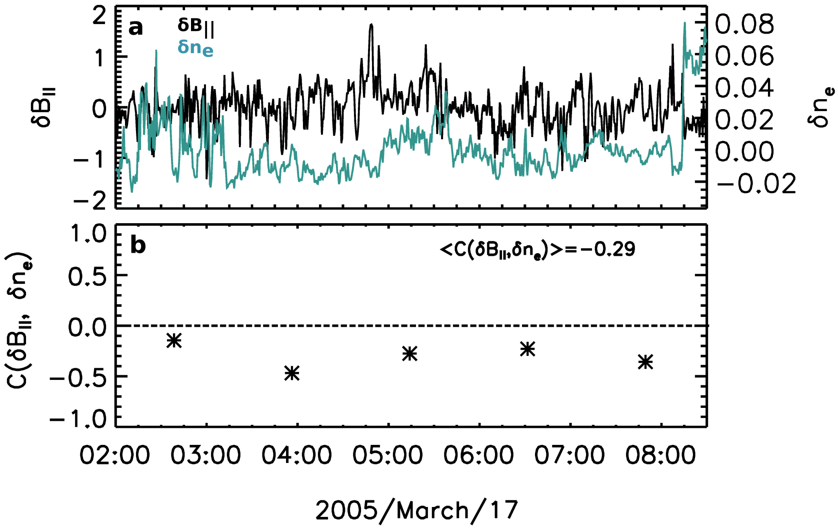

Figure 4.24: (a) The plasma density and the magnetic field magnitude in the Kronian magnetosheath; (b) The local and averaged cross correlation of the density and the parallel component of the magnetic fluctuations calculated using Pearson's method. Adapted from [Hadid *et al.*, 2015].

4.3.3.2 $f^{-5/3}$ events: Wave modes identification at MHD and sub-ion scales

In the previous section I analyzed a representative case study of turbulence having only $\sim f^{-1}$ spectrum at the MHD scales. Now, I will present the case studies which present a scaling $\sim f^{-5/3}$ to be able to compare them with the solar wind results. Since in the magnetosheath of Saturn we observed only 44 time intervals (compared to 137 in the Earth's magnetosheath) that are characterized by an inertial range, we used this latter larger statistical sample to identify the wave modes for the Kolmogorov-like events using Cluster data.

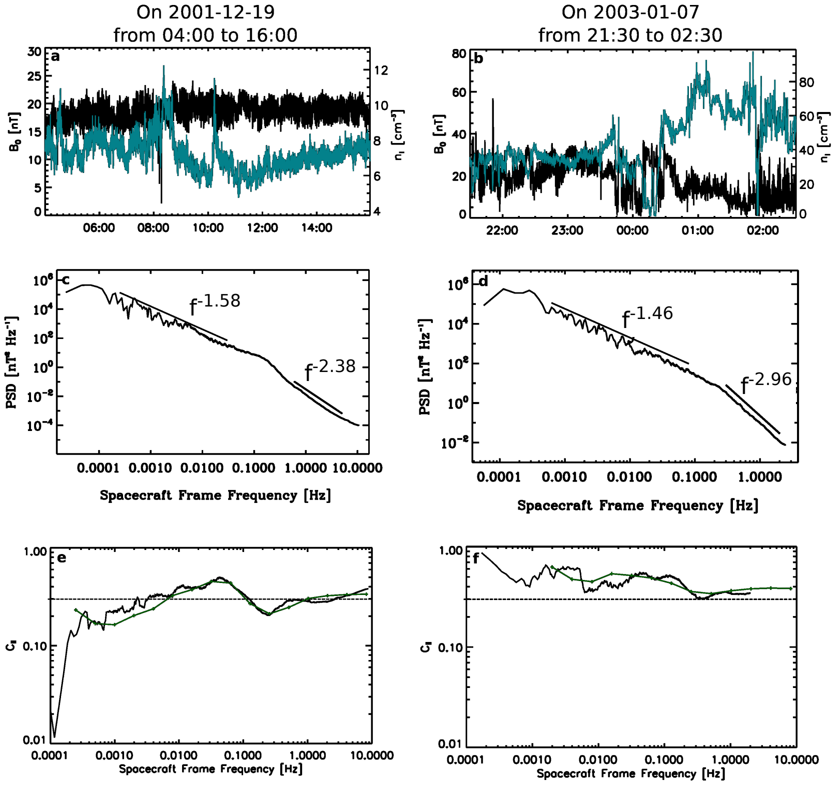

Figure 4.25: (a-b) Magnetic field magnitude and plasma density measured by the FGM and CIS and PEACE experitments onboard Cluster 3, (c-d) the corresponding FFT spectra of the magnetic fluctuations, (e-f) the global (black) and local (green) magnetic compressibilities C_B.

Following the same method we used before, we calculated the magnetic compressibilies of all the Kolmogorov-like events presented in Figure 4.18. Two examples are shown in Figure 4.25. First, in Figure 4.25-a, we observe a relatively uniform magnetic field magnitude, characteristic of incompressible Alfvénic fluctuations as frequently reported in the solar wind [Goldstein & Roberts, 1999]. This contrasts

with the case in Figure 4.25-b where strong variations in the amplitude of **B** can be seen, which are generally anticorrelated with the density fluctuations. This suggests the dominance of slow-like magnetosonic turbulence which is confirmed by the observed magnetic compressibilities shown in Figure 4.25-f, similarly to the Kronian magnetosheath. One can see that for the case of Figure 4.25-a the observed magnetic compressibility is closer to the linear Alfvén mode one, calculated from the linear solutions of Maxwell-Vlasov equations, whereas the one in Figure 4.25-b is better fit by the slow magnetosonic one. Because **B** varies much, I used both the local [Kiyani *et al.*, 2013] based on wavelet transform and the global field decomposition, using the Magnetic Field Aligned (MFA) frame, in which the Z axis is aligned along the background magnetic field $\mathbf{B}_0$, but both give the same result.
A summary of the estimated global magnetic compressibilities for all the Kolmogorov-like events and their mean values (red curves) are shown in Figure 4.26. Three distinct profiles are observed: (a) rising trend characteristic of shear Alfvén wave turbulence (35% of the events), (b) falling-off (28% of the events) and (c) steady (37% of the events), both characteristic of magnetosonic-like turbulence. The histogram (d) shows the averaged values of C_B in the frequency range $[0.004 - 0.01]$ Hz.

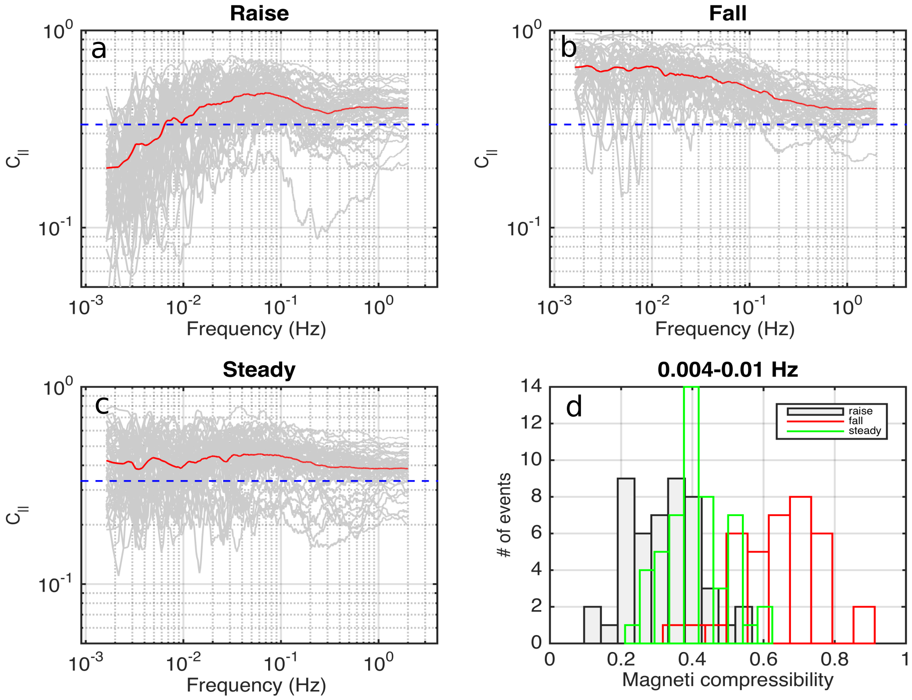

Figure 4.26: (a-b-c) Estimated magnetic compressibilities in the magnetosheath of Earth using Cluster 3 spacecraft data. The histogram of (d) shows the averaged values of C_B in the noted frequency range.

These results give the evidence of the existence of turbulence that has a Kolmogorov spectrum but in which the shear Alfvén modes are either absent or play a minor role at the MHD and the sub-ion scales. To our knowledge, at the MHD scales, all the Kolmogorov spectra reported in previous observations in the solar wind and the magnetosheaths have been attributed to incompressible Alfvénic turbulence [Bruno & Carbone, 2005] (Section 3.1.2). Theoretically, those observations can be interpreted using the phenomenology of the nonlinear coupling between counter-propagating Alfvén wavepackets [Cho & Lazarian, 2002] proposed by Iroshnikov [1964]; Kraichnan [1965] (section 2.3.2). This raises up three main questions: Do we need a new phenomenology that takes into account the compressibility ? How this compressible turbulence is cascaded into the sub-ion scales ? Does it survive up to the electron scales ?

4.3.3.3 Wave modes identification at the electron scales

It is generally thought that at the kinetic scales, the turbulent fluctuations, observed in the solar wind at quasi-perpendicular propagation, are a consequence of the transition from an Alfvénic to a Kinetic Alfvén waves (KAWs) cascade, even if other theoretical and observational studies argued in favor of the high frequency whistler waves originating from the magnetosonic fast mode.

However, when Alfvénic fluctuations are inexistant (or sub-dominant) at MHD scales, as in the cases shown above, what are the plasma modes that would populate the sub-ion range ?

Since the nonlinear equations from which the kinetic whistler and Alfvén modes derive have a similar form, these modes have characteristics in common. For instance, at $kd_i > 1$, the turbulence energy spectra produce the same spectral index (7/3), and the observed magnetic compressibility for both modes takes on an isotropic values of 1/3. Therefore C_B doesn't not allow one to discriminate between these two modes at scales $kd_i > 1$. Despite this, these two waves have one fundamental physical difference that lies in their density fluctuations at very small scales: Whistler waves are nearly incompressible characterized by $(\delta n/n_0)^2/(\delta B/B_0)^2 << 1$ whereas the KAWs are compressible with $(\delta n/n_0)^2/(\delta B/B_0)^2 \sim 1$ [Boldyrev & Perez, 2013]. Note however that this property of the whistler mode is valid at very small scales, far below the ion scales $kd_i >> 1$ (for $kd_i \sim 1$ the fast magnetosonic mode, which is the low frequency branch of the whistler mode in finite β is very compressible). In the limit $kd_i >> 1$, the normalized density and magnetic fluctuations for both modes are given by [Boldyrev & Perez, 2013]

$$\begin{aligned} \delta\tilde{n} &= \left(1+\frac{T_i}{T_e}\right)^{1/2}\frac{v_s}{v_A}\left[1+\left(\frac{v_s}{v_A}\right)^2\left(1+\frac{T_i}{T_e}\right)\right]^{1/2}\frac{\delta n}{n_0}, \\ \delta\mathbf{b}_\perp &= \frac{\delta\mathbf{B}_\perp}{B_0}, \end{aligned} \tag{4.3}$$

T_i and T_e are the ion and electron temperatures, $v_s = \sqrt{T_e/m_i}$ is the ion acoustic speed m_i is the ion mass, v_A is the Alfvén speed, n_0 is the mean density, and B_0 is the mean magnetic field strength.

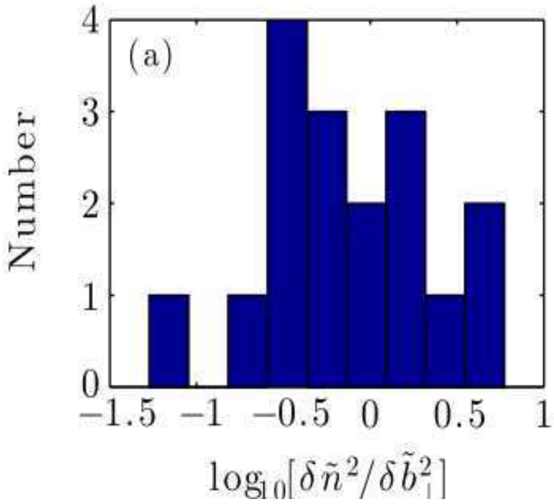

Figure 4.27: Histograms of the kinetic Alfvén ratio $(\delta\tilde{n})^2/(\delta b_\perp)^2$ in the solar wind defined in 4.3. Adapted from [Chen *et al.*, 2013].

Chen *et al.* [2013] showed that the fluctuations in the solar wind well below the sub-ion scales are dominated by the KAWs with the ratio: $(\delta\tilde{n})^2/(\delta b_\perp)^2 \sim 1$ (4.27). Following the same technique, I investigated the nature of the turbulent fluctuations close to the electron scales in the magnetosheath. Because the FGM of Cassini is not sensitive enough to measure δB down to the electron scales, and because of the ongoing recalibration process of the SCM instrument (Section 4.4.2) and the low time resolution of the ELS density (32 s), I could not use Cassini data in the Kronian magnetosheath. Therefore, I performed my study in the terrestrial magnetosheath using the Cluster data. The magnetic fluctuations at the kinetic scales were measured by the STAFF experiment when it was in burst mode, covering thus the frequency range [1-225] Hz (Section 4.2.2). Because of the low time resolution of the PEACE and CIS plasma instruments on Cluster (4 s) that does not allow one to probe into the sub-ion scales, I used the spacecraft potential data V_{sc} following the procedure described in Section 4.2.2 to compute the high time resolution of the plasma density. It can be estimated with a high cadence up to 1000 Hz, although the highest frequency part is subject to significant instrumental noise (see Figure 4.28). For a "magnetosonic-like" Kolmogorov case study of 2003/01/15 between 06:34:27-06:34:39, I computed the spectra of $\delta\tilde{n}$ (blue) and $\delta\mathbf{b}_\perp$ (black), normalized following Equations 4.3 [Schekochihin *et al.*, 2009; Boldyrev & Perez, 2013], which are shown in Figure 4.28.

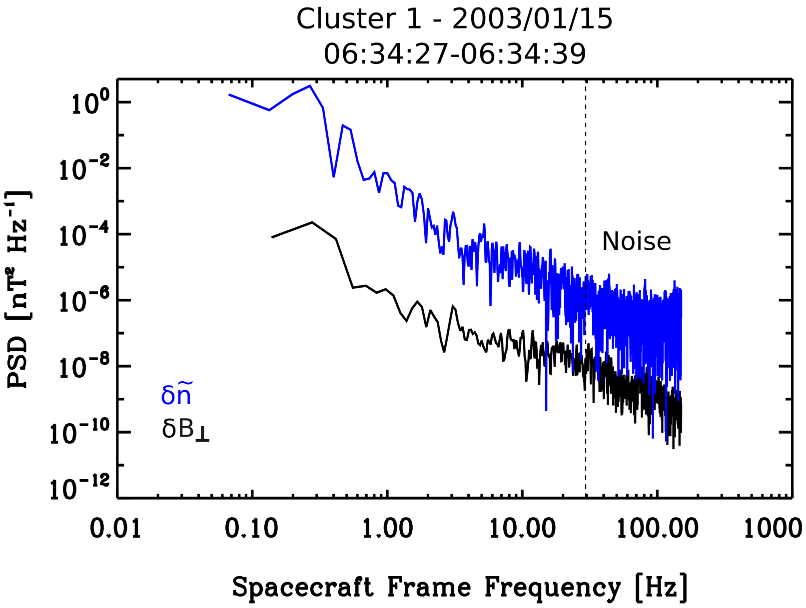

Figure 4.28: Spectrum of the density and magnetic fluctuations in the terrestrial magnetosheath, normalized according to Equations 4.3. The black dashed line represents the limit of when the spectra reach the noise level of SCM. Between ion and electron scales the spectra are of $\delta\tilde{n} \gg \delta\mathbf{b}_\perp$, ruling out the presence of incompressible whistler turbulence.

As one can see, between the ion scales $\sim$ 1 Hz and the electron scales $\sim$ 100 Hz $\delta\tilde{n} \gg \delta\mathbf{b}_\perp$ and $\delta\tilde{n}/\delta\mathbf{b}_\perp = 100$ (calculated in the frequency range [2.5-7.5] Hz which correspond to $k\rho_i = 4$ Hz and $k\rho_i = 12$ Hz). This value lies outside the histogram of the ratios obtained by Chen *et al.* [2013] (see figure 4.27) indicating the excess of the density fluctuations over the magnetic one in the magnetosheath compared to the solar wind. This observation rules out the whistler modes as the dominant mode at sub-ion scales ($kd_i \gg 1$). However, we cannot conclude that the turbulence is dominated by the KAWs, which should satisfay $\delta\tilde{n}/\delta\mathbf{b}_\perp \sim 1$. On the other hand, these results suggest that compressible fluctuations in the magnetosheath populating the inertial range and the sub-ion scales, are not damped and survive down to the electron scales. These density fluctuations might be caused by various coherent structures that form at sub-ion scales (e.g., current sheets, shocks) [Dahlburg & Einaudi, 2000; Trakhinin, 2009; Chasapis *et al.*, 2015; Perri *et al.*, 2012].

In the present study I could not do a survey on all the compressible Kolmogorov-like spectra because the high frequency magnetic field and density data are not available for all the events. In fact for telemetry reasons, the high cadence spacecraft potentiel data V_{sc} are available only with snapshot of $\sim$ 12 s per day, while the burst mode of STAFF (when available) provides only 3 hrs data per orbit. Therefore, the results obtained here need to be confirmed over a larger statistical sample, which now can be done using the high time resolution of the particles and the fields data of the new mission MMS (Magnetospheric Multiscale Mission). This is planned to be done after I defend my thesis.

4.3.4 Discussion and conclusions

In this chapter we have seen that the turbulent fluctuations in the Kronian and the terrestrial magnetosheath present some similarities but also some differences with respect to the solar wind. From the spectral point of view, the turbulent spectra at MHD scales is found to be mainly characterized by an f^{-1} scaling without forming the inertial range, and for few case studies the PSDs presented a Kolmogorov-like one $f^{-5/3}$.

At the sub-ion scales, the scaling properties seem to be more universal and showed similar results to the solar wind with spectral slopes lying between [-2.5,-3] Hz with no dependence on the location within the magnetosheath. The properties at the MHD scales were observed to depend as well on the structure of the bow-shock. These results are summarized in the table below:

	Quasi-parallel shock	**Quasi-perpendicular shock**
MHD slopes	-0.5	-1
Nature	Uncorrelated (random-like)	Uncorrelated (random-like)
sub-ion slopes	-2.5	-2.6
Nature	Multifractal	Monofractal

Table 4.1: Approximated values of the slopes and the nature of the fluctuations at the MHD and kinetic scales, behind a quasi-parallel and quasi-perpendicular bow-shocks.

The absence of the Kolmogorov inertial range and the origin of the f^{-1} (question that remains open in the solar wind) could be explained as the following: the interaction of the solar wind with the bow shock may lead to the destruction of all the preexisting correlations between the turbulent fluctuations in the solar wind. This results in suppressing the Kolmogorov inertial range and generating locally random-like fluctuations that have a scaling of $\sim f^{-1}$ over a broad range of scales. Those scales would play the same role as the energy-containing scales in the solar wind turbulence. The newly generated fluctuations behind the shock do not have "enough time" to interact sufficiently with each other and reach a fully developed turbulence state, hence a direct transition is manifested from the energy-containing range that has $\sim f^{-1}$ scaling into the sub-ion range with a scaling of $\sim f^{-2.6}$. Turbulence may reach a fully developed state and the Kolmogorov $-5/3$ spectrum may be observed, but only far away from the shock, toward the flanks, in agreement with Cluster and Cassini observations. In this scenario, one would expect that the correlation length of the turbulent fluctuation L_c must be much larger than the characteristic ion scale in the magnetosheath L_i , i.e., $L_c/L_i \gg 1$. The separation of scales would allow the turbulence cascade to proceed from the scales $\sim L_c$ to scales $\sim L_i$, where kinetic effects become important. This was actually tested as well by estimating the correlation time of the turbulent fluctuations $\tau_c = L_c/V$ and compared it to the local ion time scale which is considered here to be $\sim 1/f_{ci}$. The results shown in Figure 4.29 indicate relatively a good correlation between the regions where the Kolmogorov scaling is observed and those where the correlation time of the turbulence is much larger than the local time scale of ions. It is worth noting that the ratio L_c/L_i is related to the effective magnetic Reynolds number, as it was shown in Weygand *et al.* [2007].

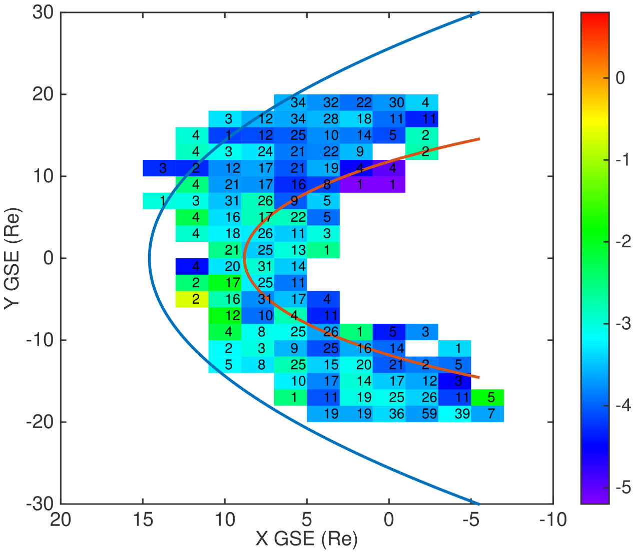

Figure 4.29: The distribution $P_R(X_{GSE}, Y_{GSE})$ of the estimated ratio $R = \log \frac{1/\tau_c}{f_{ci}}$ of the turbulent fluctuations for all the events displayed in Figure 4.18-a.

Other possible sources generating the Kolmogorov turbulence closer to the magnetopause, could be due to some local instabilities like the Kelvin-Helmotz that develop at the flank of the magnetopause [Kivelson & Zu-Yin, 1984; Wilson *et al.*, 2012; Rossi, 2015]. To have a better understanding regarding the origin of the f^{-1} spectrum, a higher order statistical study is performed (Section 4.3.2).

This study revealed as well the dominance of compressible fluctuations at the MHD scales (in the energy containing scales and the inertial range) and at the sub-ion scales. This indicates the need to go beyond the incompressible MHD theory to describe low frequency turbulence in the planetary magnetosheaths. This can be done (to some extent) within the compressible and isothermal MHD model derived recently by Banerjee & Galtier [2013]. The importance of the compressible effects observed throughout this work at MHD and kinetic scales, was the main motivation for me to apply that model first, to a "simple" system, the solar wind, before going to a more complex one, the magnetosheath.

4.4 Data limitations, some clarifications and caveats.

Analyzing in-situ spacecraft data is very exciting, however, it is not an easy task as one would think. I had to go through different stages before I obtained the resulting data sets to analyze. First, the *data collection*; I recall that the data were downloaded from different sources, AMDA, PDS and CSA. However, one has to be aware that sometimes the data update (for recalibration reasons for example) is not always simultaneous on the different databases, and this could lead to confusion and erroneous interpretations before realizing the error. Secondly, comes the *data cleaning*; after the data is collected, I had to filter out the bad case studies (dominated by gaps or instrumental noise), or the events that do not satisfy some basic criteria like stationarity (the first moment, e.g. the mean, does not change over time). Finally, comes the *data exploration* and the analysis, taking into account the caveats that could arise from the data.

In this section I will first discuss the CASSINI/CAPS measurements caveats with respect to its limited field of view (FoV), and how we could overcome this limitation, then I will explain some technical issues regarding the SCM and its different re-calibration stages in Chambon-la-Forêt facility that I did. Eventually, I will explain how the angle to the shock normal $\Theta_{\mathbf{Bn}}$ was determined and will present some clarifications mainly regarding the use of the Taylor hypothesis in magnetsheath turbulence studies.

4.4.1 Plasma moments from CASSINI/CAPS

The CAPS is fixed to the satellite body, and since Cassini is three-axis stabilized spacecraft, it prevents it from viewing the entire 4π steradians of the sky. In order to counteract this limitation, the CAPS sensors were mounted on a rotating platform driven by a motor actuator capable of sweeping the CAPS instrument by $\sim 180°$ around the spacecraft Z-axis as one can see in Figure 4.6. In this way nearly 2π angle of sky can be swept approximately every 3 min regardless of the spacecraft motion (being or not, in the FoV of the plasma flow).

Although adding a rotating platform provides a means of turning the instrument, some parts of the spacecraft and its surrounding structures occlude parts of the FoV as shown in Figure 4.30. At about $+80°$ optical remote sensing instruments obscure the CAPS FoV. In fact, encroachments are even larger than what is shown here because of multi-layer thermal insulation blankets that stand off from all spacecraft surfaces by $\sim$ 5 cm. As a result the useful rotation range of the actuator in the azimuth centered on the spacecraft -YZ plane is restricted to $-80° \leq \Psi \leq +104°$. This requires a systematic knowledge of the FoV of CAPS to check if it is seeing the plasma flow or not.

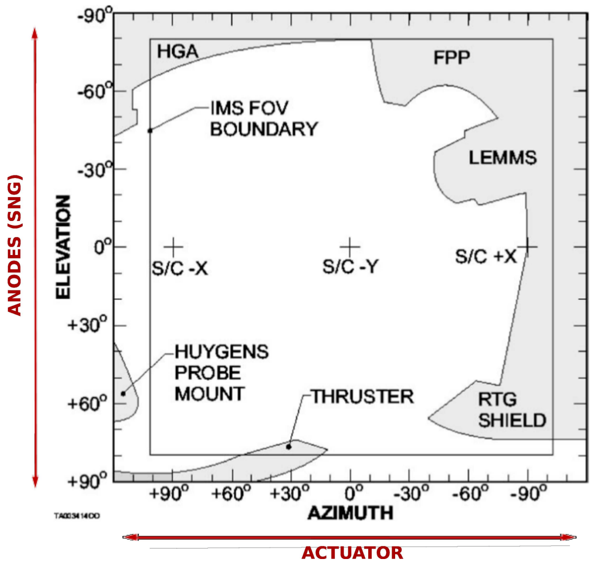

Figure 4.30: All-sky projection of the CAPS-IMS field of view (FoV). The shaded areas represent surrounding spacecraft instruments obscuring the CAPS FoV. Similar encroachments occur for IBS and ELS. Adapted from Young *et al.* [2004].

The CAPS/IBS instrument provides the ion number density of the plasma n_i, and the CAPS/ELS measures the electron density n_e. Other than the ELS, the electron density (n_e) can be also measured using the Langmuir probe or the sounder transmitter from the RPWS experiment. The Langmuir probe technique consists of applying a bias voltage to the probe, a sphere in the case of Cassini, and measuring the current to the probe as a function of the bias voltage. For a positive bias voltage it can be shown that the current is directly proportional to the electron number density [Mott-Smith & Langmuir, 1926]. To avoid any disturbance from the photoelectrons of the spacecraft body, the Debye shielding length should be smaller than the distance of the probe to the spacecraft. For the probe geometry used on Cassini and a plasma temperature of 1 eV, this restriction places a lower limit on the electron densities that can be determined accurately of about 25 cm^{-3}. Hence in Saturn's magnetosheath, where $n_e \ll 1\ cm^{-3}$, it is difficult to obtain accurate estimation of the electron number density using the Langmuir probe. Regarding the sounder transmitter, it provides a direct measurement of the electron number density, by stimulating resonances in the plasma, mainly the electron plasma frequency f_{ce} when used in conjunction with the high frequency receiver. But the sounder transmits short square pulses from $\sim$ 4 to 115 kHz and on average in the magnetosheath $f_{ce} \sim 3$ kHz which lies out of the sounder frequency range, so this technique is not suitable for calculacting the electron number density in my work. However, since the electrons have a thermal speed that is larger than the bulk flow speed downstream of the bow shock, they can be assumed to be isotropic at least on a time scale of around a minute, and so the moments given by the ELS sensor are more reliable than the ions sensors. In fact I did not really have the choice regarding the density data; assuming quasi-neutrality, I could use the electron density as a proxy for the plasma density (this imposes to be cautious when interpreting the data). Figure 4.31 shows a particular case study computed in the magnetosheath of Saturn, comparing n_e from the ELS sensor (blue), the langmuir probe (green), and with n_i from the IBS (red). One can clearly see the discrepancy in the values between at least the IBS and the ELS, (for the reason mentioned above, the Langmuir probe measurements can be exluded).

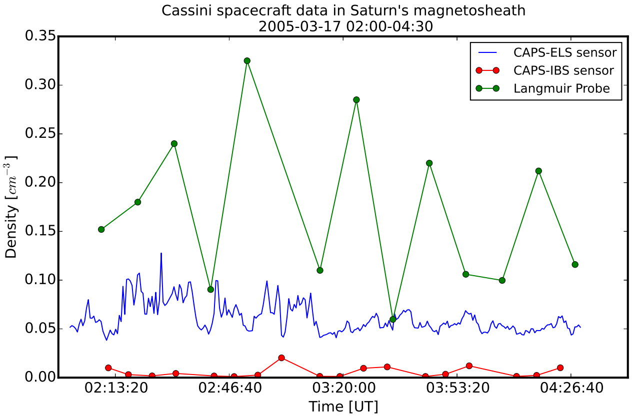

Figure 4.31: Electron density measured by CAPS/ELS and estimated using the Langmuir probe measurments. Ion density measured by the IBS sensor.

Nevertheless, this problem remains for the ion velocity measurements, especially that we do not know if the data were measured in the field of view of the plasma flow. In addition to that, for some case studies, there were no data, since the numerical moments algorithm of the CAPS instrument does not work if the spacecraft is rolling or if the instrument is not actuating.

I note that the moments of the ion distribution (density, flow velocity, temperature) provided by the Planetary Data Science (PDS), are flagged as `0:"Not-bad data"` for a corotation direction in the FoV, `1:"Not too bad data"` for a corotation direction which is not in the FoV, and `2:"Bad data"` for when the spacecraft is rolling and/or CAPS not actuating. In fact, in the magnetosheath (or the solar wind), the flags `0` or `1` are not really significant. We can have a good FoV in the corotation direction (`flag=0`), but not in the direction of the plasma flow if the direction of the latter is different than the corotation one. To overcome these difficulties, I had to re-compute the flow velocity of the plasma in the instantaneous FoV of CAPS, in the flow direction, using the actuator position and the spacecraft orientation data, by selecting only the data detected when the spacecraft is not rolling (`flag=0` and `flag=1`). I used a code originally developped by R. Modolo at LATMOS.

In order to recompute the ion plasma velocity, the first step is to determine the plasma flow direction. To do so, we reconstruct the instantaneous FoV (for each actuator scan) as a function of the total number of counts received by each anode at each accumulation time, taking into account the different satellite positions, the latitudinal (δ) and the longtitudinal (θ) angles. The analyses are carried out in the Saturn Solar Ecliptic coordinate system (SSE). This coordinate system is centered to Saturn barycenter with the X_{SSE} axis pointing from Saturn toward the Sun, the Y_{SSE} lying in Saturn's orbital plane pointing in the direction opposite to Saturn's orbital motion (towards dusk) and Z_{SSE} completing the right-handed system (Z=X×Y), as shown in Figure 4.32.

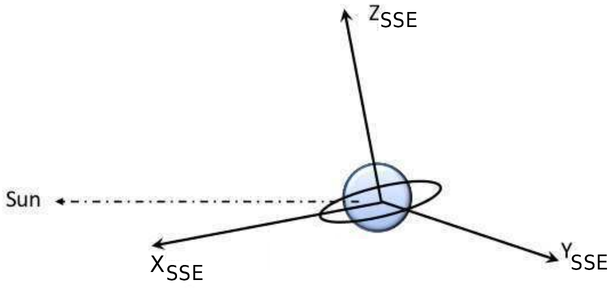

Figure 4.32: Saturn's Solar Ecliptic coordinate systems.

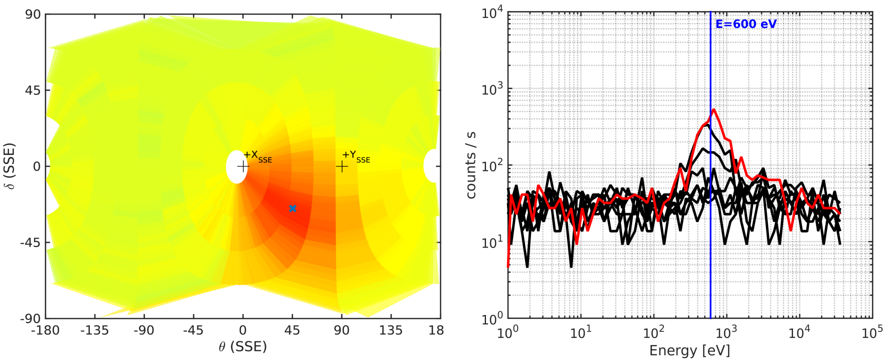

Figure 4.33: Left: SNG ion fluxes measured by CAPS plotted in the magnetosheath of Saturn, on 2005/03/17, from 02:00 to 04:30 as a function of the latitudinal (δ) and longitudinal (θ) location of the spacecraft. Right: The corresponding 1D energy spectra of the single ion fluxes observed by each of the eight anodes of CAPS. The red curve identifies the anode number 8 where the ion flux takes its highest value.

The angular distribution of the plasma in the planet's frame, is obtained in the $(\delta - \theta)$ plot presented in Figure 4.33. Hence, the flow direction is determined when the core of the distribution function is observed. Assuming that the different ion species hit the detectors at the same speed v, the ion bulk velocity is obtained by using the highest energy spectra of the single ion fluxes observed by one of the eight anodes of CAPS (see Figure 4.33). Hence, $v = \sqrt{2E_j q/m_j}$, where E_j is the energy of the peak corresponding to the population of mass m_j and charge q. Finally, the velocity components is determined instantaneously as function of the latitudinal and longitudinal angles as:

$$\mathbf{V}_{SSE} = -v\cos(\theta)\cos(\delta)\mathbf{X}_{SSE} + \sin(\theta)\cos(\delta)\mathbf{Y}_{SSE} + \sin(\delta)\mathbf{Z}_{SSE} \tag{4.4}$$

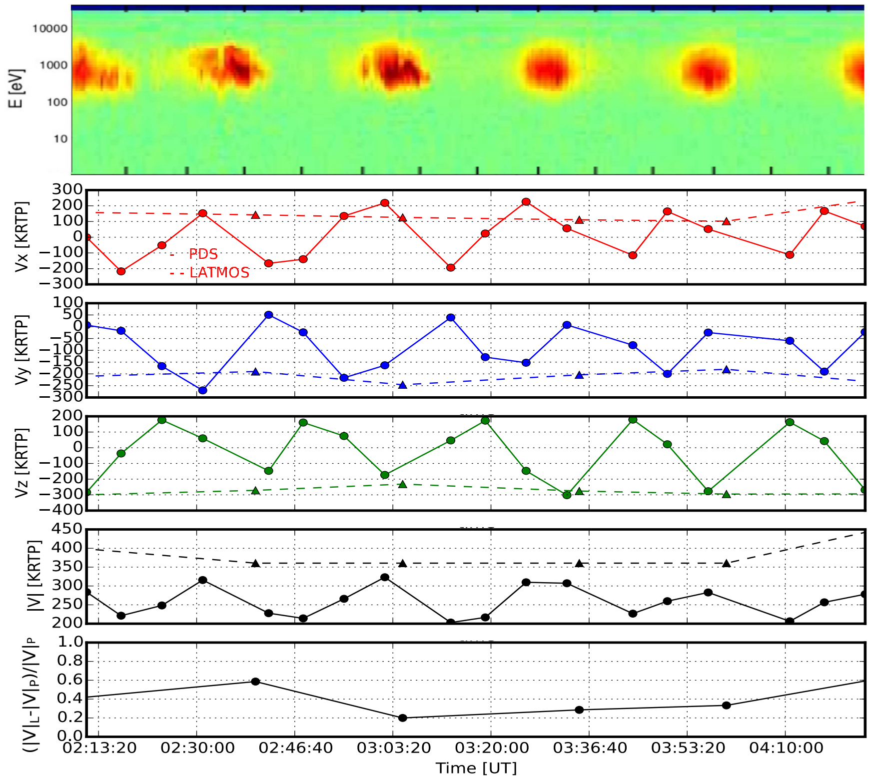

Figure 4.34: From Top to Bottom: The total number of counts averaged over the eight anodes (SNG) for the same case study presented earlier (2005/03/17), the corresponding velocity components (dashed line with triangles) compared with the velocity components provided by the PDS (solid line with circles). Last panel: relative differences between the modulus of the velocity provided by the PDS $|V|_P$ and the one computed from LATMOS code ($|V|_L$)

.

Figure 4.34, presents a comparison between the velocity components computed by the automated spacecraft algorithm provided by the PDS, and the ones I computed using the LATMOS code. One can see the differences for each component (red,

green and blue curves) between the two results. The last panel shows that the relative difference between $|V|_L$ and $|V|_P$ vary from 20% up to 60%. One inconvenience from the velocity estimation, is the degradation of the resolution, since each actuator scan results in one velocity value, noting that it is not a real problem if one is interested in the global average values. Another problem are the uncertainties on the velocity estimation ($\sim 50\,km/s$ for |V| in Figure 4.34), which are mainly related to the determination of the core of the distribution function as a function of the latitudinal (δ) and the longitudinal (θ) angles. In any case, at least using this method, one can be sure that the corresponding values of ion plasma velocities are computed in the FoV of the instrument. More details and discussions regarding this method can be found in Thomsen *et al.* [2010]; Romanelli *et al.* [2014].
It is worth noting that it takes almost 1 day to compute the velocity components on $5h$ of data, since one has to re-estimate separately for each number of counts, the ion flux and the corresponding energy spectra. In fact it is on my "to do list", to re-write the original Matlab code, on python in a more automated way.

4.4.2 High frequency δB measurements from CASSINI/SCM

In order to study kinetic turbulence at the sub-electrons scales (frequencies $\gtrsim 30$ Hz), the FGM is not sensitive enough, and the high frequency magnetic field fluctuations from the SCM measurements are needed to complete the spectra. However, these measurements included some limitations, related to the interference from the spacecraft and the calibration of the instrument. In fact the SCM are mounted on a short (1 meter long), fixed boom just under the high gain antenna (on the -x side of the spacecraft) unlike the MAG which is mounted far away from the spacecraft body on a 11 m boom. The measurements are mainly contaminated by the inertial wheels, installed in the core of the satellite body, for controlling the attitude and the rotation of the spacecraft.
The data measured by the waveform receiver were calibrated separately at LPP and Iowa University being the private investigator (PI) of RPWS. Although for both, the calibration method was based on the same calibration document, Iowa and LPP calibrations gave different results. Figure 4.35 represents the power spectral density between 1 Hz and 26 Hz computed using the calibrated data provided by Iowa (black curve) and LPP (blue curve). As one can see, the two PSDs are both much lower than the pre-launch sensitivity curve (in red) of the instrument and do not overlap. This was the first evidence that the calibration method was not correct. As a consequence, R. Piberne, the computer engineer of LPP had to go through the old calibration routines and corrected it by including a missing calibration filter. The new calibration method gave much better results that are summarized in Figure 4.36. As one can see, the red curve is now above the sensitivity curve of the SCM (green solid line) and is similar to the on board calibrated spectra provided by the LFR receiver for the same frequency range $[1-26]$ Hz. Note that, still there is no continuity between the low frequency magnetic field spectrum computed using FGM

data (black), and the high frequency SCM data (red).

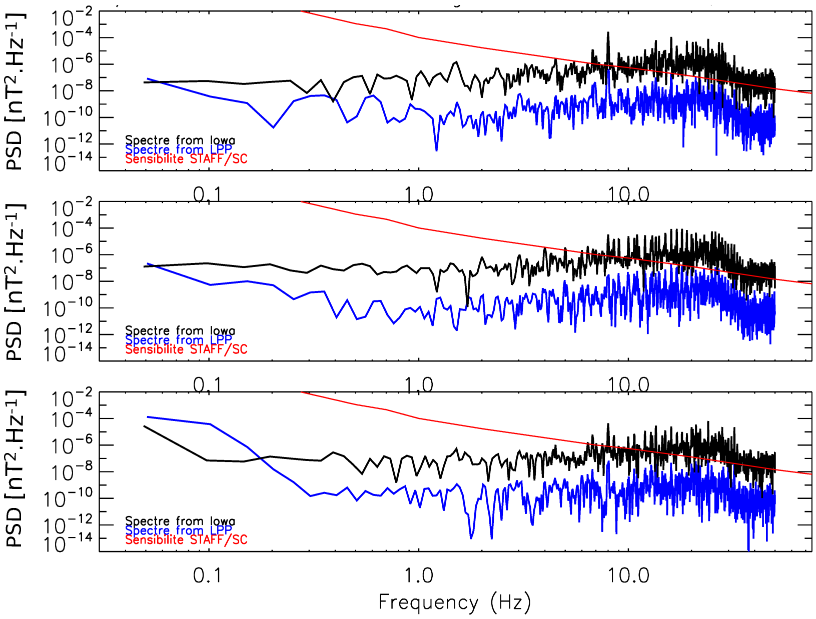

Figure 4.35: Cassini PSD of the magnetic field flufctuations of the WFR calibrated at LPP (blue curve) and Iowa University (black curve), for each of the components (Bx, first panel; By, second panel; Bz, third panel).

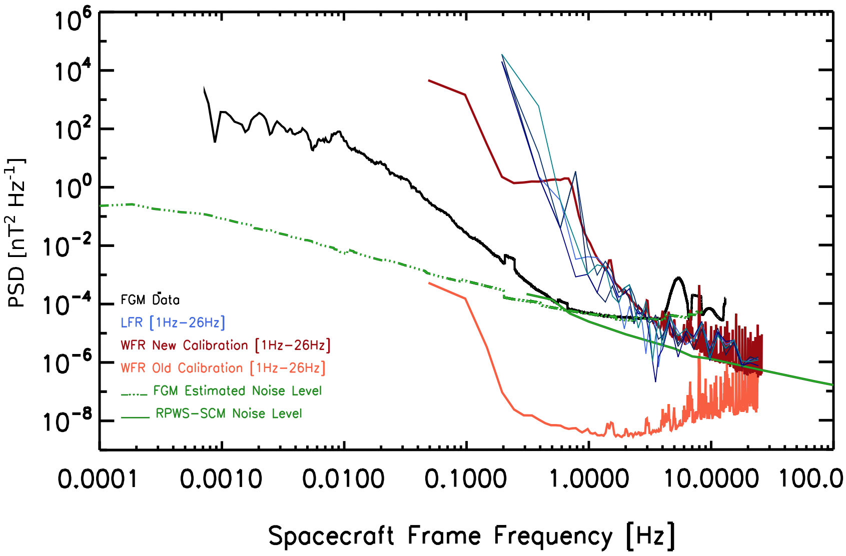

Figure 4.36: Top: Comparison between the "old" (orange) and the "new" (red) calibration method of the WFR data in the Kronian magnetosheath on 2004-06-28 from 08:02-14:06.

In addition to the data calibration issues, the information regarding the different calibrations done back in the 90's were not well archived, and the numerical information that existed were stored in "Floppies"!!
In order to understand the way the output signals of the SCM were calibrated 25 years ago, I had the great opportunity to stay three days in Chambon-la-forêt facility located at Orleans, with the engineers of LPP, D. Alison and O. Le Contel and my supervisor, F. Sahraoui to re-calibrate the Engineering Model (EM, stored at LPP) of the SCM. This calibration facility was built by previous members of the laboratory in the 1960's and then renovated in 2012. The facility consists of a set of three 1 m diameter Helmholtz loops orthogonally mounted to generate a magnetic field. At the centre is a table on which the sensors to be calibrated are put (see Figure 4.37). This facility is also equipped with big loops that were intended to compensate for the Earth's magnetic field but we did not use them for our calibration, since the SCM are only concerned with rapid (faster than 10 s) variations in the magnetic field.

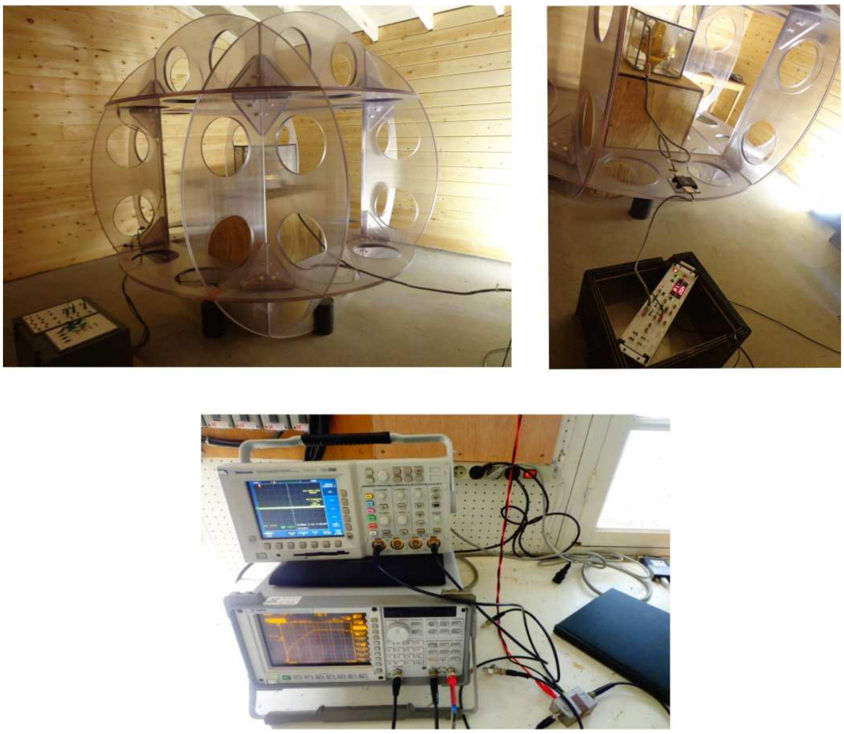

Figure 4.37: Top: Cassini engineering model (EM) sensor located within the new Helmholtz coils inside the new facility. One can see that YY' coils are connected in the connection panel (on the bottom right side of the first image) for which the 50 Hz noise is the smallest. In the second image, one can see the EM preamplifier connected to the sensor with the EM and connected to the rack GSE2 (+12/-12V power supply). The Y axis (red coaxial cable) is connected to the spectrum analyzer and the oscilloscope (Bottom Figure).

We measured the transfer functions of the EM antennas and the output noise level which is an important issue, especially that it concerns the validity of the scientific data.

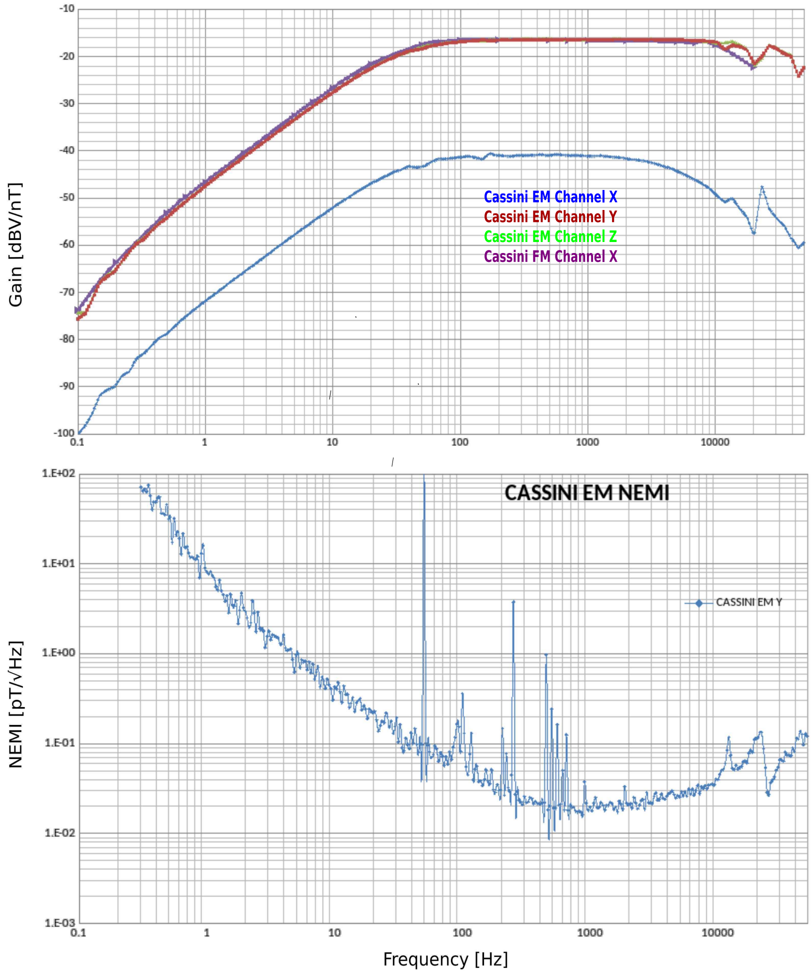

Figure 4.38: Top: Comparison between Cassini EM (gain) in dBV/nT at Chambon-la-Forêt facility and the previous FM measurements (back in the 90's in a different facility). Bottom: Cassini EM ground noise level (NEMI). The observed peaks correspond to the harmonics of the 50 Hz fundamental waveform.

Figure 4.38 shows the transfer functions measured for each channel (X, Y, and Z) of the magnetic antennas compared with the X channel of the Flight Model (FM). I note that the length of the cable that connects the antennas to the pre-amplifier, is very important for measuring the gain (or the transfer function) of an instrument (see Figure 4.37). Since we could not find any information about the length of this cable that was used during the first ground calibration years ago, we used a 1m long cable that was stored with the other equipements. As one can see, the EM and the

FM transfer functions are similar except for the X channel of the EM. This difference could come from a problem with the preamplifier. Moreover, by isolating the Cassini EM sensor and the preamplifier inside a mu-metalic box, and by covering as well the "power supply" with a mu-metallic top in order to reduce the 50 Hz tone we could measure the Noise Equivalent Magnetic Induction (NEMI), basically the sensitivity curve shown in Figure 4.38. A detailed report regarding the different calibration stages is shown in Appendix C.
Thanks to the re-calibration of the SCM at Chambon-la-forêt facility, we could fortunately obtain the good transfer function of the instrument, that will allow us to recalibrate the data. The next step of this work is to recalibrate the data and to compare the old calibration routines with the one used to calibrate THEMIS/SCM, developped at LPP (Section 5.1). In fact I have already selected some time intervals between 2004 and 2014 where the signal detected by the FGM around 1 Hz is relatively high (so I might obtain some case studies where the SCM completes the FGM spectrum), and for which the inertial wheels of the spacecraft were off, hence reducing as much as possible the interference that can pollute the SCM measurements. These cases will be tested after I defend my PhD (Chapter 7).

4.4.3 Determination of the angle $\Theta_{\mathbf{Bn}}$ between the upstream magnetic field and the shock normal

To study the quasi-parallel shock ($\Theta_{Bn} < 45°$) and the quasi-perpendicular shocks ($\Theta_{Bn} > 45°$) separately, it was important to measure the orientation of a shock, that is, to estimate its normal, in order to calculate $\Theta_{\mathbf{Bn}}$. For single spacecraft data, different techniques exist such as the coplanarity theorem applied to the magnetic field [Schwartz, 1998; Paschmann & Daly, 1998]. The magnetic coplanarity method takes advantage of two properties: that the magnetic field up and downstream of a shock ($\mathbf{B_u}, \mathbf{B_d}$ respectively) are coplanar with the shock normal and that the field jump across it is also in this plane. Therefore, the product of $\mathbf{B_u}$ and $\mathbf{B_d}$, crossed with the vector difference of the fields, should lie along the normal. The coplanarity unit vector is then given by the usual formula:

$$\mathbf{n}_{CP} = (\mathbf{B_u} \cdot \mathbf{B_d}) \times (\mathbf{B_u} - \mathbf{B_d}) \tag{4.5}$$

However, for several reasons, the coplanarity is not a very accurate method of determining shock normals. First, when $\Theta_{\mathbf{Bn}}$ is near 90°, and so $\mathbf{B_u}$ and $\mathbf{B_d}$ are closely aligned, there is considerable uncertainty in their cross product, and therefore in the final estimate of the normal [Russell *et al.*, 1983]. Secondly, it is assumed that the upstream magnetic field does not vary between the time of its measurement and the time when the downstream field is measured, often several tens of seconds later. However, this is not always the case since abrupt changes in upstream conditions should manifest themselves as sharp changes in downstream conditions. For few case studies in the magnetosheath of Saturn, I used this method to calculate $\Theta_{\mathbf{Bn}}$, however, large uncertainties arose from the non-stationarity of the magnetic field data and the wave activity upstream and downstream the shock, and the large variation of the bow-shock position (which are much faster than the spacecraft speed). Nevertheless, in the absence of a multi-spacecraft data, one could estimate $\mathbf{B_u}$ from measurements made near 1 AU using the 1.5D MHD solar wind propagation model of Zieger & Hansen [2008] at 9 AU. However, even though this model can predict the solar wind conditions near Saturn, it assumes that the solar corona is in steady state on the time scale of half a solar rotation, as a consequence its prediction efficiency highly depends on the phase of the solar cycle (highest prediction efficiency for the declining phase of the solar cycle). The model prediction depends as well on the relative positions of Saturn, the near-Earth solar wind monitor and the Sun. In fact, the best estimates of the solar wind boundary conditions at 1 AU are obtained close to the helioecliptic longitude of the spacecraft which is at the time of opposition. At last but not least, the solar wind model is still a 1-D, so it does not treat the $\mathbf{B}$ properly.

Another possibility for estimating $\Theta_{\mathbf{Bn}}$, is to use the locations of many bow shock crossings to determine an average bow shock location and so its shape. A functional form, usually a hyperbolic conic section (Equation 4.6), describing the geometry of the surface is chosen under the assumption that its position and shape are determined mainly by the dynamic pressure of the incoming solar wind. To reduce the number of free parameters the surface is often assumed to be axially symmetric about the solar wind flow direction. The general equation of a hyperbolic conic section is given by:

$$r = \frac{L}{1 + \varepsilon \cos \Theta} \tag{4.6}$$

where r is the distance from the focus of the conic section to a point on the shock surface, Θ is the corresponding polar coordinate angle with respect to the axis of symmetry, L is the size parameter (semilatus rectum), ε is the eccentricity ($\varepsilon > 0$ for a hyperbolic geometry).

The parameters that are a best fit to the observed spatial locations of the bow shock crossings are hence determined. Another technique for modeling planetary bow shocks consists in combining a semi-empirical and semi-theoretical approach by building a bow shock surface around the empirical magnetopause model.

In fact, the ideal way to determine accurately the shape and location of the bow shock for a given set of interplanetary conditions would involve a large number of probes simultaneously crossing the boundary to obtain a "snapshot" of the shock surface. Therefore the Earth bow-shock crossings compiled by the numerous single and multi-spacecraft missions (ISEE, AMPTE, ACE, Cluster,...) allowed it to be examined more accurately than the one of Saturn.

The shock angles I used for determining the structure of Saturn's bow-shock (in Section 4.3.1), were computed by A. Masters using a shock normal predicted by a semi-empirical model of the global shock surface [Went *et al.*, 2011]. This model describes the nominal orientation of the surface local to the crossing. The down side of this approach is that the normal to the shock may have been significantly perturbed from this nominal orientation at the time of the crossing. However, Achilleos *et al.* [2006] showed that in the case of Saturn's bow shock, coplanarity methods have larger uncertainties than using a bow-shock model. The error in the shock angles comes from the level of magnetic field variability in the chosen upstream interval especially for quasi-parallel shocks. Nevertheless, for each event, I was comparing the profile of the transition from the upstream region to the downstream one with the estimated $\Theta_{\mathbf{Bn}}$. Eventually, I considered only the cases that exhibit clear quasi-perpendicular (sharp transition) and quasi-parallel (fluctuating transition) profiles and discarded the other crossings.

4.4.4 Validity of the Taylor hypothesis in the solar wind and the magnetosheath

The *Taylor frozen-in-flow hypothesis* consists in assuming that the measurements taken on board the spacecraft correspond to one-dimensional spatial sample. In other words, one can suppose that the time scale over which the dynamics of the waves change is much shorter than the spacecraft passing through them. The general formula relating the frequency of the wave (or any other characteristic time scale if it is turbulence) in the plasma rest frame ω to the measured one onboard the spacecraft ω_{sc} is given by:

$$\omega_{sc} = \omega + kV \cos \Theta_{\mathbf{kV}} \tag{4.7}$$

where $\mathbf{V}$ is the plasma flow velocity forming an angle $\Theta_{\mathbf{kV}}$ with the $\mathbf{k}$ vector. If the phase speed of the wave is negligible w.r.t the flow speed (i.e., $V_\Phi = \omega/k \ll V$), then the Taylor frozen-in-flow assumption should be valid, meaning that Equation (4.7) reduces to $\omega_{sc} \sim kV \cos \Theta_{\mathbf{kV}}$, which is usually statisfied in the solar wind at MHD scales since $V_\Phi \equiv V_A \sim 50\,\mathrm{km/s} \sim V/10$.
In the magnetosheath, the Taylor hypothesis is thought to be violated since $V_\Phi \sim V_A \sim C_s \sim 100 - 200$ km/s where V_A and C_s represent respectively the Alfvén and the sound speeds considered to be the typical phase speed of the fluctuations. However, despite these typical conditions in the magnetosheath, the Taylor hypothesis can still be valid at least in the following two examples:

1) The case of strongly anisotropic turbulence ($k_\parallel \ll k_\perp$). From Equation (4.7) one can see that it is important to consider the information on the actual orientation of the wave vector $\mathbf{k}$, and not only the general phase speeds, V_A or C_s. For instance let us assume that ($k_\parallel \ll k_\perp$) ($\parallel$ and $\perp$ w.r.t the mean field $\mathbf{B_0}$) and that $\Theta_{\mathbf{kV}} \sim 0$ (this later condition can be relaxed by considering moderate oblique angles). For Alfvénic turbulence, Equation (4.7) yields $\omega_{sc} \sim k_\parallel V_A + kV \sim kV(1 + k_\parallel V_A/kV)$. This implies that even if $V \sim V_A$ one still obtains $\omega_{sc} \sim kV(1 + k_\parallel V_A/kV) \sim kV(1 + k_\parallel/k) \sim kV$. In other words, the Taylor hypothesis still works in strongly anisotropic turbulence even if the Alfvén Mach number is of the order of unity (or even larger). I recall that strong $\mathbf{k}$ vector anisotropies is predicted by most existing fluid, hybrid or kinetic models of turbulence, and is now widely accepted as a major feature of turbulence in magnetized plasmas (in the solar wind Sahraoui *et al.* [2010] have found that $k_{\parallel}/k_{\perp} \sim 1/20$ at $k\rho_i = 1$). Similar results have been obtained by Mangeney *et al.* [2006] who found that, from ion scale to electron scale, the electromagnetic fluctuations in the magnetosheath are very anisotropic and have a nearly zero frequency in the plasma frame, implying that the Taylor hypothesis is valid in that data even at electron scales. Similar conclusions have been obtained from solar wind observations [Sahraoui *et al.*, 2009, 2010; Alexandrova *et al.*, 2012].

2) The case of stationary fluctuations (i.e., zero frequency turbulence). Sahraoui *et al.* [2006] have shown in a case study, using the k-filtering technique on the Cluster data, that the magnetic fluctuations in the terrestrial magnetosheath had a nearly zero frequency in the plasma rest frame while they reached frequencies up to $\sim 20\,\omega_{ci}$ in the spacecraft frame. The fluctuations were shown to be dominated by mirror modes, which are believed to be ubiquitous in the magnetosheath.

The two examples above show that general consideration based on the Alfvén Mach number are not sufficient to validate (or invalidate) the Taylor hypothesis. Instead, it is required to know the actual phase speeds and orientations of the $\mathbf{k}$ vectors in any space plasma, the solar wind or the magnetosheath. However, to get that information it is necessary to have direct measurement of the 3D $\mathbf{k}$-vectors of the fluctuations, which requires using multi-spacecraft data and techniques such as the k-filtering method. These measurements are obviously inexistent in planetary magnetospheres. Therefore, any attempt to link observed frequencies onboard the spacecraft to wavenumber will necessarily involve assumptions, the Taylor hypothesis, or the dominance of a given plasma mode (e.g., Alfvén mode). And any of those assumptions imposes to be cautious in interpreting the data.

Chapter 5

Role of the compressibility in the solar wind.

Contents

Studying the turbulence properties in the magnetosheaths of Earth and Saturn (Chapter 4) revealed the importance of the compressible fluctuations. In this chapter, I will present the work I have done to study the role that the compressibility plays in turbulence using the exact law of compressible isothermal MHD turbulence theory [Banerjee & Galtier, 2013] as a continuation of Supratik Banerjee's PhD work. Because it is a first application of this model and since the solar wind has been studied more than the magnetosheath, I applied this model first to the solar wind so it will be easier to compare the results with the previously reported ones. Since THEMIS B/ARTEMIS P1 can reach an apogee of $\sim 60\,R_E$ (Earth Radii ~ 6400 km) in the dayside solar wind compared to $20\,R_E$ for Cluster, and since it spends much more time in the free solar wind, I used THEMIS B/ARTEMIS P1 spacecraft data and compared between the fast and the slow winds results, (the latter being more compressible than the former one). The data were downloaded from the THEMIS ftp (http://themis.ssl.berkeley.edu/data/themis/) and I performed the analysis using Python programming language which was very easy to learn and I recommend it for data analysis.

5.1 THEMIS/ARTEMIS spacecraft missions

5.1.1 Overview and objectives

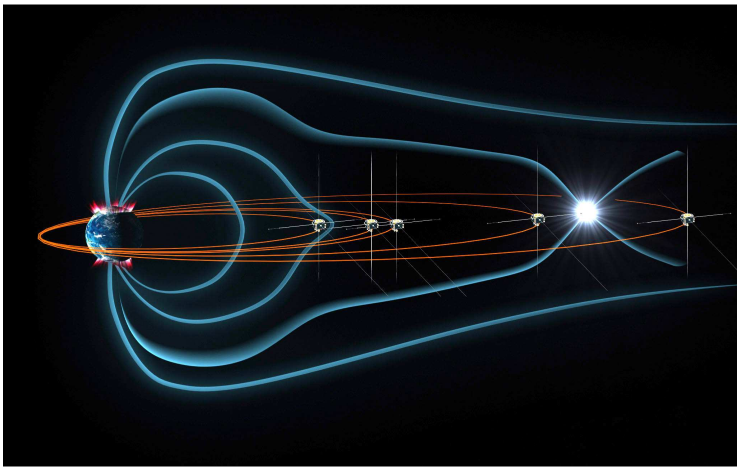

Figure 5.1: Artist concept of the five THEMIS space spacecraft traveling through the magnetic field lines around Earth. ©NASA

Contrary to Cassini, which is a single-based spacecraft, "The Time History of Events and Macroscale Interactions during Substorms" (THEMIS) mission was originally a constellation of five identical NASA satellites (THEMIS A, B, C, D, & E), named after the Goddess of justice, in Greek mythology. It was launched in 2007, and aims to determine, as its name indicates, what physical process in near-Earth space initiates the violent eruptions of the aurora that occur during substorms in the Earth's magnetosphere. In addition to that, the secondary objective of THEMIS is to understand and predict the variations in the flux of the energetic electrons in the Earth's outer radiation belts that constitute a risk to the safety of both astronauts and spacecraft. Moreover, the five probes were placed in elliptical orbits where the spacecraft line up at apogee every four days, with a separation distances ranging from 100's of km to few Earth radii. This configuration when in the dayside of Earth, especially with simultaneous multipoint measurements, is ideal for determining how the kinetic and MHD processes evolve from the solar wind, to the foreshock, the magnetosheath, and eventually in the outer magnetosphere and the magnetotail.
Since 2011, two of satellites were moved into orbit near the Moon. Those have

been renamed ARTEMIS for "Acceleration, Reconnection, Turbulence and Electrodynamics of the Moon's Interaction with the Sun". THEMIS B became ARTEMIS P1 and THEMIS C became ARTEMIS P2. The three remaining satellites (A,D, & E) remained in the magnetosphere and continue to work at their original levels of operation in conjunction with other nearby heliophysics missions such as Cluster, Van Allen Probes (VAP) and the recently launched Magnetospheric Multiscale (MMS).

Since the launch of the mission and up to date, THEMIS data helped highlight the nitty gritty details of how small changes in space plasma can lead to large variations in the near-Earth environment where many important technologies (science, weather, GPS and satellites communications) reside. Indeed, Le Contel *et al.* [2009] have reported emissions of quasi-parallel whistler waves in the near Earth tail and discussed their role in the substorm process. Shi *et al.* [2013] studied the magnetotail response to the interplanetary shocks and found that Ultra Low Frequency (ULF) waves, which are thought to be important for changes in the radiation belts, were excited inside the magnetosphere. A third interesting work was made by Korotova *et al.* [2009] who showed how the wave-particle interactions in the turbulent solar wind upstream from the bow shock act as a gate valve, affecting the bow shock orientation and strength. This leads to compressional pulsations in the dawn-side magnetosphere that could launch pressure perturbations which may in turn energize particles in the Van Allen radiation belts.

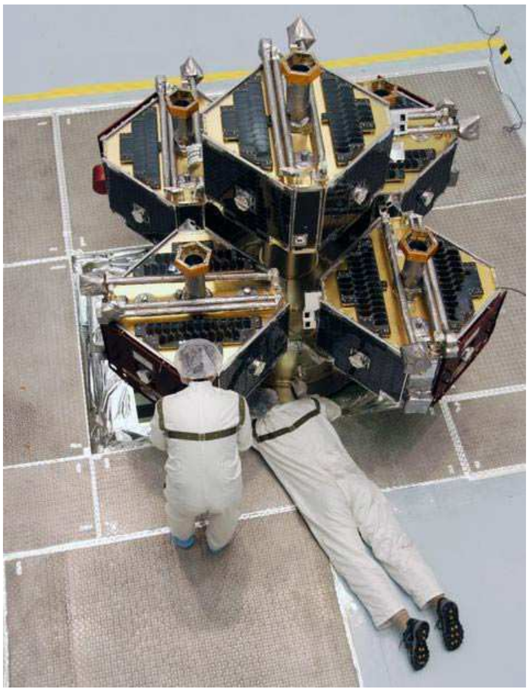

Figure 5.2: Top view of the five THEMIS spacecraft in their "wedding cake" configuration before spin-balance testing. ©NASA/George Shelton.

5.1.2 In-situ fields and particles instruments

In my work I used the magnetic field data from the Fluxgate Magnetometer (FGM) and the particles ones from the Electrostatic analyzer (ESA) from THEMIS B/ARTEMIS P1 spacecraft.

The Fluxgate Magnetometer (FGM) is designed to measure the background magnetic field and its fluctuations with a maximum sampling frequency of 64 Hz. The amplitude of variations in the field range from about 0.1 to 30 nT and is sufficiently sensitive to detect the magnetic field variation of the order of 0.01 nT. In the upper range, this instrument can measure approximately up to $\sim 10^4$ nT. The same type of instrument has been flown on many space missions in particular on Cassini-Huygens spacecraft, but due to the advances in technology, the THEMIS FGM (developed in Germany), resulted in a much lower mass of the instruments ($\sim$ 1.54 kg, including boom, cable and blankets compared to $\sim$ 10 kg to Cassini FGM!). A detailed description of the FGM experimental design and its data products, can be found in Auster *et al.* [2009].

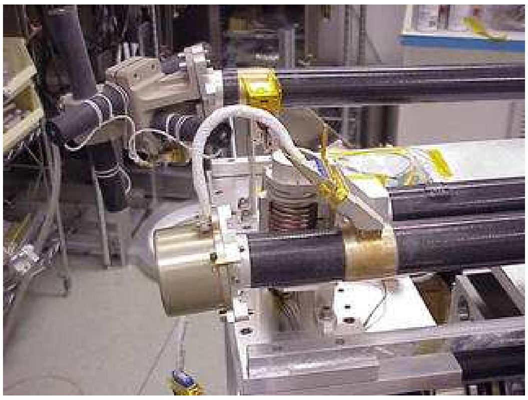

Figure 5.3: Flight unit of the FGM instrument (silver-colored cylinder at the foreground) and of the Search Coil Magnetometer (SCM) instrument (3 black colored, orthogonal rods at the background) mounted on their carbon-composite booms. The combination of these instruments measures the ambient magnetic field and its oscillations up to 4 kHz. ©NASA.

The Electrostatic Analyzer (ESA) measures the velocity distribution functions of the particles over the energy range from $\sim$ 3 eV to 30 keV. Two ESA sensors are present on each probe, one to measure ions and the other measure electrons. Contrary to Cassini, since all THEMIS probes are spin-stabilized, the spacecraft rotates, and the entire 360° field-of-view can be sampled each spin period of 3 s which is much higher than the time resolution of the Cassini CAPS/ELS sensor (ions: 8 min and electrons: 32 s). Moreover, advances in technology resulted in a much lower mass of ESA sensors (3 kg) compared to Cassini ($\sim$ 12.50 kg). The working principle of the onboard THEMIS ESAs is similar to CAPS/ELS. It consists

of a pair of two hemispherically shaped plates (see Figure 5.4) with common "fan-shaped" 180° by 5° field of view. The plates (and "hat") are maintained at different voltages. This causes the electrons and ions, the charged particles, to move in a circle inside the shell. Only the charged particles with just the right energy will follow the curve of the instrument's hemispheric shell and arrive at the particle detector at the exit (same principle of cyclotron). At this point, the detector registers the number of particles that hit it. By varying the voltages, we can find out how many particles are within each specified energy. Typically ions having energy ranging from 3-25 keV and electrons with energy up to 30 keV are detected by this analyzer. After being detected, the particles are binned into six distributions whose energy, angle, and time resolution depend upon instrument mode. We thus obtain three dimensional velocity distribution functions of ions and electrons every 3 seconds. The density, velocity, and the temperature of the ambient electrons and ions are hence calculated as the different order moments of the particle distribution function [McFadden *et al.*, 2009].
I note that the spin time resolution (3 s) of the FGM and ESA intruments was sufficient to probe into almost all the inertial range of MHD turbulence in the solar wind.

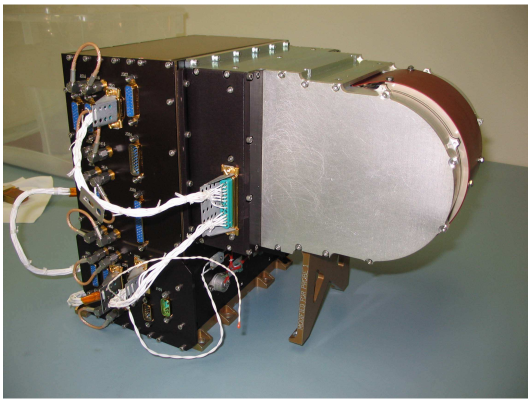

Figure 5.4: First flight model of the Electrostatic Analyzer (ESA) instrument (round structure) and the Instrument Data Processing Unit (IDPU). ©NASA.

In addition to the above two instruments that I used for this study, THEMIS has an Electric Field Instrument (EFI) for measuring electric fields in three dimensions, a Search Coil Magnetometer (SCM) also engineered at LPP for measuring the high frequency magnetic fluctuations ranging from 0.1 Hz to 4 kHz, a solid state telescope (SST) to measure the distribution function of superthermal (25 keV-6 MeV) particles, an instrument data processing unit (IDPU) to control the electronics of the above mentioned instruments. A representative diagram of the spacecraft with its onboard instruments is shown in the Figure 5.5.

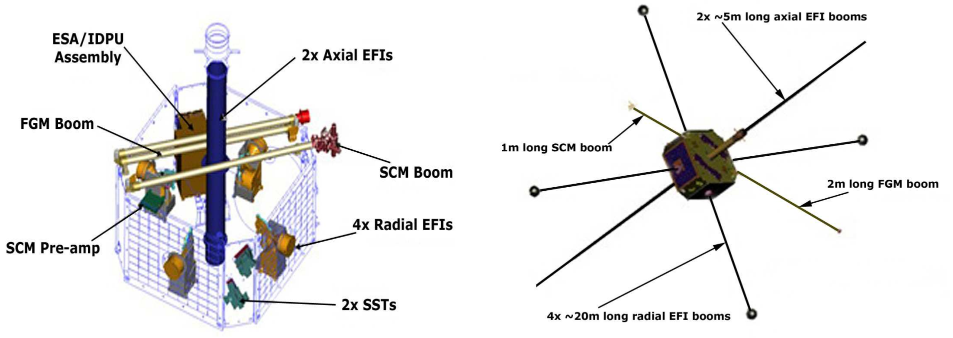

Figure 5.5: THEMIS spacecraft instruments. ©NASA.

5.2 Observations in the fast and the slow wind

In this section, I will present the statistical work regarding the estimation of the energy cascade rate of the fast and the slow solar wind turbulence using the exact law derived by Banerjee & Galtier [2013] (hereafter BG13) for compressible isothermal MHD turbulence, exploiting the in-situ data of THEMIS B/ARTEMIS P1. I compare those results to the exact incompressible MHD model of Politano & Pouquet [1998] (hereafter, PP98) and discuss as well the heuristic model of Carbone *et al.* [2009] (hereafter C09). This study highlights the role played by the compressible fluctuations in the turbulent cascade and the local heating of both wind speeds. For the sake of clarity, I recall first the different relationships of the existing models written for the energy dissipation rate.

Incompressible model: The PP98 law is written in terms of the Elsässer variables $\mathbf{z}^{\pm} = \mathbf{v} \pm \mathbf{v_A}$, where $\mathbf{v}$ is the flow velocity, $\mathbf{v_A} \equiv \mathbf{b}/\sqrt{\mu_0 \rho}$ is the normalized Alfvén velocity, with $\mathbf{b}$ the magnetic field and ρ is the plasma density (in this incompressible model, we take $\rho = \langle \rho \rangle$). It reads

$$-\frac{4}{3}\varepsilon_I \ell = \left\langle \frac{(\delta \mathbf{z}^+)^2}{2} \delta z_\ell^- + \frac{(\delta \mathbf{z}^-)^2}{2} \delta z_\ell^+ \right\rangle \langle \rho \rangle \equiv \mathcal{F}_{\mathcal{I}}(\ell)\,, \tag{5.1}$$

where the general definition of an increment of a variable ψ is used, i.e. $\delta\psi \equiv \psi(\mathbf{x} + \boldsymbol{\ell}) - \psi(\mathbf{x})$. The longitudinal components are denoted by the index ℓ with $\ell \equiv |\boldsymbol{\ell}|$, $\langle \cdot \rangle$ stands for the statistical average and ε_I is the energy dissipation rate. Note that in S.I. units, we have the relation $\langle \rho \rangle = 1.673 \times 10^{-21} \langle n_p \rangle$.

Heuristic compressible model: The heuristic C09 law is built from expression (5.1). The Elsässer variables are simply replaced by a cube-root density weighted compressible Elsässer variables $\mathbf{w}^{\pm} \equiv \rho^{1/3} \mathbf{z}^{\pm}$. Then, the law becomes

$$-\frac{4}{3}\varepsilon_W \ell = \left\langle \frac{(\delta \mathbf{w}^+)^2}{2} \delta w_\ell^- + \frac{(\delta \mathbf{w}^-)^2}{2} \delta w_\ell^+ \right\rangle \equiv \mathcal{F}_W(\ell)\,, \tag{5.2}$$

where ε_W is the dissipation rate of the total compressible energy. Note that the renormalization proposed is inspired directly by studies on supersonic interstellar turbulence [Kritsuk *et al.*, 2007*b*; Schmidt *et al.*, 2008].

Compressible model: When the source terms are neglected, the exact law BG13 for compressible isothermal MHD can be be written as:

$$-\frac{4}{3}\varepsilon_C \ell = \mathcal{F}_{C+\Phi}(\ell)\,, \tag{5.3}$$

where

$$\mathcal{F}_{C+\Phi}(\ell) = \mathcal{F}_1(\ell) + \mathcal{F}_2(\ell) + \mathcal{F}_3(\ell)\,, \tag{5.4}$$

and

$$\begin{aligned}
\mathcal{F}_1(\ell) &= \left\langle \frac{1}{2}\left[\delta(\rho\mathbf{z}^-)\cdot\delta\mathbf{z}^-\right]\delta z_\ell^+ + \frac{1}{2}\left[\delta(\rho\mathbf{z}^+)\cdot\delta\mathbf{z}^+\right]\delta z_\ell^- \right\rangle\,,\\
\mathcal{F}_2(\ell) &= \langle 2\delta\rho\delta e\delta v_\ell\rangle\,,\\
\mathcal{F}_3(\ell) &= \left\langle 2\overline{\delta}\left[\left(1+\frac{1}{\beta}\right)e + \frac{v_A^2}{2}\right]\delta(\rho_1 v_\ell)\right\rangle\,.
\end{aligned} \tag{5.5}$$

More details regarding BG13 can be found in Section 2.3.3.

5.2.1 Data selection

I used the THEMIS B/ARTEMIS P1 spacecraft data during time intervals when it was travelling in the free-streaming solar wind. The magnetic field data and plasma moments (density, velocity and temperature) were measured respectively by the FGM and the ESA instruments. All data have 3 seconds time resolution (i.e., spin period). A large survey of the THEMIS B/ARTEMIS P1 data has been performed between 2008 and 2011 that covered both the fast and slow solar wind. Fast winds are those having their average velocity $V_{sw} > 450\,\mathrm{km\,s^{-1}}$. In selecting the data, I have tried to avoid intervals that contained significant disturbances or large scale gradients (e.g., coronal mass ejection, interplanetary shocks, large scale shears) which can greatly influence and complicate the third order law [Gogoberidze *et al.*, 2013]. As mentioned above, a limiting criterion in choosing the data is the condition of having a stationary plasma β. In this work, I checked for each case separately the stationarity of the plasma β. Another parameter that has been checked is the uniformity of the angle $\Theta_{\mathbf{VB}}$, the angle between the local solar wind speed $\mathbf{V}$ and the magnetic field $\mathbf{B}$. Indeed, although the assumption of isotropy has been used to derive Equations (5.3)–(5.5), the use of the single spacecraft data to estimate the terms involved in those equation imposes that the turbulent fluctuations are sampled along the flow direction. Using the Taylor hypothesis, the time sampling of the data is converted into a 1D spatial sampling of the turbulent fluctuations along the flow direction. Therefore, the stationarity of the angle $\Theta_{\mathbf{VB}}$ is required to guarantee that the spacecraft is sampling nearly the same direction of space with respect to the local magnetic field, which would ensure a better convergence in estimating the

cascade rate. This point will be further developed in Section 5.3.4.
The obtained intervals that fulfilled all the previous criteria were divided into a series of samples of equal duration $\sim$ 35 mn, which corresponds to $\sim$ 700 data points with a 3s time resolution. This number of points is larger than those used in previous studies based on ACE spacecraft data ($\sim$ 150 with intervals of 1h and a time resolution of 24 s, e.g., MacBride *et al.* [2008]. This allows us to better estimate the moments of the turbulent field increments. The duration of 35 mn ensures having at least one correlation time of the turbulent fluctuations estimated to vary in the range $\sim 20-30$ mn. For all the selected time intervals I computed the energy cascade rates ε_I and ε_C respectively from the PP98 and the BG13 models using Equations (5.1) and (5.3)–(5.5).
To this end, I had constructed temporal structure functions of the different turbulent fields involved in those equations, namely $\mathbf{B}$, n and $\mathbf{v}$, at different time lags τ. In order to probe into the scales of the inertial range, known to lie within the frequency range $\sim[10^{-4}, 1]$ Hz (based on the observation of the Kolmogorov-like $-5/3$ magnetic energy spectrum, Bruno & Carbone [2005]; Marino *et al.* [2008]), I vary the time lag τ from 10 s to 1000 s thereby being well inside the targeted frequency range. Note that this range of scales is slightly shifted toward small scales in comparison to previous studies that used ACE data [MacBride *et al.*, 2008; Smith *et al.*, 2009*b*]. Applying a linear fit (y_C) on the resulting ε_C, I kept only the case studies for which the standard deviation $\sigma = (|\varepsilon_C| - y_C)/y_C < 40\%$. Then I filtered those cases with respect to the sign of ε_C, keeping the ones that have a constant sign for all the values of τ.
Eventually, the data selection yielded 142 samples ($\sim 1 \times 10^5$ data points) in the fast solar wind and 182 ($\sim 1.3 \times 10^5$ data points) in the slow wind. The average solar wind speed and plasma β for all the statistical samples are shown in Figure 5.6. An example of the analyzed time intervals for each wind is shown in Figure 5.7. I note that, for all this study the cascade rates (ε_I and ε_C) are given in $J.m^{-3}.s^{-1}$ and the energy flux terms in $J.m^{-2}.s^{-1}$.

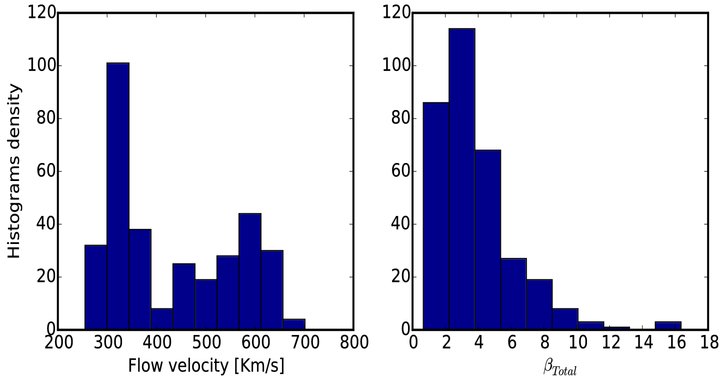

Figure 5.6: The average solar wind speed and the total plasma β for all the used data intervals using THEMIS B/ARTEMIS P1 spacecraft.

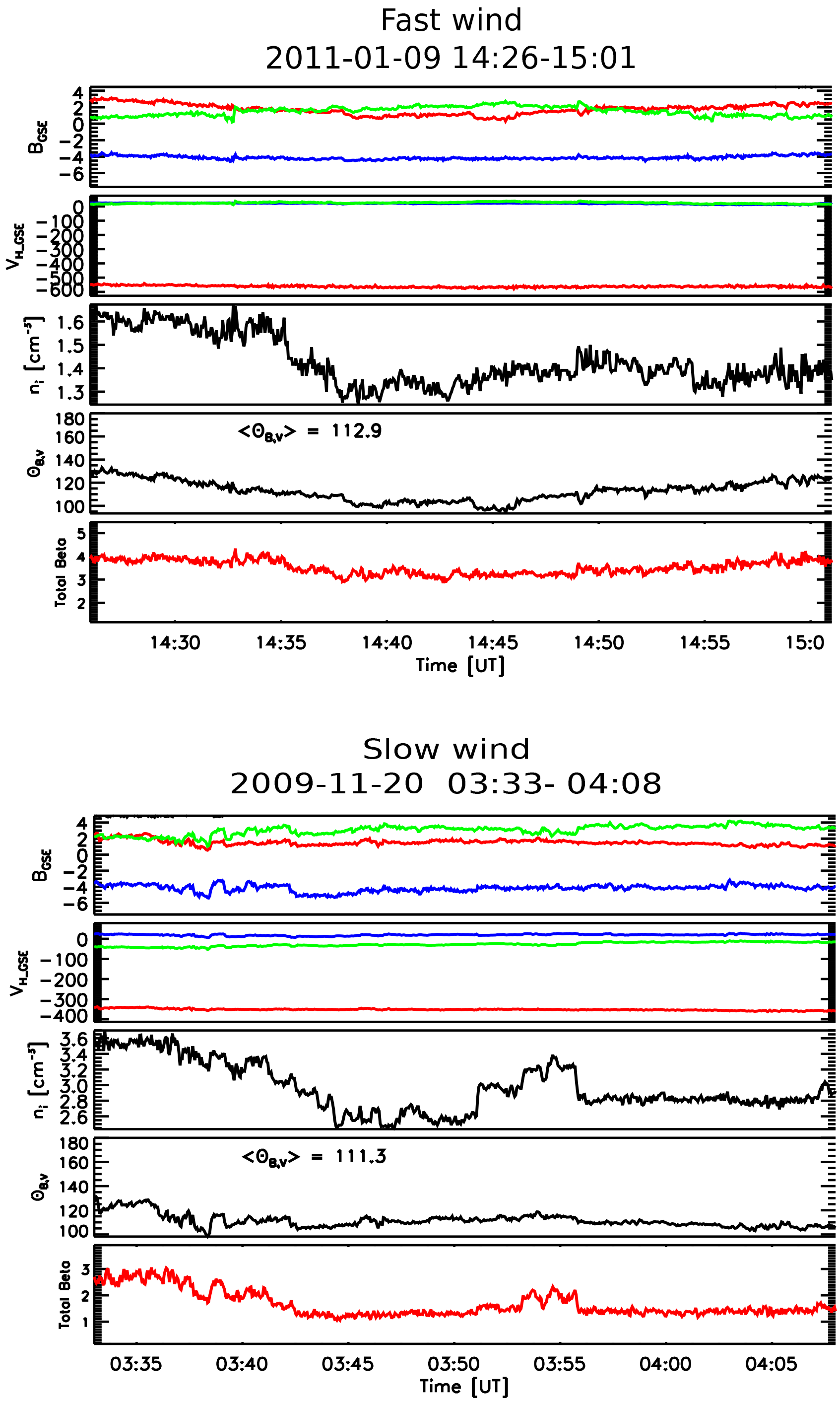

Figure 5.7: In each Figure from top to bottom: the solar wind magnetic field components, ion velocity, ion number density, $\Theta_{\mathbf{VB}}$ angle and total plasma beta ($\beta = \beta_i + \beta_e$) measured by the FGM and ESA experiments onboard the THEMIS B/ARTEMIS P1 spacecraft.

5.2.2 Scaling properties and the average cascade rates

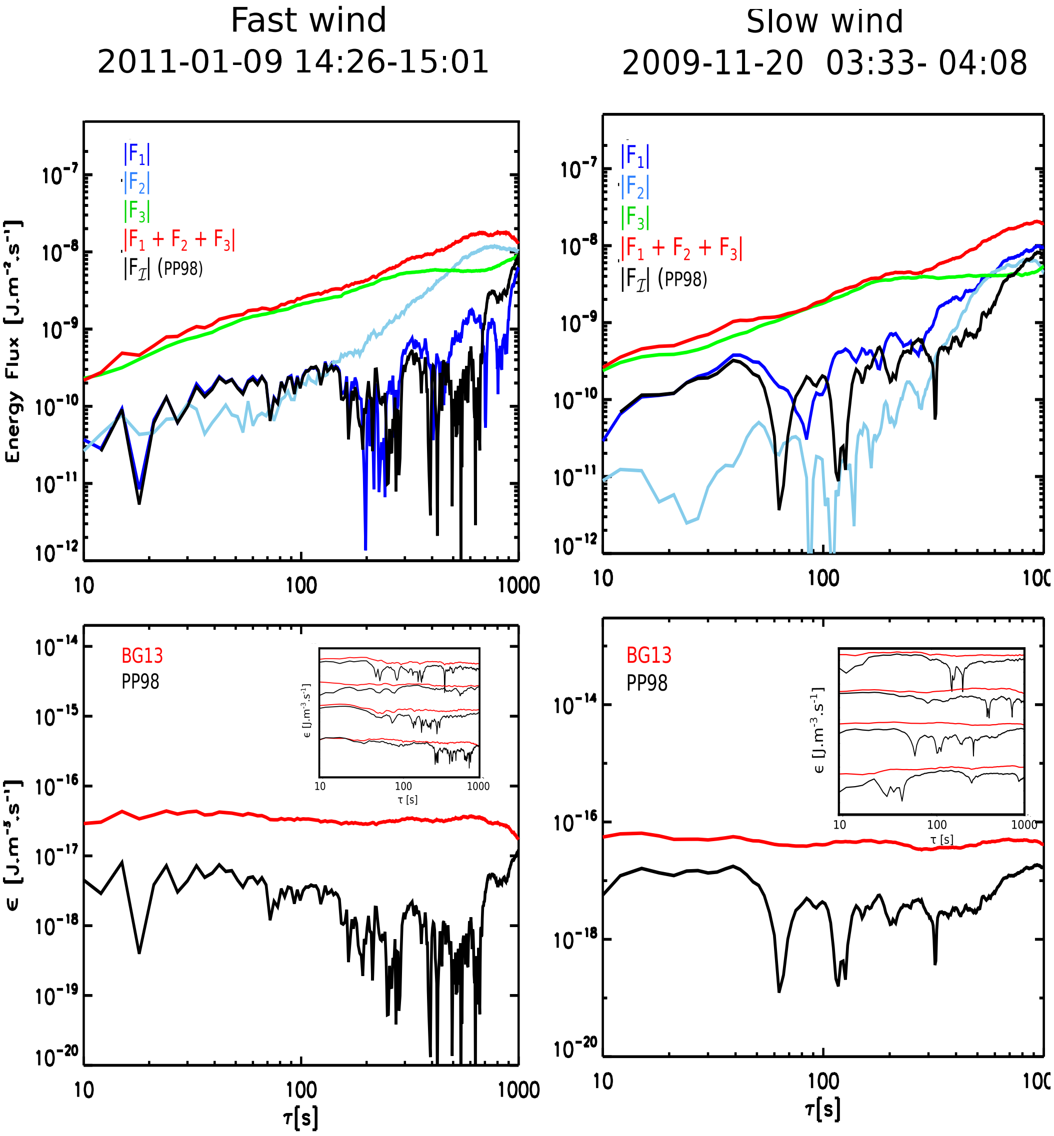

Figure 5.8: Top: comparison of the different terms $|\mathcal{F}_1|$, $|\mathcal{F}_2|$ and $|\mathcal{F}_3|$ of the flux $\mathcal{F}_{C+\Phi}$ in the fast and the slow wind. Bottom: comparison between the corresponding turbulent cascade rates (ε) given by the PP98 (black) and BG13 (red) models. The compressibilities in the fast and the slow wind, defined as $\sqrt{(\langle\rho^2\rangle - \langle\rho\rangle^2)}/\langle\rho\rangle$, are $\sim$ 13.7% and $\sim$ 15% respectively. The inserted panel, shows a few examples for which BG13 model gives a relatively more regular cascade rate over two decades, compared to the PP98 model.

Figure 5.8 shows the cascade rates computed for the two particular events of Figure 5.7. The first panel, shows the contribution of the different flux terms $|\mathcal{F}_1|$, $|\mathcal{F}_2|$

and $|\mathcal{F}_3|$ separately. Note that the flux $|\mathcal{F}_1|$ can be seen as the generalization to the compressible case of the PP98 flux, since it converges to it in the incompressible limit. For that reason we call it the Yaglom flux. We clearly see from these two examples that the main contribution comes from the new pure compressible flux $|\mathcal{F}_3|$ with up to an order of magnitude of difference with $|\mathcal{F}_1|$. In the second panel one can see that for the fast and the slow wind, the resulting compressible energy cascade rate $\langle|\varepsilon_C|\rangle$ (red) is higher than the incompressible one $\langle|\varepsilon_I|\rangle$ (black), and for the slow wind case, $\langle|\varepsilon_C|\rangle$ is more uniform and the ratio $\langle|\varepsilon_C|\rangle/\langle|\varepsilon_I|\rangle$ seems a bit larger than in the fast wind. In fact since the fast wind is in general less compressible than the slow wind, and is significantly more stationary, most of the previous studies were focused on the fast solar wind. To the best of my knowledge this is the first time that a steady cascade rate $\langle|\varepsilon_C|\rangle$ was obtained in the slow solar wind for about two decades of scales.

Figure 5.9 shows other examples of $\langle|\varepsilon_C|\rangle$ for both wind speeds chosen from the same statistical events of THEMIS B/ARTEMIS P1. Note that the slow wind shows a more uniform energy flux than the one computed in the fast wind. This would probably come from the compressible flux terms $|\mathcal{F}_2|$ and $|\mathcal{F}_3|$, that play a significant role in the slow wind.

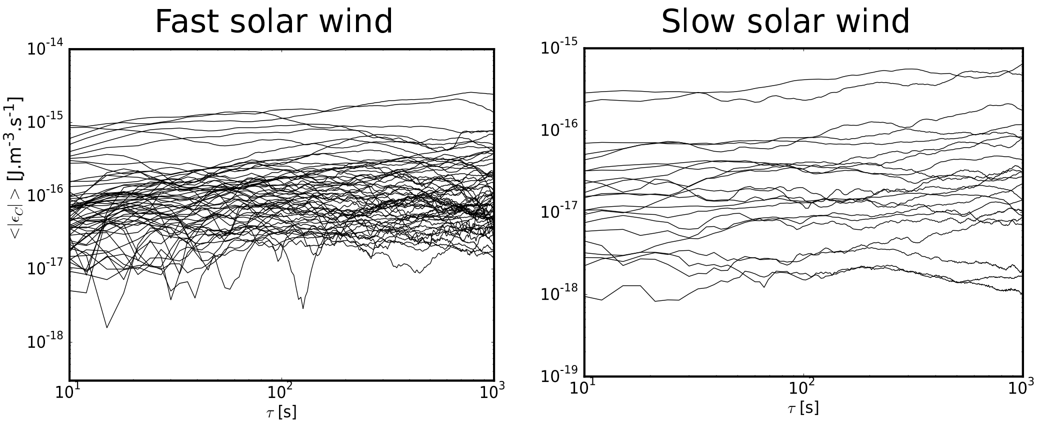

Figure 5.9: Examples of $\langle|\varepsilon_C|\rangle$ computed in the fast and the slow winds.

These results are confirmed in the statistical survey of all the samples I analyzed. Both, the histogram 5.10 and the corresponding average (absolute) values indicate that $\langle|\varepsilon_C|\rangle$ and $\langle|\varepsilon_I|\rangle$ are larger in the fast wind than in the slow wind. This confirms the previous finding regarding the incompressible cascade rate $\langle|\varepsilon_I|\rangle$ and shows that the compressibility does not change that trend.

In this work, I used the average values of $|\varepsilon_C|$ over all the values of $\tau \in [10-1000]\, s$. This may contrast with previous studies where the statistical results were given at a specific value of τ within the inertial range [Smith *et al.*, 2009*b*; Podesta *et al.*, 2010]. However this may affect the average sign of the cascade as I will show it in Section 5.3.3).

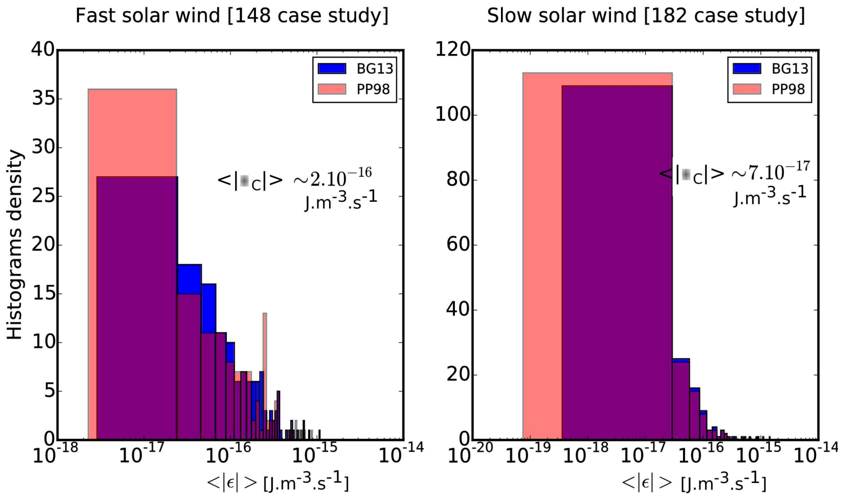

Figure 5.10: Histograms of the $\langle|\varepsilon_C|\rangle$ estimated by BG13 (red) and $\langle|\varepsilon_I|\rangle$ estimated by PP98 (blue) in the fast and slow winds.

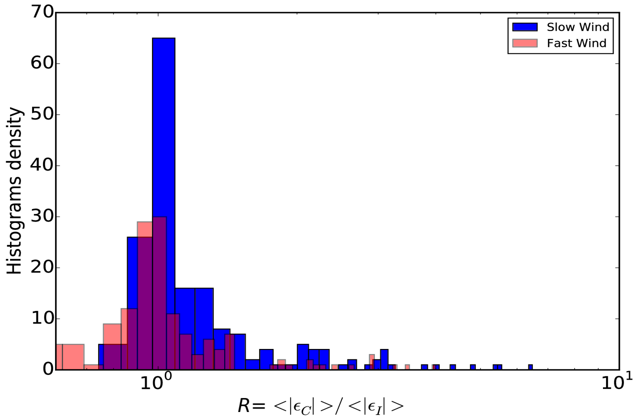

Figure 5.11: Histograms of the ratio between the compressible to the incompressible cascade rate $R = \langle|\varepsilon_C|\rangle/\langle|\varepsilon_I|\rangle$ in the fast (red) and slow (blue) winds.

Figure 5.11 compares the ratio between the compressible to the incompressible cascade rate $R = \langle|\varepsilon_C|\rangle/\langle|\varepsilon_I|\rangle$ in the fast and slow winds. One can see that for the fast and the slow wind, the histograms of R peak around 1. A first feature reported in Banerjee et al. 2016 is that the compressibility, while its average may not modify significantly cascade rate ($R = \langle|\varepsilon_C|\rangle/\langle|\varepsilon_I|\rangle \sim 1$), in some cases it does nevertheless amplify it by a factor of $3-4$. The examples of Figure 5.8 are among them and belong to the tail of the distribution in Figure 5.11. This trend is enhanced in the slow wind where the (blue) histogram of R in Figure 5.11 is found to shift to higher values (up to $6-7$) and for a larger number of events than in the fast wind. Note however that this amplification due to compressibility is much smaller than that reported in C09. This issue is discussed in Section 5.3.1.

5.2.3 Compressibility and the turbulent Mach number ($\mathcal{M}_S$)

To evidence the role of the compressibility defined as $\sqrt{(\langle\rho^2\rangle - \langle\rho\rangle^2)}/\langle\rho\rangle$ in enhancing the cascade rate $\langle|\varepsilon_C|\rangle$ w.r.t. the incompressible one $\langle|\varepsilon_I|\rangle$, I show in Figure 5.12 $\langle|\varepsilon_C|\rangle$ as a function of the wind speed and the compressibility. First, one can find the property discussed above that, overall, the fast wind have a higher $|\varepsilon_C|$ than the slow winds. Moreover, one can see an increase in the cascade rate as compressibility increases in particular in the case of the slow wind. This trend is less evident in the case of the fast solar wind possibly because the spread in the compressibility values is smaller ($\sim 3\% - 20\%$) than in the case of the slow winds ($\sim 1\% - 20\%$).

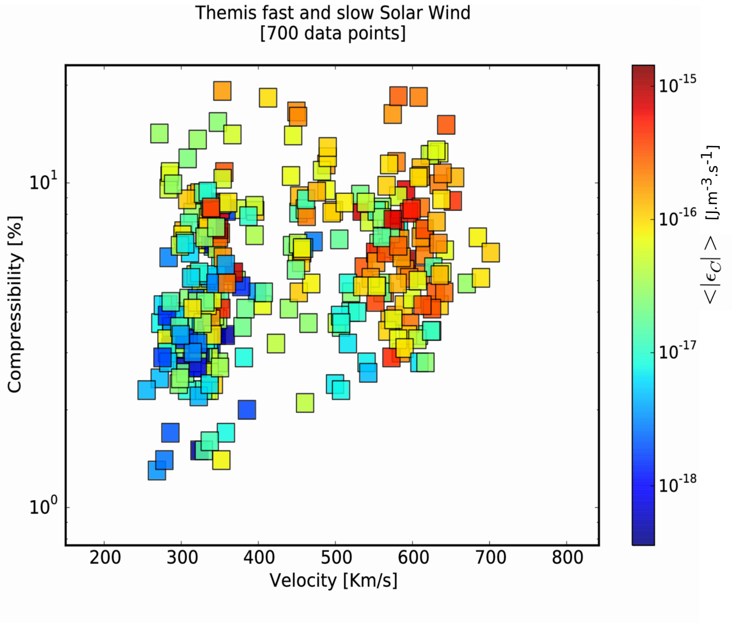

Figure 5.12: Variation of the compressible cascade rate $\langle|\varepsilon_C|\rangle$ as a function of the compressibility ($\sqrt{(\langle\rho^2\rangle - \langle\rho\rangle^2)}/\langle\rho\rangle$) and the wind speed.

Interestingly, plotting the turbulent Mach number defined as $\mathcal{M}_S = \sqrt{\frac{\delta v^2}{C_s^2}}$, ($C_s$ being the sound speed), as a function of the $\langle|\varepsilon_C|\rangle$, a good correlation appears between these two quantities. One can clearly see in Figure 5.13 that a higher value $\mathcal{M}_S$ leads to an increase of $\langle|\varepsilon_C|\rangle$ for both wind speeds, however a much better fit is observed for the slow wind than the fast wind. The least-squares fit to these data points gives the relations $\langle|\varepsilon_C|\rangle \sim {\mathcal{M}_S}^{1.5}$ and $\langle|\varepsilon_C|\rangle \sim {\mathcal{M}_S}^{2.6}$ for the fast and the slow winds respectively. These results highlight the important role that $\mathcal{M}_S$ plays in the turbulent energy cascade, but also suggest that one has to consider $\mathcal{M}_S$ rather than simply the compressibility since the former includes the characteristic fluctuating plasma velocity and so takes into account the dynamics of the system. Figure 5.14 shows no clear dependence between the compressibility and $\mathcal{M}_S$, mainly for the fast wind, whereas for the slow wind, one can observe an increase in the compressibility with the increase of $\mathcal{M}_S$, although this trend is not very clear.

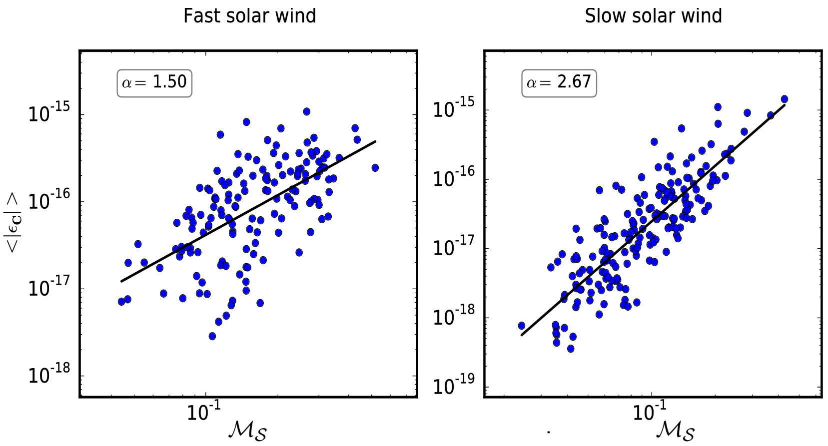

Figure 5.13: The absolute averaged energy transfer rate as a function of the turbulent Mach number in the fast and the slow wind. The black line represents a least square fit of the data in the log space. α is the corresponding correlation coefficient.

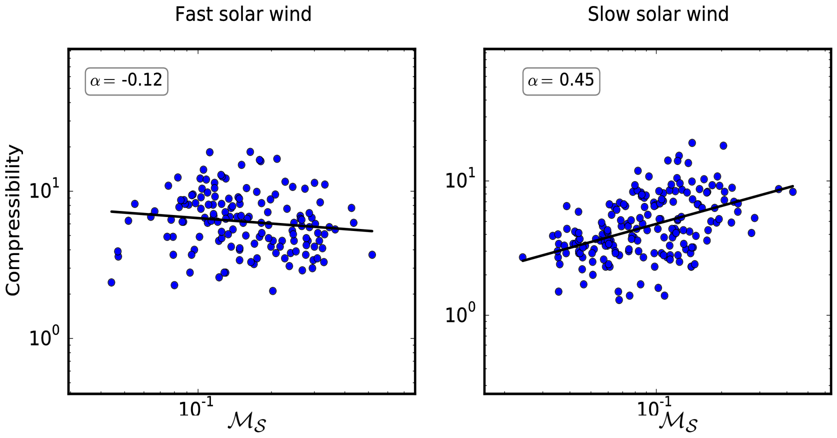

Figure 5.14: The compressibility $(\sqrt{(\langle\rho^2\rangle - \langle\rho\rangle^2)}/\langle\rho\rangle)$ as a function of the turbulent Mach number in the fast and the slow wind. The black line represents a least square fit of the data. α is the corresponding correlation coefficient.

5.2.4 Compressible cascade rate and the compressible energy

Another interesting feature that can be analyzed is the dependence of the cascade rate $\langle|\varepsilon_C|\rangle$ on the energy of the compressible turbulent fluctuations δE and the possible existence of a scaling law relating each of the energy components to ε_C. Indeed, unlike in the incompressible model PP98, the total energy of the fluctuations is not given simply by:

$$\delta E_I = \frac{\rho_0}{4}(\delta \mathbf{z}^{+2} + \delta \mathbf{z}^{-2}) \tag{5.6}$$

but includes the internal energy, hence

$$\delta E_C = \frac{\rho_0}{4}(\delta \mathbf{z}^{+2} + \delta \mathbf{z}^{-2}) + \delta U = \frac{\rho_0}{4}(\delta \mathbf{z}^{+2} + \delta \mathbf{z}^{-2}) + C_s^2 \rho_0 \ln{(1 + \frac{\rho_1}{\rho_0})} \tag{5.7}$$

where ρ_1 represents the density fluctuations.

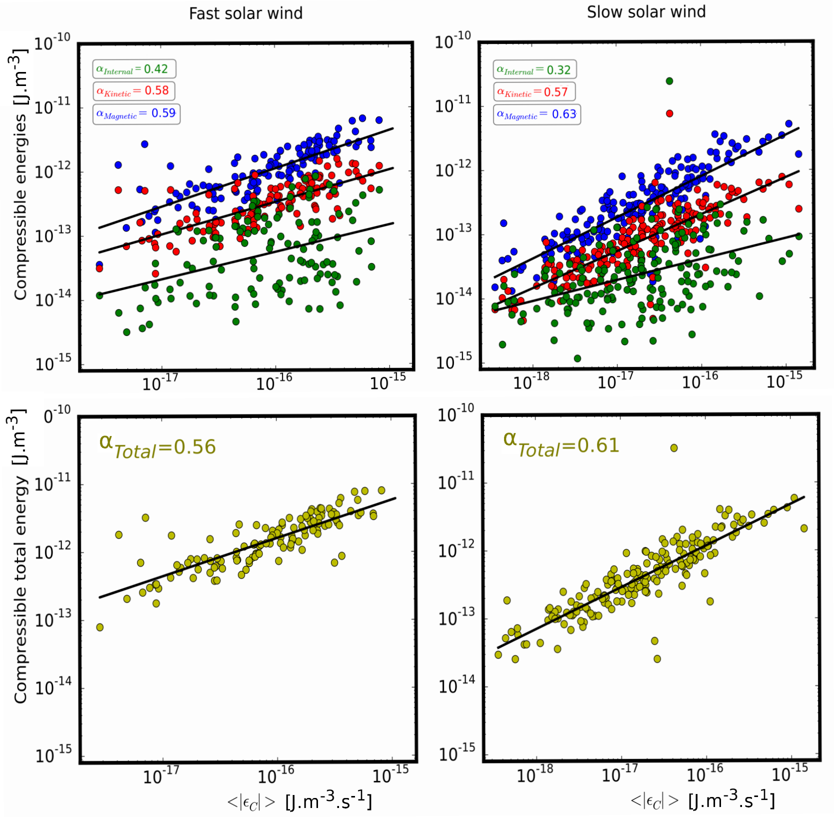

Figure 5.15: First panel: the magnetic (blue), kinetic (red) and internal (green) energies of the compressible fluctuations in the fast and slow winds. Second panel: the total compressible energy, plotted as a function of the compressible energy cascade rate $\langle|\varepsilon_C|\rangle$. The black lines are the least-square-fits with α the corresponding fit coefficient. $\delta E \sim \varepsilon_C^\alpha \to \varepsilon_C \equiv \delta E^{1/\alpha}$.

Figure 5.15 shows the estimated compressible cascade rate $\langle|\varepsilon_C|\rangle$ as function of the three components of the total energy of the fluctuations for all the statistical samples analyzed in the fast and slow solar wind. First, one can see that, statistically, the magnetic energy dominates over the kinetic and internal energies, the latter being the smallest. Second, a relatively clear power-law scaling (with some dispersion) between $|\varepsilon_C|$ and δE_i ($i = K, M, I$ for kinetic, magnetic and internal energies) can be evidenced:

$$\delta E_K \sim \varepsilon_C^{0.58} \tag{5.8}$$

and

$$\delta E_M \sim \varepsilon_C^{0.60} \tag{5.9}$$

The scaling w.r.t internal energy is steeper and is different for the two types of winds:

$$\delta E_I \sim \varepsilon_C^{0.42} \tag{5.10}$$

for the slow wind, and

$$\delta E_I \sim \varepsilon_C^{0.32} \tag{5.11}$$

for the fast wind. While the scaling of the magnetic and kinetic energies with the cascade rate are very close to the prediction from the Kolmogorov theory [Bruno & Carbone, 2005], no theoretical prediction exists so far to help interpreting the empirical laws of Equations 5.10-5.11. For both wind speeds, the total energy is dominated by the magnetic one (Figure 5.15).

5.2.5 Role of the different flux terms

To gain insight into the role played by the different flux terms involved in estimating the compressible energy cascade rate, I plot in Figure 5.16 the statistical results regarding the contribution of the different averaged compressible fluxes, $\langle|\mathcal{F}_1|\rangle$, $\langle|\mathcal{F}_2|\rangle$ and $\langle|\mathcal{F}_3|\rangle$, relative to the incompressible (Yaglom) flux $\langle|\mathcal{F}_\mathcal{I}|\rangle$ for the slow and fast winds. A first observation is that most of the samples have their compressible Yaglom flux ($\langle|\mathcal{F}_1|\rangle$) of the order of the incompressible flux ($\langle|\mathcal{F}_\mathcal{I}|\rangle$). This indicates that it is the new compressible fluxes $\langle|\mathcal{F}_2|\rangle$ and $\langle|\mathcal{F}_3|\rangle$ that contribute more in enhancing the compressible cascade rate $\langle|\varepsilon_C|\rangle$ w.r.t. $\langle|\varepsilon_I|\rangle$, than the compressible Yaglom term $\langle|\mathcal{F}_1|\rangle$. This is better seen when observing that high values of $R = \langle|\varepsilon_C|\rangle/\langle|\varepsilon_I|\rangle$ (up to ~ 4 in the fast wind and up to ~ 6 in the slow wind) are observed when $(\langle|\mathcal{F}_2|\rangle + \langle|\mathcal{F}_3|\rangle)/\langle|\mathcal{F}_\mathcal{I}|\rangle > 1$. Note that these results contrast with Carbone *et al.* [2009] where a larger amplification is observed and comes from the modification of the Yaglom term. This discrepancy will be explained in Section 5.3.1. The one observed here has a totally different origin: it is essentially due to the pure compressible terms $\mathcal{F}_2$ and $\mathcal{F}_3$ derived in the BG13 exact model. Note finally that the highest ratio $\langle|\varepsilon_C|\rangle/\langle|\varepsilon_I|\rangle$ (i.e., highest amplification of the cascade rate due to compressible fluctuations) is observed in the top-right quarter of Figure 5.16, which corresponds to the cases when all the three terms $\langle|\mathcal{F}_1|\rangle$, $\langle|\mathcal{F}_2|\rangle$ and $\langle|\mathcal{F}_3|\rangle$ dominate over the incompressible (Yaglom) term $\langle|\mathcal{F}_\mathcal{I}|\rangle$. The highest values of the ratio R are observed in this quarter for the slow wind.

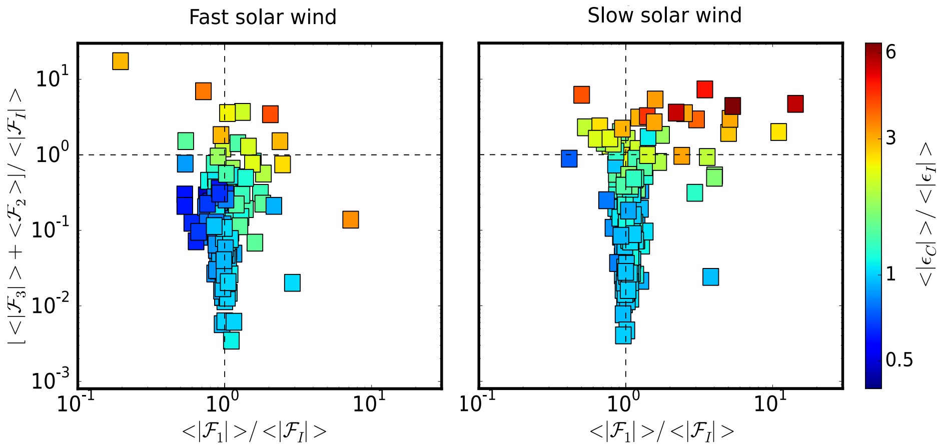

Figure 5.16: Estimation of the contribution of the compressible fluxes w.r.t. incompressible (Yaglom) flux to the compressible cascade rate for the fast (right) and slow (left) winds.

Figure 5.17 shows similarly, the flux ratios as function of the ratio between the compressible ($\delta E_C = \delta U + \delta E_K + \delta E_M$) to the incompressible energy (δE_I) of the turbulent fluctuations. As one expects, the samples for which the compressible terms ($\langle|\mathcal{F}_2|\rangle + \langle|\mathcal{F}_3|\rangle$) become of the order of (or dominate) the incompressible Yaglom term $\langle|\mathcal{F}_{\mathcal{I}}|\rangle$ correspond to cases when the total energy of the compressible fluctuations is of the order of (or larger than) the incompressible energy.

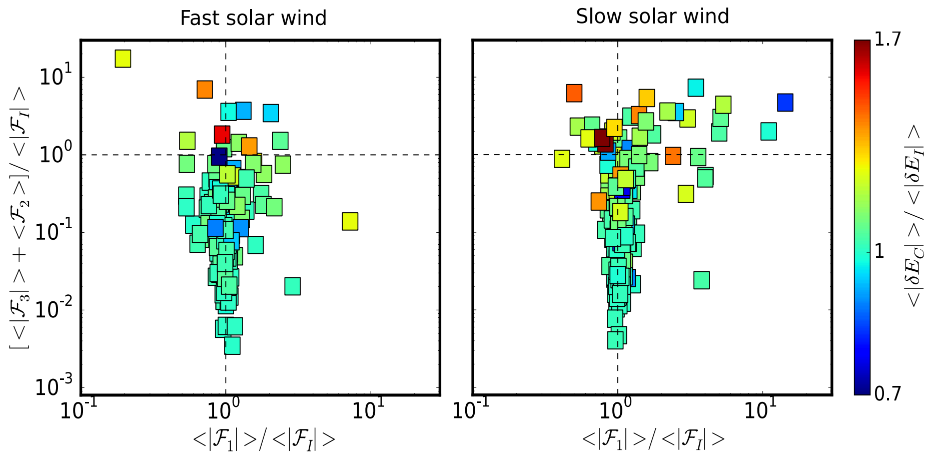

Figure 5.17: Estimation of the contribution of the compressible fluxes w.r.t. incompressible (Yaglom) flux to the compressible cascade rate for the fast (right) and slow (left) winds as function of the ratio between the compressible to incompressible energy of the turbulent fluctuations.

5.2.6 Sign of the energy transfer rate

In this section I discuss the sign of the cascade rate as estimated from the incompressible (PP98) and compressible (BG13) models. I first recall that this property can be discussed only when the dependence of the energy flux on the time increments τ used in Equations 5.5 are converted into the spatial ones l via the Taylor frozen-in-flow assumption. With the positive convention of the time increments ($\tau > 0$), the Taylor hypothesis implies $l \sim -V_{sw}\tau$. In this convention, positive (resp. negative) values of $\varepsilon_{I,C}$ correspond to a direct (inverse) energy cascade. The histogram of the signed compressible cascade rate are shown in Figure 5.18. Although the statistical samples used here is not as large as those used in previous studies based on the PP98 models (e.g., Coburn *et al.* [2015]), for all the reasons I explained in the data selection section (5.2.1), these results confirm some of the previously reported features of the solar wind. First, Figure 5.18 shows that both the histogram and the mean values (red lines) of the averaged signed cascade rates (ε_C) indicates a direct cacade in the slow solar wind and an inverse cascade in the fast winds. The values of $\langle\varepsilon_C\rangle$ are in agreement with those reported in MacBride *et al.* [2008] $\sim 1.3 \times 10^{-17} J.m^{-3}.s^{-1} \sim 3.4 \times 10^4 J.(kg.s)^{-1}$.

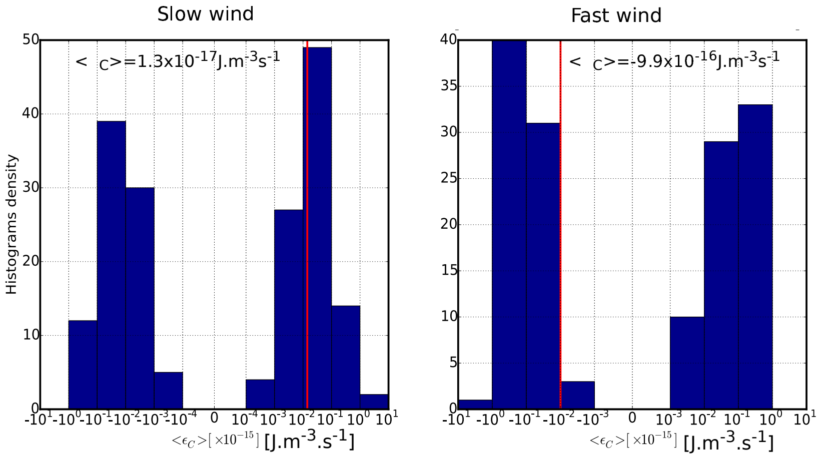

Figure 5.18: Histograms of the signed energy cascade rate estimated using the compressible model BG13 in the fast (left) and slow (right) solar wind. The red lines represent the corresponding mean values of the energy cascade.

The second observation is that the compressible fluctuations do not influence the direction of the cascade. This can be seen in Figure 5.19 showing the correlations between the estimated signed incompressible and compressible cascade rates ε_I and ε_I: most of the case studies showed the same sign for the averaged incompressible and compressible energy cascade rates.

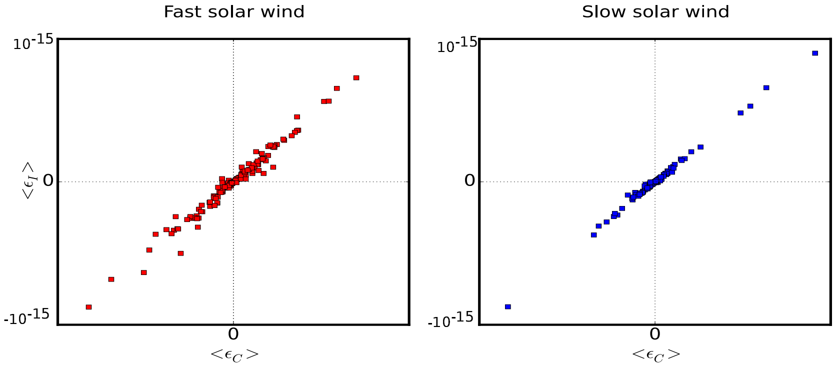

Figure 5.19: The correlations between the estimated signed incompressible and compressible cascade rates ε_I and ε_I in the fast (red) and slow (blue) winds.

To understand the difference in the direction of the cascade in the slow and the fast wind, I investigated the role of the cross helicity σ_c (defined in Equation 3.2 of Chapter 3) as suggested in Smith *et al.* [2009*b*]. The results of the analysis are shown in Figure 5.20. Several interesting features can be evidenced. First, we observe again the property reported in section 5.2.4: the fast wind has higher $\langle|\varepsilon_C|\rangle$ than the slow wind (Figure 5.20). Furthermore, we observe the known feature that the fast wind is generally characterized by higher values of cross helicity $|\sigma_c| \gtrsim 0.5$. This property is not observed in the slow solar wind where σ_c is uniformally distributed between $\sim [-0.8, +0.8]$.

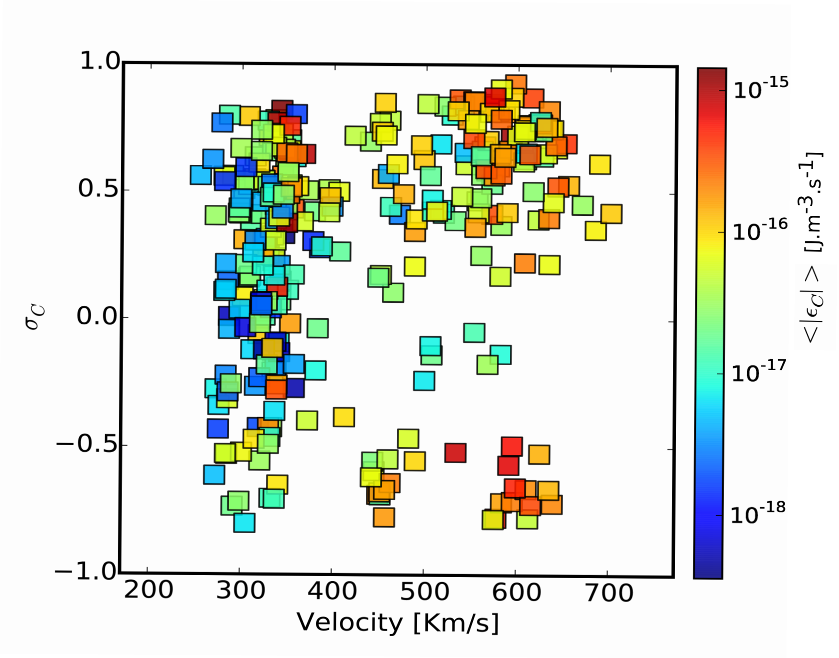

Figure 5.20: The compressible cascade rate ε_C plotted as function of the cross-helicity and the solar wind speed.

Figure 5.21 represents the variation of σ_c as a function of the angle $\Theta_{\mathbf{VB}}$ in the fast and the slow winds respectively.

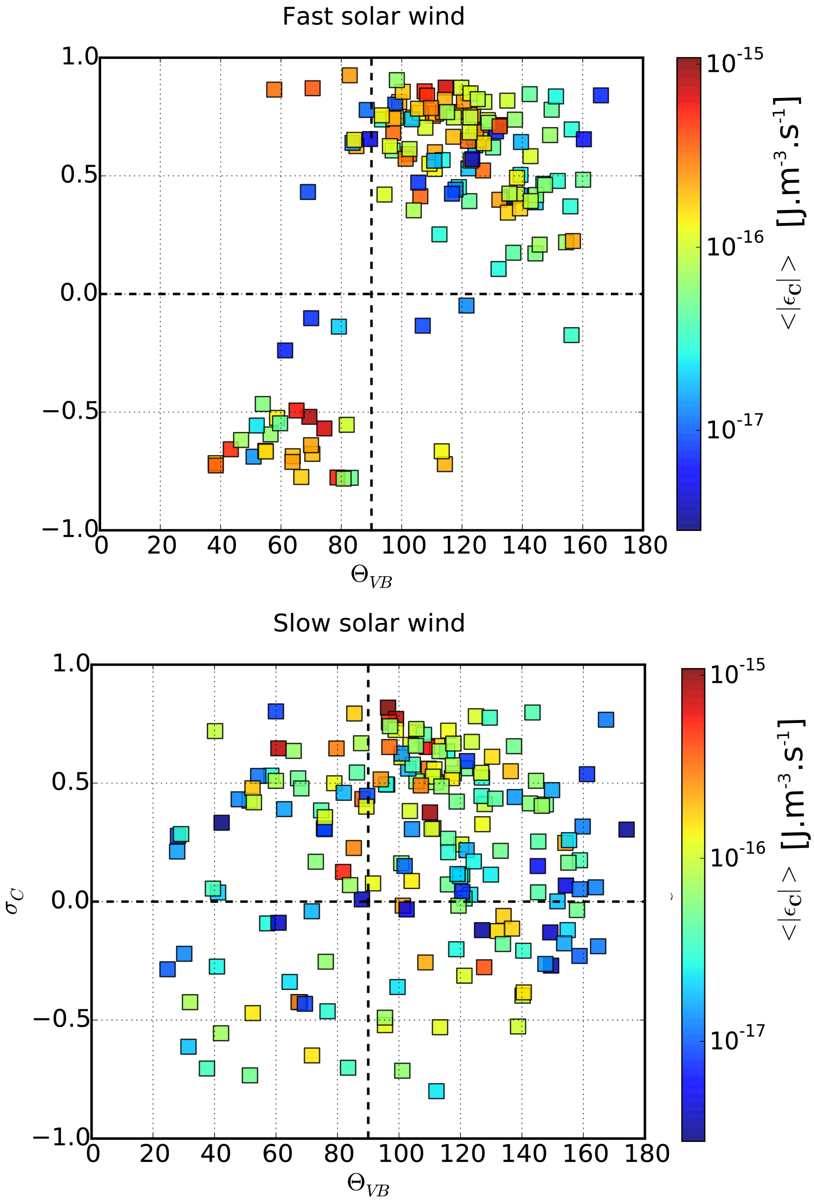

Figure 5.21: Cross-helicity (σ_c) plotted as a function of the propagation angle $\Theta_{\mathbf{VB}}$ and $\langle|\varepsilon_C|\rangle$ in the fast wind (Top) and the slow wind (Bottom). For an outward propagation, $\sigma_c \sim +1$ and is anti-parallel to $\mathbf{B}$. Whereas for an inward propagation $\sigma_c \sim -1$ and is parallel to $\mathbf{B}$.

The first panel highlights as well the fundamental aspect of the fast wind being dominated by the outward propagating Alfvén waves characterized by a propagation anti-parallel to the mean magnetic field ($\mathbf{B_0}$) ($\Theta_{\mathbf{VB}} > 90°$) as I have mentioned in

Section 3.1.1. While the slow wind (second panel), is balanced between the inward and outward propagations.
In fact the dominance of the inverse cascade in the fast solar wind (dominated by outward propagating waves) is consistent with the finding of Smith *et al.* [2009*b*] who conjectured that this process could explain the survival of regions of high cross-helicity in the fast wind at large radial distances from the Sun [Roberts *et al.*, 1987]. However, there are still no theoretical model that predicts this "inverse cascade".

5.2.7 Spatial anisotropy and the energy cascade rate

In this section I explore the anisotropy of the cascade rate and the differences between the incompressible and compressible models. The anisotropy of the cascade rate has been investigated using the PP98 model, and it was shown that ε is more anisotropic in the fast than in the slow solar wind (e.g., MacBride *et al.* [2008], Figure 5.22).

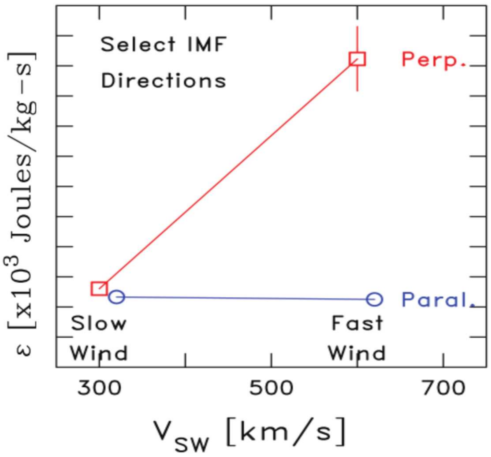

Figure 5.22: Energy cascade rate using different magnetic field directions. Adapted from MacBride *et al.* [2008].

In the previous works, the original PP98 equations were modified to fit the limit of either 1D (slab) or 2D geometry, through the approriate projection of the flux terms in the two directions, parallel and perpendiuclar w.r.t. mean field **B**. Here, I do not use that approach for either the PP98 or the BG13 models. Instead, I simply examine the dependence of the estimated cascades rates on the angle $\Theta_{\mathbf{VB}}$. As I explained above, the use of the Taylor hypothesis to convert time lag into spatial scales implies that the analysis samples only the direction along the solar wind flow. Hence, when $\Theta_{\mathbf{VB}} \sim 0°$ (resp. $\Theta_{\mathbf{VB}} \sim 90°$) the analysis yields information in the direction parallel (resp. perpendicular) to the local field **B**. It is worth recalling that the derivation of BG13 model does not require the isotropy assumption. Indeed, a simplified version for the model has been given in Banerjee & Galtier [2013] in the limit of a strong guide field. Therefore, estimating the cascade rate using that model as function of the sampling direction of space given by the angle $\Theta_{\mathbf{VB}}$ should allow gaining insight into the anisotropic nature of the fluctuations. I used this approach by spliting the statistical samples (in the fast and slow winds) as function of the angle $\Theta_{\mathbf{VB}}$. The results are given in Figure 5.23. Two important observations can be made. First, both models, PP98 and BG13, provide a cascade rate that depends on the angle $\Theta_{\mathbf{VB}}$. This dependence is even more pronounced in the slow wind than in the fast wind. This contrasts with the finding of MacBride *et al.* [2008] in Figure 5.22 who showed no significant anisotropic cascade in the slow wind. Note that their result is based on two points. However similarly to MacBride *et al.* [2008], the heating is smaller in the parallel direction than in the perpendicular one for both winds, with a lower $\langle|\varepsilon_C|\rangle$ for the slow compared to the fast one. Secondly, we can see clearly that the compressible model BG13 slightly reduces the level of anisotropy in the winds as one can see in the blue curve of $\langle|\varepsilon_C|\rangle/\langle|\varepsilon_I|\rangle$ overplotted in Figure 5.23 (although it is more visible in the fast wind). This observation can easily be understood considering that, unlike the shear Alfvén mode in the PP98 model, the BG13 model includes also the compressible MHD (slow and fast) modes, which have a parallel magnetic field component although they are minor in the solar wind. This naturally tends to isotropize the turbulent fluctuations which are no longer simply guided by the mean magnetic field as in incompressible MHD theory Cho & Lazarian [2002].

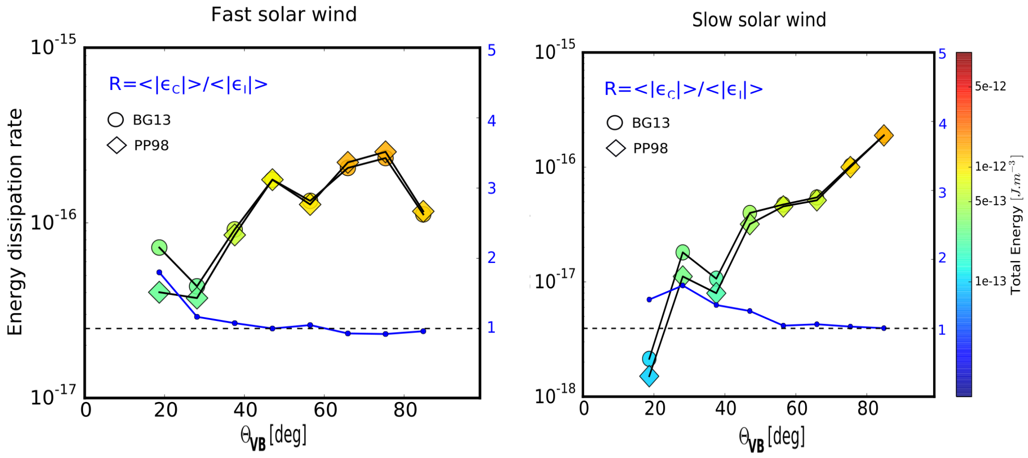

Figure 5.23: Energy dissipation rate ($\langle|\varepsilon_C|\rangle$) as a function of the averaged propagation angle $\Theta_{\mathbf{VB}}$ and the total compressible energy computed in the fast and the slow wind.

5.3 Discussions and conclusion

Before summarizing the main finding of the present statistical work, I will address some important points related to the use of the new compressible model to estimate the energy cascade rate in the solar wind and some caveats that need to be considered. These points are related to the subtile role of the background (mean) density, the velocity of the solar wind plasma, and to the role of the angle $\Theta_{\mathbf{VB}}$.

5.3.1 Discrepancy with C09: the role of mean flow velocity

Until now I have only compared the exact MHD incompressible (PP98) and compressible (BG13) models, without discussing the heuristic model (C09) of Carbone *et al.* [2009]. In the first attempt to include compressible fluctuations in solar wind turbulence studies, Carbone *et al.* [2009] found that the energy transfer rate ε_{C09} is around $10-15$ times greater than the one given by PP98 and that amplification comes from a heuristic modification of the original (incompressible) Yaglom terms in the PP98 model. In my work I showed that the compressible Yaglom term $\mathcal{F}_1$ does not play a significant role in enhancing ε_C w.r.t. the PP98 model. The amplification comes from the new flux terms $\mathcal{F}_2$ and mainly $\mathcal{F}_3$ that are not included in the C09 model. This discrepancy may originate from the role of the mean flow velocity involved in the definition of the Elsässer variables $\mathbf{z}^{\pm} = \mathbf{v} \pm \mathbf{b}/\sqrt{\mu_0\rho_0}$. Indeed, while the total flow velocity and the mean magnetic field are involved in the definition of the Elsässer variable $\mathbf{z}^{+}$ and $\mathbf{z}^{-}$, Equation 5.1 of the PP98 model used to estimate the cascade rate involves only the increments of $\mathbf{z}^{+}$ and $\mathbf{z}^{-}$. Therefore, the mean flow velocity and the mean magnetic field are suppressed while estimating the increments, which consequently depend only on the turbulent field fluctuations. This is consistent with the theoretical derivation of the exact laws in turbulence where a zero mean flow velocity is generally assumed. The difficulty arises when dealing with the density-weighted velocity given as $\mathbf{w}^{\pm} = \rho^{\mathbf{1/3}}\mathbf{z}^{\pm}$. Because of the density dependence of the modified Elsässer variables, the mean flow velocity will remain involved in estimating the field increments in Equations 5.2 of C09. In other words, the estimation of the cascade rate will involve not only the turbulent fluctuations but also the mean flow velocity, which is not relevant in turbulence studies (unless it has shear or divergence). To test this hypothesis I compared the energy transfer rates computed using PP98, BG3, C09, and a modified version of the C09 model that uses the fluctuating velocity $\delta\mathbf{v}$ instead of the total one, namely

$$\delta\mathbf{w}_m{}^{\pm} = \rho^{2/3}\Big(\delta\mathbf{V} \pm \frac{\mathbf{B}}{\sqrt{\rho\mu_0)}}\Big) \tag{5.12}$$

The results are shown in Figure 5.24. As one can see, not only the $\langle|\varepsilon|\rangle$ of C09 (blue curve) does not give a linear scaling as does the BG13 model, it also gives a cascade rate that is at least 10 times higher than the other models. However, when using the modified C09 with the variables $\delta\mathbf{w}_m$, the corresponding $\langle|\varepsilon|\rangle$ (green curve) decreases and becomes comparable to the Yaglom term of PP98 (black curve). This implies that the modified C09 model, which considers compressibility corrections to the Yaglom term in the PP98 model, does not modify significantly the energy cascade rate in agreement with our finding using the BG13 model.

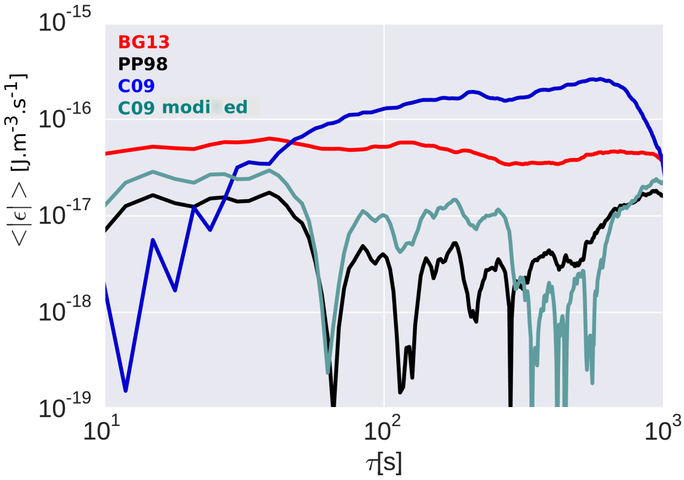

Figure 5.24: The energy dissipation rate computed using BG13 (red), PP98 (black), C09 (blue), C09 corrected (light blue).

This is confirmed by the statistical analysis performed on the C09 case studies that gave a linear scaling and a constant sign. The corresponding results are shown in Figure 5.25, which compares the ratios R of the average energy cascade rates obtained using the original and the modified C09 models to those given by the PP98 model. As one can see, R reaches values as high as ~ 50 both in the fast and the slow winds (blue histograms), while this ratio drops down to ~ 1 with the modified $C09$ model (red histogram), in agreement with our finding using the BG13 model.

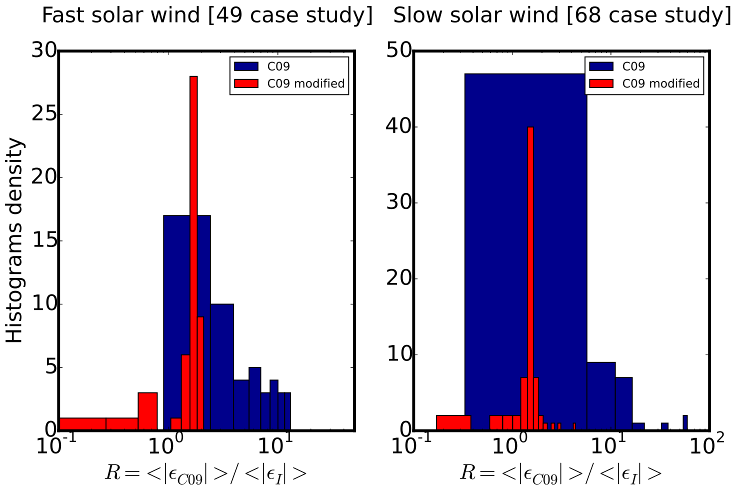

Figure 5.25: Histogram of the ratio $R = \langle|\varepsilon_{C09}|\rangle / \langle|\varepsilon_{C}|\rangle$ using the model $C09$ model (blue) and the modified one (red).

5.3.2 The role of mean plasma density

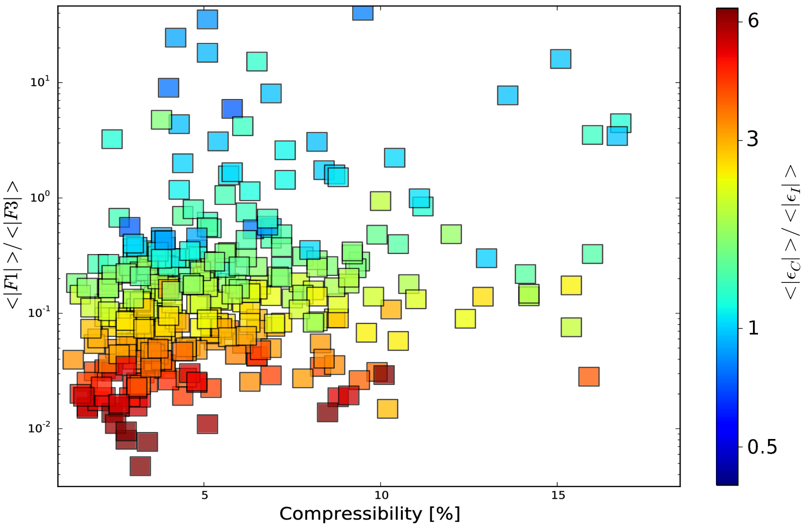

Figure 5.26: 2D plot of $\langle|\mathcal{F}_1|\rangle/\langle|\mathcal{F}_3|\rangle$ as a function of the compressibility and the ratio $\langle|\varepsilon_C|\rangle/\langle|\varepsilon_C|\rangle > 1$.

Another point that deserves enlightment is the influence of the mean density ρ_0 in the BG13 model. Indeed, the original reduced form of $\mathcal{F}_3$ includes the total density $\rho = \rho_0 + \rho_1$ [Banerjee & Galtier, 2013]:

$$\mathcal{F}_3(\ell) = \left\langle 2\overline{\delta}\left[\left(1+\frac{1}{\beta}\right)e + \frac{v_A^2}{2}\right]\delta(\rho\mathbf{v})\right\rangle \tag{5.13}$$

Written under this form, it is practically impossible to ensure that F_3 vanishes in the incompressible limit $\rho = 0$. Indeed, using spacecraft data, we do not explicitely apply the divergence operator $\nabla_{\boldsymbol{\ell}}$, but rather use $\nabla_{\boldsymbol{\ell}} \to 1/\ell$, which never goes to zero unless $\ell \to \infty$. This violates the condition of convergence between the PP98 and BG13 models in the incompressibile limit. This is well illustrated by Figure 5.26 where one can see that, at low values of compressibility $< 5\%$, the compressible cascade rate $\langle|\varepsilon_C|\rangle$ dominates over the incompressible one $\langle|\varepsilon_C|\rangle/\langle|\varepsilon_I|\rangle > 1$ and that the compressible flux term $\langle|\mathcal{F}_3|\rangle$ dominates over the incompressible Yaglom term $\langle|\mathcal{F}_I|\rangle$ ($\langle|\mathcal{F}_I|\rangle/\langle|\mathcal{F}_3|\rangle < 1$). Note that this difficulty is not present in the general form of $\mathcal{F}_3$ that uses the full divergence operator.

$$\nabla_{\boldsymbol{\ell}} \cdot \left\langle \mathcal{F}_3(\ell) \right\rangle = \nabla_{\boldsymbol{\ell}} \cdot \left\langle 2\overline{\delta}\left[\left(1+\frac{1}{\beta}\right)e + \frac{v_A^2}{2}\right]\delta(\rho\mathbf{v})\right\rangle \tag{5.14}$$

In the limit of incompressibility $\rho = \rho_0$ the divergence operator guarantees that $\nabla_{\boldsymbol{\ell}} \cdot \left\langle \mathcal{F}_3(\ell) \right\rangle = 0$ since $\nabla_{\boldsymbol{\ell}} \cdot \left\langle \mathbf{v} \right\rangle = 0$.

To guarantee the convergence of BG13 and PP98 models in the limit of incompressibility, we expand Equation (5.14) in terms of the mean density ρ_0 and the density fluctuations ρ_1:

$$\begin{aligned}\nabla_{\boldsymbol{\ell}} \cdot \left\langle \mathcal{F}_3(\ell) \right\rangle = {} & \nabla_{\boldsymbol{\ell}} \cdot \left\langle 2\overline{\delta} \left[\left(1 + \frac{1}{\beta} \right) e + \frac{v_A^2}{2} \right] \delta(\rho_0 \mathbf{v}) \right\rangle \\ & + \nabla_{\boldsymbol{\ell}} \cdot \left\langle 2\overline{\delta} \left[\left(1 + \frac{1}{\beta} \right) e + \frac{v_A^2}{2} \right] \delta(\rho_1 \mathbf{v}) \right\rangle \end{aligned} \tag{5.15}$$

Keeping the second term of Equation (5.15), the first term can be easily transformed into a source term as follows:

$$\begin{aligned}\nabla_{\boldsymbol{\ell}} \cdot \left\langle 2\overline{\delta} \left[\left(1 + \frac{1}{\beta} \right) e + \frac{v_A^2}{2} \right] \delta(\rho_0 \mathbf{v}) \right\rangle & = \nabla_{\boldsymbol{\ell}} \cdot \left\langle 2\rho_0 \left[\left(1 + \frac{1}{\beta} \right) e + \frac{v_A^2}{2} \right] (\mathbf{v}' - \mathbf{v}) + 2\rho_0 \left[\left(1 + \frac{1}{\beta} \right) e' + \frac{v_A'^2}{2} \right] (\mathbf{v}' - \mathbf{v}) \right\rangle \\ & = \nabla_{\boldsymbol{\ell}} \cdot \left\langle 2\rho_0 \left[\left(1 + \frac{1}{\beta} \right) e + \frac{v_A^2}{2} \right] \mathbf{v}' - 2\rho_0 \left[\left(1 + \frac{1}{\beta} \right) e' + \frac{v_A'^2}{2} \right] \mathbf{v} \right\rangle \\ & = \left\langle 2\rho_0 \left[\left(1 + \frac{1}{\beta} \right) e + \frac{v_A^2}{2} \right] (\nabla \cdot \mathbf{v}') + 2\rho_0 \left[\left(1 + \frac{1}{\beta} \right) e' + \frac{v_A'^2}{2} \right] (\nabla \cdot \mathbf{v}) \right\rangle \end{aligned} \tag{5.16}$$

It is only the first term that depends on ρ_1 that enters in estimating the flux terms in the spacecraft data. It naturally vanishes in the limit of incompressibility $\rho_1 = 0$. I recall that the general definition of an increment of a variable y is used, i.e. $\delta y \equiv y(\mathbf{x} + \ell) - y(\mathbf{x})$ and the primed and unprimed variables correspond to the variables at points $\mathbf{x} + \ell$ and $\mathbf{x}$ respectively.

5.3.3 Mean value of the cascade rate and the sign change of ε_I

As explained in Section 5.2.1, among the criteria that I used to select the samples is the constant sign of the estimated cascade rate ε_C over the time lag $\tau \in [10, 1000]$ s. This step is necessary in order to get reliable estimate of the mean cascade rate $\langle \varepsilon_C \rangle$ averaged over all the time lags τ. Indeed, if the sign of ε changes, the resulting average will yield (by cancellation) lower values the cascade rates. Another atlernative to this approach has been used in previous work based on performing statistical studies of the cascade rate obtained at a given value of the time at τ [MacBride *et al.*, 2008; Smith *et al.*, 2009*b*]. The choice of the particular τ value has not been justified apart from the fact that it belongs to the inertial range. The drawback of this approach is that, since the sign of ε can vary within the inertial range, the choice of the value of τ may influence the conclusion regarding the nature (direct versus inverse) of the turbulent cascade. Figure 5.27 shows the histogram of ε_I computed using PP98 at different values of τ. For $\tau = 21$ s, $\langle \varepsilon_I \rangle$ is positive, implying a direct cascade, whereas for $\tau = 81$ s, $\langle\varepsilon_I\rangle$ is negative indicating an inverse cascade. This result underlines the need to be cautious when interpreting statistical results about cascade rates estimated at a single value of the time lag τ even when is belongs to the inertial range.

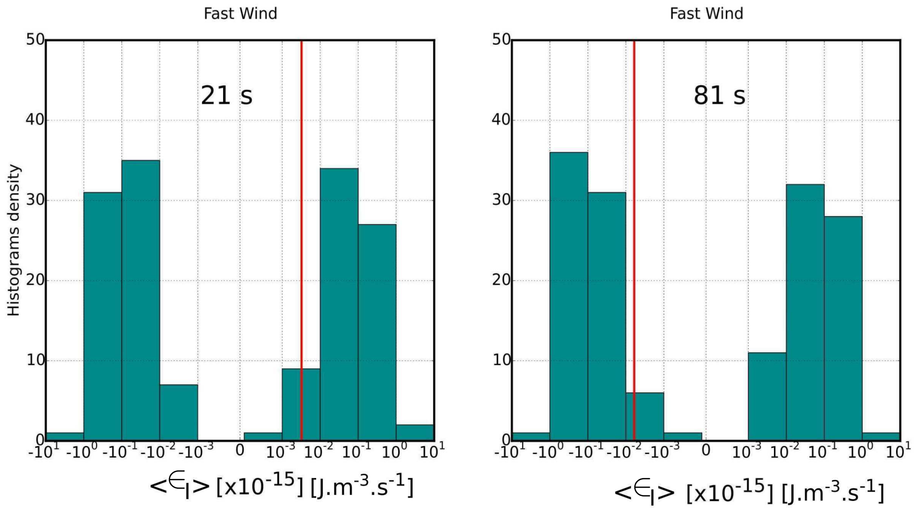

Figure 5.27: Histograms of ε_I computed in the fast wind at different values of $\tau = [21, 81]$. The red line represents the average value of ε_I for each value of τ.

5.3.4 The influence of the angle $\Theta_{\mathbf{VB}}$

In Section 5.2.1 I emphasized the importance of having relatively stationary angles $\Theta_{\mathbf{VB}}$ in order to have a more reliable estimate of the energy cascade rate (both its sign and its absolute value) when dealing with single spacecraft data, and regardless of the theoretical model used. Here I discuss two possible effects of the non stationarity of the angle $\Theta_{\mathbf{VB}}$ that may influence the estimation of the cascade rate.
Let us first start with the case of the presence of sharp variations in the angle $\Theta_{\mathbf{VB}}$ as in the example of Figure 5.28. Such sharp transitions (or discontinuities) may be due to different reasons such as the crossings of strong current sheets frequently observed in the solar wind and the magnetosheath (e.g., Gosling & Szabo [2008]; Chasapis *et al.* [2015]). I estimated the energy cascade rate using BG13 from a long but non stationary time interval (04:40-06:00) that contained two discontinuities in $\Theta_{\mathbf{VB}}$ (about 05:00 and 04:40) and from shorter one (05:05-05:38) where such discontinuities were excluded. The results are shown in Figure 5.28 (bottom). As one can see in this time interval, the long non stationary time interval yields a non uniform energy cascade rate which changes its sign, whereas the shorter one where the $\Theta_{\mathbf{VB}}$ sharp discontinuities were excluded, is more uniform and has a constant sign. This result should balance the usual wisdom arguing to use long time intervals (i.e., large number of data points) to guarantee the statistical convergence of the third order moments estimates (e.g., Podesta [2009]): the existence of a very few (i.e. statistically minor) sharp discontinuities as those in Figure 5.28 can significantly influence

the estimates of the cascade rate as we showed here.

The second possible effect of the angle $\Theta_{\mathbf{VB}}$ can come from when it is steady but has a significant variation in a single time interval. Indeed, as we argued in Section 5.2.1, the Taylor frozen-inflow assumption generally used on single spacecraft data allows one to convert the time sampling of the data into a 1D spatial sampling of the turbulent fluctuations along the flow direction. In anisotropic turbulence, the direction of the spatial sampling carries therefore a particular importance since the sampling can be either parallel ($\Theta_{\mathbf{VB}} \sim 0°$) or perpendicular ($\Theta_{\mathbf{VB}} \sim 90°$) to the mean field. These two directions, as demonstrated in Figure 5.23, have different values of the energy cascade rate. If $\Theta_{\mathbf{VB}}$ oscillates strongly between 0° and 90°, this implies that the analysis would mix between the two cascade rates estimated along the direction parallel and perpendicular to the local magnetic field, and would lead to higher uncertainty in the estimated values.

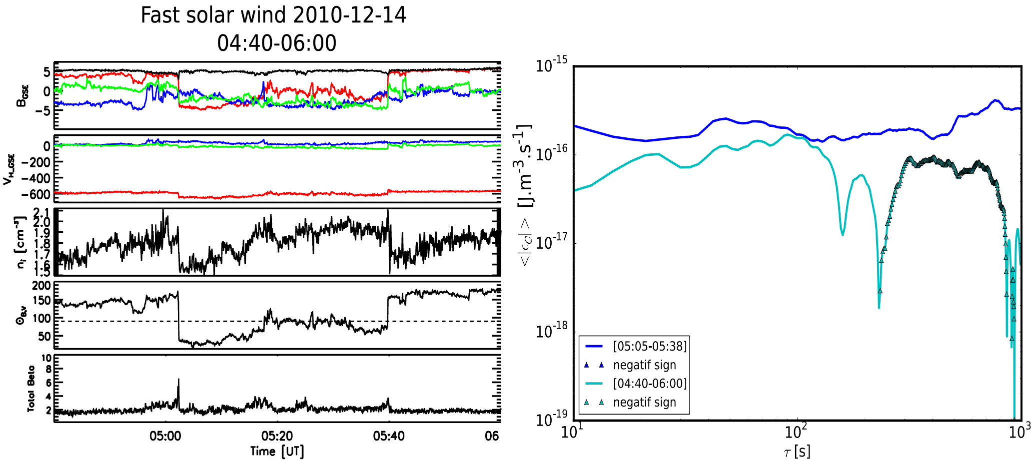

Figure 5.28: Example of the effect of $\Theta_{\mathbf{VB}}$ rotation. Left: from top to bottom, magnetic field components, the ion velocity, ion density, propagation angle, total beta. Right: comparison between $\langle|\varepsilon_C|\rangle$ computed on a time interval including sharp discontinuities (cyan, 04:40-06:00), and by excluding them (dark blue 05:05-05:38).

5.3.5 Heating of the fast solar wind

As it is mentioned in the introduction (Section 1.2), the solar wind plasma is known to cool down more slowly than expected from an adiabatic spherical expansion and therefore a source of local heating is needed to explain that observation. Turbulence is seen as a possible source of solar wind heating *via* the cascade of energy towards small-scales. The turbulent cascade implies a forward flux of energy which ultimately will be converted at small-scales into heating by some kinetic processes [see e.g. Sahraoui *et al.*, 2009, 2010].

Using a simple power law model [Vasquez *et al.*, 2007; Marino *et al.*, 2008], one can obtain an estimate for the energy needed to heat up the fast solar wind at 1

AU. For a power-law of type $T(r) \sim r^{-\xi}$, with T the proton temperature and r the heliocentric distance, the model can be written as:

$$\varepsilon_h = \frac{3}{2}\left(\frac{4}{3} - \xi\right)\frac{V_{sw} k_B T(r)}{m_p r}\,, \tag{5.17}$$

where ε_h is the energy flux rate (per unit mass). The typical values in the fast wind are: $V_{sw} = 625\,\mathrm{km\,s^{-1}}$, $T = 30\,\mathrm{eV}$, $r = 1.5 \times 10^{11}\,\mathrm{m}$ and $\xi = 0.49$ which was observed with Ulysses data [Marino *et al.*, 2008] and can be used as an estimation of the upper limit of the required heating rate. Using Equation (5.17), we get $\varepsilon_h \sim 1.5 \times 10^4\,\mathrm{J\,kg^{-1}s^{-1}}$ whence the heating energy flux rate per unit volume $3.3 \times 10^{-17}\ \mathrm{J\,m^{-3}s^{-1}}$. Therefore, unlike the incompressible flux (near or slightly less than $10^{-17}\mathrm{J\,m^{-3}s^{-1}}$), the compressible flux rate ($\sim 10^{-16}\mathrm{J\,m^{-3}s^{-1}}$) is found to be sufficient for explaining the non-adiabatic heating of the fast solar wind. It is worth noting that the first direct determination of the inertial range energy cascade rate, using an anisotropic form of Yaglom's law for magnetohydrodynamic turbulence, was obtained in the solar wind with multispacecraft Cluster measurements by Osman *et al.* [2011*b*].

5.3.6 Conclusion

In this work, the role of compressible fluctuations in the energy cascade was studied using a large statistical sample (324 events of 35 min each), in the fast and the slow wind (known to have different levels of compressibility). For that, I used the exact law derived for compressible isothermal magnetohydrodynamics and in-situ observations from the THEMIS B/ARTEMIS P1 spacecraft. A turbulent energy cascade was evidenced in both winds over two decades of scales, which is broader than the previous estimates made from an exact incompressible law. A term-by-term analysis of the compressible model revealed new insight into the role played by the compressible fluctuations in the energy cascade. The compressible fluctuations are shown to amplify (up to ~ 4 times for the fast wind and ~ 6 times for the slow wind) the turbulent cascade rate with respect to the incompressible model. Moreover, the study highlighted other interesting points related to: the role of the turbulent Mach number which seems to play a more important role than compressibility in increasing $\langle|\varepsilon_C|\rangle$, the nature of the cascade in the fast and the slow wind which was shown to be dominated by an inverse cascade and direct cascade respectively, and finally the role of the compressibility in slightly isotropizing the energy cascade rate mainly for the slow wind.

In the last part, the role played by the mean velocity vector and the background density in increasing artificially the energy cascade rate if they are used, was noted as well. Eventually, this new estimated cascade rate was shown to provide the adequate energy dissipation required to account for the local heating of the non-adiabatic fast solar wind. Based on these results, I tried to apply this model in the magnetosheath, which is even more compressible than the solar wind. This will be the focus of the next and last Chapter of my thesis.

Chapter 6

Role of the compressibility in the planetary magnetosheath.

Contents

In the previous chapter I presented the role of the density fluctuations in the solar wind in modifying the cascade rate in the inertial range. The study revealed major differences between the fast and the more compressible slow wind especially with respect to the contribution of the different flux terms on the energy cascade rate. How does this compare to a much more compressible and more complex medium like the planetary magnetosheaths ? Is the IK phenomenology of the inward and outward propagations still valid in the planetary magnetosheaths ? and many other questions that remain open, that I will investigate in this chapter using the same Kolmogorov-like cases studied with Cluster data in Chapter 4.

6.1 Preliminary observations in the terrestrial magnetosheath

As I explained in Chapter 4, the CAPS/IMS of Cassini instruments present some limitations with respect to the FoV of the ions measurements (see section 4.4.1), which implies higher uncertainties in the measurements. Therefore I performed this preliminary study first in the terrestrial magnetosheath using Cluster 3 spacecraft data before possibly applying it to the Cassini data in the near future.

6.1.1 Data selection

For the sake of obtaining the magnetosheath Cluster data, I used the same Kolmogorov-like statistical events studied in the terrestrial magnetosheath (Section 4.3). In that list of events, I checked those that showed no sharp discontinuities in $\Theta_{\mathbf{VB}}$ and a relatively stationary β. These conditions could be found in the solar wind, however, in the magnetosheath, which is a highly dynamical environment, it was not an easy task to find many events that satisfy these criteria. Similarly to the solar wind case, I selected only the case studies that give a linear scaling, however no filtering was done with respect to the sign of ε_C, since for 70% of the events ε_C were not characterized by a constant sign. Moreover, I used the cases for which the ion and electron densities from HIA and PEACE instruments respectively gave similar values. In total I studied 31 time intervals with a compressible-like magnetic compressibility, C_B ("steady" and the "fall" of Figure 4.26) and 12 case studies with an Alfvénic like C_B ("raise" of Figure 4.26).

The averaged plasma β and flow velocity of the Kolmogorov-like events studied in the Magnetosheath are shown in Figure 6.1.

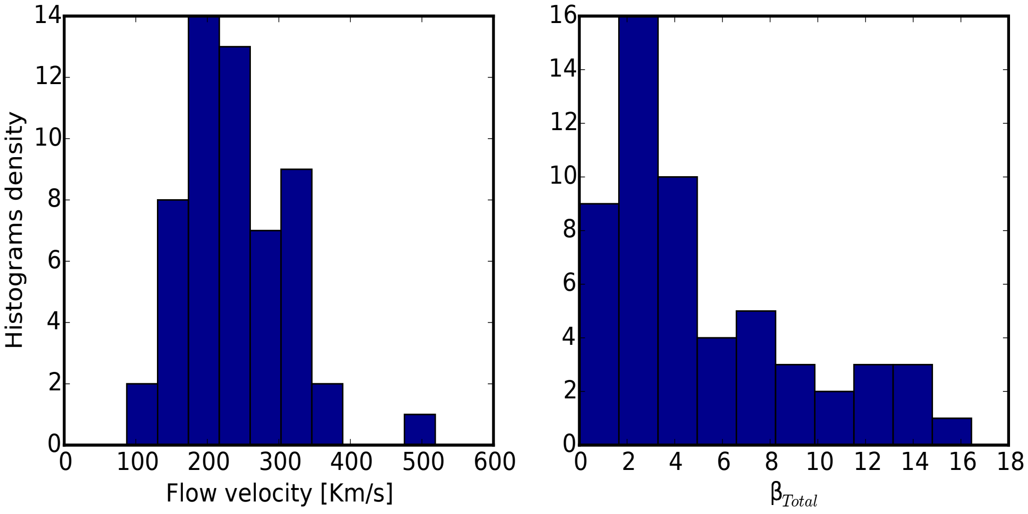

Figure 6.1: Averaged flow velocity and the total plasma beta in the terrestrial magnetosheath.

6.1.2 Scaling properties and the average cascade rates

In this section I will present two particular case studies, with a relatively stationnary β and $\Theta_{\mathbf{VB}}$ (see Figure 6.2). Those events have different wave properties at the MHD scales. The first one in Figure 6.2-(left) is characterized by an $f^{-5/3}$ scaling with an Alfvénic-like magnetic compressibility C_B, and (right) by Kolmogorov scaling but with a magnetosonic-like C_B.

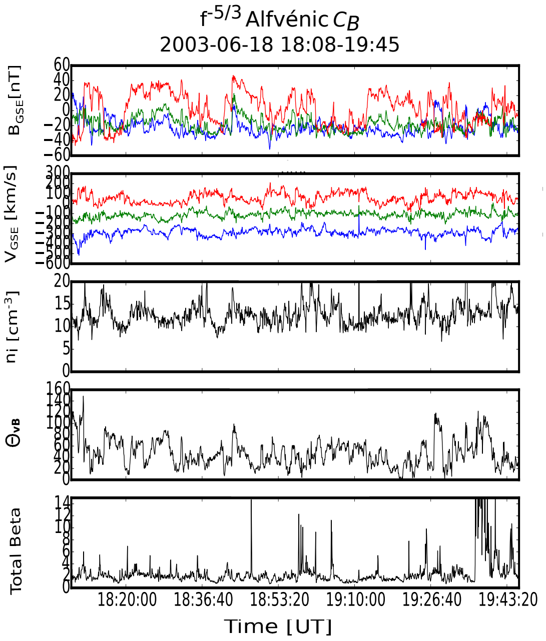

Figure 6.2: Magnetosheaths events for which the inertial range is characterized by (left) an Alfvénic type of the magnetic compressibility and (right) a magnetosonic like one. From top to bottom: magnetic field vector, velocity vector, ion density, propagation angle $\Theta_{\mathbf{VB}}$, and the total plasma beta.

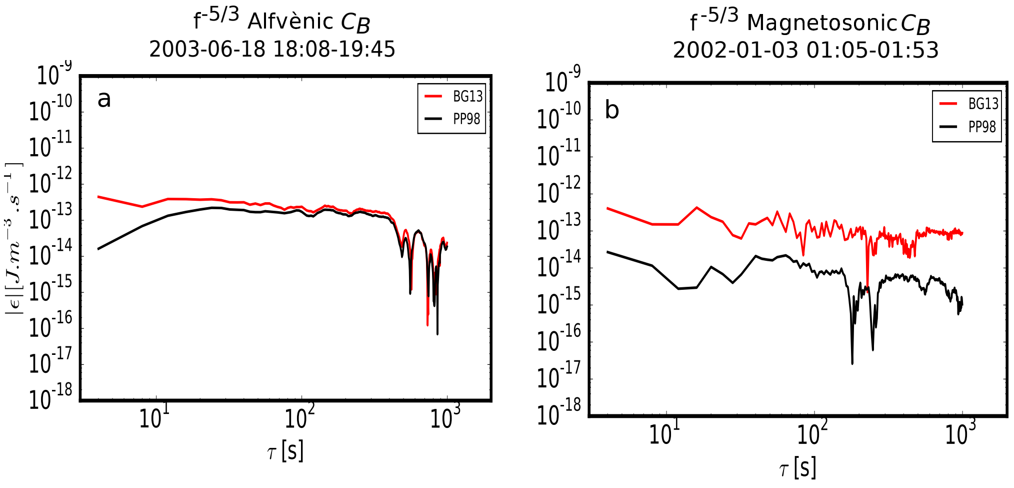

Figure 6.3: (a-b) The energy dissipation rates computed for the two particular events using the isothermal compressible MHD model (BG13), in a comparison with the incompressible model (PP98).

The corresponding energy flux terms and the energy cascade rates for each of them are presented in Figure 6.3. Three observations can be made: First for the Alfvénic like case (a), the "Yaglom term" $\mathcal{F}_1$ dominates over the compressible ones ($\mathcal{F}_3$ and $\mathcal{F}_2$) and overlapp with the incompressible Yaglom term (black). The resulting total energy flux is then similar to the one computed using PP98. However, regarding the compressible case (b), $\mathcal{F}_3$ and the compressible Yaglom type term $\mathcal{F}_1$ dominate over the incompressible Yaglom term. Secondly, the incompressible energy cascade rate in the Alfvénic case (c) gives higher level of $\langle|\varepsilon|\rangle$ compared to the magnetosonic case. Thirdly, compared to the solar wind, $\langle|\varepsilon_C|\rangle$ is three orders of magnitude higher $\sim 10^{-13}$ [J.m^{-3}.s^{-1}].

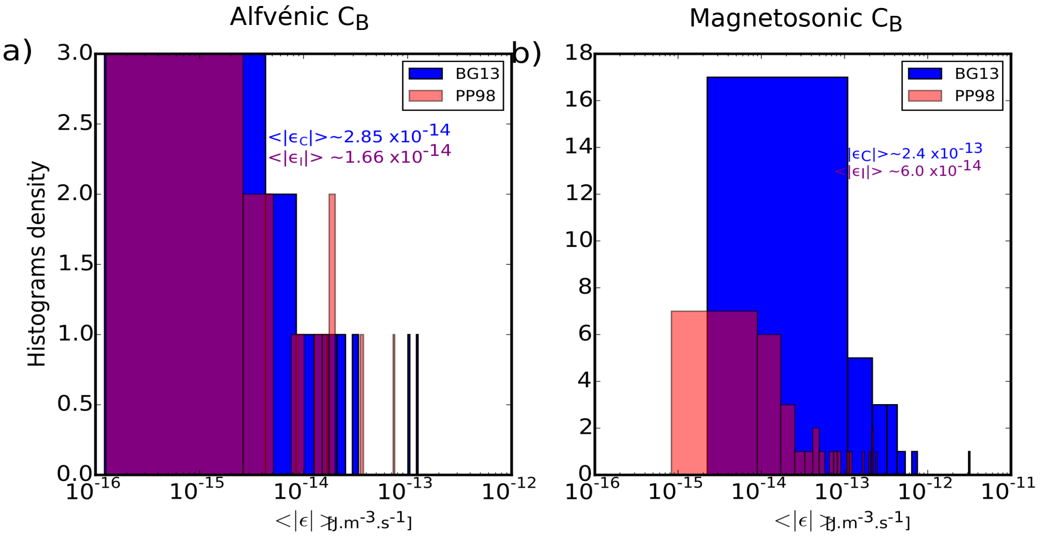

Figure 6.4: Histograms of the averaged values of the compressible energy cascade rate computed using BG13 (blue) compared with the incompressible one calculated using PP98 (red), for two groups of events: (a) showing and Alfvénic-like C_B and (b) a magnetosonic-like C_B.

The histograms in Figure 6.4 summarize the averaged values of the compressible ($\langle|\varepsilon_C|\rangle$, computed using BG13- in pink) and incompressible ($\langle|\varepsilon_I|\rangle$, computed using PP98- in blue) cascade rates for the (a) Alfvénic and the (b) magnetosonic-like events characterized with an inertial range. A major difference can be observed between these two cases: For the Alfvénic-like time intervals, the histograms of $\langle|\varepsilon_C|\rangle$ and $\langle|\varepsilon_I|\rangle$ are almost identical (similarly to the solar wind results) being concentrated within $[10^{-16}, 3\times10^{-15}]$ J.m^{-3}.s^{-1}. Nevertheless, a small shift of the compressible cascade rate towards higher values can be noted. This is reflected in the mean of both hisotograms where $\langle|\varepsilon_C|\rangle \sim 2.85\times10^{-14}$ and $\langle|\varepsilon_I|\rangle \sim 1.66\times10^{-14}$ J.m^{-3}.s^{-1}. Regarding the magnetosonic-like events, the histogram of $\langle|\varepsilon_C|\rangle$ are clearly shifted to higher $\langle|\varepsilon|\rangle$ with respect to $\langle|\varepsilon_I|\rangle$. In this case we have, $\langle|\varepsilon_C|\rangle \sim 2.4\times10^{-13}$ and $\langle|\varepsilon_I|\rangle \sim 6.0\times10^{-14}$ J.m^{-3}.s^{-1}, with one order of magnitude difference between BG13 and PP98. In fact these are the first estimation of ε_C in the magnetosheath turbulence.

6.1.3 Compressibility and the turbulent Mach number ($\mathcal{M}_S$)

Similarly to the study I showed in the solar wind, I plot in Figure 6.5 the compressibility ($\sqrt{(\langle\rho^2\rangle - \langle\rho\rangle^2)/\langle\rho\rangle}$) as a function of $\langle|\varepsilon_C|\rangle$ to highlight the role of the density fluctuations in increasing the compressible cascade rate.

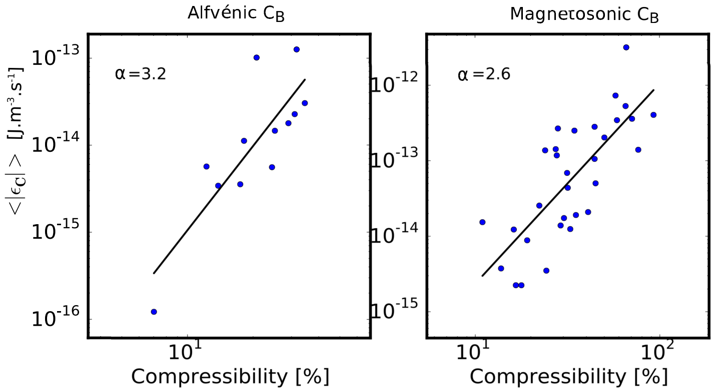

Figure 6.5: Total energy cascade rate as a function of the plasma compressibility for the Alfvénic and the magnetosonic-like events. The black line is a least square fit of the measurements with α the corresponding fitting index.

Moreover, we have seen in the previous chapter (Section 5.2.4), that the turbulent Mach number ($\mathcal{M}_S$) plays an important role (mainly in the more compressible one, slow wind) in increasing the energy cascade rate. To see if this property persists as well in the magnetosheath, I represented those two quantities in Figure 6.6.

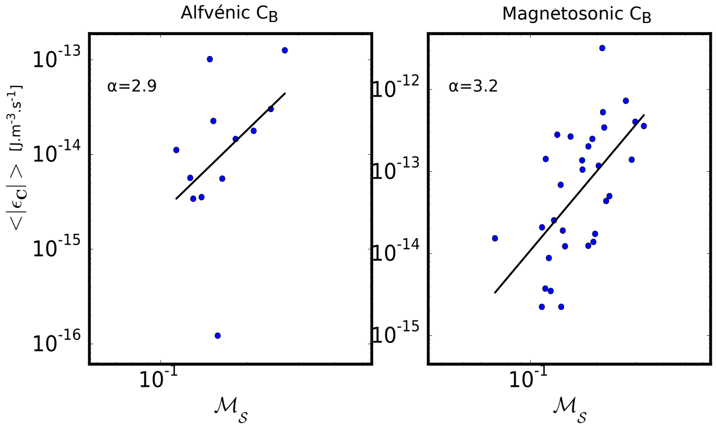

Figure 6.6: Compressible energy cascade rate as a function of the turbulent Mach number for the Alfvénic and the magnetosonic like events. The black line is a least square fit of the measurements with α the corresponding fitting index.

One can see that in the "magnetosonic-like" cases, we obtain a better correlation than the "Alfvénic-like" (less compressible) events. Note that this could be due to the fact that in the latter case we have much less case studies than the former one. Eventually, Figure 6.7 shows that, the compressibility increases, when increasing $\mathcal{M}_S$ for the Alfvénic and magnetosonic like events, on the contrary to the solar wind results (Figure 5.14) where no particular dependence was observed.

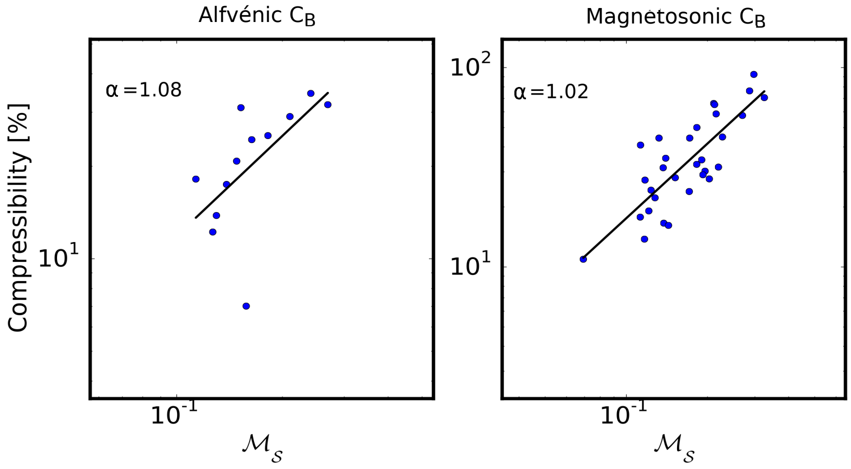

Figure 6.7: Compressibility as a function of the turbulent Mach number for the Alfvénic and the magnetosonic like events. The black line is a least square fit of the measurements with α the corresponding fitting index.

6.1.4 Compressible cascade rate and the compressible energy

The dependence of $|\varepsilon_C|$ on the compressible kinetic, magnetic, internal and total energies (defined in Section 5.2.4), is shown in Figure 6.8. Similarly to the solar wind, higher are the compressible energies, higher is $\langle|\varepsilon_C|\rangle$. However, in the magnetosheath, the averaged total compressible energy (second panel) is more enhanced ($\sim 10^{-10}\,J.m^{-3}$) than the ones in the solar wind ($\sim 10^{-12}\,J.m^{-3}$). Also for each class of the events, the scalings found in the magnetosheath differ from the ones depicted in the solar wind: for the Alfvénic cases we have, $\delta E_M \sim \delta E_K \sim \varepsilon_C^{0.40}$ and $\delta U \sim \varepsilon_C^{0.80}$, and $\delta E_M \sim \delta E_K \sim \varepsilon_C^{0.36}$ and $\delta U \sim \varepsilon_C^{0.62} \sim$ to the Kolmogorov scaling, for the magnetosonic-like cases.

Moreover, one can see that for the Alfvénic cases the dominant contribution comes mainly from the magnetic energy, whereas for the magnetosonic-like events, the internal energy is more enhanced, it is at the same order as the kinetic and the magnetic one, and so it is those three energies (δU, δE_M and δE_K) that conribute to the resulting total energy.

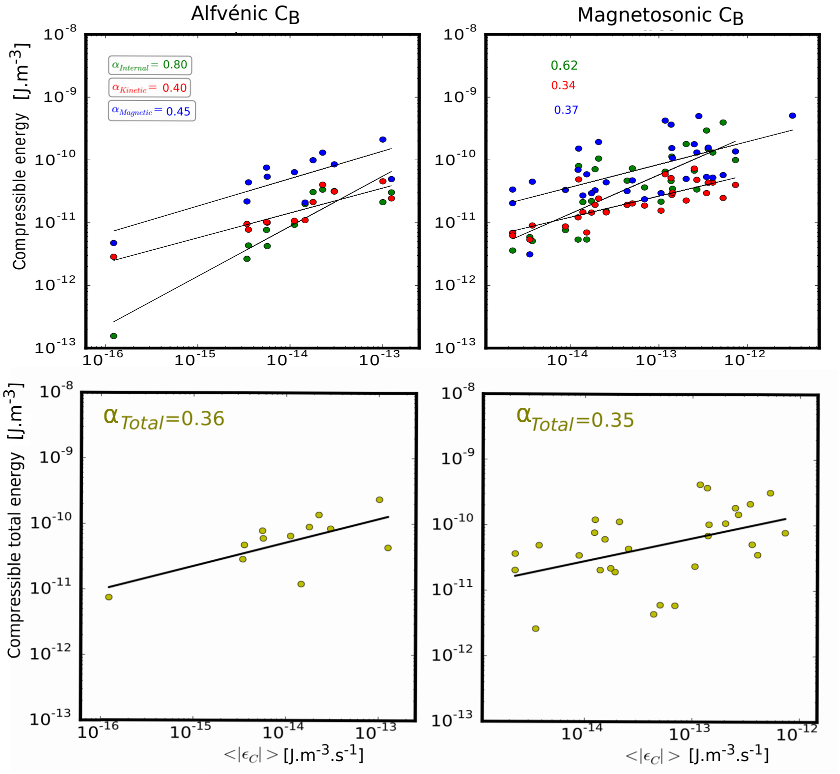

Figure 6.8: First Panel: the magnetic (blue), kinetic (red) and internal (green) energies of the compressible fluctuations in the terrestrial magnetosheath. Second Panel: the total compressible energy, plotted as a function of the compressible energy cascade rate $\langle|\varepsilon_C|\rangle$. The black lines are the least-square-fits with α the corresponding fit coefficient. $\delta E \sim \varepsilon_C^{\alpha} \rightarrow \varepsilon_C \equiv \delta E^{1/\alpha}$.

6.1.5 Role of the different flux terms

To understand the role of the different flux terms ($\langle|\mathcal{F}_1|\rangle$, $\langle|\mathcal{F}_2|\rangle$ and $\langle|\mathcal{F}_3|\rangle$) for each class of the events (Alfvénic and magnetosonic like), Figure 6.9 shows the statistical results of their different contributions with respect to the incompressible flux $\langle|\mathcal{F}_I|\rangle$. Regarding the "magnetosonic-like" cases, similar results to the ones found in the slow wind can be observed, in the sense that for some of the time intervals, $\langle|\mathcal{F}_1|\rangle \sim \langle|\mathcal{F}_I|\rangle$, and it is the compressible terms $\langle|\mathcal{F}_2|\rangle$ and $\langle|\mathcal{F}_3|\rangle$ that contribute to enhance $\langle|\varepsilon_C|\rangle$ with respect to $\langle|\varepsilon_I|\rangle$.

Regarding the "Alfvén-like" case studies, one can see that $\langle|\mathcal{F}_1|\rangle > \langle|\mathcal{F}_I|\rangle$ for most of the events whereas $(\langle|\mathcal{F}_3|\rangle + \langle|\mathcal{F}_2|\rangle)/\langle|\mathcal{F}_1|\rangle < 1$, which means that the compression in those cases come essentially from the "Yaglom" term, $\langle|\mathcal{F}_1|\rangle$. This contrasts with the solar wind observations presented in Chapter 5.

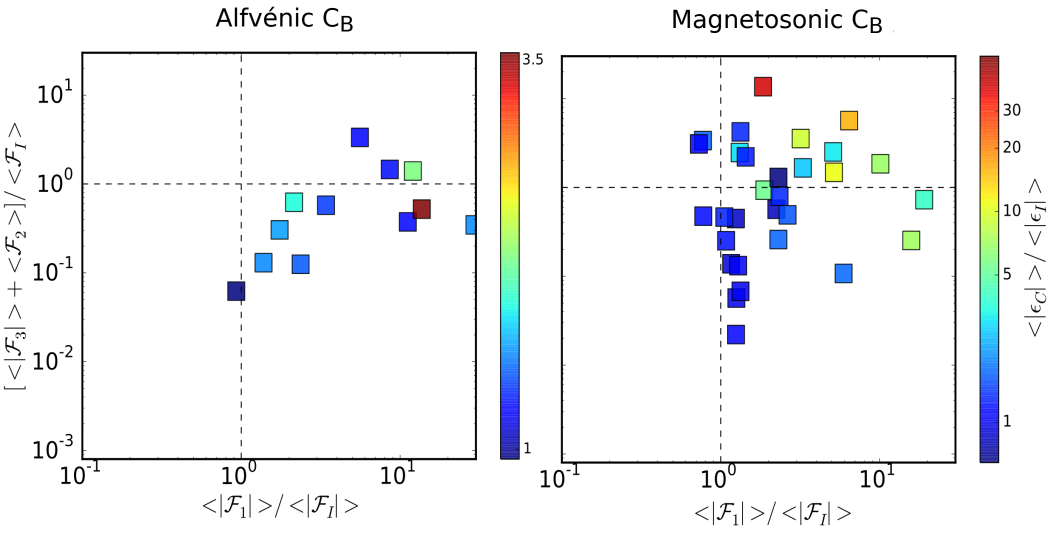

Figure 6.9: Estimation of the contribution of the compressible fluxes w.r.t. incompressible (Yaglom) flux to the compressible cascade rate for the Alfvénic (right) and the magnetosonic-like (left) events as a function of the ratio between the compressible to incompressible energy of the turbulent fluctuations.

6.1.6 Cross-Helicity and inward-outward propagations

In the solar wind, the inertial range can be described by the Iroshnikov-Kraichnan phenomenology by which counter propagating Alfvén wave-packets interact nonlinearly cascading the energy towards the smaller scales. In the previous chapter (Section 5.3.3), I have verified using the normalized cross-helicity (σ_C) that the fast wind is indeed characterized by outward propagating waves anti-parallel to the local magnetic field. In the magnetosheath the outward and inward propagation might be not suitable because the velocity is not radial anymore (the flow is diverted by the bow-shock around the magnetopause). However, it is interesting to see how does the cross-helicity vary with the angles $\Theta_{\mathbf{VB}}$ compared with the solar wind analysis, for the Alfvénic and compressible like events. The results are shown in Figure 6.10. Interestingly, the Alfvénic-like has mainly a negative $\sigma_C \sim -0.4$ and a parallel propagation, which is the characteristic of an inward propagating wave. Whereas for the magnetosonic-like events, the data seem balanced between inward and outward propagation. Note that this difference between the two cases could come from the difference in the number of samples I analyzed. The reason for which this study will be extended to a larger number of data samples.

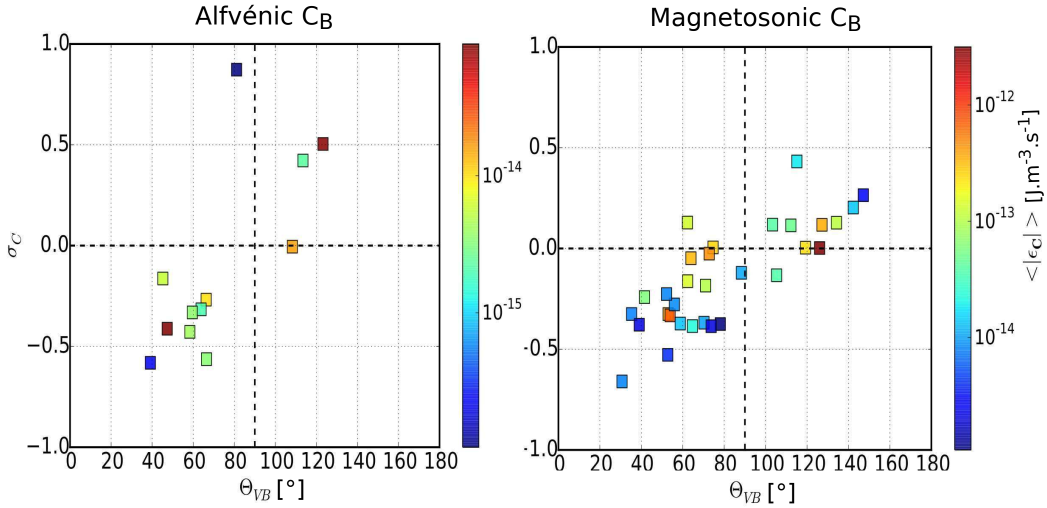

Figure 6.10: Cross-helicity (σ_c) as a function of the propagation angle $\Theta_{\mathbf{VB}}$ for the Alfvénic and the magnetosonic like events.

6.2 Discussions and conclusions

These preliminary results regarding the role of the compressibility in the magnetosheath of Earth give the first estimation of the energy dissipation rate in the magnetosheath. They present some similarities with respect to the solar wind, for instance the role of the compressibility and the Mach number, the contribution of the different flux terms. But also a main difference: the energy dissipation rate is found to be at least two orders of magnitude higher than the one observed in the solar wind (of the order of $\sim 10^{-14}$ compared $\sim 10^{-16}$ in the solar wind).
Moreover, comparing two classes of Kolmogorov-like events, categorized as Alfvénic and magnetosonic-like cases, this study revealed that the "magnetosonic-like" events have a much higher $\langle|\varepsilon_C|\rangle$, similarly to the slow wind, they correlate better with turbulent Mach number and the compressible terms ($\langle|\mathcal{F}_2|\rangle$ and $\langle|\mathcal{F}_3|\rangle$) seem to play the major role in increasing $\langle|\varepsilon_C|\rangle$. Moreover, from the cross-helicity analysis, those events were shown to be balanced between inward and outward propagation. Whereas for the Alfvénic-like events, I have found that it is mainly the Yaglom term $\langle|\mathcal{F}_1|\rangle$ that amplifies the resulting energy cascade rate for the cases when $\langle|\varepsilon_C|\rangle > \langle|\varepsilon_I|\rangle$ (some cases were found to have $\langle|\varepsilon_C|\rangle \sim \langle|\varepsilon_I|\rangle$). In addition to that and interestingly, the "Alfvénic" cases showed a similar dependence of the cross-helicity on $\Theta_{\mathbf{VB}}$ to the one depicted in the fast solar wind with a concentration of the events in the "inward propagation". However, these results need to be confirmed on a larger statistical sample that would include the magnetosheath of Saturn.
All the results obtained in this thesis using the BG13 model need to be considered within the limitations inherent to the two major approximations used. First, until now we have neglected the source terms (Appendix A) since a reliable evaluation of

local velocity divergences is not possible using single spacecraft data. This assumption is based on the fact that the source terms are only important for supersonic turbulence, as it has been shown by Kritsuk *et al.* [2013]; Servidio [2015], whereas the solar wind turbulence is subsonic. A reliable estimation of the sources terms w.r.t. flux terms will be done using numerical simulations of 3D compressible MHD turbulence in the isothermal limit. This is the part of the project of a post-doc, Nahuel Andrés, recently arrived to LPP. The results are expected for the next upcoming months. I expect to participate in this project by analyzing the data of the numerical simulations. The second limitation is related to the isothermal closure equation used. While all fluid-like closures, can be questioned when applied to collisionless media such as the solar wind or the planetary magnetosheaths, a generalization of the BG13 to a polytropic closure, as it was done for the case of hydrodynamic turbulence [Banerjee & Galtier, 2013], will make the model more realistic to describe low frequency turbulence in those media. It is however clear that a more realistic closures that would include kinetic effects such as the Landau damping are needed [Passot & Henri, 2007], even if such a derivation of exact analytical models for those closures remain a difficult task and so far out of reach.

CHAPTER 7

Summarizing ...

Contents

7.1 Answered and unanswered questions

Through the course of my thesis I have aimed to obtain a better and more critical understanding regarding the role of the compressible fluctuations in the planetary magnetosheaths and how they affect the turbulence properties compared to the solar wind. It was based on in-situ observations using Cassini, THEMIS B/ARTHEMIS P1 and Cluster spacecraft particles and fields data. I would like to note that I spent a non negligible time in selecting one by one each event I studied using Cassini and THEMIS data verifying all the requirements needed before performing the statistical studies.

I started my thesis work by investigating the properties of the turbulent fluctuations in the Kronian magnetosheath using Cassini spacecraft data and compared them to the ones observed at the Earth magnetosheath (Chapter 4). The main questions that I tried to answer for this part were the following:

- *What are the scaling laws of the magnetosheath turbulence at MHD and kinetic scales ? Are they "universal" or do they depend on the local (or distant) plasma conditions ?*

Using ~ 400 events in different locations within the Kronian magnetosheath, I have showed different spectral properties of the turbulent fluctuations at the MHD and kinetic (sub-ion) scales. At the MHD scales, turbulence did not seem to be "universal". It actually depends on the geometry of the shock and the location within the magnetosheath, or in other words, to the distance with respect to the boundaries of the magnetosheath, the bow-shock and the magnetospause. Closer to the bow-shock, the spectra did not show any inertial range, with slope values ~ -1 behind a quasi-perpendicular shock, and shallower ones ~ -0.5 behind a quasi-parallel shock. The Kolmogorov law appeared to be present towards the flanks and closer to the magnetopause. Regarding the kinetic scales, the spectral properties seemed to be more "universal". The study showed no dependence on the structure of the shock, neither on the location within the magnetosheath. In the sub-solar region and in the flanks, behind a quasi-parallel and perpendicular bow-shock, the slopes $\in [-2.2, -3.0]$, similarly to the solar wind. In order to have a better understanding regarding the two regimes, I performed a study using higher order statistics. The PDFs of the magnetic field increments, and the scaling exponents of the structure functions, revealed, the random nature of the turbulence at the MHD scales. At the sub-ion scales, the fluctuations behind a quasi-perpendicular bow-shock were monofractal, and behind a quasi-parallel bow-shock, the fluctuations were multifractal. In a collaborative work with Shiyong Huang, we have done a much larger survey $\sim$ 1600 events, that covers all the terrestrial magnetosheath using Cluster 3 spacecraft. This statistical work confirmed the results observed in the magnetosheath of Saturn: at MHD scales, the dominance of the f^{-1} spectra closer to the shock and in the subsolar regions, and the presence of the $f^{-5/3}$ only closer to the magnetopause and the flank regions. The origin of the f^{-1} power law and its transition to form the $f^{-5/3}$ Kolmogorov-law in the solar wind, are still a matter of debate and are thought to be related to Alfvén waves reflections and interactions inside the solar corona that drives the turbulence. In the magnetosheaths, it is the bow-shock that takes the role of driving the turbulence and injecting the energy. Hence the fully developed turbulence in the solar wind, encountering the shock, will be "reset" to zero and all the correlations will be destroyed resulting in a random like turbulence. Turbulence then needs "some time" to develop and so an inertial range is formed only when the correlation time of turbulence is much larger than the local ion time scale.

Despite the different plasma parameters in both regions, and apart from the positive slopes observed in the magnetosheath of Saturn, this work shows that the properties of turbulence are the same in the terrestrial and the kronian magnetosheath, however they differ from the MHD to the sub-ion scales.

- *What is the nature of the plasma fluctuations (Alfvénic ? magnetosonic ?) that carry the energy cascade from the MHD to the sub-ion scales in the magnetosheath ? How do they compare with the solar wind ?*

Other than the spectral properties, I have identified the different types of the fluctuations in the magnetosheath of Saturn for the f^{-1} events and Earth for the $f^{-5/3}$ events. To do that I computed the magnetic compressibility C_B and compared it to the theoretical kinetic Maxwell-Vlasov solutions and the compressible Hall-MHD ones. This comparison in the Kronian magnetosheath showed that for the time intervals with an absence of the inertial range, the MHD and the sub-ion scales are dominated by magnetosonic-like modes ($C_B > 1/3$ and is relatively uniform). The anti-correlation between $\delta B_\parallel$ and δB_n could distinguish between the fast and the slow modes, and confirmed the dominance of the slow/mirror ones.

Going back to Earth, the results of the Kolmogorov-like events, revealed three different profiles of the magnetic compressibilities: an "Alfvénic-like rising" profile, and a "compressible-like falling and steady" ones. Interestingly, this study evidenced the existence of turbulent fluctuations that have an inertial range, but in which the cascade is not populated by Alfvénic fluctuations, or those incompressible waves are present but play a minor role in the inertial range. These results indicate that one has to go beyond incompressible MHD theory to describe the turbulent properties in the planetary magnetosheaths. The importance of the compressible fluctuations observed in this first chapter of my research work, and the derivation of the exact law for compressible isothermal MHD (BG13) turbulence by Banerjee & Galtier [2013], motivated me to apply this model in the solar wind and the magnetosheath and to anwser the following questions:

- *What is the role of the compressibe fluctuations in the solar wind and magnetosheath ? How do they affect the cascade (dissipation) rate ? Do they influence the spatial anisotropy of the turbulence ? How do they depend of the Mach number ? Is the Iroshnikov-Kraichnan phenomenology applicable in compressible MHD turbulence or a new phenomenology is needed to characterize the energy cascade ?*

Chapter 5, consists of the second part of my research work in which I studied the role that the compressibility plays in turbulence by applying the exact compressible isothermal model first in the slow and the fast solar wind. In fact, this had allowed me to compare the application of the model with the previous exact incompressible MHD one (PP98) that was applied in the solar wind as well.
Using a list of 330 time intervals from THEMIS B/ARTEMIS P1 spacecraft, a turbulent energy cascade was obtained over two decades of scales for both wind speeds which was broader than the ones estimated from PP98. A term-by-term analysis of the compressible model revealed new insights into the role played by the density fluctuations, interestingly for few events, the compressible energy cascade rate $|\varepsilon_C|$ were amplified with respect to the incompressible one $|\varepsilon_I|$. Moreover, this study showed the role of the turbulent Mach number rather than the compressibility in increasing $|\varepsilon_C|$, and confirmed previous results regarding the inverse cascade nature of turbulence in the fast wind being dominated by outward propagating waves. Eventually, the compressible fluctuations were shown to affect the spatial anisotropy of the turbulence. $|\varepsilon_C|$ was higher for a perpendicular $\Theta_{\mathbf{VB}}$ than a parallel one, and mainly for the fast wind, compressibility isotropized "a bit" the cascade rate.

The last chapter of my thesis results, is Chapter 6, and present for the first time, preliminary results regarding the role of the compressbility in a much more complex and compressible medium than the solar wind, the planetary magnetosheaths. Using Cluster data, for only few ($\sim$ 40) time intervals from the Kolmogorov-like events in the terrestrial magnetosheath, I showed first, a higher level of the energy dissipation rate compared to the solar wind, but also an interesting difference between the Alfvénic-like and the magnetosonic-like case studies. In fact, the Alfvénic-like events, were more similar to the fast wind ($|\varepsilon_C| \sim |\varepsilon_I|$) whereas for the compressible-like events $|\varepsilon_C| \gg |\varepsilon_I|$ similarly to the slow wind results. The turbulent Mach number

was shown to play an important role in increasing the compressible energy dissipation rate.
This work has led to six publications, four either published or submitted:

- L. Z. Hadid et al. (2015). "Nature of the MHD and Kinetic Scale Turbulence in the Magnetosheath of Saturn: Cassini Observations." ApJL, Volume 813, Number 2.
- S. Banerjee, and L. Z. Hadid, et al. (2016). "Scaling of compressible magnetohydrodynamic turbulence in the fast solar wind." ApJL, Volume 829, Number 2.
- L. Z. Hadid, et al. (2016). "Energy cascade rate in compressible fast and slow solar wind turbulence." ApJ, under revision.
- S. Y. Huang and L. Z. Hadid, et al. (2016). "On the Existence of the Kolmogorov Inertial Range in Terrestrial Magnetosheath Turbulence." ApJL, submitted.

and two others that are under preparation:

- L. Z. Hadid, et al. "Estimation of the energy cascade rate in the planetary magnetosheaths", in preparation.
- L. Z. Hadid, et al. "High frequency turbulent fluctuations in the Kronian magnetosheath", in preparation.

7.2 Outlook on prospective work

The study presented in my thesis, although starting from very simple and basic ideas of the solar wind turbulence properties (scaling laws, propagation modes), it has provided insight into the potential of the schemes studied as well as highlighting older pending problems. I will conclude this thesis with a brief summary of some suggestions for future work.

1. The first thing I plan to do is to continue the work I have started regarding the role of the compressible fluctuations in the magnetosheath of Earth, but on a much larger statistical events from Cluster data. I will separate the events as well with respect to the geometry of the shock (quasi-parallel vs quasi-perpendicular) and the location within the magnetosheath to check if these two factors affect the energy cascade rate. Eventually I will try to see if it is possible to apply this model in the Kronian magnetosheath, for few cases for which I can re-estimate accurately the ion velocity.

2. I will test as well the simplified scaling law obtained by Banerjee & Galtier [2013] in the presence of a strong (w.r.t. the fluctuations) magnetic field and compare it with the results obtained in the solar of when $\Theta_{\mathbf{VB}} \sim 90°$.

3. Using MMS data, I am willing to study the magnetic field fluctuations and the possible wave modes at the kinetic scales, to see if they are magnetosonic or Alfvénic-like.

4. During my work with Cassini data, I have selected some case studies in the solar wind at 10 AU. where the magnetic field fluctuations are higher than the estimated sensitivity level of FGM. I plan to study those cases, in addition to other ones in the solar wind at 0.5 AU (around Mercury), to see how do the turbulence properties evolve with the radial distance, but also how do they compare to the properties of the solar wind at 1 AU.

5. In chapter 4, we did a survey of the slopes values at MHD scales in the terrestrial magnetosheath using Cluster data. The Kolmogorov scaling law appeared to be near the flanks and closer to the magnetopause. However I haven't done a higher order statistical study with respect to the terrestrial bow-shock geometry. It would be interesting to see if the results will be similar as well to the Kronian magnetosheath. I showed as well in Section 4.4.1 the difficulty in using the Matlab code for recalculating the ion velocities of CAPS. It shouldn't be difficult to re-write the code on Pyton, so it will be much faster and easier to use.

6. Eventually, I would like to do a theoretical work by trying to derive the MHD counter part of the exact compressible polytropic hydrodyanmical, noting that the derivation is much more complicated than the isothermal case since the sound speed is no longer a constant and the plasma pressure is no longer linear to the plasma density.

APPENDIX A

Exact law of compressible isothermal MHD: Source terms

The compressible flux term used in my thesis was just a part of the total flux term obtained for compressible MHD turbulence. I recall the origin exact relation for compressible MHD turbulence in an isothermal plasma in the following:

$$\begin{aligned}
-2\varepsilon = {} & \frac{1}{2}\nabla_{\boldsymbol{\ell}} \cdot \left\langle \left[\frac{1}{2}\delta(\rho\mathbf{z}^{\pm}) \cdot \delta\mathbf{z}^{\pm} + \delta\rho\delta e\right] \delta\mathbf{z}^{\pm} + \left[\frac{1}{2}\delta(\rho\mathbf{z}^{\pm}) \cdot \delta\mathbf{z}^{\pm} + \delta\rho\delta e\right] \delta\mathbf{z}^{\pm} + \overline{\delta}(e + \frac{v_A^2}{2})\delta(\rho\mathbf{z}^{\pm} + \rho\mathbf{z}^{\pm}) \right\rangle \\
& - \frac{1}{4}\left\langle \frac{1}{\beta'}\nabla' \cdot (\rho\mathbf{z}^{\pm}e') + \frac{1}{\beta}\nabla \cdot (\rho'\mathbf{z}^{\pm\prime}e) + \frac{1}{\beta'}\nabla' \cdot (\rho\mathbf{z}^{\pm}e') + \frac{1}{\beta}\nabla \cdot (\rho'\mathbf{z}^{\pm\prime}e) \right\rangle \\
& + (\nabla \cdot \mathbf{v})\left\langle \left[R_E' - E' - \frac{\overline{\delta}\rho}{2}(\mathbf{v_A}' \cdot \mathbf{v_A}) - \frac{P'}{2} + \frac{P_M'}{2}\right] \right\rangle + \left\langle (\nabla' \cdot \mathbf{v}') \left[R_E - E - \frac{\overline{\delta}\rho}{2}(\mathbf{v_A} \cdot \mathbf{v_A}') - \frac{P}{2} + \frac{P_M}{2}\right] \right\rangle \\
& + \left\langle (\nabla \cdot \mathbf{v_A}) \left[R_H - R_H' + H' - \overline{\delta}\rho(\mathbf{v}' \cdot \mathbf{v_A})\right] \right\rangle + \left\langle (\nabla' \cdot \mathbf{v_A}') \left[R_H' - R_H + H - \overline{\delta}\rho(\mathbf{v} \cdot \mathbf{v_A}')\right] \right\rangle
\end{aligned}$$

The first two lines represent the flux terms whereas the following two lines consist of the source terms, where the unprimed quantities represent the properties at the point $\mathbf{x}$ and the primed quantities correspond to the point $\mathbf{x}'$ (with $\mathbf{x}' = \mathbf{x} + \mathbf{r}$). E and H are respectively the energy density and the cross-helicity density, written as:

$$\begin{aligned}
E(x) &= \frac{\rho}{2}(\mathbf{v} \cdot \mathbf{v} + \mathbf{v_A} \cdot \mathbf{v_A}) + \rho e \\
H(x) &= \rho\mathbf{v} \cdot \mathbf{v_A}
\end{aligned} \tag{A.1}$$

R_E and R_H are the two-point correlation functions associated to the total energy and the compressible cross- helicity density respectively:

$$\begin{aligned}
R_E(x) &= \frac{\rho}{2}(\mathbf{v} \cdot \mathbf{v}' + \mathbf{v_A} \cdot \mathbf{v_A}') + \rho e' \\
H(x) &= \frac{\rho}{2}(\mathbf{v} \cdot \mathbf{v_A}' + \mathbf{v_A} \cdot \mathbf{v}')
\end{aligned} \tag{A.2}$$

Appendix B

Cassini magnetosheath events

This list of events will be published on AMDA platform.

2004-06-27T09:48:23	2004-06-27T10:28:00
2004-06-27T18:16:56	2004-06-27T19:48:03
2004-06-28T00:30:57	2004-06-28T02:40:42
2004-06-28T07:39:56	2004-06-28T13:45:47
2004-10-25T06:16:42	2004-10-25T06:47:42
2004-10-25T12:48:50	2004-10-25T14:40:29
2004-10-25T16:02:34	2004-10-25T23:59:59
2004-11-03T15:22:32	2004-11-03T17:27:13
2004-11-04T19:06:15	2004-11-04T21:35:51
2004-12-12T01:01:45	2004-12-12T04:00:00
2004-12-12T09:58:40	2004-12-12T15:55:43
2004-12-23T00:24:02	2004-12-23T07:18:24
2004-12-23T13:34:44	2004-12-23T17:16:55
2005-01-04T06:08:46	2005-01-04T08:11:34
2005-01-23T20:45:01	2005-01-23T22:08:00
2005-01-24T00:20:38	2005-01-24T02:40:49
2005-02-23T20:01:39	2005-02-23T21:46:04
2005-03-05T16:46:42	2005-03-05T17:00:00
2005-03-05T19:02:02	2005-03-05T20:44:35
2005-03-06T03:05:20	2005-03-06T12:53:45
2005-03-14T07:05:27	2005-03-14T12:38:24
2005-03-14T14:17:44	2005-03-14T16:13:27
2005-03-14T22:58:47	2005-03-14T23:43:56
2005-03-15T17:52:17	2005-03-15T20:03:18
2005-03-15T20:41:26	2005-03-15T23:25:55
2005-03-16T02:57:52	2005-03-16T06:31:47
2005-03-17T02:06:04	2005-03-17T08:22:23
2005-03-19T00:01:34	2005-03-19T02:09:44
2005-03-19T08:39:54	2005-03-19T19:02:31
2005-03-19T20:01:04	2005-03-19T21:01:45
2005-03-20T00:08:11	2005-03-20T01:57:25
2005-03-25T05:28:47	2005-03-25T12:10:00
2005-03-27T05:57:57	2005-03-27T06:28:40
2005-03-27T12:27:49	2005-03-27T17:59:33

2005-04-11T09:08:47	2005-04-11T23:45:31
2005-04-12T04:02:15	2005-04-12T10:04:03
2005-04-19T22:29:54	2005-04-19T23:24:06
2005-04-20T01:33:25	2005-04-20T05:07:29
2005-04-20T20:18:06	2005-04-21T01:09:27
2005-04-21T09:04:10	2005-04-21T10:35:09
2005-04-24T04:38:32	2005-04-24T05:30:00
2005-04-30T13:32:36	2005-05-01T00:02:36
2005-05-07T05:04:15	2005-05-07T07:00:39
2005-05-09T11:22:21	2005-05-09T19:10:18
2005-05-17T05:13:39	2005-05-17T09:09:14
2005-05-17T09:58:02	2005-05-17T19:23:25
2005-05-25T05:02:16	2005-05-25T07:16:12
2005-05-25T13:56:11	2005-05-25T16:38:10
2005-05-27T05:31:58	2005-05-27T15:54:51
2005-05-27T16:30:26	2005-05-27T23:50:53
2005-06-23T05:40:09	2005-06-23T06:29:55
2005-06-23T12:44:07	2005-06-23T13:59:18
2005-06-23T17:47:43	2005-06-23T19:30:45
2005-06-24T12:08:04	2005-06-24T15:17:59
2005-07-02T18:25:24	2005-07-02T20:16:43
2005-07-10T18:48:21	2005-07-11T03:52:26
2005-07-11T11:38:41	2005-07-11T14:13:26
2005-07-11T19:14:05	2005-07-11T21:04:41
2005-07-11T21:09:11	2005-07-11T23:03:38
2005-07-29T00:51:40	2005-07-29T14:11:38
2005-07-29T22:11:50	2005-07-30T08:54:30
2005-08-08T09:21:11	2005-08-08T12:54:28
2005-08-08T16:07:43	2005-08-08T18:51:47
2005-08-28T08:09:59	2005-08-28T09:30:57
2005-08-28T13:37:26	2005-08-28T16:15:53
2005-08-28T15:25:55	2005-08-29T02:09:53
2005-08-29T04:37:54	2005-08-29T09:31:19
2005-08-30T22:14:07	2005-08-31T03:41:30
2005-08-31T05:13:50	2005-08-31T16:17:01
2005-09-12T06:51:54	2005-09-12T09:10:41
2005-10-06T19:15:47	2005-10-07T08:48:17
2005-10-09T01:23:26	2005-10-09T07:47:59
2005-10-19T01:35:22	2005-10-19T12:10:25
2005-10-20T04:36:29	2005-10-20T12:24:20
2005-10-20T23:44:11	2005-10-21T02:17:33
2005-10-21T07:24:49	2005-10-21T09:30:19
2005-10-26T12:21:03	2005-10-26T13:44:57
2005-11-03T22:24:15	2005-11-04T00:46:10

2005-11-09T07:59:48	2005-11-09T11:10:48
2005-11-09T18:22:24	2005-11-10T09:51:37
2005-11-19T15:49:27	2005-11-19T16:55:21
2005-11-20T06:05:11	2005-11-20T07:46:41
2005-12-01T23:54:59	2005-12-02T02:17:39
2005-12-02T15:59:44	2005-12-02T17:27:00
2005-12-16T17:55:50	2005-12-16T20:31:17
2005-12-17T13:09:33	2005-12-17T14:18:54
2005-12-19T20:22:34	2005-12-20T08:23:11
2005-12-31T06:16:42	2005-12-31T09:29:30
2006-01-08T13:03:01	2006-01-08T15:50:14
2006-01-31T01:11:44	2006-01-31T03:58:57
2006-02-03T02:37:41	2006-02-03T05:24:53
2006-02-03T19:49:51	2006-02-03T21:14:18
2006-02-06T10:10:45	2006-02-06T22:36:11
2006-02-08T13:45:58	2006-02-08T16:03:30
2006-02-17T20:36:32	2006-02-17T23:59:56
2006-02-18T00:00:00	2006-02-18T23:59:00
2006-02-19T00:00:00	2006-02-19T02:59:56
2006-03-12T16:11:03	2006-03-12T18:54:16
2006-03-12T21:35:48	2006-03-12T23:40:38
2006-03-13T02:30:06	2006-03-13T04:46:26
2006-03-13T13:44:27	2006-03-13T15:03:05
2006-03-13T21:10:08	2006-03-13T22:27:56
2006-03-15T20:31:44	2006-03-15T23:16:18
2007-03-12T01:04:33	2007-03-12T03:58:56
2007-03-12T15:22:36	2007-03-12T17:37:31
2007-03-13T13:17:35	2007-03-13T15:43:38
2007-03-14T04:00:54	2007-03-14T09:01:59
2007-03-14T09:48:36	2007-03-14T23:43:06
2007-03-15T01:01:06	2007-03-15T05:08:55
2007-04-02T08:09:21	2007-04-02T10:37:55
2007-04-27T10:42:10	2007-04-27T15:24:31
2007-04-27T12:03:45	2007-04-27T15:30:11
2007-04-27T17:12:15	2007-04-27T19:02:17
2007-04-27T17:20:19	2007-04-27T18:45:39
2007-04-27T20:22:16	2007-04-27T22:36:49
2007-04-27T20:35:47	2007-04-27T22:48:45
2007-04-28T00:14:39	2007-04-28T01:09:39
2007-04-28T13:13:30	2007-04-28T20:46:35
2007-04-28T13:26:01	2007-04-28T20:42:04
2007-05-04T13:48:38	2007-05-04T16:30:59
2007-05-04T16:39:28	2007-05-04T18:36:04
2007-05-06T11:22:40	2007-05-06T13:15:43

2007-05-06T20:43:51	2007-05-06T21:42:34
2007-05-07T11:57:10	2007-05-07T12:45:06
2007-05-15T02:05:08	2007-05-15T04:52:01
2007-05-20T17:40:53	2007-05-20T18:45:00
2007-05-22T17:54:53	2007-05-22T22:15:43
2007-05-23T04:04:22	2007-05-23T06:48:22
2007-05-23T20:00:20	2007-05-23T21:20:04
2007-05-30T11:43:03	2007-05-30T12:54:10
2007-06-01T19:09:11	2007-06-01T21:44:14
2007-06-02T17:45:26	2007-06-02T23:19:31
2007-06-03T16:44:23	2007-06-03T20:23:59
2007-06-06T16:09:51	2007-06-06T17:27:39
2007-06-07T02:12:25	2007-06-07T05:26:29
2007-06-14T03:23:08	2007-06-14T06:05:05
2007-06-14T09:11:00	2007-06-14T12:30:43
2007-06-14T14:24:28	2007-06-14T17:42:06
2007-12-27T19:47:17	2007-12-27T23:51:54
2007-12-28T05:41:31	2007-12-28T15:10:49
2008-02-10T20:53:34	2008-02-10T23:59:59
2008-02-11T04:51:31	2008-02-11T09:46:57
2008-02-15T00:57:13	2008-02-15T02:48:29
2008-02-15T03:17:56	2008-02-15T04:58:34
2008-02-16T08:56:39	2008-02-16T23:00:59
2011-04-07T11:06:05	2011-04-07T13:56:58
2011-04-08T04:05:50	2011-04-08T09:43:37
2011-10-04T00:29:29	2011-10-04T04:34:06
2011-10-04T11:41:57	2011-10-04T12:13:59
2011-10-04T13:21:29	2011-10-04T15:19:22
2011-10-04T21:47:31	2011-10-04T22:26:50
2011-10-05T00:10:01	2011-10-05T05:51:59
2011-11-19T02:29:09	2011-11-19T05:20:23
2011-11-19T10:51:30	2011-11-19T23:51:10
2011-12-06T20:43:06	2011-12-06T23:59:59
2011-12-07T00:00:58	2011-12-07T08:50:58
2011-12-07T11:13:20	2011-12-07T23:53:42
2011-12-29T14:37:53	2011-12-29T23:59:30
2012-01-22T21:13:59	2012-01-22T23:59:59
2012-01-23T00:00:38	2012-01-23T05:48:38
2012-01-23T13:52:48	2012-01-23T20:55:06
2012-02-24T07:45:06	2012-02-24T08:46:18
2012-03-04T05:39:19	2012-03-04T17:04:59
2012-07-02T06:20:52	2012-07-02T08:31:34
2012-07-02T22:37:57	2012-07-02T23:59:59
2012-08-16T00:01:40	2012-08-16T06:36:32

2012-09-14T09:14:18	2012-09-14T13:15:46
2012-09-14T21:24:41	2012-09-14T23:23:18
2012-09-15T00:00:18	2012-09-15T02:23:18
2012-09-15T05:03:17	2012-09-15T09:45:04
2014-02-22T05:50:55	2014-02-22T08:58:04
2014-02-22T13:46:40	2014-02-22T21:44:52
2014-02-23T00:21:18	2014-02-23T07:01:17
2014-02-23T08:09:24	2014-02-23T11:08:47
2014-02-23T13:57:39	2014-02-23T17:32:08
2014-03-22T08:19:27	2014-03-22T09:56:08
2014-03-22T11:11:50	2014-03-22T23:59:07
2014-03-23T00:00:07	2014-03-23T04:28:07
2014-05-11T19:55:27	2014-05-11T23:55:09
2014-05-12T02:17:57	2014-05-12T05:09:17
2014-05-12T08:10:53	2014-05-12T16:54:09
2014-05-26T21:52:29	2014-05-26T23:59:05
2014-05-27T07:07:52	2014-05-27T10:51:00
2014-05-27T16:40:33	2014-05-27T23:55:51
2014-05-28T00:00:00	2014-05-28T02:55:51
2005-04-18T17:17:40	2005-04-18T21:40:42
2005-04-18T09:49:14	2005-04-18T13:56:11
2005-09-03T02:08:14	2005-09-03T11:47:57
2005-09-21T15:53:36	2005-09-03T17:19:02
2005-10-16T07:46:10	2005-10-16T11:06:14
2005-10-09T19:41:00	2005-10-09T21:53:08

APPENDIX C

Cassini SCM calibration report

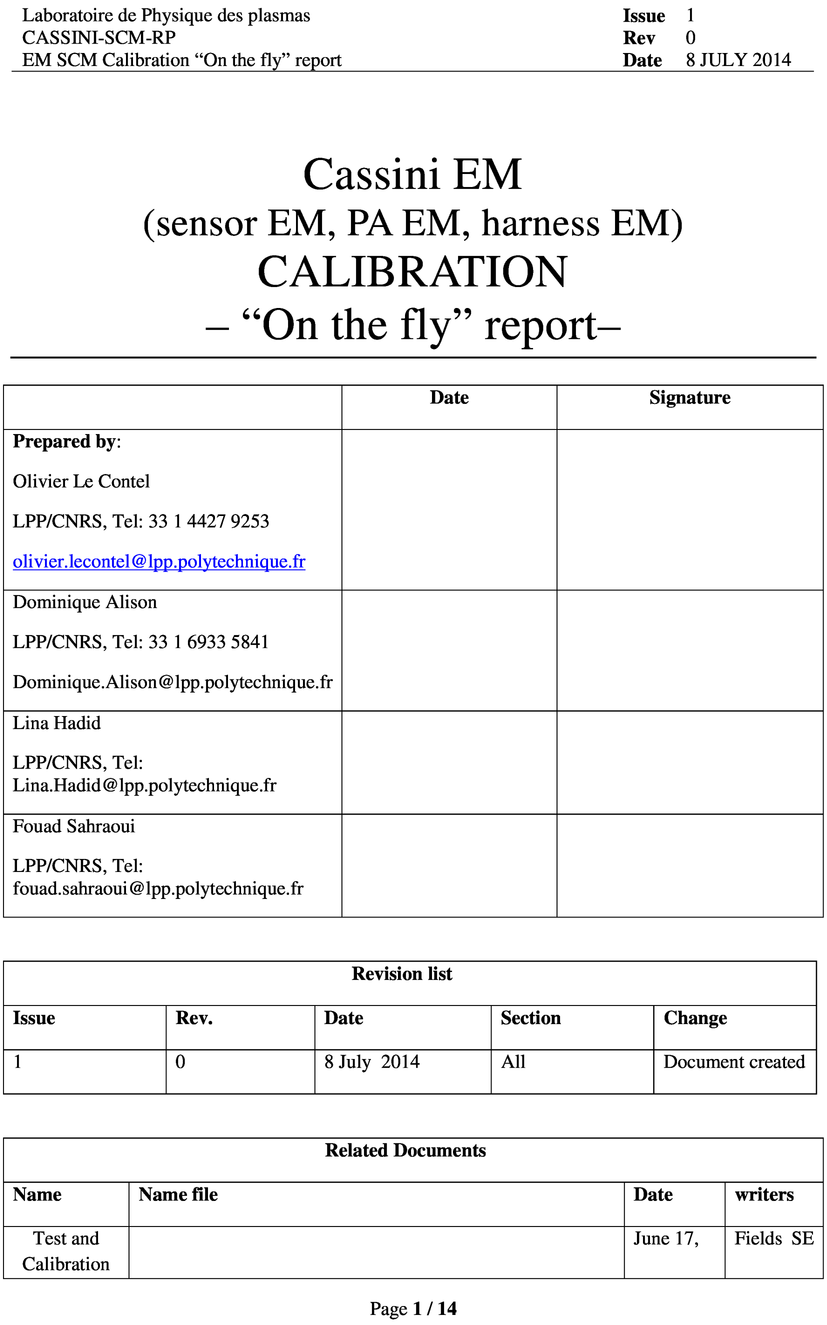

Cassini EM
(sensor EM, PA EM, harness EM)
CALIBRATION
– "On the fly" report–

	Date	**Signature**
Prepared by: Olivier Le Contel LPP/CNRS, Tel: 33 1 4427 9253 olivier.lecontel@lpp.polytechnique.fr		
Dominique Alison LPP/CNRS, Tel: 33 1 6933 5841 Dominique.Alison@lpp.polytechnique.fr		
Lina Hadid LPP/CNRS, Tel: Lina.Hadid@lpp.polytechnique.fr		
Fouad Sahraoui LPP/CNRS, Tel: fouad.sahraoui@lpp.polytechnique.fr		

Revision list

Issue	**Rev.**	**Date**	**Section**	**Change**
1	0	8 July 2014	All	Document created

Related Documents

Name	**Name file**	**Date**	**writers**
Test and Calibration		June 17,	Fields SE

Plan		2014	team
SCM Cassini calibration plan at Chambon-la-forêt facility	SCM_Cassini_calibration_plan_chambon_issue1_Rev0.docx	June, 2014	SCM team

Table of Contents

1 SCM transfer function nominal frequency band (SCM TF-NF) – X,Y and Z axis in the new facility

Date of the test	19 June 2014, EM : SCM TF-NF Start: Stop:
Setup	EM: SCM sensor + SCM PA + harness + Cassini rack GSE2 inside the new facility and in the mumetal box (Fig. 2). The mu metal box being grounded to the rack ground.
Software (pc-p-mags)	MMS_FM_PREAMP.exe, option 1 Data stored in the directory pointed by the relative path ..\DATA **MMS-FM_PREAMP_Etalonnage_V3.exe, option v**
Software generated from (pc-p-mags)	
Instruments	Agilent 35670A **(option v : 3.5 Vrms, 0.1Hz-50kHz, 100 pts/sweep)** Outside the new facility

	SCM GSE harness JA2 (PA to rack), JA1 (sensor to PA)
	Cassini rack GSE2 (provide the power supply +12V/-12V)
	Injection box (10 Ohms) connected to the new connection front
	New tri-axis Helmholtz coils connected to the connection box
	Coaxial cables: Output Signal Red one

Positionings of the wood box and of the tri-axis antennas have been checked. No saver on the pigtail, savers at the input and output of the PA have been kept.

Figure 1 : (Left) Cassini EM sensor located within the new Helmholtz coils inside the new facility. One can see that the YY' coils are connected in the connection panel (on the bottom of the photo) for which the 50 Hz noise is the smallest. **(Middle)** Cassini EM preamplifier connected to the sensor with the EM harness and connected to the rack GSE2 **(Right)** Rack GSE2 (+12/-12V power supply) connected to Cassini EM PA. The Y axis (red coaxial cable) is connected to the spectrum analyzer.

Tri-axis Cassini aligned with the new facility axis: Bx -> XX', By ->YY', Bz -> ZZ'

X channel

50 Hz noise level on X channel: 199 mVrms

Gain in the flat band: ~1-3 dB

Y channel

50 Hz noise level on Y channel (512 pts averaging): 25 mVrms

Gain in the flat band: ~22 dBV/V (22- 39 = - 17 dBV/nT) with a correction factor equal to 39

Z channel :

50 Hz noise level on Z channel (512 pts averaging): 245 mVpp.

Gain in the flat band: ~22 dB

As the X channel gain is much smaller than Y and Z, we rotate the Cassini tri-axis to check that this effect is not due to the facility (New tri-axis Helmholtz coils). BY aligned with XX’ and BX aligned with YY’. **Same result => pb coming from X channel PA or sensor.**

It is possibly due to JFET. Indeed JFET have a gain named gfs which depends on the drain current. Drain current is provided by the diode. If the diode which generates the current does not work well causing a drain current smaller than expected, therefore the gain gfs can be smaller.

Unlikely that the issue comes from the resistors.

In order to reduce the 50 Hz noise, the rack is put inside the mumetal box

Without mumetal box grounded to the rack ground, we get 3 mVrms and interferences. After grounding the mumetal box to the ground rack, we still have 3-4 mVrms but the interferences are no longer present.

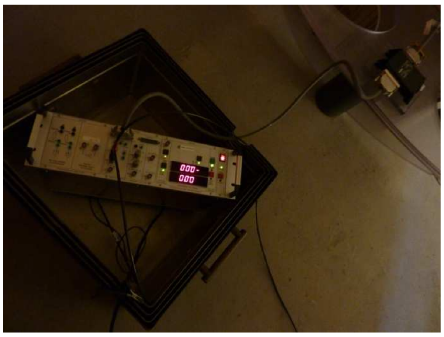

Figure 2 : Rack GSE2 (+12/-12V power supply) connected to Cassini EM PA and located to the mumetal box in order to reduce the 50Hz tone produced by the power supply. The mumetal box is grounded to the rack ground. The Y axis (red coaxial cable) is connected to the spectrum analyzer.

Y channel

Filename: Jun_19_12h08_flex_Cassini_Y_Rackdansmumetal_GAIN+PHASE.txt

X channel

Filename: Jun_19_12h53_flex_Cassini_X_Rackdansmumetal_GAIN+PHASE.txt

Z channel :

Filename: Jun_19_13h01_flex_Cassini_Z_rackdansmumetal_GAIN+PHASE.txt

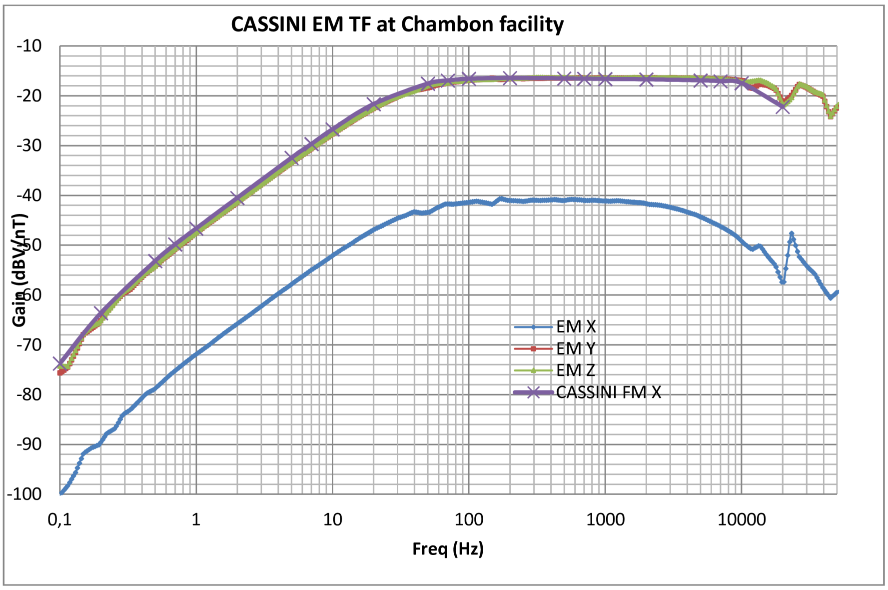

Figure 3 : Comparison between Cassini EM (gain) in dBV/nT in the new facility and previous FM measurements (in the previous facility).

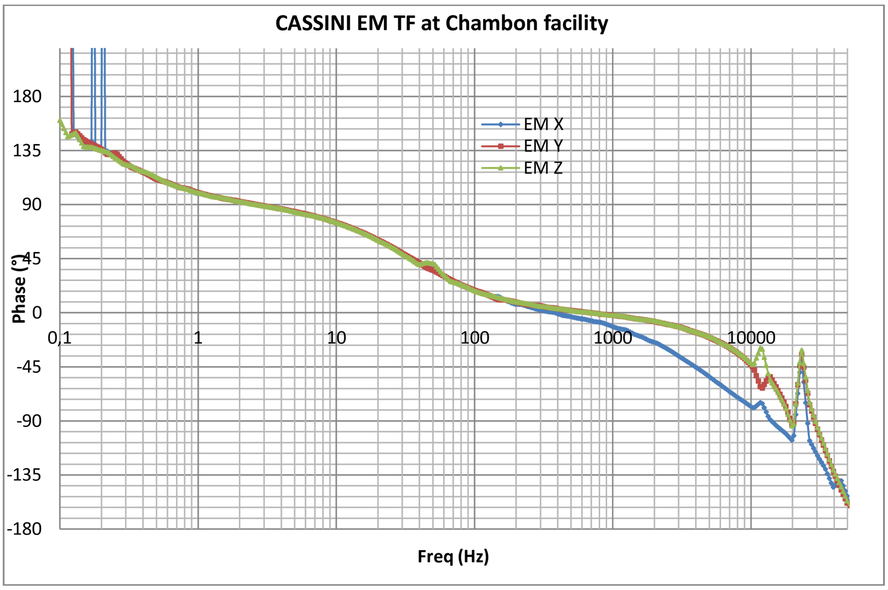

Figure 4 : Cassini EM phase in degree in the new facility.

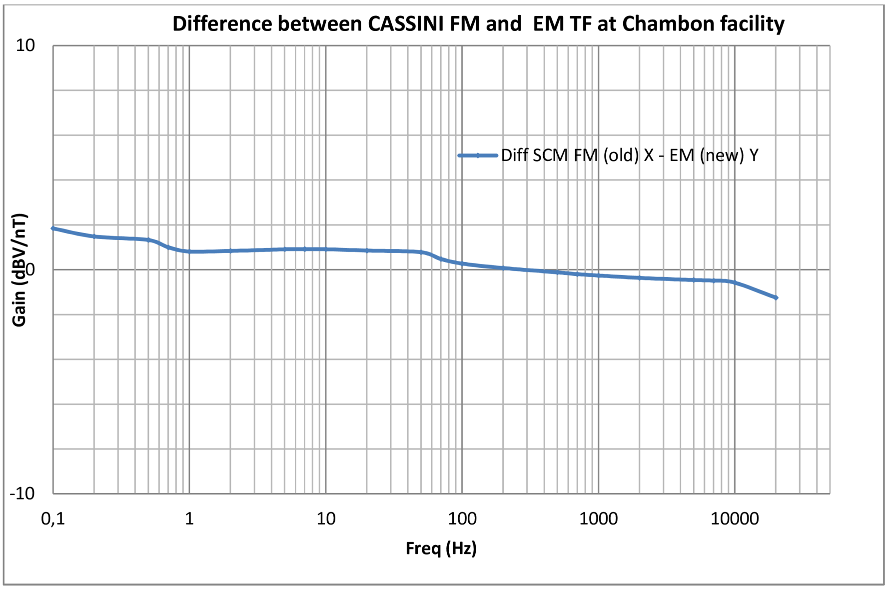

Figure 5 : Difference between Cassini FM (measured in the previous facility in 90's) and Cassini EM measured in the new facility.

Summary:

The gain difference about 1 dBV/nT between FM and EM in the 50 Hz – 10 kHz range is expected as it has been found on MMS and on BepiColombo. This difference is supposed to be due to mutual coupling between AC and DC Helmholtz coils in the previous facility. Yet, the gain difference below 50 Hz is not expected and could come from different sources: hardware difference between FM and EM, calibration setup difference, … To be investigated. Note that the secondary resonance (~20 kHz) is still present on Cassini search-coil while it has been removed on THEMIS, Bepi and MMS.

2 Calibration circuit transfer function (CCTF) –X, Y and Z axis in the new facility

Date of the test	19 June 2014, CCTF measurements (X, Y, Z) Start: Stop:
Setup	EM: SCM sensor + SCM PA + harness + Cassini rack GSE2 inside the new facility and in the mumetal box (Fig. 6). The mu metal box being grounded to the rack ground.
Software (pc-p-mags)	MMS_FM_EtalonnageV3.exe Data stored in the directory pointed by the relative path ..\DATA

Software generated from (pc-p-mags)	
Instruments	Agilent 35670A (1 Vrms, 1Hz-50kHz, 100 pts) outside the new facility
	SCM GSE harness JA2 (PA to rack), JA1 (sensor to PA)
	Cassini rack GSE2 (provide the power supply +12V/-12V)
	Coaxial cables: long coaxial cables for source(blue) and signal(red)

No saver on the pigtail, savers at the input and output of the PA have been kept. The sensor is located within the new Helmholtz coils in the new facility yet the coils are not used as the calibration signal is directly injected into the secondary windings of the search-coil.

1Hz-50KHz, 1 Vrms, 100 pts/sweep

Channel X : plateau – 44 dBV/V. **Large gain difference compared with Y and Z channels.**

Filename: Jun_19_15h12_flex_Cassini_Cal_X_GAIN+PHASE.txt

Channel Y : plateau – 17 dBV/V

Filename: Jun_19_15h16_flex_Cassini_Cal_Y_GAIN+PHASE.txt

Channel Z : plateau – 17 dBV/V

Filename: Jun_19_15h23_flex_Cassini_Cal_Z_GAIN+PHASE.txt

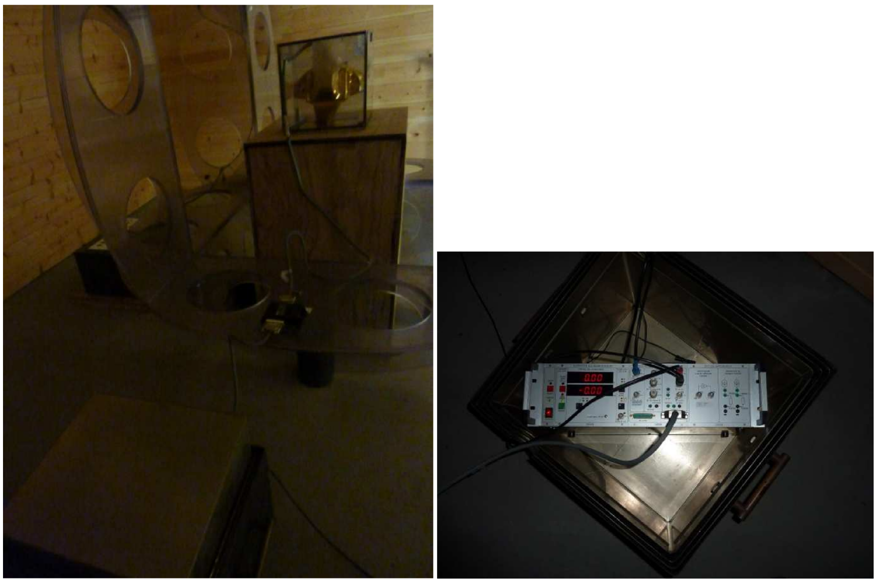

Figure 6 : Setup for the EM onboard cal signal measurements. **Left**: EM sensor is located at the center of the new facility (but Helmholtz coils are not used), EM PA is connected to the rack GSE2 which is located in the mumetal box to reduce the 50 Hz tone. **Right**: Calibration signal is injected into the EM PA via the rack GSE2 cal entry (blue coaxial cable). The X channel is measured (red coaxial cable). The mumetal box is still grounded to the rack ground.

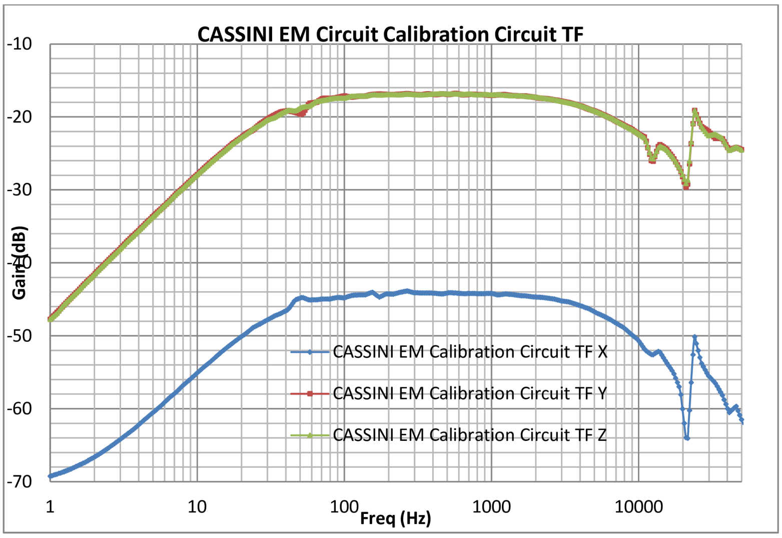

Figure 7: Cassini EM Calibration circuit transfer function (in Gain dBV/V).

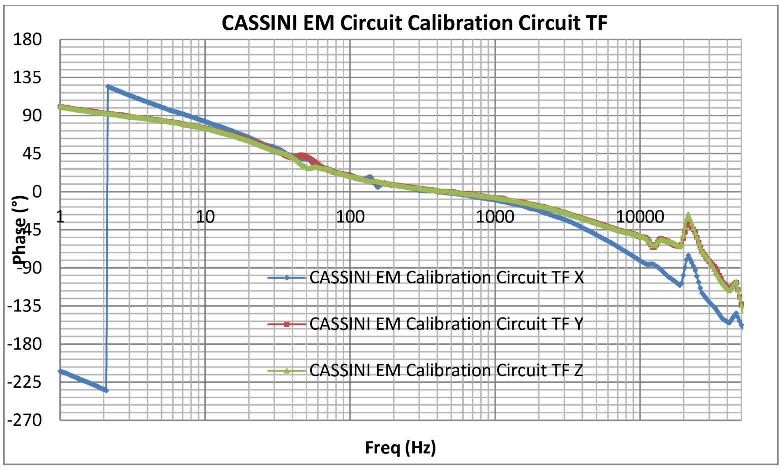

Figure 8 : Cassini EM Calibration circuit transfer function (in phase).

Summary about CASSINI EM SCM CCTF measurements:

The gain issue on the X channel is confirmed. The CCTF should be compared with the measured CCTF onboard Cassini at different stage of the mission in order to follow the behavior and stability of the search-coil frequency response.

3 SCM output Noise measurements for Y channel

Estimation of the noise at 1 kHz (-110. dBV/sqrt(Hz)) for the Y channel

Be = Bs –G = -110 +17 = - 93 dBV/sqrt(Hz) ~ 22 FemtoT/sqrt(Hz)

-17 dBV/nT (22-39)

Date of the test	19 June 2014, CASSINI SCM output Noise - Y channel Start Stop
Setup	EM: SCM sensor + SCM PA + harness inside the mumetal box in the new facility (Fig. 9). The Cassini rack GSE2 is outside the mumetal box and put on mumetal top. The mu metal box and the mumetal top being grounded to the rack ground.
Software (pc-p-mags)	**MMS_FM_EtalonnageV3.exe option s** Data stored in the directory pointed by the relative path ..\DATA
Software generated from	

(pc-p-mags)	
Instruments	Agilent 35670A (0.1Hz-50kHz, 1600 pts)
	SCM GSE harness JA2 (PA to rack), JA1 (sensor to PA)
	Cassini rack GSE2 (provide the power supply +12V/-12V)
	Coaxial cables: Only one (red)

Figure 9 : Cassini EM sensor and PA inside the mumetal box for output noise measurement of the Y channel. The rack GSE2 has been covered with mumetal tops in order to reduce the 50 Hz tone.

[0.1Hz-50kHz], 1600 points per sweep. The first band 0.03-0.3 Hz is skipped.

Filename: Jun_19_16h01_flex_Cassini_Y_NOISE_PA_SC_LF.txt

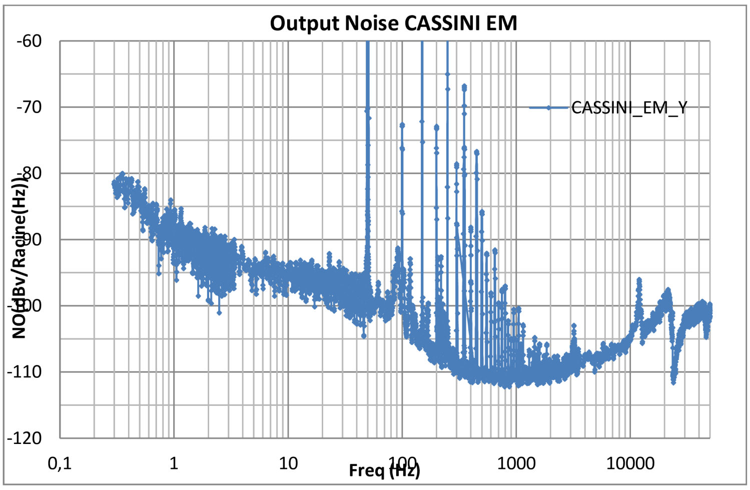

Figure 10: Cassini EM Output noise in dbV/sqrt(Hz). 50 Hz tone and harmonics are still present despite the fact that the sensor and the pa are in the mumetal box and the rack has been covered by mumetal tops.

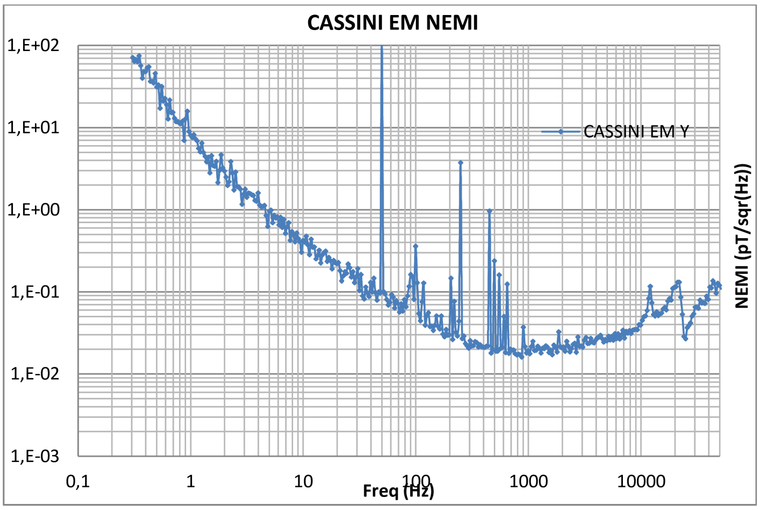

Figure 11: Cassini EM NEMI.

4 SCM cross talk between Y and Z channels

Date of the test	19 June 2014, CASSINI SCM cross talk between Y and Z channels Start Stop
Setup	EM: SCM sensor + SCM PA + harness inside the new facility. The Cassini rack GSE2 is inside the mumetal box.The mu metal box being grounded to the rack ground.
Software (pc-p-mags)	**MMS_FM_EtalonnageV3.exe option s** Data stored in the directory pointed by the relative path ..\DATA
Software generated from (pc-p-mags)	
Instruments	Agilent 35670A (3.5 mVrms, 10Hz-50kHz, 100 pts)
	SCM GSE harness JA2 (PA to rack), JA1 (sensor to PA)
	Cassini rack GSE2 (provide the power supply +12V/-12V)
	Coaxial cables: Only one (red)

Figure 12 : Cross talk setup. Cassini sensor located within the new Helmholtz tri-axis coils and the rack GSE2 is located in the grounded mumetal box (not shown).

The X channel is not used due to the detected anomaly on the gain.

SCM By aligned with YY’

B generated along YY’

Y channel: 22 dB in flat band

Filename: Jun_19_17h24_flex_Cassini_CT_By_Ys_GAIN+PHASE.txt

Z channel : - 20 dB in flat band

Filename : Jun_19_17h26_flex_Cassini_CT_By_Zs_GAIN+PHASE.txt

B generated along ZZ’

Z channel : 22 dB in flat band

Filename: Jun_19_17h29_flex_Cassini_CT_Bz_Zs_GAIN+PHASE.txt

Y channel :

Filename: Jun_19_17h31_flex_Cassini_CT_Bz_Ys_GAIN+PHASE.txt

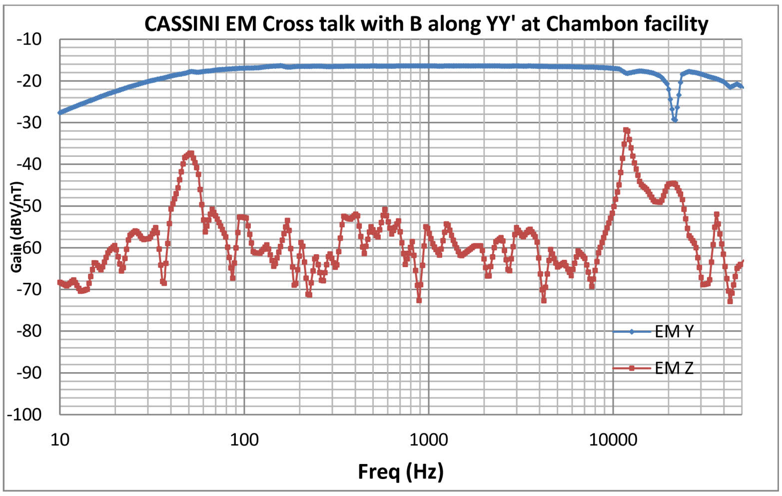

Figure 13: Cross talk between EM Y and EM Z when B is generated along YY’.

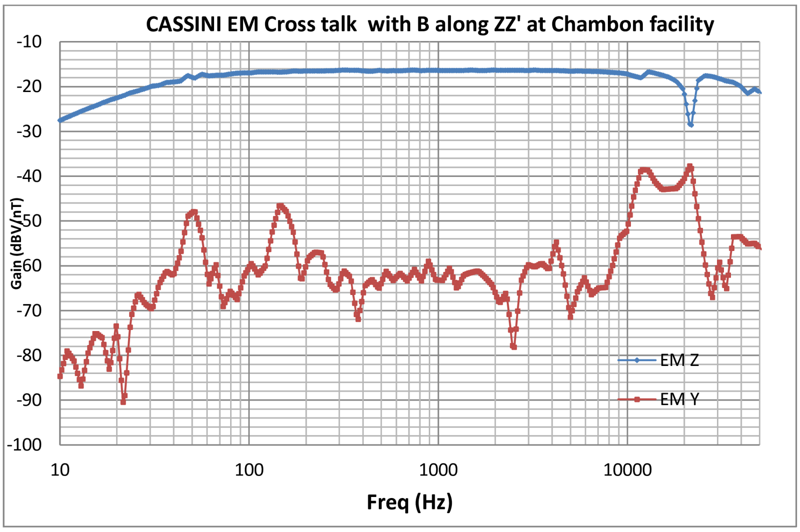

Figure 14: Cross talk between EM Z and EM Y when B is generated along ZZ'.

Summary of cross talks:

We measure the usual ~ 44 dBV/nT difference in the flat band between the channel corresponding to the injected B field and the orthogonal channel.

APPENDIX D

Observations in-situ de la turbulence compressible dans les magnétogaines planétaires et le vent solaire.

La Turbulence est l'une des dix grandes énigmes de la physique. L'un des rôles les plus importants de la turbulence est sa capacité à transporter et à diffuser la matière ainsi qu'à dissiper l'énergie. Ce rôle devient encore plus important dans les milieux sans collisions comme la plupart des plasmas du système solaire. Parmi les différents plasmas spatiaux, le vent solaire et les magnétogaines planétaires représentent les meilleurs laboratoires pour l'étude des propriétés de la turbulence. Les fluctuations de densité dans le vent solaire étant faibles, à basses fréquences ces dernières sont généralement décrites par la théorie de la MHD incompressible. Malgré son incompressibilité, l'effet de la compressibilité dans le vent solaire a fait l'objet de nombreux travaux depuis des décennies, à la fois théoriques, numériques et observationnels.

L'objectif principal de ma thèse est d'étudier le role de la compressibilité dans les magnétogaines planétaires (de la Terre et de Saturne) en comparaison avec un milieu beaucoup plus étudié et moins compressible (quasi incompressible), le vent solaire. Ce travail a été realisé en utilisant des données in-situ de trois sondes spatiales, Cassini, Cluster et THEMIS B/ARTEMIS P1.

La première partie de ma thèse a été consacrée à l'étude des propriétés de la turbulence dans la magnétogaine de Saturne aux échelles MHD et sub-ionique, en comparaison avec celle de la Terre. Cette étude a été réalisé en utilisant les données Cassini et Cluster respectivement. Du point de vu spectral, les résultats ont montré que les lois de puissances aux echelles MHD dependent sur la localisation dans la magnétogaine. Mais aussi l'absence du spectre de Kolmogorov ($f^{-5/3}$) derrière le choc, et une tendance de sa formation vers les flancs de la magnétogaine et plus proche de la magnétopause. De plus, les spectres sont plutôt dominés par une loi de puissance $\sim f^{-1}$ derrière un choc quasi-perpendiculaire, et $\sim f^{-0.5}$ derrière un choc quasi-parallèle. En ce qui concerne les échelles cinétiques (sub-ioniques), les propriétés spectrales semblent être plus "universelles". L'étude n'a montré aucune dépendance par rapport à la structure du choc, ni par rapport à la localisation dans la magétogaine. Les valeurs de pentes varient de [-2.2, -3.0], de manière similaire au vent solaire. Ces résultats ont été confirmés dans la magnétogaine de la terre par une étude basée sur les données Cluster. Afin de mieux comprendre l'absence des spectres en $f^{-5/3}$ et l'origine des spectres avec les pentes en f^{-1}, la nature statistique des fluctuations magnétiques a été determinée en calculant les densités de probabilités (PDFs) des incréments du champ magnétique. Aux echelles MHD derrière un choc quasi-perpendiculaire et parallèle, les PDFs sont gaussiens, ce qui caractérise la nature aléatoire des fluctuations, alors qu'aux echelles sub-ioniques, derrière un choc quasi-perpendiculaire et parallèle, je montre que les fluctuations sont plutôt mono-fractales et multi-fractales respectivement. En calculant la compressibilité magnétique, j'ai aussi caractérisé la nature compressible des fluctuations dans la magnétogaine (de Saturne et de la Terre) dominées par des modes de propagations de types magnétosoniques, lentes.

La première partie de mon travail a révélée l'importance des fluctuations compressibiles dans la magnétogaine de la Terre et de Saturne. Ainsi, dans la deuxième partie, j'ai étudié l'effet de la compressibilité sur le taux de transfert de l'énergie dans la zone inertielle. Pour cela, j'ai appliqué la loi exacte de la turbulence isotherme et compressible, dérivée récement par Banerjee & Galtier [2013], en utilisant une liste d'intervalles de temps (330 cas) dans le vent rapide et lent avec les données THEMIS B/ARTEMIS P1. Une analyse basée sur les différents termes du modèle a montré le rôle des fluctuations de densité sur l'augmentation du taux de tranfert de l'énergie par rapport à celui estimé par le modèle incompressible de Politano & Pouquet [1998]. En plus, ce travail a mis en évidence le rôle du nombre du Mach turbulent plutôt que la compressibilité, sur l'amplification du taux de tranfert, et a confirmé la nature de la cascade inverse dans le vent rapide.

Enfin, une première application de ce modèle dans la magnétogaine de la Terre est présentée en utilisant les données Cluster. En se basant sur les cas d'études présentant la zone inertielle, le taux de dissipation de l'énergie a été calculé pour les cas dont la compréssibilité magnétique est "Alfvénique" d'une part et "magnétosonique" d'une autre part. Cette étude préliminaire a révélé une première estimation du taux de dissipation dans la magnétogaine, en particulier celle de la Terre. Ce dernier, est 100 plus élevé que celui estimé dans le vent solaire. D'une autre part ce travail a montré que les résultats des cas "Alfvéniques" sont plutôt comparable à ceux du vent rapide, alors que ceux des cas "magnétosonique", sont plus comparable á aux résultats du vent lent.

Bibliography

Achilleos, N., Bertucci, C., Russell, C. T., Hospodarsky, G. B., Rymer, A. M., Arridge, C. S., Burton, M. E., Dougherty, M. K., Hendricks, S., Smith, E. J. & Tsurutani, B. T. 2006 Orientation, location, and velocity of saturn's bow shock: Initial results from the cassini spacecraft. *Journal of Geophysical Research: Space Physics* **111** (A3), n/a–n/a, a03201. (Cited on page 90.)

Alexandrova, O. 2008 Solar wind vs magnetosheath turbulence and Alfven vortices. *Nonlin. Proc. Geophys.* **15**, 95–108. (Cited on page 35.)

Alexandrova, O., Lacombe, Mangeney, Grappin & Maksimovic, M. 2012 Solar wind wind Turbulent spectrum at the plasma kinetic. *Astrophys. J.* . (Cited on pages 32and 91.)

Alexandrova, O., Lacombe, C. & Mangeney, A. 2008 Spectra and anisotropy of magnetic fluctuations in the Earth's magnetosheath: Cluster observations. *Ann. Geophys.* **26**, 3585–3596. (Cited on pages 33,35and 57.)

Alexandrova, O., Mangeney, A., Maksimovic, M., Cornilleau-Wehrlin, N., Bosqued, J.-M. & André, M. 2006 Alfvén vortex filaments observed in magnetosheath downstream of a quasi-perpendicular bow shock. *J. Geophys. Res.* **111** (A10), 12208–+. (Cited on pages 32and 35.)

Alexandrova, O., Mangeney, A., Maksimovic, M., Lacombe, C., Cornilleau-Wehrlin, N., Lucek, E. A., Decreau, P. M. E., Bosqued, J.-M., Travnicek, P. & Fazakerley, A.N. 2004 Cluster observations of finite amplitude alfven waves and small-scale magnetic filaments downstream of a quasi-perpendicular shock. *J. Geophys. Res.* **109**, A05207. (Cited on page 35.)

Alexandrova, O. & Saur, J. 2008 Alfven vortices in saturn"s magnetosheath: Cassini observations. *Geophysical Research Letters* **35** (15), n/a–n/a, l15102. (Cited on page 35.)

Alexandrova, O., Saur, J., Lacombe, C., Mangeney, A., Mitchell, J., Schwartz, S. J. & Robert, P. 2009 Universality of Solar-Wind Turbulent Spectrum from MHD to Electron Scales. *Phys. Rev. Lett.* **103** (16), 165003. (Cited on page 32.)

Anderson, Brian J., Fuselier, Stephen A., Gary, S. Peter & Denton, Richard E. 1994 Magnetic spectral signatures in the earth's magnetosheath and plasma depletion layer. *Journal of Geophysical Research: Space Physics* **99** (A4), 5877–5891. (Cited on page 34.)

Armstrong, J. W., Rickett, B. J. & Spangler, S. R. 1995 Electron density power spectrum in the local interstellar medium. *Astrophysical Journal* **443**, 209–221. (Cited on page 37.)

Auster, H. U., Glassmeier, K. H., Magnes, W., Aydogar, O., Baumjohann, W., Constantinescu, D., Fischer, D., Fornacon, K. H., Georgescu, E., Harvey, P., Hillenmaier, O., Kroth, R., Ludlam, M., Narita, Y., Nakamura, R., Okrafka, K., Plaschke, F., Richter, I., Schwarzl, H., Stoll, B., Valavanoglou, A. & Wiedemann, M. 2009 *The THEMIS Fluxgate Magnetometer*, pp. 235–264. New York, NY: Springer New York. (Cited on page 96.)

Bale, S. D., Kellogg, P. J., Mozer, F. S., Horbury, T. S. & Rème, H. 2005 Measurement of the electric fluctuation spectrum of magnetohydrodynamic turbulence. *Phys. Rev. Lett.* **94** (21), 215002. (Cited on pages 28and 30.)

Bame, S. J., Asbridge, J. R., Feldman, W. C., Montgomery, M. D. & Kearney, P. D. 1975 Solar wind heavy ion abundances. *Solar Physics* **43** (2), 463–473. (Cited on page 6.)

Bame, S. J., Hundhausen, A. J., Asbridge, J. R. & Strong, I. B. 1968 Solar wind ion composition. *Phys. Rev. Lett.* **20**, 393–395. (Cited on page 6.)

Banerjee, Robi, Klessen, Ralf S. & Fendt, Christian 2007 Can protostellar jets drive supersonic turbulence in molecular clouds? *The Astrophysical Journal* **668** (2), 1028. (Cited on page 38.)

Banerjee, S. & Galtier, S. 2013 Exact relation with two-point correlation functions and phenomenological approach for compressible magnetohydrodynamic turbulence. *Phys. Rev. E* **87**, 013019. (Cited on pages 13,15,23,41,78,93,98,113,117,132,135,137and 164.)

Banerjee, S. & Galtier, S. 2014 A kolmogorov-like exact relation for compressible polytropic turbulence. *Journal of Fluid Mechanics* **742**, 230–242. (Cited on page 21.)

Barba, L. A. & Velasco Fuentes, O. U. 2008 Lagrangian flow geometry of tripolar vortex. In *IUTAM Symposium on Hamiltonian Dynamics, Vortex Structures and Turbulence* (ed. Alexey V. Borisov, Valery V. Kozlov, Ivan S. Mamaev & Mikhail A. Sokolovskiy), pp. 247–256. Springer, doi: 10.1007/978-1-4020-6744-0_21. (Cited on page 3.)

Barnes, Aaron 1966 Collisionless damping of hydromagnetic waves. *Physics of Fluids* **9** (8), 1483–1495. (Cited on page 28.)

Bavassano, B., Dobrowolny, M., Mariani, F. & Ness, N. F. 1982 Radial evolution of power spectra of interplanetary alfvénic turbulence. *Journal of Geophysical Research: Space Physics* **87** (A5), 3617–3622. (Cited on page 29.)

Belcher, J. W. & Davis, Jr. L. 1971 Large-Amplitude Alfvén Waves in the Interplanetary Medium, 2. *J. Geophys. Res.* **76** (16), 3534. (Cited on pages 28and 29.)

Belmont, G. & Rezeau, L. 2001 Magnetopause reconnection induced by magnetosheath hall-mhd fluctuations. *J. Geophys. Res.* **106**. (Cited on page 11.)

Bieber, John W., Wanner, Wolfgang & Matthaeus, William H. 1996 Dominant two-dimensional solar wind turbulence with implications for cosmic ray transport. *Journal of Geophysical Research: Space Physics* **101** (A2), 2511–2522. (Cited on page 29.)

Biskamp, Dieter 1993 *Nonlinear Magnetohydrodynamics*. Cambridge University Press, cambridge Books Online. (Cited on page 23.)

Biskamp, D, Schwarz, E & Drake, JF 1996 Two-dimensional electron magnetohydrodynamic turbulence. *Phys. Rev. Lett.* **76** (8), 1264–1267. (Cited on page 29.)

Boldyrev, S. & Perez, J. C. 2013 The Physics of Kinetic-Alfvén Turbulence. In *Numerical Modeling of Space Plasma Flows (ASTRONUM2012)* (ed. N. V. Pogorelov, E. Audit & G. P. Zank), *Astronomical Society of the Pacific Conference Series*, vol. 474, p. 3. (Cited on pages 29,74and 75.)

Bourouaine, S., Alexandrova, O., Marsch, E. & Maksimovic, M. 2012 On spectral breaks in the power spectra of magnetic fluctuations in fast solar wind between 0.3 and 0.9 au. *The Astrophysical Journal* **749** (2), 102. (Cited on page 31.)

Breech, B., Matthaeus, W. H., Minnie, J., Bieber, J. W., Oughton, S., Smith, C. W. & Isenberg, P. A. 2008 Turbulence transport throughout the heliosphere. *Journal of Geophysical Research: Space Physics* **113** (A8), n/a–n/a. (Cited on page 28.)

Bruno, R. & Bavassano, B. 1991 Origin of low cross-helicity regions in the inner solar wind. *Journal of Geophysical Research: Space Physics* **96** (A5), 7841–7851. (Cited on page 40.)

Bruno, R. & Bavassano, B. 1993 Cross-helicity depletions in the inner heliosphere, and magnetic field and velocity fluctuation decoupling. *Planet. Space Sci.* **41**, 677–685. (Cited on page 40.)

Bruno, R. & Carbone, V. 2005 The Solar Wind as a Turbulence Laboratory. *Living Rev. Solar Phys.* **2** (4). (Cited on pages xiii,22,28,31,33,40,74,100and 108.)

Bruno, R., Carbone, V., Vörös, Z., D'Amicis, R., Bavassano, B., Cattaneo, M. B., Mura, A., Milillo, A., Orsini, S., Veltri, P., Sorriso-Valvo, L., Zhang, T., Biernat, H., Rucker, H., Baumjohann, W., Jankovičová, D. & Kovács, P. 2009 Coordinated study on solar wind turbulence during the venus-express, ace and ulysses alignment of august 2007. *Earth, Moon, and Planets* **104** (1), 101–104. (Cited on page 30.)

Bruno, R., Trenchi, L. & Telloni, D. 2014 Spectral slope variation at proton scales from fast to slow solar wind. *The Astrophysical Journal Letters* **793** (1), L15. (Cited on page 32.)

Brunt, C. M., Heyer, M. H. & Mac Low, M.-M. 2009 Turbulent driving scales in molecular clouds. *Astronomy and Astrophysics* **504**, 883–890. (Cited on page 38.)

Burch, J. L., Moore, T. E., Torbert, R. B. & Giles, B. L. 2016 Magnetospheric multiscale overview and science objectives. *Space Science Reviews* **199** (1), 5–21. (Cited on page 5.)

Burgers, J.M. 1948 A mathematical model illustrating the theory of turbulence. In – (ed. Richard Von Mises & Theodore Von Karman), *Advances in Applied Mechanics*, vol. 1, pp. 171 – 199. Elsevier. (Cited on page 38.)

Burlaga, L. F. 1991 Intermittent turbulence in the solar wind. *Journal of Geophysical Research: Space Physics* **96** (A4), 5847–5851. (Cited on pages xivand 33.)

Burlaga, L. F. & Turner, J. M. 1976 Microscale 'alfvén waves' in the solar wind at 1 au. *Journal of Geophysical Research* **81** (1), 73–77. (Cited on page 29.)

Camporeale, Enrico & Burgess, David 2011 The Dissipation of Solar Wind Turbulent Fluctuations at Electron Scales. *The Astrophysical Journal* **730**, 114. (Cited on page 30.)

Carbone, V., Marino, R., Sorriso-Valvo, L., Noullez, A. & Bruno, R. 2009 Scaling laws of turbulence and heating of fast solar wind: The role of density fluctuations. *Phys. Rev. Lett.* **103**, 061102. (Cited on pages xiv,40,41,98,108and 115.)

Cattaneo, M. B. Bavassano, Moreno, G., Russo, G. & Richardson, J. D. 2000 Mhd turbulence in saturn's magnetosheath downstream of a quasi-parallel bow shock. *Journal of Geophysical Research: Space Physics* **105** (A10), 23141–23152. (Cited on pages 35and 71.)

Cerri, S. S., Califano, F., Jenko, F., Told, D. & Rincon, F. 2016 Subproton-scale Cascades in Solar Wind Turbulence: Driven Hybrid-kinetic Simulations. *Astrophysical Journal Letters* **822**, L12. (Cited on page 30.)

Chapman, Gary T. & Tobak, Murray" 1985 *Theoretical Approaches to Turbulence*, chap. Observations, Theoretical Ideas, and Modeling of Turbulent Flows—Past, Present, and Future, pp. 19–49. New York, NY: Springer New York. (Cited on page 4.)

Chasapis, A., Retino, A., Sahraoui, F., Vaivads, A., Khotyaintsev, Yu. V., Sundkvist, D., Greco, A., Sorriso-Valvo, L. & Canu, P. 2015 Thin current sheets and associated electron heating in turbulent space plasma. *The Astrophysical Journal Letters* **804** (1), L1. (Cited on pages 36,76and 119.)

Chen, C. H. K., Boldyrev, S., Xia, Q. & Perez, J. C. 2013 Nature of sub-proton scale turbulence in the solar wind. *Phys. Rev. Lett.* **110**, 225002. (Cited on pages xvii,30,75and 76.)

Chen, C. H. K., Leung, L., Boldyrev, S., Maruca, B. A. & Bale, S. D. 2014 Ion-scale spectral break of solar wind turbulence at high and low beta. *Geophysical Research Letters* **41** (22), 8081–8088. (Cited on page 31.)

Cho, J. & Lazarian, A. 2002 Compressible sub-alfvenic mhd turbulence in low-β plasmas. *Phys. Rev. Lett.* **88**, 245001. (Cited on pages 74and 114.)

Cho, J. & Lazarian, A. 2004 The Anisotropy of Electron Magnetohydrodynamic Turbulence. *ApJ Lett.* **615**, L41–L44. (Cited on page 30.)

Coburn, Jesse T., Forman, Miriam A., Smith, Charles W., Vasquez, Bernard J. & Stawarz, Julia E. 2015 Third-moment descriptions of the interplanetary turbulent cascade, intermittency and back transfer. *Philosophical Transactions of the Royal Society of London A: Mathematical, Physical and Engineering Sciences* **373** (2041). (Cited on page 110.)

Coleman Jr., P. J. 1968 Turbulence, viscosity and dissipation in the solar-wind plasma. *Astrophys. J.* **153**, 371. (Cited on page 8.)

Cornilleau-Wehrlin, N., Mirioni, L., Robert, P., Bouzid, V., Maksimovic, M., de Conchy, Y., Harvey, C. C. & Santolík, O. 2010 *STAFF Instrument Products Distributed Through the Cluster Active Archive*, pp. 159–168. Dordrecht: Springer Netherlands. (Cited on page 53.)

Crooker, N. U., Siscoe, G. L., Russell, C. T. & Smith, E. J. 1982 Factors controlling degree of correlation between isee 1 and isee 3 interplanetary magnetic field measurements. *Journal of Geophysical Research: Space Physics* **87** (A4), 2224–2230. (Cited on page 29.)

Czaykowska, A., Bauer, T. M, Treumann, R. A. & Baumjohann, W. 2001 Magnetic field fluctuations across the Earth's bow shock. *Annales Geophysicae* **19**, 275–287. (Cited on page 35.)

Dahlburg, R. B. & Einaudi, G. 2000 The compressible plane current-vortex sheet. *Physics of Plasmas* **7**, 1356–1365. (Cited on page 76.)

Dasso, S., Milano, L. J., Matthaeus, W. H. & Smith, C. W. 2005 Anisotropy in fast and slow solar wind fluctuations. *The Astrophysical Journal Letters* **635** (2), L181. (Cited on page 29.)

Dessler, A. J. & Fejer, J. A. 1963 Interpretation of k_p index and m-region geomagnetic storms. *Planetary Space Sciences* **11**, 505–511. (Cited on page 10.)

Dib, Sami, Bell, Eric & Burkert, Andreas 2006 The supernova rate-velocity dispersion relation in the interstellar medium. *The Astrophysical Journal* **638** (2), 797. (Cited on page 38.)

Dmitruk, Pablo, Matthaeus, W. H. & Seenu, N. 2004 Test particle energization by current sheets and nonuniform fields in magnetohydrodynamic turbulence. *The Astrophysical Journal* **617** (1), 667. (Cited on page 32.)

Dmitruk, P., Mininni, P. D., Pouquet, A., Servidio, S. & Matthaeus, W. H. 2011 Emergence of very long time fluctuations and $1/f$ noise in ideal flows. *Phys. Rev. E* **83**, 066318. (Cited on page 30.)

Dougherty, M. K., Kellock, S., Southwood, D. J., Balogh, A., Smith, E. J., Tsurutani, B. T., Gerlach, B., Glassmeier, K.-H., Gleim, F., Russell, C. T., Erdos, G., Neubauer, F. M. & Cowley, S. W. H. 2002 The cassini magnetic field investigation. *Space Science Reviews* **114**, 331–383. (Cited on pages xiv,48and 49.)

Dudok de Wit, T. & Krasnosel'Skikh, V. V. 1996 Non-Gaussian statistics in space plasma turbulence: fractal properties and pitfalls <a>. *Nonlinear Processes in Geophysics* **3**, 262–273. (Cited on page 36.)

Elsasser, Walter M. 1950 The hydromagnetic equations. *Phys. Rev.* **79**, 183–183. (Cited on page 21.)

Erdos, G. & Balogh, A. 1996 Statistical properties of mirror mode structures observed by ulysses in the magnetosheath of jupiter. *Journal of Geophysical Research: Space Physics* **101** (A1), 1–12. (Cited on page 71.)

Fairfield, D. H. 1976 Magnetic fields of the magnetosheath. *Reviews of Geophysics* **14** (1), 117–134. (Cited on page 34.)

Falgarone, E., Puget, J.-L. & Perault, M. 1992 The small-scale density and velocity structure of quiescent molecular clouds. *Astronomy and astrophysics* **257**, 715–730. (Cited on page 37.)

Federrath, C., Klessen, R. S. & Schmidt, W. 2008 The density probability distribution in compressible isothermal turbulence: Solenoidal versus compressive forcing. *ApJL* **688**, L79. (Cited on page 39.)

Federrath, C., Roman-Duval, J., Klessen, R. S., Schmidt, W. & Mac Low, M. M. 2010 Comparing the statistics of interstellar turbulence in simulations and observations. solenoidal versus compressive turbulence forcing. *AAP* **512**, A81. (Cited on pages xiv,38and 39.)

Filbert, Paul C. & Kellogg, Paul J. 1979 Electrostatic noise at the plasma frequency beyond the earth's bow shock. *Journal of Geophysical Research: Space Physics* **84** (A4), 1369–1381. (Cited on pages xviand 64.)

Frisch, U. 1995 *Turbulence*. Cambridge University Press. (Cited on pages xiii,16,19and 32.)

Galtier, S. & Banerjee, S. 2011 Exact relation for correlation functions in compressible isothermal turbulence. *Phys. Rev. Lett.* **107**, 134501. (Cited on pages 21and 23.)

Garnier, J., Lisak, M. & Picozzi, A. 2012 Toward a wave turbulence formulation of statistical nonlinear optics. *J. Opt. Soc. Am. B* **29** (8), 2229–2242. (Cited on page 3.)

Gary, S. P., Chang, O. & Wang, J. 2012 Forward cascade of Whistler turbulence: three-dimensional particle-in-cell simulations. *ApJ* **755** (142). (Cited on pages 9,30and 32.)

Gary, S. Peter, Fuselier, Stephen A. & Anderson, Brian J. 1993 Ion anisotropy instabilities in the magnetosheath. *Journal of Geophysical Research: Space Physics* **98** (A2), 1481–1488. (Cited on page 34.)

Gary, S. P., Saito, S. & Li, H. 2008 Cascade of whistler turbulence: Particle-in-cell simulations. *Geophys. Res. Lett.* **35** (L02104). (Cited on page 30.)

Gary, S. P. & Smith, C. W. 2009 Short-wavelength turbulence in the solar wind: Linear theory of whistler and kinetic Alfvén fluctuations. *J. Geophys. Res.* **114**, A12105. (Cited on page 67.)

Gary, S. Peter & Winske, Dan 1992 Correlation function ratios and the identification of space plasma instabilities. *Journal of Geophysical Research: Space Physics* **97** (A3), 3103–3111. (Cited on page 71.)

Gary, S. Peter & Winske, Dan 1993 Simulations of ion cyclotron anisotropy instabilities in the terrestrial magnetosheath. *Journal of Geophysical Research: Space Physics* **98** (A6), 9171–9179. (Cited on page 34.)

Gazis, Paul R. & Lazarus, Alan J. 1982 Voyager observations of solar wind proton temperature: 1-10au. *Geophysical Research Letters* **9** (4), 431–434. (Cited on page 8.)

Génot, V., Broussillou, L., Budnik, E., Hellinger, P., Trávníček, P. M., Lucek, E. & Dandouras, I. 2011 Timing mirror structures observed by cluster with a magnetosheath flow model. *Annales Geophysicae* **29** (10), 1849–1860. (Cited on page 35.)

Génot, Vincent, Budnik, E., Jacquey, C., Dandouras, I. & Lucek, E. 2009 In *Mirror modes observed with Cluster in the Earth's magnetosheath: statistical study and IMF solar wind dependence*, , vol. -. World Scientific Publishing, ADVANCES IN GEOSCIENCES. (Cited on page 34.)

Gogoberidze, G., Perri, S. & Carbone, V. 2013 The yaglom law in the expanding solar wind. *The Astrophysical Journal* **769** (2), 111. (Cited on page 99.)

Gold, T. 1959 Motions in the magnetosphere of the earth. *Journal of Geophysical Research* **64** (9), 1219–1224. (Cited on page 9.)

Goldreich, P. & Sridhar, S. 1995 Toward a theory of interstellar turbulence. 2: Strong alfvenic turbulence. *Astrophysical Journal* **438**, 763–775. (Cited on page 22.)

Goldstein, M. L. & Roberts, D. A. 1999 Magnetohydrodynamic turbulence in the solar wind. *Physics of Plasmas* **6** (11), 4154–4160. (Cited on pages 28and 72.)

Goldstein, M. L., Roberts, D. A. & Fitch, C. A. 1994 Properties of the fluctuating magnetic helicity in the inertial and dissipation ranges of solar wind turbulence. *Journal of Geophysical Research: Space Physics* **99** (A6), 11519–11538. (Cited on pages 29,31and 32.)

Goldstein, M. L., Roberts, D. A. & Matthaeus, W. H. 1995 Magnetohydrodynamic Turbulence In The Solar Wind. *Annu. Rev. Astron. Astrophys.* **33**, 283–326. (Cited on page 28.)

Gosling, J.T. & Pizzo, V.J. 1999 Formation and evolution of corotating interaction regions and their three dimensional structure. *Space Science Reviews* **89** (1), 21–52. (Cited on page 8.)

Gosling, J. T. & Szabo, A. 2008 Bifurcated current sheets produced by magnetic reconnection in the solar wind. *jgr* **113**, A10103. (Cited on page 119.)

Grappin, R., Mangeney, A. & Marsch, E. 1990 On the origin of solar wind mhd turbulence - helios data revisited. *JGR* **95**, 8197–8209. (Cited on page 31.)

Grappin, R., Velli, M. & Mangeney, A. 1991 Alfvenic versus standard turbulence in the solar wind. *Annales Geophysicae* **9**, 416–426. (Cited on page 31.)

Gurnett, D. A., Kurth, W. S., Kirchner, D. L., Hospodarsky, G. B., Averkamp, T. F., Zarka, P., Lecacheux, A., Manning, R., Roux, A., Canu, P., Cornilleau-Wehrlin, N., Galopeau, P., Meyer, A., Boström, R., Gustafsson, G., Wahlund, J.-E., Åhlen, L., Rucker, H. O., Ladreiter, H. P., Macher, W., Woolliscroft, L. J. C., Alleyne, H., Kaiser, M. L., Desch, M. D., Farrell, W. M., Harvey, C. C., Louarn, P., Kellogg, P. J., Goetz, K. & Pedersen, A. 2004 The Cassini Radio and Plasma Wave Investigation. *Space Science Reviews* **114**, 395–463. (Cited on pages xiv,49and 50.)

Gustafsson, G., BostrÖM, R., Holback, B., Holmgren, G., Lundgren, A., Stasiewicz, K., ÅHLÉN, L., Mozer, F. S., Pankow, D., Harvey, P., Berg, P., Ulrich, R., Pedersen, A., Schmidt, R., Butler, A., Fransen,

A. W. C., Klinge, D., Thomsen, M., FÄLTHAMMAR, C.-G., Lindqvist, P.-A., Christenson, S., Holtet, J., Lybekk, B., Sten, T. A., Tanskanen, P., Lappalainen, K. & Wygant, J. 1997 The electric field and wave experiment for the cluster mission. *Space Science Reviews* **79** (1), 137–156. (Cited on page 54.)

Hadid, L. Z., Sahraoui, F., Kiyani, K. H., Retino, A., Modolo, R., Canu, P., Masters, A. & Dougherty, M. K. 2015 Nature of the mhd and kinetic scale turbulence in the magnetosheath of saturn: Cassini observations. *The Astrophysical Journal Letters* **813** (2), L29. (Cited on pages xv,xvi,58,59,65,66,69and 71.)

Hamilton, K., Smith, C. W., Vasquez, B. J. & Leamon, R. J. 2008 Anisotropies and helicities in the solar wind inertial and dissipation ranges at 1AU. *J. Geophys. Res.* **113**, A01106. (Cited on page 31.)

Hasegawa, H, Fujimoto, M, Phan, TD, Reme, H, Balogh, A, Dunlop, MW, Hashimoto, C & TanDokoro, R 2004 Transport of solar wind into earth's magnetosphere through rolled-up kelvin-helmholtz vortices. *NATURE* **430**, 755–758. (Cited on page 11.)

Hassler, D. M., Dammasch, I. E., Lemaire, P., Brekke, P., Curdt, W., Mason, H. E., Vial, J.-C. & Wilhelm, K. 1999 Solar wind outflow and the chromospheric magnetic network. *Science* **283**, 810–813. (Cited on page 7.)

Hnat, B., Chapman, S. C. & Rowlands, G. 2004 Scaling, asymmetry and a Fokker-Planck model of the fast and slow solar wind as seen by WIND. *Physics of Plasmas* **11** (4), 1326–1332. (Cited on page 32.)

Hnat, B., Chapman, S. C. & Rowlands, G. 2005 Compressibility in Solar Wind Plasma Turbulence. *Phys. Rev. Lett.* **94** (204502). (Cited on page 40.)

Howes, G. G. 2009 Limitations of Hall MHD as a model for turbulence in weakly collisional plasmas. *Nonlin. Proc. Geophys.* **16**, 219. (Cited on page 68.)

Howes, G. G. 2015 A dynamical model of plasma turbulence in the solar wind. *Philosophical Transactions of the Royal Society of London Series A* **373**, 20140145–20140145. (Cited on page 9.)

Howes, G. G., Bale, S. D., Klein, K. G., Chen, C. H. K., Salem, C. S. & TenBarge, J. M. 2012 The slow-mode nature of compressible wave power in solar wind turbulence. *The Astrophysical Journal Letters* **753** (1), L19. (Cited on pages 30and 71.)

Howes, G. G., Cowley, S. C., Dorland, W., Hammett, G. W., Quataert, E. & Schekochihin, A. A. 2008*a* A model of turbulence in magnetized plasmas: Implications for the dissipation range in the solar wind. *J. Geophys. Res.* **113** (A12), 5103–+. (Cited on pages 9,29and 30.)

Howes, G. G., Dorland, W., Cowley, S. C., Hammett, G. W., Quataert, E., Schekochihin, A. A. & Tatsuno, T. 2008*b* Kinetic simulations of magnetized turbulence in astrophysical plasmas. *Phys. Rev. Lett.* **100** (6), 065004. (Cited on pages 30and 32.)

Howes, G. G., TenBarge, J. M., Dorland, W., Quataert, E., Schekochihin, A. A., Numata, R. & Tatsuno, T. 2011 Gyrokinetic Simulations of Solar Wind Turbulence from Ion to Electron Scales. *Phys. Rev. Lett.* **107**, 035004. (Cited on page 32.)

Huang, S. Y., Sahraoui, F., Deng, X. H., He, J. S., Yuan, Z. G., Zhou, M., Pang, Y. & Fu, H. S. 2014 Kinetic turbulence in the terrestrial magnetosheath: Cluster observations. *The Astrophysical Journal Letters* **789** (2), L28. (Cited on pages 35and 59.)

Hubert, D., Harvey, C. C. & Russell, C. T. 1989 Observations of magnetohydrodynamic modes in the earth's magnetosheath at 0600 lt. *Journal of Geophysical Research: Space Physics* **94** (A12), 17305–17309. (Cited on page 34.)

Hubert, D., Lacombe, C., Harvey, C. C., Moncuquet, M., Russell, C. T. & Thomsen, M. F. 1998 Nature, properties, and origin of low-frequency waves from an oblique shock to the inner magnetosheath. *Journal of Geophysical Research: Space Physics* **103** (A11), 26783–26798. (Cited on page 34.)

Iroshnikov, P. S. 1964 Turbulence of a Conducting Fluid in a Strong Magnetic Field. *Soviet Astronomy* **7**, 566–571. (Cited on pages 22,31and 74.)

Ito, A., Hirose, A., Mahajan, S. M. & Ohsaki, S. 2004 Remarks on the discrete Alfvén wave spectrum induced by the Hall current. *Phys. Plasmas* **11** (12), 5643–5647. (Cited on page 68.)

Johnstone, A. D., Alsop, C., Burge, S., Carter, P. J., Coates, A. J., Coker, A. J., Fazakerley, A. N., Grande, M., Gowen, R. A., Gurgiolo, C., Hancock, B. K., Narheim, B., Preece, A., Sheather, P. H., Winningham, J. D. & Woodliffe, R. D. 1997 Peace: A plasma electron and current experiment. *Space Science Reviews* **79** (1), 351–398. (Cited on page 54.)

Kanani, S. J., Arridge, C. S., Jones, G. H., Fazakerley, A. N., McAndrews, H. J., Sergis, N., Krimigis, S. M., Dougherty, M. K., Coates, A. J., Young, D. T., Hansen, K. C. & Krupp, N. 2010 A new form of saturn's magnetopause using a dynamic pressure balance model, based on in situ, multi-instrument cassini measurements. *Journal of Geophysical Research: Space Physics* **115** (A6), a06207. (Cited on pages xv,59and 61.)

Karimabadi, H., Roytershteyn, V., Vu, H. X., Omelchenko, Y. A., Scudder, J., Daughton, W., Dimmock, A., Nykyri, K., Wan, M., Sibeck, D., Tatineni, M., Majumdar, A., Loring, B. & Geveci, B. 2014 The link between shocks, turbulence, and magnetic reconnection in collisionless plasmas. *Physics of Plasmas* **21** (6). (Cited on pages xvi,9,30,36,65and 66.)

Kaufmann, Richard L., Horng, Jiann-Tsorng & Wolfe, Allan 1970 Large-amplitude hydromagnetic waves in the inner magnetosheath. *Journal of Geophysical Research* **75** (25), 4666–4676. (Cited on page 71.)

Kivelson, Margaret Galland & Southwood, David J. 1996 Mirror instability ii: The mechanism of nonlinear saturation. *Journal of Geophysical Research: Space Physics* **101** (A8), 17365–17371. (Cited on pages 34and 35.)

Kivelson, Margaret Galland & Zu-Yin, Pu 1984 The kelvin-helmholtz instability on the magnetopause. *Planetary and Space Science* **32** (11), 1335 – 1341. (Cited on page 78.)

Kiyani, K., Chapman, S. C., Hnat, B. & Nicol, R. M. 2007 Self-similar signature of the active solar corona within the inertial range of solar-wind turbulence. *Phys. Rev. Lett.* **98**, 211101. (Cited on page 32.)

Kiyani, K. H., Chapman, S. C., Sahraoui, F., Hnat, B., Fauvarque, O. & Khotyaintsev, Yu. V. 2013 Enhanced Magnetic Compressibility and Isotropic Scale Invariance at Sub-ion Larmor Scales in Solar Wind Turbulence. *ApJ* **763** (1), 10. (Cited on pages 67,69and 73.)

Kiyani, K. H., Chapman, S. C. & Watkins, N. W. 2009*a* Pseudononstationarity in the scaling exponents of finite-interval time series. *Phys. Rev. E* **79** (3), 036109. (Cited on page 67.)

Kiyani, K. H., Chapman, S. C., Yu. V. Khotyaintsev, Dunlop, M. W. & Sahraoui, F. 2009*b* Global Scale-Invariant Dissipation in Collisionless Plasma Turbulence. *Phys. Rev. Lett.* **103** (7), 075006. (Cited on pages 32and 33.)

Kiyani, Khurom H., Osman, Kareem T. & Chapman, Sandra C. 2015 Dissipation and heating in solar wind turbulence: from the macro to the micro and back again. *Philosophical Transactions of the Royal Society of London A: Mathematical, Physical and Engineering Sciences* **373** (2041). (Cited on pages xiii,30and 31.)

Klein, K. G., Howes, G. G., TenBarge, J. M., Bale, S. D., Chen, C. H. K. & Salem, C. S. 2012 Using synthetic spacecraft data to interpret compressible fluctuations in solar wind turbulence. *The Astrophysical Journal* **755** (2), 159. (Cited on page 71.)

Klein, L., Bruno, R., Bavassano, B. & Rosenbauer, H. 1993 Anisotropy and minimum variance of magnetohydrodynamic fluctuations in the inner heliosphere. *J. Geophys. Res.* **98** (17), 17,461–17,466. (Cited on page 40.)

Klessen, R. S. & Hennebelle, P. 2010 Accretion-driven turbulence as universal process: galaxies, molecular clouds, and protostellar disks. *Astronomy and astrophysics* **520**, A17. (Cited on page 38.)

Kolmogorov, A. N. 1941 The local structure of turbulence in incompressible viscous fluid for very large Reynolds numbers. *C. R. Acad. Sci. URSS* **30**, 301. (Cited on pages 15and 19.)

Kolmogorov, A. N. 1991 Dissipation of energy in the locally isotropic turbulence. *Proceedings: Mathematical and Physical Sciences* **434** (1890), 15–17. (Cited on page 18.)

Korotova, G. I., Sibeck, D. G., Kondratovich, V., Angelopoulos, V. & Constantinescu, O. D. 2009 Themis observations of compressional pulsations in the dawn-side magnetosphere: a case study. *Annales Geophysicae* **27** (10), 3725–3735. (Cited on page 95.)

Kraichnan, R. 1965 Inertial-Range Spectrum of Hydromagnetic Turbulence. *Physics of Fluids* **8**, 1385–1387. (Cited on pages 22,31and 74.)

Kritsuk, A. G., Norman, M. L., Padoan, P. & Wagner, R. 2007*a* The Statistics of Supersonic Isothermal Turbulence. *ApJ* **665**, 416–431. (Cited on page 41.)

Kritsuk, A. G., Padoan, P., Wagner, R. & Norman, M. L. 2007*b* Scaling laws and intermittency in highly compressible turbulence. In *Turbulence and Nonlinear Processes in Astrophysical Plasmas* (ed. D. Shaikh & G. P. Zank), *American Institute of Physics Conference Series*, vol. 932, pp. 393–399. (Cited on pages 38,41and 99.)

Kritsuk, A. G., Wagner, R. & Norman, M. L. 2013 Energy cascade and scaling in supersonic isothermal turbulence. *Journal of Fluid Mechanics* **729**, R1. (Cited on page 132.)

Lacombe, C. & Belmont, G. 1995 Proceedings of the d2.1 symposium of cospar scientific commission d waves in the earth's magnetosheath: Observations and interpretations. *Advances in Space Research* **15** (8), 329 – 340. (Cited on page 67.)

Lacombe, C., Belmont, G., Hubert, D., Harvey, C. C., Mangeney, A., Russell, C. T., Gosling, J. T. & Fuselier, S. A. 1995 Density and magnetic field fluctuations observed by isee 1-2 in the quiet magnetosheath. *Annales Geophysicae* **13** (4), 343–357. (Cited on page 34.)

Lacombe, C, Samsonov, A A, Mangeney, A, Maksimovic, M, Cornilleau-Wehrlin, N, Harvey, C C, Bosqued, J M & Travnicek, P 2006 Cluster observations in the magnetosheath - Part 2: Intensity of the turbulence at electron scales. *Annales Geophysicae* **24** (1), 3523–3531. (Cited on page 35.)

Larson, R. B. 1981 Turbulence and star formation in molecular clouds. *Monthly Notices of the Royal Astronomical Society: Letters* **194**, 809–826. (Cited on page 37.)

Le Contel, O., Roux, A., Jacquey, C., Robert, P., Berthomier, M., Chust, T., Grison, B., Angelopoulos, V., Sibeck, D., Chaston, C. C., Cully, C. M., Ergun, B., Glassmeier, K.-H., Auster, U., McFadden, J., Carlson, C., Larson, D., Bonnell, J. W., Mende, S., Russell, C. T., Donovan, E., Mann, I. & Singer, H. 2009 Quasi-parallel whistler mode waves observed by themis during near-earth dipolarizations. *Annales Geophysicae* **27** (6), 2259–2275. (Cited on page 95.)

Leamon, R. J., Matthaeus, W. H., Smith, C. W. & Wong, H. K. 1998 Contribution of Cyclotron-resonant Damping to Kinetic Dissipation of Interplanetary Turbulence. *ApJ Lett.* **507**, L181–L184. (Cited on pages 8,29,31and 32.)

Leckband, J.A, Burgess, D, Pantellini, F.G.E & Schwartz, S.J 1995 Ion distributions associated with mirror waves in the earth's magnetosheath. *Advances in Space Research* **15** (8-9), 345 – 348, proceedings of the D2.1 Symposium of {COSPAR} Scientific Commission D. (Cited on pages xivand 34.)

Lion, Sonny, Alexandrova, Olga & Zaslavsky, Arnaud 2016 Coherent events and spectral shape at ion kinetic scales in the fast solar wind turbulence. *The Astrophysical Journal* **824** (1), 47. (Cited on page 32.)

Lorenz, Edward N. 1963 Deterministic nonperiodic flow. *Journal of the Atmospheric Sciences* **20** (2), 130–141. (Cited on page 4.)

Loureiro, N. F., Schekochihin, A. A. & Zocco, A. 2013 Fast collisionless reconnection and electron heating in strongly magnetized plasmas. *Phys. Rev. Lett.* **111**, 025002. (Cited on page 9.)

Lundin, R., Sauvaud, J.-A., Réme, H., Balogh, A., Dandouras, I., Bosqued, J. M., Carlson, C., Parks, G. K., Mobius, E., Kistler, L. M., Klecker, B., Amata, E., Formisano, V., Dunlop, M., Eliasson, L., Korth, A., Lavraud, B. & McCarthy, M. 2003 Evidence for impulsive solar wind plasma penetration through the dayside magnetopause. *Annales Geophysicae* **21** (2), 457–472. (Cited on page 11.)

Mac Low, Mordecai-Mark & Klessen, Ralf S. 2004 Control of star formation by supersonic turbulence. *Rev. Mod. Phys.* **76**, 125–194. (Cited on page 38.)

MacBride, Benjamin T., Smith, Charles W. & Forman, Miriam A. 2008 The turbulent cascade at 1 au: Energy transfer and the third-order scaling for mhd. *The Astrophysical Journal* **679** (2), 1644. (Cited on pages xix,100,110,113,114and 118.)

Mandelbrot, B. B. 1999 A multifractal walk down. *Scientific American* **71**. (Cited on page 4.)

Mangeney, A., Lacombe, C., Maksimovic, M., Samsonov, A. A., Cornilleau-Wehrlin, N., Harvey, C. C., Bosqued, J.-M. & Travnivcek,

P. 2006 Cluster observations in the magnetosheath; part 1: anisotropies of the wave vector distribution of the turbulence at electron scales. *Annales Geophysicae* **24** (12), 3507–3521. (Cited on pages 35,68and 91.)

Mangeney, A., Salem, C., Veltri, P. & Cecconi, B. 2001 Intermittency in the solar wind turbulence and the Haar wavelet transform. In *Proceedings of the Sheffield Space Plasma meeting 2001*. (Cited on page 32.)

Marino, R., Sorriso-Valvo, L., Carbone, V., Noullez, A., Bruno, R. & Bavassano, B. 2008 Heating the Solar Wind by a Magnetohydrodynamic Turbulent Energy Cascade. *Astrophys. J. Lett.* **677**, L71–L74. (Cited on pages 100,120and 121.)

Markovskii, S. A., Vasquez, B. J. & Smith, C. W. 2008 Statistical analysis of the high-frequency spectral break of the solar wind turbulence at 1AU. *Astrophys. J.* **675**, 1576. (Cited on page 31.)

Marsch, E., Muhlhauser, K.-H., Schwenn, R., Rosenbauer, H., Pilipp, W. & Neubauer, F. M. 1982 Solar wind protons: Three-dimensional velocity distributions and derived plasma parameters measured between 0.3 and 1 au. *Journal of Geophysical Research: Space Physics* **87** (A1), 52–72. (Cited on pages xiiiand 8.)

Masters, A., Stawarz, L., Fujimoto, M., Schwartz, S.J., Sergis, N., Thomsen, M.F., Retino, A., Hasegawa, H., Zieger, B., Lewis, G.R., Coates, A.J., Canu, P. & Dougherty, M.K. 2013 Electron acceleration to relativistic energies at a strong quasi-parallel shock wave. *Nature Physics* **9**, 164–167. (Cited on page 12.)

Matthaeus, W. H., Ambrosiano, J. J. & Goldstein, M. L. 1984 Particle-acceleration by turbulent magnetohydrodynamic reconnection. *Physical Review Letters* **53**, 1449–1452. (Cited on page 32.)

Matthaeus, W. H., Breech, B., Dmitruk, P., Bemporad, A., Poletto, G., Velli, M. & Romoli, M. 2007 Density and magnetic field signatures of interplanetary $1/f$ noise. *The Astrophysical Journal Letters* **657** (2), L121. (Cited on page 30.)

Matthaeus, W. H. & Brown, M. R. 1988 Nearly incompressible magnetohydrodynamics at low mach number. *Phys. Fluids* **31**, 3634–3644. (Cited on page 40.)

Matthaeus, W. H., Dasso, S., Weygand, J. M., Milano, L. J., Smith, C. W. & Kivelson, M. G. 2005 Spatial Correlation of Solar-Wind Turbulence from Two-Point Measurements. *Phys. Rev. Lett.* **95**, 231101. (Cited on pages 5and 9.)

Matthaeus, W. H. & Goldstein, M. L. 1986 Low-Frequency 1/f Noise in the Interplanetary Magnetic Field. *Phys. Rev. Lett.* **57** (4), 495–498. (Cited on pages 9and 30.)

Matthaeus, William H., Goldstein, Melvyn L. & Montgomery, David C. 1983 Turbulent generation of outward-traveling interplanetary alfvénic fluctuations. *Phys. Rev. Lett.* **51**, 1484–1487. (Cited on page 28.)

Matthaeus, W. H., Goldstein, M. L. & Roberts, D. A. 1990 Evidence for the Presence of Quasi-Two-Dimensional Nearly Incompressible Fluctuations in the Solar Wind. *J. Geophys. Res.* **95**, 20673. (Cited on pages 28and 29.)

Matthaeus, W. H., Minnie, J., Breech, B., Parhi, S., Bieber, J. W. & Oughton, S. 2004 Transport of cross helicity and radial evolution of alfvénicity in the solar wind. *Geophysical Research Letters* **31** (12), n/a–n/a. (Cited on page 28.)

McComas, D. J., Bame, S. J., Barraclough, B. L., Feldman, W. C., Funsten, H. O., Gosling, J. T., Riley, P., Skoug, R., Balogh, A., Forsyth, R., Goldstein, B. E. & Neugebauer, M. 1998 Ulysses' return to the slow solar wind. *Geophysical Research Letters* **25** (1), 1–4. (Cited on pages xiiiand 7.)

McComas, D. J., Barraclough, B. L., Funsten, H. O., Gosling, J. T., Santiago-Munoz, E., Skoug, R. M., Goldstein, B. E., Neugebauer, M., Riley, P. & Balogh, A. 2000 Solar wind observations over ulysses' first full polar orbit. *Journal of Geophysical Research: Space Physics* **105** (A5), 10419–10433. (Cited on page 7.)

McFadden, J. P., Carlson, C. W., Larson, D., Ludlam, M., Abiad, R., Elliott, B., Turin, P., Marckwordt, M. & Angelopoulos, V. 2009 *The THEMIS ESA Plasma Instrument and In-flight Calibration*, pp. 277–302. New York, NY: Springer New York. (Cited on page 97.)

Meyrand, Romain & Galtier, Sébastien 2013 Anomalous $k^{-8/3}$ Spectrum in Electron Magnetohydrodynamic Turbulence. *Physical Review Letters* **111** (2), 264501. (Cited on page 30.)

Montgomery, D., Brown, M. R. & Matthaeus, W. H. 1987 Density fluctuation spectra in magnetohydrodynamic turbulence. *J. Geophys. Res.* **92** (11), 282–284. (Cited on pages 38and 40.)

Montgomery, David & Turner, Leaf 1981 Anisotropic magnetohydrodynamic turbulence in a strong external magnetic field. *Physics of Fluids* **24** (5), 825–831. (Cited on page 29.)

Moreno, G., Bavassano Cattaneo, M. B., Russo, G. & Richardson, J. D. 1999 MHD Turbulence in the Saturn's Magnetosheath Downstream of a Quasi Perpendicular and a Quasi Parallel Shock. In *Plasma Turbulence and Energetic*

Particles in Astrophysics (ed. M. Ostrowski & R. Schlickeiser), pp. 154–160. (Cited on page 35.)

Mott-Smith, H. M. & Langmuir, Irving 1926 The theory of collectors in gaseous discharges. *Phys. Rev.* **28**, 727–763. (Cited on page 80.)

Nakamura, Fumitaka & Li, Zhi-Yun 2007 Protostellar turbulence driven by collimated outflows. *The Astrophysical Journal* **662** (1), 395. (Cited on page 38.)

Osman, K. T., Matthaeus, W. H., Greco, A. & Servidio, S. 2011*a* Evidence for inhomogeneous heating in the solar wind. *The Astrophysical Journal Letters* **727** (1), L11. (Cited on pages 9,30and 32.)

Osman, K. T., Wan, M., Matthaeus, W. H., Weygand, J. M. & Dasso, S. 2011*b* Anisotropic third-moment estimates of the energy cascade in solar wind turbulence using multispacecraft data. *Phys. Rev. Lett.* **107**, 165001. (Cited on page 121.)

Ossenkopf, V. & Mac Low, M.-M. 2002 Turbulent velocity structure in molecular clouds. *Astronomy and Astrophysics* **390**, 307–326. (Cited on page 38.)

Padoan, P., Nordlund, A. & Jones, B. J. T. 1997 The universality of the stellar initial mass function. *Monthly Notices of the RAS* **288**, 145–152. (Cited on page 39.)

Parashar, T. N., Servidio, S., Shay, M. A., Breech, B. & Matthaeus, W. H. 2011 Effect of driving frequency on excitation of turbulence in a kinetic plasma. *Physics of Plasmas* **18** (9). (Cited on page 32.)

Parker, N. G., Allen, A. J., Barenghi, C. F. & Proukakis, N. P. 2015 A quantum storm in a teacup. *ArXiv e-prints* . (Cited on page 3.)

Paschmann, G. & Daly, P. W. 1998 Analysis Methods for Multi-Spacecraft Data. ISSI Scientific Reports Series SR-001, ESA/ISSI, Vol. 1. ISBN 1608-280X, 1998. *ISSI Scientific Reports Series* **1**. (Cited on pages 52and 88.)

Passot, T. & Henri, P. 2007 Collisionless magnetohydrodynamics with gyrokinetic effects. *Phys. Plasmas* **14**, 082502. (Cited on pages 8and 132.)

Passot, T. & Vázquez-Semadeni, E. 1998 Density probability distribution in one-dimensional polytropic gas dynamics. *PRE* **58**, 4501–4510. (Cited on page 39.)

Pedersen, A. 1995 Solar wind and magnetosphere plasma diagnostics by spacecraft electrostatic potential measurements. *Annales Geophysicae* **13** (2), 118–129. (Cited on page 55.)

Perri, S., Goldstein, M. L., Dorelli, J. C. & Sahraoui, F. 2012 Detection of small-scale structures in the dissipation regime of solar-wind turbulence. *Phys. Rev. Lett.* **109**, 191101. (Cited on page 76.)

Pizzo, V. 1978 A three-dimensional model of corotating streams in the solar wind, 1. theoretical foundations. *Journal of Geophysical Research: Space Physics* **83** (A12), 5563–5572. (Cited on pages xiiiand 7.)

Podesta, J. J. 2009 Dependence of solar-wind power spectra on the direction of the local mean magnetic field. *The Astrophysical Journal* **698** (2), 986. (Cited on page 119.)

Podesta, J. J., Borovsky, J. E. & Gary, S. P. 2010 A kinetic Alfven wave cascade subject to collisionless damping cannot reach electron scales in the solar wind at 1 AU. *Astrophys. J.* **712**, 685. (Cited on page 103.)

Podesta, John J. & TenBarge, Jason M. 2012 Scale dependence of the variance anisotropy near the proton gyroradius scale: Additional evidence for kinetic alfvén waves in the solar wind at 1 au. *Journal of Geophysical Research: Space Physics* **117** (A10), n/a–n/a. (Cited on pages 30,67,68and 69.)

Poincaré, H. 1899 *Les méthodes nouvelles de la mécanique céleste: Invariants intégraux. Solutions périodiques du deuxième genre. Solutions doublement asymptotiques. 1899. Les méthodes nouvelles de la mécanique céleste* . Gauthier-Villars et fils. (Cited on page 4.)

Politano, H. & Pouquet, A. 1998 von kármán–howarth equation for magnetohydrodynamics and its consequences on third-order longitudinal structure and correlation functions. *Phys. Rev. E* **57**, R21–R24. (Cited on pages 13,15,21,40,98and 164.)

Proment, D., Nazarenko, S. & Onorato, M. 2009 Quantum turbulence cascades in the gross-pitaevskii model. *Phys. Rev. A* **80**, 051603. (Cited on page 3.)

Reme, H., Bosqued, J. M., Sauvaud, J. A., Cros, A., Dandouras, J., Aoustin, C., Bouyssou, J., Camus, Th., Cuvilo, J., Martz, C., Medale, J. L., Perrier, H., Romefort, D., Rouzaud, J., D'Uston, C., Mobius, E., Crocker, K., Granoff, M., Kistler, L. M., Popecki, M., Hovestadt, D., Klecker, B., Paschmann, G., Scholer, M., Carlson, C. W., Curtis, D. W., Lin, R. P., Mcfadden, J. P., Formisano, V., Amata, E., Bavassano-Cattaneo, M. B., Baldetti, P., Belluci, G., Bruno, R., Chionchio, G., Di Lellis, A., Shelley, E. G., Ghielmetti, A. G., Lennartsson, W., Korth, A., Rosenbauer, H., Lundin, R., Olsen, S., Parks, G. K., Mccarthy, M. & Balsiger, H. 1997 The cluster ion spectrometry (cis) experiment. *Space Science Reviews* **79** (1), 303–350. (Cited on page 53.)

Retinò, A., Sundkvist, D., Vaivads, A., Mozer, F., André, M. & Owen, C. J. 2007 In situ evidence of magnetic reconnection in turbulent plasma. *Nature Physics* **3**, 236. (Cited on pages 6and 36.)

REYNOLDS, O. 1883 *An Experimental Investigation of the Circumstances which Determine Whether the Motion of Water Shall be Direct Or Sinuous: And of the Law of Resistance in Parallel Channels*. *Philosophical transactions* . Royal Society of London. (Cited on page 15.)

RICHARDSON, JOHN D., PAULARENA, KAROLEN I., LAZARUS, ALAN J. & BELCHER, JOHN W. 1995 Radial evolution of the solar wind from imp 8 to voyager 2. *Geophysical Research Letters* **22** (4), 325–328. (Cited on page 8.)

RICHARDSON, L. F. 1922 Weather prediction by numerical process. cambridge (university press). *Quarterly Journal of the Royal Meteorological Society* **48** (203), 282–284. (Cited on page 20.)

ROBERTS, D. AARON 2010 Demonstrations that the solar wind is not accelerated by waves or turbulence. *The Astrophysical Journal* **711** (2), 1044. (Cited on page 31.)

ROBERTS, D. A., GOLDSTEIN, M. L., KLEIN, L. W. & MATTHAEUS, W. H. 1987 Origin and evolution of fluctuations in the solar wind: Helios observations and helios-voyager comparisons. *Journal of Geophysical Research: Space Physics* **92** (A11), 12023–12035. (Cited on page 113.)

ROMANELLI, N., MODOLO, R., DUBININ, E., BERTHELIER, J.-J., BERTUCCI, C., WAHLUND, J. E., LEBLANC, F., CANU, P., EDBERG, N. J. T., WAITE, H., KURTH, W. S., GURNETT, D., COATES, A. & DOUGHERTY, M. 2014 Outflow and plasma acceleration in titan's induced magnetotail: Evidence of magnetic tension forces. *Journal of Geophysical Research: Space Physics* **119** (12), 9992–10,005, 2014JA020391. (Cited on page 84.)

RÖNMARK, K. 1982 WHAMP-Waves in homogeneous, anisotropic multicomponent plasmas. *Kiruna Geophys. Inst. KGI Report 179, Univ. of Umea, Kiruna, Sweden.* **179**. (Cited on page 67.)

ROSSI, CLAUDIA 2015 Kelvin-Helmholtz instability at the magnetopause : theory and observations. Theses, Université Pierre et Marie Curie - Paris VI. (Cited on page 78.)

RUSSELL, C. T., GOSLING, J. T., ZWICKL, R. D. & SMITH, E. J. 1983 Multiple spacecraft observations of interplanetary shocks: Isee three-dimensional plasma measurements. *Journal of Geophysical Research: Space Physics* **88** (A12), 9941–9947. (Cited on page 88.)

SAHRAOUI, F., BELMONT, G. & GOLDSTEIN, M. L. 2012 New insight into short-wavelength solar wind fluctuations from Vlasov theory. *Astrophys. J.* **748**, 100. (Cited on pages 29,67and 69.)

SAHRAOUI, F., BELMONT, G., PINÇON, J. L., REZEAU, L., BALOGH, A., ROBERT, P. & CORNILLEAU-WEHRLIN, N. 2004 Magnetic turbulent spectra in the magnetosheath: New insights. *Annales Geophysicae* **22**, 2283. (Cited on page 34.)

Sahraoui, F., Belmont, G., Rezeau, L. & Cornilleau-Wehrlin, N. 2006 Anisotropic turbulent spectra in the terrestrial magnetosheath as seen by the cluster spacecraft. *Phys. Rev. Lett.* **96** (7), 075002. (Cited on pages 5,11,13,34,35,68,71and 91.)

Sahraoui, F., Goldstein, M. L., Belmont, G., Canu, P. & Rezeau, L. 2010 Three Dimensional Anisotropic k Spectra of Turbulence at Subproton scales in the Solar Wind. *Phys. Rev. Lett.* **105**, 131101. (Cited on pages 9,30,32,68,91and 120.)

Sahraoui, F., Goldstein, M. L. & Khotyaintse, Yu. V. 2009 Evidence of a Cascade and Dissipation of Solar-Wind Turbulence at the Electron Gyroscale. *Phys. Rev. Lett.* **102** (23), 231102. (Cited on pages 9,28,30,32,91and 120.)

Sahraoui, F., Huang, S. Y., Belmont, G., Goldstein, M. L., Retino, A., Robert, P. & Patoul, J. De 2013 Scaling of the electron dissipation range of solar wind turbulence. *The Astrophysical Journal* **777** (1), 15. (Cited on pages 32and 59.)

Sahraoui, F., Pinçon, J. L., Belmont, G., Rezeau, L., Cornilleau-Wehrlin, N., Robert, P., Mellul, L., Bosqued, J. M., Balogh, A., Canu, P. & Chanteur, G. 2003 Ulf wave identification in the magnetosheath: The k-filtering technique applied to cluster ii data. *J. Geophys. Res.* **108**, 1335. (Cited on pages 35and 68.)

Saito, S., Gary, S. P., Li, H. & Narita, Y. 2008 Whistler turbulence: Particle-in-cell simulations. *Phys. Plasmas* **15** (102305). (Cited on page 30.)

Salem, C. S., Howes, G. G., Sundkvist, D., Bale, S. D., Chaston, C. C., Chen, C. H. K. & Mozer, F. S. 2012 Identification of Kinetic Alfven Wave Turbulence in the Solar Wind. *ApJ Lett.* **745**, L9. (Cited on page 67.)

Schekochihin, A. A., Cowley, S. C., Dorland, W., Hammett, G. W., Howes, G. G., Quataert, E. & Tatsuno, T. 2009 Astrophysical Gyrokinetics: Kinetic and Fluid Turbulent Cascades in Magnetized Weakly Collisional Plasmas. *Astrophys. J. S.* **182**, 310–377. (Cited on pages xxiii,6,8,9,30and 75.)

Schmidt, W. 2009 Large Eddy Simulations of Supersonic Turbulence. *ArXiv e-prints* . (Cited on pages 38and 39.)

Schmidt, W. 2013 *Numerical Modelling of Astrophysical Turbulence*. *SpringerBriefs in Astronomy* -. Springer International Publishing. (Cited on page 37.)

Schmidt, W., Federrath, C. & Klessen, R. 2008 Is the scaling of supersonic turbulence universal? *Physical Review Letters* **101** (19), 194505. (Cited on pages 39and 99.)

Schwartz, S. J. 1998 Shock and Discontinuity Normals, Mach Numbers, and Related Parameters. *ISSI Scientific Reports Series* **1**, 249–270. (Cited on page 88.)

Schwartz, S. J., Burgess, D. & Moses, J. J. 1996 Low-frequency waves in the earth's magnetosheath: present status. *Annales Geophysicae* **14** (11), 1134–1150. (Cited on page 35.)

Scudder, J. D., Cao, Xuejun & Mozer, F. S. 2000 Photoemission current-spacecraft voltage relation: Key to routine, quantitative low-energy plasma measurements. *Journal of Geophysical Research: Space Physics* **105** (A9), 21281–21294. (Cited on page 55.)

Servidio, S 2015 *Private Communication* . (Cited on page 132.)

Shi, Q. Q., Hartinger, M., Angelopoulos, V., Zong, Q.-G., Zhou, X.-Z., Zhou, X.-Y., Kellerman, A., Tian, A. M., Weygand, J., Fu, S. Y., Pu, Z. Y., Raeder, J., Ge, Y. S., Wang, Y. F., Zhang, H. & Yao, Z. H. 2013 Themis observations of ulf wave excitation in the nightside plasma sheet during sudden impulse events. *Journal of Geophysical Research: Space Physics* **118** (1), 284–298. (Cited on page 95.)

Sibeck, D. G., Lopez, R. E. & Roelof, E. C. 1991 Solar wind control of the magnetopause shape, location, and motion. *Journal of Geophysical Research: Space Physics* **96** (A4), 5489–5495. (Cited on pages xviand 64.)

Smith, Charles W., Goldstein, Melvyn L. & Matthaeus, William H. 1983 Turbulence analysis of the jovian upstream 'wave' phenomenon. *Journal of Geophysical Research: Space Physics* **88** (A7), 5581–5593. (Cited on pages 28and 71.)

Smith, Charles W., Goldstein, Melvyn L., Matthaeus, William H. & Vinas, Adolfo F. 1984 Correction to "turbulence analysis of the jovian upstream 'wave' phenomenon". *Journal of Geophysical Research: Space Physics* **89** (A10), 9159–9160. (Cited on page 28.)

Smith, C. W., Hamilton, K., Vasquez, B. J. & Leamon, R. J. 2006 Dependence of the dissipation range spectrum of inter-planetary magnetic fluctuations on the rate of energy cascade. *ApJ* **645**, L85. (Cited on page 31.)

Smith, Charles W., Stawarz, Joshua E., Vasquez, Bernard J., Forman, Miriam A. & MacBride, Benjamin T. 2009*a* Turbulent cascade at 1 au in high cross-helicity flows. *Phys. Rev. Lett.* **103**, 201101. (Cited on page 32.)

Smith, Charles W., Stawarz, Joshua E., Vasquez, Bernard J., Forman, Miriam A. & MacBride, Benjamin T. 2009*b* Turbulent cascade at 1 au in high cross-helicity flows. *Phys. Rev. Lett.* **103**, 201101. (Cited on pages 100,103,111,113and 118.)

Song, P., Russell, C. T. & Gary, S. P. 1994 Identification of low-frequency fluctuations in the terrestrial magnetosheath. *Journal of Geophysical Research: Space Physics* **99** (A4), 6011–6025. (Cited on pages 34and 71.)

Song, P., Russell, C. T. & Thomsen, M. F. 1992 Slow mode transition in the frontside magnetosheath. *Journal of Geophysical Research: Space Physics* **97** (A6), 8295–8305. (Cited on page 34.)

Sorriso-Valvo, L., Carbone, V., Veltri, P., Consolini, G. & Bruno, R. 1999 Intermittency in the solar wind turbulence through probability distribution functions of fluctuations. *GRL* **26**, 1801–1804. (Cited on pages xiv,32and 33.)

Southwood, David J. & Kivelson, Margaret G. 1993*a* Mirror instability: 1. physical mechanism of linear instability. *Journal of Geophysical Research: Space Physics* **98** (A6), 9181–9187. (Cited on page 34.)

Southwood, David J. & Kivelson, Margaret G. 1993*b* Mirror instability: 1. physical mechanism of linear instability. *Journal of Geophysical Research: Space Physics* **98** (A6), 9181–9187. (Cited on page 71.)

Sridhar, S. & Goldreich, P. 1994 Toward a theory of interstellar turbulence. 1: Weak Alfvenic turbulence. *Astrophysical Journal* **432**, 612–621. (Cited on page 22.)

Stawicki, O., Gary, S. P. & Li, H. 2001 Solar wind magnetic fluctuation spectra: Dispersion versus damping. *J. Geophys. Res.* **106** (A5), 8273. (Cited on page 29.)

Stix, T.H. 1992 *Waves in Plasmas*. American Inst. of Physics. (Cited on page 67.)

Sundkvist, D., Retinò, A., Vaivads, A. & Bale, S. D. 2007 Dissipation in turbulent plasma due to reconnection in thin current sheets. *Phys. Rev. Lett.* **99**, 025004. (Cited on pages 35,36,57and 65.)

Supratik, B. 2014 Compressible turbulence in space and astrophysical plasmas: Analytical approach and in-situ data analysis for the solar wind. Theses, Université Paris Sud. (Cited on pages xiiiand 22.)

Thomsen, M. F., Reisenfeld, D. B., Delapp, D. M., Tokar, R. L., Young, D. T., Crary, F. J., Sittler, E. C., McGraw, M. A. & Williams, J. D. 2010 Survey of ion plasma parameters in saturn's magnetosphere. *Journal of Geophysical Research: Space Physics* **115** (A10). (Cited on page 84.)

Trakhinin, Yuri 2009 The existence of current-vortex sheets in ideal compressible magnetohydrodynamics. *Archive for Rational Mechanics and Analysis* **191** (2), 245–310. (Cited on page 76.)

Tsinober, A. 2001 *An informal introduction to turbulence*. Kluwer Academic Publishers. (Cited on page 3.)

Tsurutani, B. T., Smith, E. J., Anderson, R. R., Ogilvie, K. W., Scudder, J. D., Baker, D. N. & Bame, S. J. 1982 Lion roars and nonoscillatory drift mirror waves in the magnetosheath. *Journal of Geophysical Research: Space Physics* **87** (A8), 6060–6072. (Cited on page 35.)

Tu, C.-Y. & Marsch, E. 1995 MHD Structures, Waves and Turbulence in the Solar wind: Observations and Theories. *Space Sci. Rev.* **73**. (Cited on pages 28,32and 33.)

Tu, C.-Y. & Marsch, E. 1997 Two-fluid model for heating of the solar corona and acceleration of the solar wind by high-frequency alfvén waves. *Solar Physics* **171** (2), 363–391. (Cited on page 7.)

Tu, C.-Y., Marsch, E. & Rosenbauer, H. 1990 The dependence of mhd turbulence spectra on the inner solar wind stream structure near solar minimum. *Geophysical Research Letters* **17** (3), 283–286. (Cited on page 28.)

Vasquez, B. J., Smith, C. W., Hamilton, K., MacBride, B. T. & Leamon, R. J. 2007 Evaluation of the turbulent energy cascade rates from the upper inertial range in the solar wind at 1 au. *J. Geophys. Res. (Space Physics)* **112**, 7101. (Cited on page 120.)

Vázquez-Semadeni, Enrique, Passot, Thierry & Pouquet, Annick 1996 Influence of cooling-induced compressibility on the structure of turbulent flows and gravitational collapse. *The Astrophysical Journal* **473** (2), 881. (Cited on pages 11and 36.)

Velli, Marco, Grappin, Roland & Mangeney, André 1989 Turbulent cascade of incompressible unidirectional alfvén waves in the interplanetary medium. *Phys. Rev. Lett.* **63**, 1807–1810. (Cited on page 30.)

Veltri, P. & Mangeney, A. 1998 Scaling laws and intermittent structures in solar wind MHD turbulence. In *AIP Conference Proceedings*, , vol. 471, pp. 543–546. AIP. (Cited on page 32.)

Violante, L., Cattaneo, M. B. Bavassano, Moreno, G. & Richardson, J. D. 1995 Observations of mirror waves and plasma depletion layer upstream of saturn's magnetopause. *Journal of Geophysical Research: Space Physics* **100** (A7), 12047–12055. (Cited on pages 35and 71.)

Went, D. R., Hospodarsky, G. B., Masters, A., Hansen, K. C. & Dougherty, M. K. 2011 A new semiempirical model of saturn's bow shock based on propagated solar wind parameters. *Journal of Geophysical Research: Space Physics* **116** (A7), a07202. (Cited on pages xv,58,59,61and 89.)

Weygand, J. M., Matthaeus, W. H., Dasso, S., Kivelson, M. G. & Walker, R. J. 2007 Taylor scale and effective magnetic Reynolds number determination from plasma sheet and solar wind magnetic field fluctuations. *Journal of Geophysical Research (Space Physics)* **112**, A10201. (Cited on page 78.)

Wicks, R. T., Horbury, T. S., Chen, C. H. K. & Schekochihin, A. A. 2010 Power and spectral index anisotropy of the entire inertial range of turbulence in the fast solar wind. *Monthly Notices of the Royal Astronomical Society: Letters* **407** (1), L31–L35. (Cited on page 31.)

Wilson, R. J., Delamere, P. A., Bagenal, F. & Masters, A. 2012 Kelvin-helmholtz instability at saturn's magnetopause: Cassini ion data analysis. *Journal of Geophysical Research: Space Physics* **117** (A3), n/a–n/a, a03212. (Cited on page 78.)

Wilson, R. J., Tokar, R. L., Henderson, M. G., Hill, T. W., Thomsen, M. F. & Pontius, D. H. 2008 Cassini plasma spectrometer thermal ion measurements in saturn's inner magnetosphere. *Journalng of Geophysical Research: Space Physics* **113** (A12), a12218. (Cited on page 51.)

Dudok de Wit, T. 2004 Can high-order moments be meaningfully estimated from experimental turbulence measurements? *Phys. Rev. E* **70**, 055302. (Cited on page 19.)

Dudok de Wit, T., Alexandrova, O., Furno, I., Sorriso-Valvo, L. & Zimbardo, G. 2013 Methods for characterising microphysical processes in plasmas. *Space Science Reviews* **178** (2), 665–693. (Cited on page 33.)

Wu, P., Perri, S., Osman, K., Wan, M., Matthaeus, W. H., Shay, M. A., Goldstein, M. L., Karimabadi, H. & Chapman, S. 2013 Intermittent heating in solar wind and kinetic simulations. *The Astrophysical Journal Letters* **763** (2), L30. (Cited on page 33.)

Yordanova, E., Vaivads, A., André, M., Buchert, S. C. & Vörös, Z. 2008 Magnetosheath Plasma Turbulence and Its Spatiotemporal Evolution as Observed by the Cluster Spacecraft. *Phys. Rev. Lett.* **100** (20), 205003. (Cited on pages 11,36and 65.)

Young, D. T., Berthelier, J. J., Blanc, M., Burch, J. L., Coates, A. J., Goldstein, R., Grande, M., Hill, T. W., Johnson, R. E., Kelha, V., McComas, D. J., Sittler, E. C., Svenes, K. R., Szegö, K., Tanskanen, P., Ahola, K., Anderson, D., Bakshi, S., Baragiola, R. A., Barraclough, B. L., Black, R. K., Bolton, S., Booker, T., Bowman, R., Casey, P., Crary, F. J., Delapp, D., Dirks, G., Eaker, N., Funsten, H., Furman, J. D., Gosling, J. T., Hannula, H., Holmlund, C., Huomo, H., Illiano, J. M., Jensen, P., Johnson, M. A., Linder, D. R., Luntama, T., Maurice, S., McCabe, K. P., Mursula, K., Narheim, B. T., Nordholt, J. E., Preece, A., Rudzki, J., Ruitberg, A., Smith, K., Szalai, S., Thomsen, M. F., Viherkanto, K., Vilppola, J., Vollmer, T., Wahl, T. E., Wüest, M., Ylikorpi, T. & Zinsmeyer, C. 2004 Cassini Plasma Spectrometer Investigation. *Space Science Reviews* **114**, 1–112. (Cited on pages xiv,xvii,51and 80.)

ZANK, G. P. & MATTHAEUS, W. H. 1990 Nearly incompressible hydrodynamics and heat conduction. *Phys. Rev. Lett.* **64**, 1243–1246. (Cited on page 40.)

ZIEGER, BERTALAN & HANSEN, KENNETH C. 2008 Statistical validation of a solar wind propagation model from 1 to 10 au. *Journal of Geophysical Research: Space Physics* **113** (A8), n/a–n/a, a08107. (Cited on page 89.)

Printed in France
Centre Poly-media
École Polytechnique

Abstract

Among the different astrophysical plasmas, the solar wind and the planetary magnetosheaths represent the best laboratories for studying the properties of fully developed plasma turbulence. Because of the relatively weak density fluctuations ($\sim 10\%$) in the solar wind, the low frequency fluctuations are usually described using the incompressible MHD theory. Nevertheless, the effect of the compressibility (in particular in the fast wind) has been a subject of active research within the space physics community over the last three decades.

My thesis is essentially dedicated to the study of compressible turbulence in different plasma environments, the planetary magnetosheaths (of Saturn and Earth) and the fast and slow solar wind. This was done using in-situ spacecraft data from the Cassini, Cluster and THEMIS/ARTEMIS satellites.

I first investigated the properties of MHD and kinetic scale turbulence in the magnetosheath of Saturn using Cassini data at the MHD scales and compared them to known features of the solar wind turbulence. This work was completed with a more detailed analysis performed in the magnetosheath of Earth using the Cluster data. Then, by applying the recently derived exact law of compressible isothermal MHD turbulence to the in-situ observations from THEMIS and CLUSTER spacecrafts, a detailed study regarding the effect of the compressibility on the energy cascade (dissipation) rate in the fast and the slow wind is presented. Several new empirical laws are obtained, which include the power-law scaling of the energy cascade rate as function of the turbulent Mach number. Eventually, an application of this exact model to a more compressible medium, the magnetosheath of Earth, using the Cluster data provides the first estimation of the energy dissipation rate in the magnetosheath, which is found to be up to two orders of magnitude higher than that observed in the solar wind.

Keywords: Turbulence, compressible turbulence, astrophysical plasmas, solar wind, planetary magnetosheaths, Earth, Saturn, in-situ observations

Résumé

Parmi les différents plasmas spatiaux, le vent solaire et les magnétogaines planétaires représentent les meilleurs laboratoires pour l'étude des propriétés de la turbulence. Les fluctuations de densité dans le vent solaire étant faibles, à basses fréquences ces dernières sont généralement décrites par la théorie de la MHD incompressible. Malgré son incompressibilité, l'effet de la compressibilité dans le vent solaire a fait l'objet de nombreux travaux depuis des décennies, à la fois théoriques, numériques et observationnels.

Le but de ma thèse est d'étudier le rôle de la compressibilité dans les magnétogaines planétaires (de la Terre et de Saturne) en comparaison avec un milieu beaucoup plus étudié et moins compressible (quasi incompressible), le vent solaire. Ce travail a été realisé en utilisant des données in-situ de trois sondes spatiales, Cassini, Cluster et THEMIS B/ARTEMIS P1.

La première partie de mon travail a été consacrée à l'étude des propriétés de la turbulence dans la magnétogaine de Saturne aux échelles MHD et sub-ionique, en comparaison avec celle de la Terre en utilisant les données Cassini et Cluster respectivement. Ensuite j'ai appliqué la loi exacte de la turbulence isotherme et compressible dans le vent rapide et lent en utilisant les données THEMIS B/ARTEMIS P1, afin d'étudier l'effet et le rôle de la compressibilité sur le taux de transfert de l'énergie dans la zone inertielle. Enfin, une première application de ce modèle dans la magnétogaine de la Terre est présentée en utilisant les données Cluster.

Mots clés: Turbulence, turbulence compressible, plasmas astrophysiques, vent solaire, magnétogaines planétaires, Terre, Saturne, analyse de données